HAL
open science

Grain growth by the Galerkin method for the formation of planets

Maxime Lombart

To cite this version:

Maxime Lombart. Grain growth by the Galerkin method for the formation of planets. Earth and Planetary Astrophysics [astro-ph.EP]. Université de Lyon, 2020. English. NNT : 2020LYSEN043 . tel-03106225

HAL Id: tel-03106225

https://theses.hal.science/tel-03106225

Submitted on 11 Jan 2021

HAL is a multi-disciplinary open access archive for the deposit and dissemination of scientific research documents, whether they are published or not. The documents may come from teaching and research institutions in France or abroad, or from public or private research centers.

L'archive ouverte pluridisciplinaire **HAL**, est destinée au dépôt et à la diffusion de documents scientifiques de niveau recherche, publiés ou non, émanant des établissements d'enseignement et de recherche français ou étrangers, des laboratoires publics ou privés.

Numéro National de Thèse : 2020LYSEN043

THÈSE DE DOCTORAT DE L'UNIVERSITÉ DE LYON

opérée par

l'École Normale Supérieure de Lyon

École Doctorale N°52
École Doctorale de Physique et d'Astrophysique de Lyon

Discipline : Physique
Spécialité : Astrophysique

Soutenue publiquement le vendredi 18 septembre 2020

par Maxime LOMBART

Croissance des grains par méthode de Galerkine pour la formation des planètes

-

Grain growth by the Galerkin method for the formation of planets

---

Devant le jury composé de :

BOCCALETTI Anthony, Directeur de recherche, LESIA	Rapporteur
CHARNOZ Sébastien, Professeur, IPGP	Rapporteur
MICHAUT Chloé, Professeure, LGLTPE	Examinatrice
RAYNAL Florence, Chargée de recherche, École Centrale de Lyon	Examinatrice
TEYSSIER Romain, Professeur, CTAC	Examinateur
YSARD Nathalie, Chargée de recherche, Université Paris-Sud	Examinatrice
LAIBE Guillaume, Maître de Conférences, CRAL	Directeur

ABSTRACT

Recent spatially resolved observations of protoplanetary discs have revealed the presence of structures with complex morphologies, indicating the probable presence of protoplanets inside. How could the grains in the disc have formed these structures? How will they evolve? To answer these questions, we need to understand how grains grow inside the disc. However, numerical resolution of the coagulation equation by traditional methods requires prohibitive sampling, making it impossible to integrate it into a three-dimensional hydrodynamic code.

The goal of this thesis is the development of an algorithm to solve the coagulation equation while respecting the constraints guided by astrophysics: rigorous conservation of mass while keeping a precision lower than the hydrodynamic errors on a mass spectrum relevant to the observations. Sampling must be minimal to allow coupling with a hydrodynamic code. To do so, the coagulation equation is solved by an original numerical scheme based on the discontinuous Galerkin method and a high order integration. The efficiency of the method is demonstrated on the known solutions of the equation and transferred to the context of planet formation.

Work carried out in parallel with this study will be presented. Firstly, an analysis of extra-solar planet observations made with the SPHERE/VLT instrument. Secondly, the numerical resolution of stochastic equations to understand grain sedimentation in turbulent disks.

RÉSUMÉ

Les récentes observations spatialement résolues de disques protoplanétaires ont révélé la présence de structures à la morphologie complexe, indiquant la présence probable de protoplanètes à l'intérieur. Comment les grains contenus dans le disque ont-ils pu former ces structures ? Comment vont elles évoluer ? Pour répondre à ces questions, il faut comprendre comment les grains grossissent dans le disque. Or, la résolution numérique de l'équation de coagulation par les méthodes traditionnelles requiert un échantillonnage prohibitif, rendant impossible son intégration dans un code hydrodynamique tri-dimensionnel.

Le but de cette thèse est le développement d'un algorithme permettant de résoudre l'équation de coagulation en respectant les contraintes guidées par l'astrophysique : conservation rigoureuse de la masse en gardant une précision inférieure aux erreurs hydrodynamique sur un spectre de masse pertinent pour les observations. L'échantillonnage doit-être minimal pour permettre un couplage avec un code hydrodynamique. Pour ce faire, l'équation de coagulation est résolue par un schéma numérique original reposant sur la méthode de Galerkine discontinue et une intégration d'ordre élevé. L'efficacité de la méthode est démontrée sur les solutions connues de l'équation et transférée au contexte de la formation des planètes.

Des travaux réalisés en parallèle de cette étude seront présentés. En premier lieu, une analyse d'observations de planètes extra-solaires réalisées avec l'instrument SPHERE/VLT. En second lieu, la résolution numérique d'équations stochastiques pour comprendre la sédimentation des grains dans les disques turbulents.

REMERCIEMENTS

L'accomplissement de cette thèse n'aurait pas pu se faire sans le soutient de très nombreuses personnes.

Tout d'abord je remercie grandement Guillaume, mon super directeur de thèse, pour m'avoir formé, guidé et soutenu pendant cette belle thèse. Tout à commencé par le stage de M1 à Saint Andrews (Écosse). J'ai tout de suite su que faire une thèse sous ta direction serait top. J'ai énormément appris en travaillant à tes côtés, aussi bien scientifiquement qu'humainement. Ce projet sur la croissance des grains dans les disques par la résolution de l'équation de Smoluchowski est fantastique. Au début, j'ai un peu pris peur en voyant l'équation (qu'est-ce que c'est que ce truc ?!!!). Mais plus j'étudiais cette équation, utilisée dans de nombreux domaines allant des mathématiques à la biologie en passant par l'astrophysique, plus elle était fascinante. Merci beaucoup de m'avoir proposé ce sujet de thèse, j'ai toujours été très motivé par ce "petit" côté challenge, même si j'ai beaucoup stressé en obtenant les résultats que quelques semaines avant de rendre le manuscrit (mission accomplished). Bien sûr, il ne fallait pas oublier de maîtriser le contexte, merci de m'avoir enseigné toutes les connaissances sur la physique des disques protoplanétaires. Nos nombreuses discussions sur la physique ont toujours été très formatrice avec parfois un débit d'idées à la seconde assez impressionnante, comme dirait un certain mathématicien "ça va être sport". Ces trois années ont été parsemé d'aventures notamment un trajet Lyon-Milan non pas en train mais ta voiture qui faisait un certain bruit. Heureusement que le café italien est efficace pour ne pas s'endormir. Certains dans le labo te surnomme "Big Laibowski" mais je pense qu'il y aura des vis à serrer et des points à mettre sur les i pour pas que le labo tombe sous le contrôle des doctorants. Je suis assez fier d'avoir été ton premier doctorant.

Je remercie également Benoît pour ces trois années. Merci pour tes conseils et ton soutient tout au long de cette thèse. J'ai toujours souhaité finir l'algorithme rapidement pour vous le vendre pour RAMSES, car c'est gratuit uniquement pour les codes SPH. Comme il n'est pas encore fini, je serai plus indulgent et j'ai hâte de pouvoir travailler avec Ugo et toi dans le future. Un grand merci d'avoir accepté de faire des sorties vélos avec moi et de m'attendre dans les côtes. Vous avez essayé avec Quentin de me dégoûter en tentant le mur d'Yzeron, mais c'était mal me connaître. Étant très sportif mais pas bien affûté (contrairement à d'autres), j'ai toujours suivi les différentes aventures sportives proposées par Benoît. La hiérarchie était toujours respectée, j'étais dans la ligne de brasse alors que Ugo enseignait le crowl à Benoît. Par contre en course à pied, je me suis toujours incliné même au 10km du Run in Lyon. Alors selon des rumeurs, une équipe de farfelu du labo te nommerai "Big Ben". Comme pour Guillaume, il va falloir resserrer des vis pour garder le contrôle. Merci encore pour ces belles années !

J'imagine que ça n'a pas été facile tous les jours pour l'équipe de supporter des thésards pas toujours très fute-fute, dont je faisais parti bien sûr. Pour cela, on a trouvé la parade terrible qui est d'apporter des croissants et pains au chocolat (et non chocolatine) tout chaud. On a même pensé à servir les cafés aux permanents mais on s'est dit que juste s'occuper de l'entretien de la machine à café suffirait. Un grand merci à Gilles (le boss de l'équipe) pour son soutient durant ces années. J'ai beaucoup appris en écoutant les différents discussions physiques en salle café. J'ai aussi pu apprendre plein d'histoires croustillantes sur les gens du labo de physique de l'ENS. Il paraîtrait que tu as battu

le record du semi-marathon. Merci encore pour ces délicieux repas de Noël organisés au labo, les huîtres ont définitivement leur place au menu. Je suis un peu déçu que le concert qu'on avait prévu pour ton anniversaire n'ai pas eu lieu. Un grand merci d'avoir durement négocier avec l'administration pour que Guillaume soit officiellement mon directeur de thèse. Il va de soi que la bouteille de châteaux Margaux 1964 te sera livrée dans les plus brefs délais. Je souhaite remercier Christophe pour ces années et aussi pour m'avoir permis de rencontrer Guillaume pour mon stage de M1. Je n'aurais sans doute pas pu faire cette thèse sans cela. Merci aussi pour ton aide pour enseigner aux agrégatifs de chimie, j'espère leur avoir appris des choses pendant les colles. J'ai tout fait pour empêcher qu'Étienne ou Quentin te lance des nerfs à travers notre porte de bureau. Avec le bureau des thésards le plus bruyant en face de ton bureau, je te remercie de nous avoir supporter. Merci à Gérard pour ton soutient. Merci également pour mon inscription en thèse, et d'avoir suivi mon travail ces années. Merci beaucoup pour l'implémentation de cette satané fonction hypergéométrique2F1, j'ai peur qu'elle un retour fracassant d'ici peu. Merci à Jérémy pour ton soutient et ton aide. Tes remarques sont toujours pertinentes. Merci d'avoir écouter mon histoire ennuyante sur Smoluchowski lors de mes entraînements pour la soutenance et merci pour ton aide. C'était un plaisir de pouvoir t'aider à encadrer les TP d'agreg de physique. C'est super d'avoir commencé la basse mais la batterie c'est mieux. Merci également à Jenny pour le soutient. C'était également un plaisir de t'aider pour les TP d'agreg. Tu es maintenant une pro en moteur à courant continu. Sans doute un poil trop chaud cet EWASS mais heureusement les purple boys veillaient au bon fonctionnement des ventilos. Je remercie également les autres permanents du labo Isabelle, Rolf, Doris, Thomas pour les discussions et les moments passés ensemble avec toute l'équipe.

Un grand merci à Stéphanie sans qui le labo s'écroulerait. Pour les thésards tu es un peu comme notre "maman", tout se passe bien administrativement grâce à toi, et quand on a un problème on vient te voir. C'était toujours un plaisir de te signer des autographes et de t'aider pour aller chercher les gros cartons de papiers attendant à la maison du courrier. Merci également pour ce superbe séjour de ski à Avoriaz.

Maintenant ça va se gâter car je vais parler de cette équipe de thésards incroyables. Tout d'abord, un grand merci à Ugo que j'ai connu au M2 astro de Paris. Ugo a joué tous les rôles, amis, collègues et coloc. Nos aventures airbnb c'était sympa mais on était content d'avoir trouvé cet appartement. Merci énormément de m'avoir supporter pendant ces trois années, ça n'a pas du être simple. C'était toujours un plaisir d'écouter tes solos de guitare tout en buvant une bière. Ce groupe de musique (Iron Maidens) qu'on a eu un peu mal à monter a été une superbe expérience. On aura sans doute eu plus de réputation avec le groupe qu'avec nos publications. Même si le fromage nous a ensorcelé, on a essayé de tenir bon en allant exploré Lyon en footing et même en s'entraînant durement pour les 10km du Run in Lyon. A cela s'est ajouté des séances de muscu intensives. Merci pour ta bonne humeur et ton soutient durant ces belles années, et notamment pendant ce premier confinement où on devait écrire nos thèses. Hâte de pouvoir commencer ce projet de croissance des grains dans les collapses, tu vas voir on va direct former des mega-Jupiter.

Merci à toi "Etch" ou "Evgeny" ou Étienne pour ces belles années. Co-bureau remarquable, mais il faut toujours rester vigilant au nerf qu'on peut recevoir. Merci de ton aide sur mes questions de physiques et de maths. J'ai essayé de t'aider pour un code en f77 mais pas facile. Cette fête de la science avec la chambre à brouillard a été une superbe expérience, j'espère que les élèves ont compris quelques choses et qu'ils ont été émerveillé en voyant ces petits électrons traverser la chambre. En tous cas on s'est bien

amusé. Faudra qu'on s'inscrive en doublette à des tournoi de molkky, on jouait pas mal. C'était cool d'aller te voir jouer dans l'équipe une de basket de l'ENS, mais je pensais te voir dunker. J'espère que le plante se porte bien.

Quentin ou "couennetine" pour les intimes est une personne incroyablement affûtée. Merci pour ces belles années. Merci de ton aide pour mes présentations, mes calculs et mes questions sur la physique. J'ai essayé de comprendre tes calculs, mais il y a beaucoup trop d'indices. Et du coup, est-ce que tu as compris Newton ? Merci pour ton fichier de configuration pour la biblio, ça marche au top, on a des belles couleurs. Merci pour ces belles sorties sportives. Merci de m'avoir attendu dans les côtes avec Benoît. J'en profite pour remercier également le club de vélo de Villeurbannes de m'avoir accepté dans leurs sorties. C'était super de rouler en groupe surtout pour la première sortie de 100km dans les monts d'or. Dans ce groupe, il fallait pas être trop en queue de peloton sinon Quentin devait m'attendre pour que je reste pas seul. Quentin est la seule personne que je connaisse à avoir casser son pédalier en deux dans une côte, belle performance. Mais bon quand il a compris et qu'il s'est acheté un beau vélo en carbone, là c'est devenu compliqué. Déjà que je n'arrivais pas à te suivre avant mais là en plus si tu voles, je ne peux plus rien faire. Le problème avec Quentin c'est qu'il est fort dans beaucoup de sports, j'ai pas réussi à le battre ni au badminton, ni au vélo mais j'ai juste réussi une seule fois en course à pied. Un souvenir incroyable, j'avais trouvé la faille pour le battre au 10km du Run in Lyon, il était juste malade. Merci pour ce beau cadeau. Pour te remercier de me supporter en tant que collègue et en tant que partenaire de sport, je te redescendais assez souvent de la tomme des Bauges pour faire une bonne matouille.

Je suis très honoré d'avoir pris le bureau d'un beau et jeune chercheur au CNRS du nom de Florian. Merci à toi pour ces années. Nos discussions scientifiques ont toujours été très enrichissantes. Merci de ton aide pour ma préparation à la soutenance de thèse. Je retiens la question sur le fonctionnement d'un interféromètre type ALMA. J'espère qu'on arrivera à suivre ton modèle de parcours professionnel, en obtenant un poste permanent en un temps record. Merci beaucoup de nous avoir aider avec Ugo au début quand on galérait avec les logements, et encore désolé pour la Chartreuse, maintenant on sait que tu préfères un bon whisky tourbé. Comme pour Étienne, j'ai toujours espéré voir un dunk, rien qu'un petit, en allant voir tes nombreux matches de basket. Merci à Andrea et à toi pour ce beau séjour au ski, j'en garde de très beaux souvenirs, ça me manque. La prochaine fois on t'emmène dans le champ à bosses.

Mon cher Pierre, merci pour ces belles années. Ta grande compréhension de la physique m'a toujours fasciné, on aurait pu échanger de sujet, tu aurais très bien réussi. J'ai essayé de suivre tes aventures cosmologiques mais tes calculs sur tes feuilles de brouillon étaient beaucoup trop petit, il fallait une loupe. En tout cas, un grand bravo d'avoir pris le contrôle de notre faim le midi. Il ne fallait pas qu'on aille manger trop tôt ni trop tard. Je n'ai pas encore trouvé quelqu'un qui demande une calzone ouverte dans une pizzeria.

Merci à Arthur, alias Charlet1 pour ces années. Cette simulation de trou noir avec la particule qui oscille est incroyable, c'est presque une œuvre d'art. J'espère que j'ai pu t'aider au mieux sur ton sujet et sur tes codes python.

Je remercie grandement toutes les personnes du labo pour la super ambiance. C'est toujours un plaisir de venir au labo, prendre un café ensemble le matin, déguster des pains au chocolat, ou juste une moitié pour certain, puis la deuxième moitié juste après. Merci Quentin pour la feuille de café, tu es passé maître en approximation polynomiale. Merci à la machine à café de nous maintenir éveillé bien sûr. Merci d'avoir créé la médaille Jaupart&Vigneron, la compétition est rude pour l'obtenir. Le dernier détenteur est Timothée il me semble, avec une belle confusion entre tableau et mur. Merci pour

cette raclette et cette crêpe party au labo. Merci aussi à tout ses moments externe au labo, la tradition du Ninkasi pour fêter la publication de papiers ou pas, et aussi toutes les autres sorties pour découvrir la gastronomie lyonnaise. J'espère pouvoir retrouver cette même ambiance dans les prochains laboratoires où je vais atterrir.

Je remercie les personnes du labo de physique qui ont participé à cette super ambiance. Un grand merci à Barbara pour les délicieux gâteaux, j'ai essayé de rivaliser mais je n'arrivais pas à suivre en qualité et en fréquence.

Je remercie également tous les stagiaires qui sont passés au labo : Émile, que j'ai pu encadré partiellement, Benoît, Timothée, Guillaume, Célia, Enzo, Armand et tous ceux que j'oublie de mentionner.

Un grand merci aux thésards du labo de physique, c'est toujours bien de voir autre chose que de l'astrophysique. Merci à Lucile, Noémie, Marine, Delphine. Un merci particulier pour Lucile. On a commencé nos thèses en même temps et on s'est soutenu mutuellement ces trois années. Tu es souvent venu manger avec nous au m7 et quand l'occasion se présentait, notamment pour des pauses gâteaux, je débarquais au m1. C'était toujours cool de venir voir ta manip. Par contre aller à la piscine pour prendre des grands par ceux qui doublaient, c'était tout de suite moins marrant.

Je remercie tous les enseignants que j'ai côtoyer pendant mes heures d'encadrements des TP d'agregs et aussi pour le TD projet numérique, j'ai énormément appris. Merci à Ralf et Agilio, j'espère qu'on a donner envie aux élèves à bien coder. Je remercie tout particulièrement les techniciens pour leurs aides précieuses pour les TP.

Bien sûr je remercie toutes les personnes du CRAL à l'observatoire que j'ai rencontré. Merci à Jeff, Anthony, Arnaud, Kieran, Hossam. Si besoin, Kieran tu traduiras pour Hossam. Merci pour toutes ses discussions sur la coagulation, la dynamique des disques, j'ai énormément appris. La présentation de soutenance de thèse d'Anthony est l'une des plus incroyable que j'ai vu avec celle de Mark. J'ai essayé d'épauler Arnaud lors d'un hackaton pour mettre stepinski en mono-fluide, mais pas facile quand on commence à entrer dans les entrailles de PHANTOM, on prend vite peur. Merci aussi pour ces moments de détentes autour d'une bière ou d'un coca ou d'une verre de côte du Rhône dans les bouchons. Et pas facile de savoir quel plat commander dans un petit restaurant de nouilles à Shanghai, n'est-ce pas Jeff ? C'est dommage qu'on ai pas pu se croiser en plongée à Palm Cove.

Merci à Nicolás d'être venu nous voir à Lyon. On ne se lasse pas de t'écouter parler de systèmes étoile-disque assez incroyable, et de parler de science en général, sans oublier le bar le soir, ou aller voir des films de montagnes. Ce restaurant l'Écume, c'était incroyable. Les aventures du petit Nicolás reprennent avec la fabuleuse équipe de Monash plus loin dans le texte.

Je remercie tous les collaborateurs. Tout d'abord un grand merci à Gaël pour son soutient, ce stage de M2 a été une super expérience. On a réussi à finir le travail commencé pendant la thèse, c'était très enrichissant. Je remercie Léon pour les discussions sur l'équation de Smoluchowski, j'ai énormément appris. Merci à Thomas pour les discussions sur le méthode de Galerkin. Merci à Charles-Édouard pour les discussions mathématiques impressionnantes.

I thank the Dustbusters consortium which gave me the opportunities to visit Monash University (Australia) during my Ph.D. It was a really great working experience, I learned a lot on the physics of discs. I could meet lot of experts and start collaborations. It is a very stimulating working environment with all these Dustbusters members.

I warmly thank the amazing SPH group at Monash: Daniel, Christophe, Valentin, Daniel, Sergei, David, Bella and people I met. It was a great experience to work with

you, I learned a lot on physics of disc, on the best way to code in Fortran of course and on general physics. Thank you for the great workshops and all visitors. I thank all Dustbusters members I met at Monash Nicolás (again !), Bennedeta, Rebecca, Claudia, Maria-Giulia, Giulia, Enrico, Martina, Giovanni (please come back to us), Josh and also Fabien and Mathias. I thank all people I met at Monash and I forgot to mention. In Australia, you definitively need a guide book to learn how tim-tam break works, how vegemite is a trap and how to avoid to met dangerous animals. Thank you very much Valentin for all the visits in Australia, around Melbourne and around Palm Cove with smooth radio, the landscapes are amazing. We managed to find platypus and avoid crocodiles. Thank you for these nice tennis matches and the jacuzzi of course. I would like to come back to play snooker and continue to find hidden bars. Thank you Daniel for the visits around Melbourne and the advices. I should definitively come back to try your pizza oven. Next time we could go for diving. Thank you Christophe for your advices to visit Australia. This scuba diving formation was amazing, you are a great scuba diving partner. Thanks also Valentin, it was a great experience. Of course, Nicolás was in the same boat than us, thank for your scuba diving advices. Next time Christophe, we should go for biking, I am trained now thanks to Benoît and Quentin. Thank you Daniel for all the great moments. Your cocktails are amazing, we are still waiting for the Dustbuster cocktails. Thanks to Fabien, Valentin, Mathias and Nicolás for these great moments in Grampians. I tried to climb on rock, it was super. Thank you for this experience. Thank you Nicolás and Felipe for this adventure at Wilson Promontary national park. We saw a nice wombat. And it was important to mention that we are not guides for tourists. Thank you Benedetta for this last month at Monash before covid. It was great to work in the same open space, I could learn a lot on self-gravitating disc. We did some running in the campus but we did not break the glass at the entrance. Thank you for the visits near Melbourne thanks to the nice Valentin's car, so thank you Valentin.

I thank all people I met at this great conference in Palm Cove. It was a great moment. We tried to launch a Dustbusters music band, let's see for the future. The visit of the crocodile farm was amazing. I suspects the organisers of the conference to try to make expert on discs disappear. Thanks to Christophe, Valentin and Sebastian since we managed to avoid dangerous meeting with big spiders, casoars and crocodiles during our adventure around Palm Cove. I thank Vaishali for these resting walks in the Monash campus with a moka. It was great. I warmly thank my host family near Melbourne for the amazing moments.

I thank all people I met in Australia for the greats moments.

Je remercie la Dream Team pour leur soutient durant ces trois années. Merci pour ceux qui ont pu venir à Lyon. C'est toujours un plaisir de vous voir.

Merci à Boris, Louise, Hélène et Kévin pour votre soutient. Faudrait qu'on reparte à l'aventure au Chili.

Merci à Peter, Ludovic et Thibaut, c'est toujours très important pour moi de vous revoir sur Annecy, pour une sortie vélo, du skating ou juste une bière.

Merci à Franck pour son soutient et ces belles parties de tennis.

Merci au groupe Jazz Lacrymo, c'était un plaisir de pouvoir jouer avec vous. Merci également à Ugo, Camille et Ambroise pour cette belle aventure du groupe Iron Maidens.

Merci bien sûr à Sophie, Johan, le petit Lucien, Margaux, Éric, Carine et Ruben pour leur soutient.

Je remercie toutes les personnes que j'ai pu oublié de mentionner

Je remercie chaleureusement mes parents et mon frère qui m'ont toujours soutenu depuis le début de mon aventure scientifique. Merci à ma tante qui a pu venir à ma soutenance. Je remercie également Cristina. Je remercie toute ma famille pour leur soutient.

CONTENTS

I CHAPTERS

1 INTRODUCTION 3
- 1.1 Planet formation 3
- 1.2 Observations of discs 5
- 1.3 Meteoritic data 9
- 1.4 Basic model of protoplanetary discs 9
  - 1.4.1 Keplerian motion 10
  - 1.4.2 Thermal profile 10
  - 1.4.3 Vertical structure of gas 10
  - 1.4.4 Radial structure 11
  - 1.4.5 Turbulence 11
- 1.5 Dust evolution in discs 12
  - 1.5.1 Drag 12
  - 1.5.2 Vertical settling 13
  - 1.5.3 Stochastic turbulence in discs 14
  - 1.5.4 Radial drift 16
- 1.6 Grain growth 17
  - 1.6.1 Contact between grains 17
  - 1.6.2 Grain-grain interactions 18
  - 1.6.3 Bouncing barrier 19
  - 1.6.4 Fragmentation barrier 19
- 1.7 Numerical simulations 19
- 1.8 Scientific objectives of the thesis 20
- 1.9 Outline of the thesis 21

2 DUST COAGULATION AND FRAGMENTATION 23
- 2.1 Introduction 23
  - 2.1.1 Dust coagulation 23
  - 2.1.2 Dust fragmentation 24
- 2.2 Smoluchowski equation 24
  - 2.2.1 Analytic solutions 28
  - 2.2.2 Self-preserving solutions 30
  - 2.2.3 Physical coagulation kernels 33
  - 2.2.4 Conservative form 33
- 2.3 Collisional fragmentation model 34
  - 2.3.1 Analytic solutions 35
  - 2.3.2 Conservative form 37
- 2.4 Coagulation-fragmentation equation 37
- 2.5 Summary 38

3 NUMERICAL SOLUTION OF THE SMOLUCHOWSKI EQUATION 39
- 3.1 Introduction 39
  - 3.1.1 Method of moments 39
  - 3.1.2 Point-based methods 40
  - 3.1.3 Finite element methods 41
  - 3.1.4 Requirements from hydrodynamical simulations 42
  - 3.1.5 Code PHANTOM 43

3.1.6 Scientific objectives of the Ph.D. Thesis . . . 45
3.2 High-order solver for Smoluchowski equation . . . 45
3.2.1 Discontinuous Galerkin method . . . 45
3.2.2 Evaluation of the flux . . . 48
3.2.3 Evaluation of the integral of the flux . . . 56
3.2.4 Slope limiter . . . 56
3.2.5 High-order time solver . . . 57
3.2.6 Algorithm flowchart . . . 59
3.2.7 Design . . . 59
3.3 Summary . . . 59
4 BENCHMARKS OF THE HIGH-ORDER SOLVER 61
4.1 Introduction . . . 61
4.2 Error measurements . . . 61
4.3 Benchmark for coagulation . . . 62
4.3.1 Constant kernel . . . 63
4.3.2 Additive kernel . . . 67
4.3.3 Multiplicative kernel . . . 72
4.4 Future developments for the Discontinuous Galerkin scheme . . . 72
4.4.1 Ballistic kernel . . . 76
4.5 Summary . . . 79
5 DUST SETTLING FOR SMALL GRAINS IN PROTOPLANETARY DISCS 81
5.1 Context . . . 81
5.2 Introduction . . . 82
5.3 Physical model . . . 83
5.3.1 Balance of forces . . . 83
5.3.2 Modelling dusty turbulence . . . 86
5.3.3 Link with previous works . . . 89
5.4 Mathematical analysis . . . 93
5.4.1 Rescaling . . . 93
5.4.2 Asymptotic expansions . . . 94
5.4.3 Steady-state dust distributions . . . 96
5.5 Numerical results . . . 97
5.5.1 Numerical scheme . . . 97
5.5.2 Numerical dust distributions . . . 100
5.6 Discussion . . . 101
5.7 Conclusion . . . 101
6 VLT/SPHERE SURVEY FOR EXOPLANETS AROUND YOUNG EARLY-TYPE STARS 103
6.1 Context . . . 103
6.2 Introduction . . . 105
6.3 Target Properties . . . 106
6.4 Observations . . . 106
6.5 Data reduction and analysis . . . 109
6.6 Companion candidate detection and characterization . . . 112
6.7 Detection limits and survey completeness . . . 115
6.8 Discussion . . . 116
6.9 Conclusions . . . 119
7 CONCLUSION AND FUTURE WORKS 121
7.1 Summary of the Ph.D works . . . 121
7.2 Future works . . . 123
7.2.1 Fragmentation . . . 123

7.2.2 3D simulations of dusty discs with dust growth/fragmentation . . 123
7.2.3 3D simulations of dusty protostellar collapses 124
7.2.4 Future developments for the DG scheme 126
7.2.5 Future physics developments 127

II APPENDIX

A CHAPTER 2 133
A.1 Conservative form of the Smoluchowski equation 133
B CHAPTER 3 135
B.1 Derivation of the flux 135
B.1.1 Simple integral 136
B.1.2 First double integral 137
B.1.3 Second double integral 141
B.1.4 Fortran scheme for flux term 144
B.2 Derivation of integral of the flux 145
B.2.1 Derivation of double integrals 147
B.2.2 Derivation of the triple integrals 148
B.2.3 Fortran scheme for integral of the flux term 158
C CHAPTER 4 163
C.1 Derivation of the flux for ballistic kernel 163
C.1.1 Inner integral 163
C.1.2 Outer integral 165
C.1.3 `Fortran` scheme 168
D CHAPTER 5 171
D.1 Derivation of the limiting equations 171
D.1.1 Analysis in Regime 1 171
D.1.2 Analysis in Regime 2 171
D.1.3 Analysis in Regime 3 174
E CHAPTER 6 177
E.1 MCMC orbital fit of HIP 117452 BaBb 177

BIBLIOGRAPHY 179

Part I

CHAPTERS

1 INTRODUCTION

"Of all the natural sciences, astronomy is the one with the longest chain of discoveries." – Pierre-Simon Laplace

1.1 Planet formation . . . 3
1.2 Observations of discs . . . 5
1.3 Meteoritic data . . . 9
1.4 Basic model of protoplanetary discs . . . 9
1.4.1 Keplerian motion . . . 10
1.4.2 Thermal profile . . . 10
1.4.3 Vertical structure of gas . . . 10
1.4.4 Radial structure . . . 11
1.4.5 Turbulence . . . 11
1.5 Dust evolution in discs . . . 12
1.5.1 Drag . . . 12
1.5.2 Vertical settling . . . 13
1.5.3 Stochastic turbulence in discs . . . 14
1.5.4 Radial drift . . . 16
1.6 Grain growth . . . 17
1.6.1 Contact between grains . . . 17
1.6.2 Grain-grain interactions . . . 18
1.6.3 Bouncing barrier . . . 19
1.6.4 Fragmentation barrier . . . 19
1.7 Numerical simulations . . . 19
1.8 Scientific objectives of the thesis . . . 20
1.9 Outline of the thesis . . . 21

1.1 PLANET FORMATION

One of the most fundamental problems of science is the origin of the Solar System. How planets form is still a pending question of contemporary astrophysics. In 1995, Mayor and Queloz (1995) detected the first solar-type planet 51 Pegasi b orbiting around the star 51 Pegasi. This discovery has been a revolution in astrophysics and especially on the planet formation process. For this discovery, M. Mayor and D. Queloz were awarded of the Nobel Prize in 2019. The interest in the process of planet formation has drastically grown in the last 20 years due principally to the discovery of several planetary systems outside the Solar System. The large number of planets further discovered ($\sim$ 4000 to date http://exoplanet.eu) has revealed the ubiquitous character of planets around stars and an unexpected diversity in the architectures of planetary systems (Cassan et al., 2012). Some remarkable planetary systems have been detected so far (Figure 1.1). The TRAnsiting Planets and PlanetesImals Small Telescope–South (TRAPPIST-South) located at La Silla in Chile observed the TRAPPIST-1 planetary system composed of seven planets. These planets have sizes between Mars and Earth and three of them are located in habitable zone where liquid water can be supported at the surface of the planet. The planets undergo mean-motion resonances. Other planetary systems such as Kepler-186 and Kepler-452 have been observed by the Kepler spacecraft. The planet Kepler-452b has also similar properties to Earth.

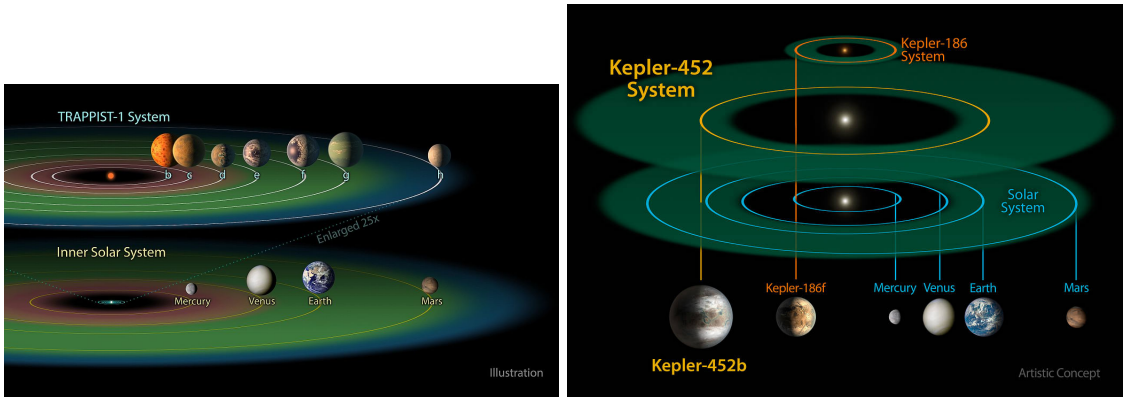

Figure 1.1: Left: Illustration of the TRAPPIST-1 planetary system. Seven planets have been detected closed to their host star compared to the Solar System. Right: Illustration of the Kepler-186 and Kepler-452 planetary systems. The detected planet Kepler-452b has almost the same properties than Earth. Credits: NASA/JPL-Caltech and NASA Ames/JPL-CalTech/R.Hurt.

Planet formation originates from molecular clouds, which are mainly composed of molecular hydrogen (H_2). Molecular clouds contain dust ($\sim$ 1% of their mass). The molecular cloud collapses by gravity, accumulating in its centre the matter which will form a young star. By conservation of angular momentum, a disc composed of gas and dust gravitates around the star (Mendoza V., 1966; Safronov, 1972; Testi et al., 2014). The disc is usually called protoplanetary disc since it contains the material to form planet embryos. Protoplanetary discs are supposed to be the cradle of planet formation. First stage of planet formation consists of the formation of solid rocks of size $\sim$ 1km called planetesimals (Chiang and Youdin, 2010). However, planetesimal formation remains poorly understood. Grains have first to concentrate and grow by hit-and-stick collisions up to forming pebbles (see Chapter 2). Then, high hydrodynamical local grain concentration are triggered by the so-called streaming instability (Youdin and Goodman, 2005; Jacquet et al., 2011; Jaupart and Laibe, 2020). This mechanism is a linear instability developing from radial drift of dust grains. When the local dust-to-gas ratio is of the order unity, small clumps of solid material form spontaneously as a result of a traffic jam generated by local differential drifts. Then, the local over-density of solids reaches a critical threshold, solid clumps collapse gravitationally to form planetesimals of size $100 - 1000$m. The streaming instability mechanism allows to overcome the metre-size barrier problem of planet formation. Once planetesimals are formed, they continue to grow by accreting pebbles which are solid rocks of size $\sim$ 1cm (Lambrechts and Johansen, 2012). These growing planetesimals will form solid cores that are the seeds for terrestrial or gas giant planets (Pollack et al., 1996; Alibert et al., 2005). The discovery of "hot Jupiters" revealed the importance of considering the migration of these planets within the disc (Lin et al., 1996). Indeed, planets hardly form close to the star (Bodenheimer et al., 2000). Protoplanets are therefore expected to form at large radii and to migrate inwards. Orbital migration is driven by exchange of angular momentum via planet-disc tidal interactions. Tides transfer angular momentum inside the disc by exciting Lindblad resonances. This angular momentum is further carried away by waves and is deposited inside the disc as these waves are dissipated. The tidal torque acting on the planet usually decreases the orbital angular momentum of the planet, leading generally to inward migration. In this case, the migration is called type I (Goldreich and Tremaine, 1980; Baruteau et al., 2014). If the planet is massive enough, tides split the disc into an inner disc and an outer disc. The planet is locked into a gap, and migrates inwards as the gas

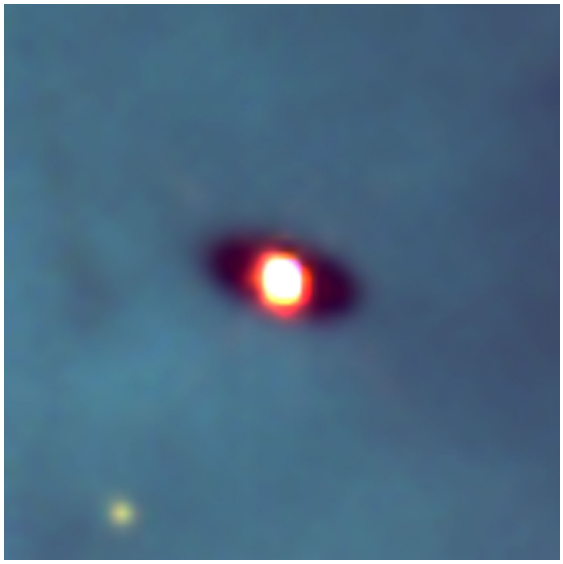

Figure 1.2: Image of a protoplanetary disc in optical wavelength in the Orion Nebula observed by the Hubble Space Telescope. Credits: Mark McCaughrean (Max-Planck-Institute for Astronomy), C. Robert O'Dell (Rice University), and NASA/ESA

is accreted onto the star (Lin and Papaloizou, 1986; Baruteau et al., 2014). In this case the migration is called of type II. Additional mechanisms developing at corotation also trigger planet migration (Masset and Papaloizou, 2003). Planets can undergo resonances as they migrate, shaping the architecture of planetary systems (Baruteau et al., 2014). Some models examine the planetary dynamics of the Solar System to explain the current architecture. The "Grand Tack" model (Walsh et al., 2012) simulates the few million years after the formation of the first solids and before the formation of the Earth. The model proposes that Jupiter and Saturn migrate inwards (type II migration). At some point, they merge their gaps and lock into 3:2 resonance, and further undergo outwards migration. This model gives an explanation for the mass of Mars and the distribution of solids inside the main asteroid belt. The "Nice Model" (Tsiganis et al., 2005) simulates the final major dynamical event that shapes the Solar System. It describes the reshuffling of giant planets' orbits and accounts for the late bombardment of the inner Solar System (Morbidelli et al., 2010).

1.2 OBSERVATIONS OF DISCS

The first observation of discs have been realised with the Infrared Astronomical Satellite (IRAS) (Strom et al., 1989). These observations at near-infrared wavelengths revealed the presence of circumstellar discs, containing small dust grains, associated with young solar-type pre-main sequence stars. Thereafter, the first detectors at millimetre wavelengths at the James Clark Maxwell Telescope (JCMT) showed the presence of large dust grains in many discs (Weintraub et al., 1989). Evidence of flattened morphology of discs have been highlighted in optical wavelengths with the Hubble Space Telescope (Hubble). Figure 1.2 shows disc shadows in a bright nebular background (O'dell and Wen, 1994).

Improvements in sensitivity, resolution and wavelength coverage leaded to an acceleration of discoveries of discs. The Spitzer Space Telescope (Spitzer) have greatly expanded the knowledge in discs (Werner, 2005). Interferometry probed shorter wavelengths including into the sub-millimetre regime with the Submillimetre Array (SMA) (Ho et al., 2004). High spatial observations in sub-millimetre wavelengths have been realised to

reveal particular structures in discs (Andrews and Williams, 2007). The development of new instruments such as Very Large Telescope (VLT) and the Atacama Large Millimetre/-submillimetre Array (ALMA) have drastically improved the sensitivity and resolution for observations of discs.

Recent spatially resolved observations with ALMA revealed the presence of substructures, such as rings, spirals, gaps and horseshoes in discs around young stars (e.g. van der Marel et al. (2013), ALMA Partnership et al. (2015), Andrews et al. (2016), and Andrews (2020)). The DSHARP survey (Andrews et al., 2018; Andrews, 2020) provided an important collection of observations of dusty discs (see Figure 1.3). Rings, spirals, horseshoes and shadows have also been detected at infrared wavelengths by the Spectro-Polarimetric High-contrast Exo-planet REsearch (SPHERE/VLT) instrument (e.g Avenhaus et al. (2014), Benisty et al. (2015), Benisty et al. (2017), Avenhaus et al. (2018), and Boccaletti et al. (2020a) and see Figure 1.3). Structures in protoplanetary discs have also been observed with other instruments such as the Gemini Planet Imager (GPI) instrument (e.g. Hung et al. (2015)), the Subaru/HiCIAO instrument (Tamura, 2009; Muto et al., 2012; Uyama et al., 2018). The next generation of instruments such as SPHERE+ (Boccaletti et al., 2020b), the improvement of SPHERE, the Extremely Large Telescope (ELT) with the Mid-infrared ELT Imager and Spectrograph (METIS/ELT) (Brandl et al., 2016) and the James Webb Telescope (JWST) (Gardner et al., 2006) will drastically increase the performance for detecting planets and observing protoplanetary discs at high resolution. The excellent sensitivity and angular resolution of these instruments at near- to mid-infrared wavelengths will revolutionise our understanding of the inner regions of protoplanetary discs.

The variety of structures observed in protoplanetary discs was unexpected. Explain the origin of these structures was the principal challenge of the last five years. The presence of these structures could be signposts of planets. The high spectral resolution ALMA line observations provides channel velocity maps of the gas. A new technique consists to detect a deviation from the Keplerian velocity of the gas in these channel maps, which suggest the presence of a gravitational companion. Pinte et al. (2018) and Teague et al. (2018) detected gravitational companions in observing local kinks from the Keplerian velocity of ^{12}CO. These channel maps can be reproduced by the 3D hydrodynamic code `PHANTOM` simulating the evolution of planets within the disc. Pinte et al. (2020) detected 9 exoplanets in protoplanetary discs, with some of them inside a gap for the first time (see Figure 1.6). Recent observations in direct imaging revealed the presence of massive planets inside the disc around PDS 70 (Müller et al., 2018; Keppler et al., 2018; Christiaens et al., 2019; Keppler et al., 2019) and a potential ongoing planet formation in the disc around AB Aurigae (Boccaletti et al., 2020a), see Figure 1.4. These observations are the deepest images ever obtained with SPHERE for AB Aurigae in scattered light. The presence of potential planet in formation is suggested by the analysis of the form of spirals in the disc. Kraus et al. (2020) have recently detected with ALMA three rings around the triple star system GW Orionis (Figure 1.5). These observations confirm evidence of disc tearing, i.e. disc warped and broke into precessing rings. If planet can form in the warped disc, this could explain the presence of planets on oblique orbits.

These observations probed the distribution of dust grains within the disc (millimetre pebbles with ALMA and micron-in-size grains from the top layers with SPHERE/VLT). How these structures form and connect to planet formation is a pending question of contemporary astrophysics. How planets can form in less than one million year, the typical lifetime of observed discs? The solid material arising from the interstellar medium have to grow over 30 orders of magnitude in mass to form planets in such a short time (Chiang and Youdin, 2010; Testi et al., 2014).

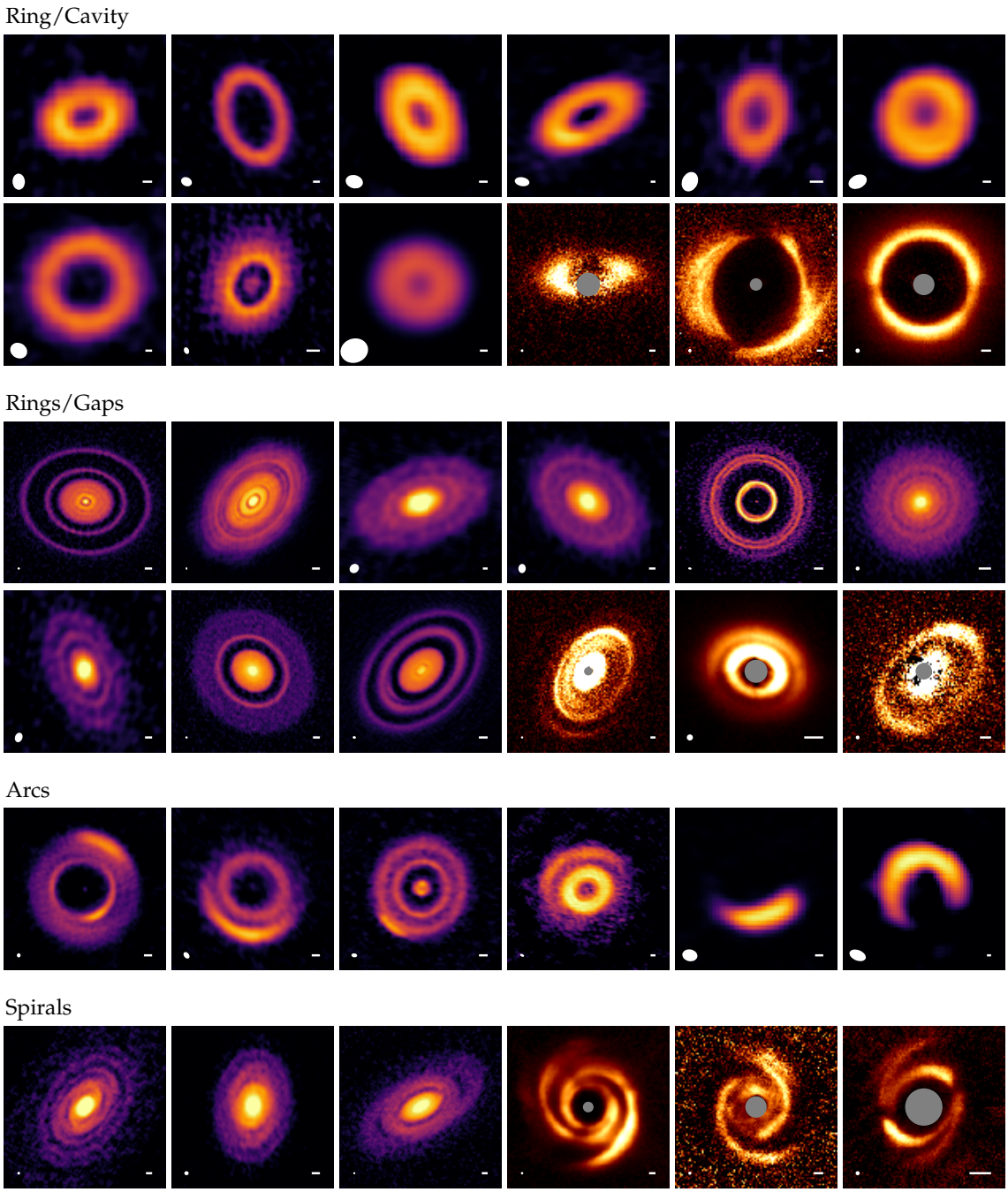

Figure 1.3: Gallery of discs with subs-structures. The continuum emission is observed at $\lambda = 0.9\,\mathrm{mm}$. The scattered light is observed at $\lambda = 1.6\,\mu\mathrm{m}$. Resolutions of observations are marked with white ellipses in the lower left corners of each panel. The 10 AU scalebars are shown in the lower right corners. For the scattered light images, the grey circles mark their coronagraphic spots. Credits: Andrews (2020)

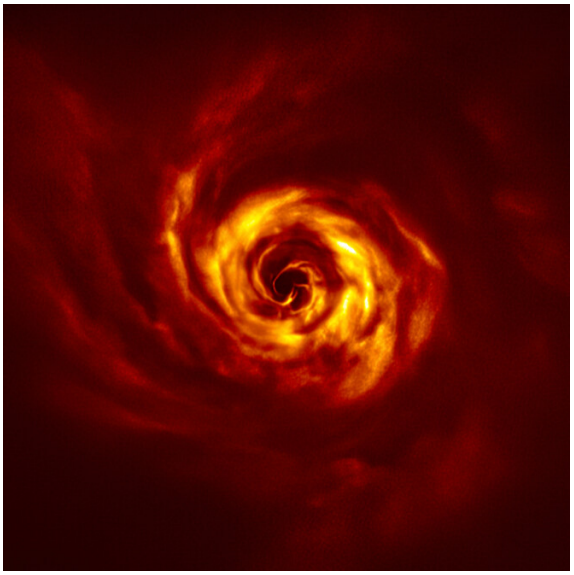

Figure 1.4: Observation of the AB Aurigae system obtained with SPHERE in scattered light. The presence of planets in this disc explains the form of the spirals (Boccaletti et al., 2020a).

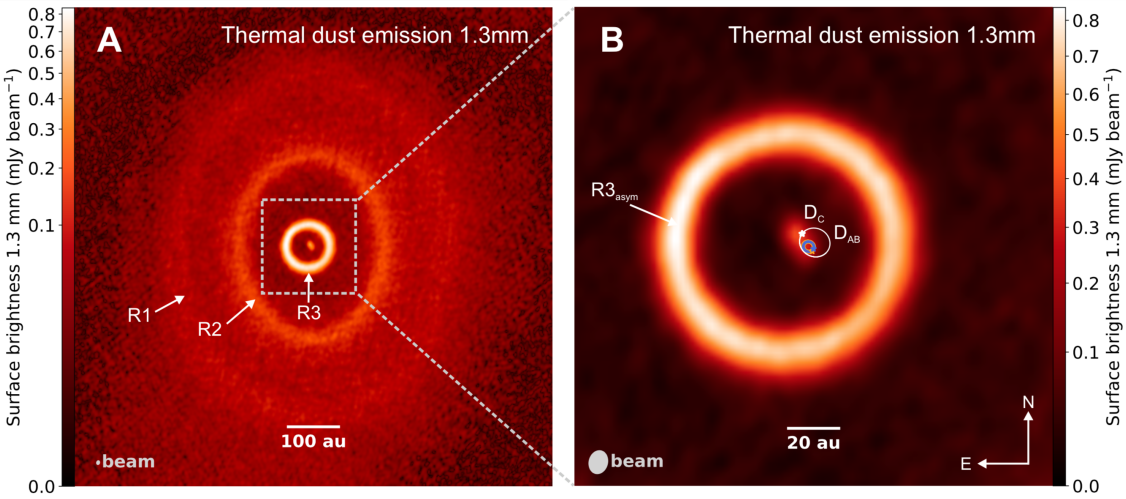

Figure 1.5: Observation of the disc components around GW Orionis with ALMA in millimetre wavelength. Left: Image of the discs where three rings (R1,R2 and R3) are detected. Right: Image of the inner part of the disc with the ring R3 and the three stars. This triple stars system is composed of three rings where planets can form (Kraus et al., 2020).

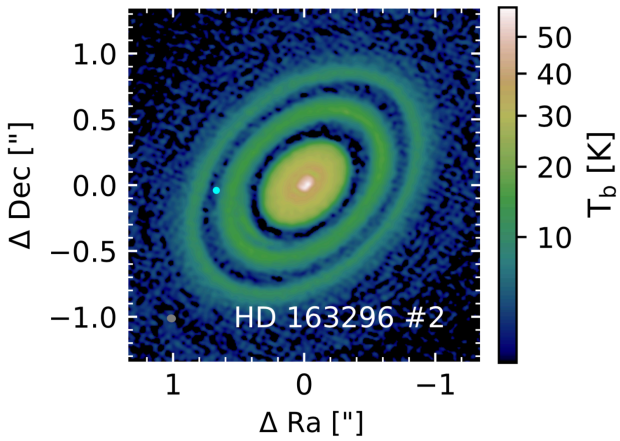

Figure 1.6: Observation of the disc around HD163296 in the continuum emission at $\lambda = 1.3\,\mathrm{mm}$. The green dot represents the indirect detection of a planet of mass $3M_{\mathrm{Jup}}$ with the kinematic detection (Pinte et al., 2018). The planet is detected in a gap. Credits: Pinte et al. (2020).

1.3 METEORITIC DATA

Our Solar System is composed of a reservoir of solid materials which testifies to the history of the formation of planetary systems. In particular, the study of the primitive rocky meteorites (Nittler and Ciesla, 2016), called chondrites, allows to follow the grain growth during the evolution of the disc. Chondrites are composed mainly of chondrules which are spherical millimetre-sized particles. Chondrules are made of silicate materials, olivine, pyroxene and calcium aluminium inclusions (CAI) embedded in a fine-grained matrix (Scott, 2007). Most CAIs formed as fined-grained condensates from a gas of solar composition in a high temperature environment ($> 1300\,\mathrm{K}$) at low pressure ($< 10^{-4}\,\mathrm{bar}$). Their dating is obtained by the analysis of the decay of short-lived radionucleides. Their ages give an estimation of the age of the Sun, 4.567 Gyr. Chondrules are thought to have formed by coalescence of dust aggregates that were rapidly melted and cooled at lower temperature ($< 1000\,\mathrm{K}$) and higher pressure ($> 10^{-3}\,\mathrm{bar}$). Recent measurements of absolute ages of the chondrules found that they were formed over a period that span from CAI formation to a few million years beyond (Connelly et al., 2012). Chondrule, CAIs and the matrix of one chondrite originate from different reservoirs, implying mixing during the early stages of planet formation (Burbine et al., 2002; Scott, 2007). Dust aggregates made of micrometer-in-size grains and millimetre-in-size chondrules had to be present at the formation of the Solar system (Scott, 2007). Similar grain sizes are found in cometary materials (Blum et al., 2017). Therefore, dust growth has to be efficient during the early stages of planet formation.

1.4 BASIC MODEL OF PROTOPLANETARY DISCS

Protoplanetary discs are composed of gas and dust orbiting their host star. In the mid-plane of a typical disc, the mean free path is of order $\lambda_{\mathrm{g}} \sim 10\,\mathrm{m}$ for a gas essentially made of molecular hydrogen. This is much larger than the typical size of a dust grain. Therefore, the gas is considered as a collection of particles colliding with the dust grain. The appropriate drag regime is the so-called Epstein drag regime for dilute media (Epstein, 1924; Whipple, 1972; Lynden-Bell and Pringle, 1974; Weidenschilling, 1977a). The mean free path between dust grains in the mid plane is of order $\lambda_{\mathrm{d}} \sim 100\,\mathrm{km}$.

At the scales of order astronomical units, gas and dust can be treated as continuous phases. Dust collisional pressure and viscosity are usually neglected. The basic model of protoplanetary discs has been developed by Whipple (1972), Lynden-Bell and Pringle (1974), Weidenschilling (1977a), Pringle (1981), Nakagawa et al. (1981), Dubrulle et al. (1995), and Takeuchi and Lin (2002), where gas and dust evolution are described by fluid mechanics.

1.4.1 *Keplerian motion*

The disc is composed of a continuous medium orbiting a star of mass M_*. Each fluid element of the medium (gas and dust) moves on a Keplerian circular orbit (Armitage, 2019). The Keplerian angular velocity at a radius r writes $\Omega_\mathrm{K} = \sqrt{\mathcal{G}M_*/r^3}$. The fluid element experiences a local shear that relates to a differential rotation. The typical timescale in the disc is the orbital period at 1 au $T_\mathrm{K} = 1\,\mathrm{yr}\,(r/1\,\mathrm{au})^{3/2}$, around a one-Solar mass star.

1.4.2 *Thermal profile*

The temperature profile in discs results from the thermal balance between heating from the central star and cooling by the continuum radiation in the infrared (Chiang and Goldreich, 1997; Woitke, 2015). At most radii, the dust opacity is high enough for the disc to be optically thick to the stellar radiation (Armitage, 2019). Considering only geometrical effects, the radial thermal profile writes in the form $T(r) \propto r^{-q}$. Realistic disc structures provide $q \sim 0.4$ (Pinte and Laibe, 2014). At 1 au the typical temperature value is a few hundreds of Kelvin. Discs are optically thick and almost vertically isothermal, except in the very top layers (D'Alessio et al., 1998).

1.4.3 *Vertical structure of gas*

The vertical structure of gas density in discs is determined by the condition of hydrostatic equilibrium. This equilibrium results from the balance of the gravity of the star and pressure of the gas in the vertical direction. The disc is considered as isothermal, with constant sound speed c_s and pressure $P = \rho_\mathrm{g} c_\mathrm{s}^2$. The vertical hydrostatic equilibrium for a non-magnetic, non-self-gravitating, and vertically isothermal disc writes in cylindrical coordinates

$$\frac{\partial P}{\partial z} = -\rho_\mathrm{g} \frac{\mathcal{G}M_\star z}{(r^2+z^2)^{3/2}}. \tag{1.1}$$

The sound speed is considered independent of z, then

$$\rho_\mathrm{g}(r,z) = \rho_{\mathrm{g},0} \exp\left[-\frac{\mathcal{G}M_\star}{c_\mathrm{s}^2}\left(\frac{1}{r} - \frac{1}{\sqrt{r^2+z^2}}\right)\right] \underset{z \ll r}{\approx} \rho_{\mathrm{g},0} \exp\left[-\frac{z^2}{2H_\mathrm{g}^2}\right], \tag{1.2}$$

with $\rho_{\mathrm{g},0}$ the gas density at $z = 0$ and $H_\mathrm{g} = c_\mathrm{s}/\Omega_\mathrm{K}$ the typical pressure scale height of the disc. $\rho_{\mathrm{g},0}$ depends of the surface density of the gas $\Sigma_\mathrm{g}(R) = \int_{-\infty}^{\infty} \rho_\mathrm{g}(R,z)\,\mathrm{d}z$,

$$\rho_{\mathrm{g},0} = \frac{1}{\sqrt{2\pi}} \frac{\Sigma_\mathrm{g}}{H_\mathrm{g}}. \tag{1.3}$$

Therefore, in a very good approximation, the gas has a vertical gaussian profile (Armitage, 2019).

1.4.4 *Radial structure*

For a disc in vertical hydrostatic equilibrium, the azimuthal component of the momentum equation writes

$$\rho_g \left(\frac{\partial v_r}{\partial t} + v_r \frac{\partial v_r}{\partial r} - \frac{v_\phi^2}{r} \right) = -\rho_g \frac{\mathcal{G} M_\star r}{(r^2 + z^2)^{3/2}} - \frac{\partial P}{\partial r}. \tag{1.4}$$

At steady-state, the momentum equation writes in the mid-plane

$$\frac{v_\phi^2}{r} = \frac{\mathcal{G} M_\star}{r^2} + \frac{1}{\rho_g} \frac{\partial P}{\partial r}. \tag{1.5}$$

The negative pressure gradient maintains a globally negative correction to the Keplerian rotation of order H^2/r^2 (Whipple, 1972; Weidenschilling, 1977a). Then the azimuthal velocity writes

$$v_\phi = \left[\frac{\mathcal{G} M_\star}{r} + \frac{r}{\rho} \frac{\partial P}{\partial r} \right]^{1/2} \approx v_K + \frac{r}{2\rho v_K} \frac{\partial P}{\partial r} < v_K. \tag{1.6}$$

Considering a disc with $\Sigma \propto r^{-1}$, $T \propto r^{-1/2}$, one obtains $c_s \propto r^{-1/4}$, $\rho_g \propto r^{-9/4}$ and $P \propto r^{-11/4}$. Equation 1.6 writes (Armitage, 2019)

$$v_\phi = v_K \left[1 - \frac{11}{4} \left(\frac{H_g}{r} \right)^2 \right]^{1/2}. \tag{1.7}$$

The deviation from the Keplerian velocity is of the order of $(H_g/r)^2$. For a disc with $H_g/r = 0.05$ at 1 au, the difference between v_ϕ and v_K is about 0.3%. This differential velocity triggers dust drift (see below).

1.4.5 *Turbulence*

In discs, turbulence acts as one source with winds and self-gravitating waves for the transport of angular momentum (Lodato, 2008). Although Reynolds numbers are of the order 10^{12}, the Keplerian differential rotation prevents the development of purely hydrodynamical turbulence through local shears. More precisely, the flow is stable under the Rayleigh criterion. The origin of the turbulence in discs comes from the so-called magneto-rotational instability (Balbus and Hawley, 1991). Turbulence in disc is conveniently modelled by an effective viscosity (Prandtl's mixing-length theory). Shakura and Sunyaev (1973) parametrised the turbulent efficiency by an effective viscosity $\nu = \alpha c_s H_g$, where α is a dimensionless parameter. In general, $\alpha \sim 10^{-4} - 10^{-3}$ (values from ideal MHD simulations, Fromang and Nelson (2009)). These values reproduce observed accretion rates and are consistent with models and observations. Energy is injected at the large scale H. The typical turbulent velocity is of order $\sqrt{\alpha} c_s$. The turbulent activity of the gas sustains a stochastic diffusivity of small grains, since they are coupled to the gas (see Chapter 5). Turbulence generates relative differential velocities between dust grains that drive the outcome of collisions (see Chapter 5, Youdin and Lithwick (2007)).

1.5 DUST EVOLUTION IN DISCS

1.5.1 *Drag*

Dust play a crucial role in planet formation. Pebbles provide the primary material to form planetary cores, whereas small grains set the thermal balance of the disc. Usually, dust and gas are treated as fluids. Dust fluid is pressureless and do not thermalised with the gas. Dust and gas are coupled by the drag that acts as a source for exchanging momentum.

1.5.1.1 *Epstein regime*

Drag originates from microscopic collision between one grain and gas molecules. The drag force $\boldsymbol{F}_\mathrm{d}$ is obtained by summing the mean rate of momentum exchange by single gas molecule of negligible mass to the grain during a collision. The drag force writes $\boldsymbol{F}_\mathrm{d} \approx \boldsymbol{p}_\mathrm{c}/t_\mathrm{c}$, where $\boldsymbol{p}_\mathrm{c} = -m\Delta\boldsymbol{v}$ and t_c the mean collision time. m is the mass of a spherical grain. In the case of a spherical uncharged grain and specular reflexion on the surface of the grain, a factor 4/3 is added Baines et al. (1965). The mean collision time for ballistic collision writes $t_\mathrm{c} = (n_\mathrm{g}\sigma v_\mathrm{th})^{-1}$, where n_g is the number density of gas molecules, σ the cross section of the grain and $v_\mathrm{th} = c_\mathrm{s}\sqrt{\frac{8}{\pi\gamma}}$ the thermal velocity of the gas. γ is the adiabatic index of the gas. In the Epstein regime, the drag force writes for spherical grains

$$\boldsymbol{F}_\mathrm{d} = -m\frac{\Delta\boldsymbol{v}}{t_\mathrm{s}}, \tag{1.8}$$

where m is the mass of a grain, $\Delta\boldsymbol{v}$ the differential velocity between the gas and the grain and t_s the stopping time of a single grain

$$t_\mathrm{s} = \sqrt{\frac{\pi\gamma}{8}}\frac{\rho_\mathrm{grain}s}{\rho_\mathrm{g}c_\mathrm{s}}. \tag{1.9}$$

ρ_grain is the intrinsic density of a grain with typical value $\rho_\mathrm{grain} = 3\,\mathrm{g.cm}^{-3}$ (Love et al., 1994) and $\rho_\mathrm{g} = n_\mathrm{g}m_\mathrm{g}$. The stopping time t_s is the typical time for dust grains to reach gas velocity (Epstein, 1924; Baines et al., 1965). Drag is stronger as collisions with the gas molecules are more frequent. If solids reach zones where $\lambda_\mathrm{g} \leq s$, equation 1.9 expresses according to the Stokes law. These two regimes are reconnected by analytic approximations (Whipple, 1972).

1.5.1.2 *The Stokes number*

A key parameter for the dust dynamics is the Stokes number St, defined as the ratio between the local stopping time t_s and the orbital time (Whipple, 1972; Safronov, 1972). Grains with St $\ll 1$ stick to the gas, and they follow the gas motion. Their dynamics is drag-dominated. Grains with St $\gg 1$ do not feel the drag from the gas, they follow N-body orbits that are slightly damped. Their dynamics is gravity-dominated. Maximal decoupling and damping is reached at St ~ 1. Solids differentiate from the gas and concentrate strongly, making this case of prime importance for planet formation. Typically, St ~ 1 are the millimetre-in-size grains observed with ALMA. St $\propto s$, therefore, grains undergo dynamical motions that depend on their sizes. Therefore, dust growth impacts strongly the dust dynamics.

1.5.2 *Vertical settling*

The seminal theory of dust settling was established by Dubrulle et al. (1995). This model is widely used to estimate dust scale heights in discs. Dullemond and Dominik (2004b) and Dullemond and Dominik (2005a) pioneered models of dust settling coupled to Monte-Carlo methods for radiative transfer, a technique extended to ray tracing by Pinte et al. (2006) and Pinte et al. (2007). In the vertical direction, drag makes the orbital inclinations of the grains relax towards the mid-plane of the disc (Adachi et al., 1976). The vertical component of the gravity in cylindrical coordinates is

$$-\frac{\mathcal{G}Mz}{(r^2+z^2)^{3/2}} \approx -\Omega_{\rm K}^2 z, \tag{1.10}$$

where $z \ll r$. The vertical component of the drag exerted by the gas on grains is

$$F_{{\rm d},z} = -m_{\rm d}\frac{(\dot{z}-v_{{\rm g},z})}{t_{\rm s}}. \tag{1.11}$$

Assuming vertical hydrostatic equilibrium, $v_{{\rm g},z}=0$. Combining equations 1.9 and 1.2, the stopping time writes

$$t_{\rm s}(z) \approx t_{z,0}\,{\rm e}^{\frac{z^2}{2H^2}}, \tag{1.12}$$

where $z \ll r$ and $t_{{\rm s},0} \equiv \frac{\rho s}{\rho_{{\rm g},0}c_{\rm s}}\sqrt{\frac{\pi\gamma}{8}}$. $t_{{\rm s},0}$ denotes the stopping time in the mid-plane. The balance of forces for a single grain in vertical direction is

$$\ddot{z} + \frac{{\rm e}^{-\frac{z^2}{2H^2}}}{t_{\rm s0}}\dot{z} + \Omega_{\rm K} z = 0. \tag{1.13}$$

The Gaussian weight ensures that grains are decoupled from the gas in the top layer of the discs. Allowing the rescaling $Z \equiv z/H$ and $T \equiv t\Omega_{\rm K}$, equation 1.13 writes

$$\ddot{Z} + {\rm St}_0^{-1}\,{\rm e}^{-\frac{Z^2}{2}}\,\dot{Z} + Z = 0, \tag{1.14}$$

where ${\rm St}_0$ is the Stokes number of the grain in the mid-plane. For $Z \ll 1$, when grains are close to the mid-plane, equation 1.14 reduces to the damped harmonic oscillator

$$\ddot{Z} + {\rm St}_0^{-1}\dot{Z} + Z = 0. \tag{1.15}$$

Grains relax to the mid-plane in a settling time scale $T_{\rm sett}$. According to the three cases of solution for equation 1.15, the settling time scale can be well approximated by $T_{\rm sett} = \frac{{\rm St}_0^2+1}{{\rm St}_0}$ (Youdin and Lithwick, 2007; Laibe et al., 2014a). Therefore, grains relax to the mid-plane in a typical time

$$t_{\rm sett} \sim \frac{{\rm St}_0^2+1}{{\rm St}_0}\Omega_{\rm K}^{-1}. \tag{1.16}$$

Settling efficiency is optimal for ${\rm St}_0 \sim 1$. Large grains orbit around the star by crossing the mid-plane and their orbital inclinations relax slowly to zero due to the drag force. Small grains are stuck to the gas and, therefore, do not cross the mid-plane. In the very top layers of the disc, gas density decreases, therefore small grains decouple until they reach $z \sim H$ in one orbital period. Settling efficiency increases when grains grow and therefore decouple from the gas (Laibe et al., 2014a).

1.5.3 *Stochastic turbulence in discs*

Stochastic models are convenient to analyse the link between the dust scale height and the turbulent activity in the disc. The turbulent eddies of the gas transport the dust grains in a random manner, corresponding a diffusion process for the dust. The diffusion coefficient is defined as $D \equiv 2\int_0^{+\infty}\langle v_g(0)v_{g(t)}\rangle \mathrm{d}t$ (Batchelor, 1950; Fromang and Papaloizou, 2006; Carballido et al., 2006). In discs, vortices are stretched by differential rotation in a few orbits. Therefore, correlations at large scales develop for times $t_e \sim \Omega_K^{-1}$. The equation of motion of the gas in the vertical direction writes

$$\frac{\mathrm{d}v_g}{\mathrm{d}t} = -\frac{v_g}{t_e} + \frac{\sqrt{D}}{t_e}\dot{w}, \tag{1.17}$$

where $\dot{w}$ defines a purely diffusive process: $\langle \dot{w}(t)\rangle = 0$ and $\langle \dot{w}(t)\dot{w}(t')\rangle = \delta(t-t')$. The velocity of gas has the following properties

$$\begin{aligned} &\langle v_g(t)\rangle = 0, \\ &\langle v_g(t)v_g(t')\rangle = \frac{D}{2t_e}\,\mathrm{e}^{-\frac{|t-t'|}{t_e}}. \end{aligned} \tag{1.18}$$

The diffusion coefficient can also be written using the α prescription $D = \alpha c_s H/2$ (Dullemond and Dominik, 2004a). According to the Wiener-Khinchin theorem, the power spectrum $S(\omega)$ writes

$$S(\omega) = \frac{1}{2\pi}\int_{-\infty}^{+\infty}\mathrm{e}^{-i\omega t}\langle v_g(0)v_g(t)\rangle \mathrm{d}t = \frac{D}{2\pi(1+\omega^2 t_e^2)}. \tag{1.19}$$

The turbulent velocity of the gas $v_{g,T}$ expresses

$$v_{g,T}^2 \equiv \int_{-\infty}^{+\infty} S(\omega)\mathrm{d}\omega = \frac{\alpha c_s^2}{t_e\Omega_K^{-1}} \quad \Rightarrow \quad v_{g,T} \sim \sqrt{\alpha}c_s. \tag{1.20}$$

The equation of motion of grains in vertical direction equation 1.13 writes with equations 1.18 in dimensionless quantities

$$\begin{aligned} \mathrm{d}Z &= V\mathrm{d}T, \\ \mathrm{d}V\mathrm{St}^{-1}V\mathrm{d}T + Z\mathrm{d}T &= \sqrt{2\alpha}\xi\mathrm{St}^{-1}\mathrm{d}T, \\ \mathrm{d}\xi &= -\frac{\xi}{\tau_e}\mathrm{d}T + \frac{\mathrm{d}w}{\tau_e}, \end{aligned} \tag{1.21}$$

where $\tau_e \equiv t_e\Omega$.

1.5.3.1 *Small grains*

The dynamics of small grains ($\mathrm{St} \ll 1$) is drag-dominated. Assuming that inertia is neglected in the disc ($dV = 0$) and also turbulent correlations ($\tau_e \to 0$), equation 1.21 writes

$$\begin{aligned} \mathrm{d}Z &= V\mathrm{d}T, \\ V\mathrm{d}T &= \mathrm{St}Z\mathrm{d}T + \sqrt{2\alpha}\xi\mathrm{d}T, \\ \xi\mathrm{d}T &= \mathrm{d}w. \end{aligned} \tag{1.22}$$

One obtains

$$\mathrm{d}Z = \underbrace{-\mathrm{St}_0 Z\,\mathrm{e}^{Z^2/2}\,\mathrm{d}T}_{\text{vertical settling}} + \underbrace{\sqrt{2\alpha}\mathrm{d}w}_{\text{turbulent stirring}} \quad . \tag{1.23}$$

Equation 1.23 shows that the distribution of small grains results from competition between turbulent stirring and vertical settling. Equation 1.23 is equivalent to a Fokker-Plank equation giving the probability density function of small grains p as (Risken, 1996)

$$\frac{\partial p}{\partial T} = \frac{\partial}{\partial Z}\left(\mathrm{St}_0 Z\,\mathrm{e}^{Z^2/2}\,p\right) + \alpha\frac{\partial^2 p}{\partial Z^2}. \tag{1.24}$$

At steady-state, solution to equation 1.24 writes

$$p(Z)_\infty \propto \mathrm{e}^{-\frac{\mathrm{e}^{Z^2/2}}{\alpha/\mathrm{St}_0}}\,. \tag{1.25}$$

The ratio α/St_0 measures the balance between turbulent stirring and vertical settling. For $\alpha/\mathrm{St}_0 \ll 1$, equation 1.25 writes $p(Z)_\infty \propto \mathrm{e}^{-\frac{Z^2/2}{\alpha/\mathrm{St}_0}}$. Small grains concentrate close to the mid-plane in a layer of thickness $H_\mathrm{d}/H = \sqrt{\alpha/\mathrm{St}_0}$ where gas density is almost constant. For $\alpha/\mathrm{St}_0 \geq 1$, small grains distribution looks like a rectangle shape with typical width of order $\sim 2-3H$. In this case, small grains decouple in the top layers and inertia can not be negligible.

1.5.3.2 *Large grains*

Large grains with $\mathrm{St}_0 \gg 1$ are decoupled from the gas. They orbit close to the mid-plane where gas has almost constant density. For large grains, inertia can not be negligible. Assuming turbulent correlations are neglected ($\tau_\mathrm{e} \to 0$), equation 1.21 writes

$$\begin{aligned} \mathrm{d}Z &= Z\mathrm{d}T, \\ \mathrm{d}V + \mathrm{St}_0^{-1}V\mathrm{d}T + Z\mathrm{d}T &= \mathrm{St}_0^{-1}\sqrt{\alpha}\mathrm{d}\xi. \end{aligned} \tag{1.26}$$

The system of equations 1.26 is equivalent to the following Fokker-Plank equation

$$\frac{\partial p}{\partial T} + V\frac{\partial p}{\partial Z} + \frac{\partial}{\partial V}\left(\left[-\mathrm{St}_0^{-1}V - Z\right]p\right) - \alpha\mathrm{St}_0^{-2}\frac{\partial^2 p}{\partial V^2} = 0, \tag{1.27}$$

for which the steady state solution writes

$$p(Z,V)_\infty = \frac{\mathrm{St}_0}{2\pi\alpha}\,\mathrm{e}^{-\frac{2}{\alpha/\mathrm{St}_0}\left(\frac{Z^2}{2}+\frac{V^2}{2}\right)}\,. \tag{1.28}$$

The distribution of large grains is Gaussian at steady state. The dust scale height is still $H_\mathrm{d}/H = \sqrt{\alpha/\mathrm{St}_0}$. The steady distribution in velocity is reached for a typical stopping time. The steady scale height is reached for a typical settling time. The mean turbulent velocity of grains is obtained by taking the variance of equation 1.28 as $v_\mathrm{d,T} = c_\mathrm{s}\sqrt{\alpha/\mathrm{St}_0}$. In this case, the diffusion coefficient of dust grains in the vertical direction is α/St_0. A refined model can be obtained by including finite correlation (Youdin and Lithwick, 2007) to take into account that turbulent stirring balances epicyclic oscillations of particles and not vertical. The stochastic differential equation on large grains writes

$$\begin{aligned} \mathrm{d}Z &= V\mathrm{d}T, \\ \mathrm{d}V + \mathrm{St}_0^{-1}V\mathrm{d}T + Z\mathrm{d}T &= \sqrt{2\alpha}\xi\mathrm{St}_0^{-1}\mathrm{d}T, \\ \mathrm{d}\xi &= -\frac{\xi}{\tau_\mathrm{e}}\mathrm{d}T + \frac{\mathrm{d}w}{\tau_\mathrm{e}}. \end{aligned} \tag{1.29}$$

By using the identity $\frac{\mathrm{d}\langle\xi g\rangle}{\mathrm{d}T} = \langle\xi\frac{\mathrm{d}g}{\mathrm{d}T}\rangle - \frac{\langle\xi g\rangle}{\tau_\mathrm{e}}$ and $\langle\xi\xi\rangle = 1/2$, one obtains the system of equations

$$\begin{aligned}
\frac{\mathrm{d}\langle ZZ\rangle}{\mathrm{d}t} &= 2\langle ZV\rangle,\\
\frac{\mathrm{d}\langle ZV\rangle}{\mathrm{d}t} &= -\langle ZZ\rangle - \mathrm{St}_0^{-1}\langle ZV\rangle + \langle VV\rangle + \sqrt{2\alpha}\mathrm{St}_0^{-1}\langle\xi Z\rangle,\\
\frac{\mathrm{d}\langle VV\rangle}{\mathrm{d}t} &= -2\langle ZV\rangle - 2\mathrm{St}_0^{-1}\langle VV\rangle + 2\sqrt{2\alpha}\mathrm{St}_0^{-1}\langle\xi V\rangle,\\
\frac{\mathrm{d}\langle\xi Z\rangle}{\mathrm{d}t} &= -\frac{1}{\tau_\mathrm{e}}\langle\xi Z\rangle + \langle\xi V\rangle,\\
\frac{\mathrm{d}\langle\xi V\rangle}{\mathrm{d}t} &= -\langle\xi Z\rangle - \left(\mathrm{St}_0^{-1} + \frac{1}{\tau_\mathrm{e}}\right)\langle\xi V\rangle + \mathrm{St}_0^{-1}\sqrt{\alpha/2}.
\end{aligned} \tag{1.30}$$

Steady state solutions $\langle ZZ\rangle_\infty$ and $\langle VV\rangle_\infty$ of the system of equations 1.30 give

$$\begin{aligned}
H_\mathrm{d}/H &= \sqrt{\alpha/\mathrm{St}_0}\sqrt{\frac{1+\tau_\mathrm{e}/\mathrm{St}_0}{1+\tau_\mathrm{e}/\mathrm{St}_0+\tau_\mathrm{e}^2}},\\
v_{\mathrm{d,T}}/c_\mathrm{s} &= \sqrt{\alpha}\sqrt{\frac{\tau_\mathrm{e}}{\mathrm{St}_0+\tau_\mathrm{e}+\mathrm{St}_0\tau_\mathrm{e}^2}}.
\end{aligned} \tag{1.31}$$

For $\mathrm{St}_0 \gg 1$ and τ_e, results differ by a factor $\sqrt{2}$ compared to the purely diffusive regime.

Models were refined to understand the role played by different drag regime (Garaud and Lin, 2004), by refined models of turbulence (Schräpler and Henning, 2004; Jacquet, 2013; Ormel and Liu, 2018), turbulent dead zones (Ciesla, 2007), turbulent correlations (Youdin and Lithwick, 2007), grain growth (Laibe and Price, 2014a) or winds (Riols and Lesur, 2018). Several aspects of dust settling were quantified with (magneto)-hydrodynamical simulations: the role of dust feed-back (Barrière-Fouchet et al., 2005; Johansen and Klahr, 2005; Johansen et al., 2006), turbulence (Takeuchi and Lin, 2002; Carballido et al., 2006; Fromang and Papaloizou, 2006; Fromang and Nelson, 2009; Ciesla, 2010; Turner et al., 2010; Charnoz et al., 2011; Johansen et al., 2011; Carballido et al., 2011; Zhu et al., 2015; Stoll and Kley, 2016; Lin, 2019), and grain growth/fragmentation (Zsom et al., 2011). Dust vertical settling is discussed in Chapter 5. The dust vertical settling is a source of differential velocities between grains leading to potential collisions.

1.5.4 *Radial drift*

The drag force leads to migration of grains towards inner radii, called the radial drift (Whipple, 1972; Adachi et al., 1976; Weidenschilling, 1977a; Nakagawa et al., 1986; Takeuchi and Lin, 2002). Due to its radial pressure gradient, the gas orbit at a sub-Keplerian velocity. A freely dust particle orbits at Keplerian velocity. Drag force tends to decelerate the dust particle, leading to a loose of angular momentum. Therefore, the dust particles spiral inward towards regions of higher pressure (Testi et al., 2014). Conservation of momentum for gas and dust write

$$\begin{aligned}
\frac{\partial \boldsymbol{v}_\mathrm{g}}{\partial t} + (\boldsymbol{v}_\mathrm{g}\cdot\nabla)\,\boldsymbol{v}_\mathrm{g} &= \frac{K}{\rho_\mathrm{g}}(\boldsymbol{v}_\mathrm{d}-\boldsymbol{v}_\mathrm{g}) - \nabla\Phi - \frac{1}{\rho_\mathrm{g}}\nabla P,\\
\frac{\partial \boldsymbol{v}_\mathrm{d}}{\partial t}\,(\boldsymbol{v}_\mathrm{d}\cdot\nabla)\,\boldsymbol{v}_\mathrm{d} &= -\frac{K}{\rho_\mathrm{d}}(\boldsymbol{v}_\mathrm{d}-\boldsymbol{v}_\mathrm{g}) - \nabla\Phi.
\end{aligned} \tag{1.32}$$

The stationary velocities in the mid-plane are obtained with $\partial/\partial t$ and performing a perturbative expansion under the form $\boldsymbol{v} = \boldsymbol{v}_\mathrm{K} + v_P\mathbf{e}_{\boldsymbol{\theta}}$, where $v_P \equiv \frac{1}{\rho_\mathrm{g}\Omega_\mathrm{K}}\frac{\partial P}{\partial r}$ appears as a

typical optimal drift velocity and $\mathbf{e}_\theta$ is the unity vector in azimuthal direction. Solving the system of equations

$$\begin{aligned}
\frac{\partial v_{g,r}}{\partial t} &= \frac{K}{\rho_g}\left(v_{d,r} - v_{g,r}\right) + 2\Omega_K v_{g,\theta} - \Omega_K v_P, \\
\frac{\partial v_{g,\theta}}{\partial t} &= \frac{K}{\rho_g}\left(v_{d,\theta} - v_{g,\theta}\right) - \frac{\Omega_K}{2} v_{g,r}, \\
\frac{\partial v_{d,r}}{\partial t} &= -\frac{K}{\rho_d}\left(v_{d,r} - v_{g,r}\right) + 2\Omega_K v_{d,\theta}, \\
\frac{\partial v_{d,\theta}}{\partial t} &= -\frac{K}{\rho_d}\left(v_{d,\theta} - v_{g,\theta}\right) - \frac{\Omega_K}{2} v_{d,r},
\end{aligned} \tag{1.33}$$

provides the velocities in stationary regime

$$\begin{aligned}
v_{g,r}^{st} &= -\frac{\epsilon v_P}{\mathrm{St} + \mathrm{St}^{-1}\left(1+\epsilon\right)^2}, \\
v_{g,\theta}^{st} &= \frac{1}{2}\frac{v_P}{1+\epsilon}\left(1 + \epsilon\frac{\mathrm{St}^2}{\left(1+\epsilon\right)^2 + \mathrm{St}^2}\right), \\
v_{d,r}^{st} &= \frac{v_P}{\mathrm{St} + \mathrm{St}^{-1}\left(1+\epsilon\right)^2}, \\
v_{d,\theta}^{st} &= \frac{1}{2}\frac{1+\epsilon}{\left(1+\epsilon\right)^2 + \mathrm{St}^2} v_P,
\end{aligned} \tag{1.34}$$

where $\epsilon \equiv \rho_d/\rho$ is the dust mass concentration, with $\rho = \rho_g + \rho_d$. $v_{g,r}^{st}$ denotes the gas drift powered by back-reaction. $v_{g,\theta}^{st}$ denotes the sub-Keplerian rotation corrected by back-reaction. $v_{d,r}^{st}$ denotes the drift of grains towards pressure maxima. $v_{d,\theta}^{st}$ denotes the rotation of grains slowed down by drag. Grains drift towards inner regions of discs. Drift efficiency depends on the size of the grains and is maximal for $\mathrm{St} \sim 1$. Such grains should fall onto the central star before forming planetesimals, which lead to the so-called radial drift barrier problem. For discs modelled by Minimum Mass Solar Nebulae, $\mathrm{St} \sim 1$ correspond to solid of size $\sim$ 1m. Therefore, the so-called radial-drift barrier is called the metre-size barrier of planet formation. To maintain the presence of dust in discs and form planets, dust may pile-up at some specific locations that consist of local pressure maxima. Local traps offer a powerful alternative to concentrate grains and then to make fast dust growth easier. Some mechanisms of dust trap have been proposed: vortices (Johansen et al., 2004), dead zones (Dzyurkevich et al., 2010), spiral arms (Dipierro et al., 2015), self-induced dust traps (Gonzalez et al., 2017) combined with snow-lines (Vericel and Gonzalez, 2020), streaming instability (Jaupart and Laibe, 2020).

1.6 GRAIN GROWTH

1.6.1 *Contact between grains*

The process of grain-grain collision is detailed from macroscopic point of view. Two spherical compact grains in contact undergo two interactions when subjected to a load: an adhesive surface tension and a repulsive elastic force, which prevent grains to interpenetrate (Johnson et al., 1971; Derjaguin et al., 1975; Chokshi et al., 1993). Figure 1.7 illustrates the geometry of the Hertz contact model (Hertz et al., 1896). Two spherical grains of radius R_1 and R_2 interpenetrate on a length $\delta = \delta_1 + \delta_2$ with $\delta \ll R_1$ and $\delta \ll R_2$. An important parameter of the problem is the contact area between grains

which is a circle of radius a. The displacement of each sphere writes $\delta_i \sim a^2/R_i$ with $\delta_i \ll R_i$. Therefore, $\delta \sim a^2/R$ with $R = R_1R_2/(R_1+R_2)$ the "reduced" radius of the grains. The force F required to maintain the grains in static contact is the sum of the radially averaged pressure p exerted onto each element on the contact area

$$F(a) = 2\pi \int_0^a p(r) r \mathrm{d}r \sim \pi a^2 \langle p \rangle. \tag{1.35}$$

The binding energy at the contact circle is $\mathcal{E}_\mathrm{s} = -2\pi a^2 \gamma \sim -\gamma R \delta$ where γ is the surface energy per unit area of each surface. In the elastic domain, the relation between pressure and radial strain $\frac{\partial \xi_i}{\partial r}$ is linear, then $\langle p \rangle \sim E|\frac{\partial \xi_i}{\partial r}|$, where E is the Young modulus of the grains. E depends on the grains properties. Strain is dominated by the radial deformation of the grains with $\frac{\partial \xi_r}{\partial r} \sim \delta/a$. Therefore, $F(\delta) \sim E\sqrt{R}\delta^{3/2}$ and the elastic deformation energy writes $\mathcal{E}_\mathrm{el} = \int F \mathrm{d}\delta \sim E\sqrt{R}\delta^{5/2}$. From $\mathcal{E}_\mathrm{s}$ and $\mathcal{E}_\mathrm{el}$, a typical length δ_c and a typical energy $\mathcal{E}_\mathrm{c}$. Under a separating force, the grains stretch, form a neck connecting the two and finally separate at the critical displacement $\delta = -\delta_\mathrm{c}$ with $\delta_\mathrm{c} \sim \left(\gamma^2 R/E^2\right)^{1/3}$. $\mathcal{E}_\mathrm{c}$ corresponds to the energy required to separate grains. The typical length and energy depend on the grain sizes and their material properties. Stable equilibrium is obtained for sticking grains maintained by an adhesive energy of order $\sim \mathcal{E}_\mathrm{c}$ in an interpenetration of order $\sim \delta_\mathrm{c}$. The criteria to consider that two grains stick is based on the comparison of kinetic energy $\mathcal{E}_\mathrm{k}$ and the critical energy $\mathcal{E}_\mathrm{c}$. Let us consider two colliding grains with relative kinetic energy at infinity $\mathcal{E}_\mathrm{k} = \frac{1}{2}mv^2$. Grains remain bounded after contact if $\mathcal{E}_\mathrm{k} \leq \mathcal{E}_\mathrm{c}$, i.e. when the collision velocity is smaller than the critical velocity value (Chokshi et al., 1993)

$$v_c \sim \frac{\gamma^{5/6} R^{-5/6}}{\rho^{1/2} E^{1/3}}, \tag{1.36}$$

where ρ is the intrinsic density of grains. Small grains can stick even at high collision velocity since surface tension has an important contribution. Grains can stick easier if they are soft, porous and composed of adhesive materials. Sticking is more likely to occur for ice coated grains (Blum and Wurm, 2008; Musiolik et al., 2016).

The study of collision between aggregates, composed of a chain of grains, is more complex. Indeed, energy is distributed in the aggregate by elastic waves that excite individual contact between grains. Aggregates can stick, bounce but also can be compacted, eroded or fragmented. These different processes are tabulated from lab experiments (Blum and Wurm, 2008; Güttler et al., 2010; Blum, 2010; Musiolik et al., 2016; Gundlach et al., 2018; Steinpilz et al., 2019; Musiolik and Wurm, 2019), numerical simulations (Dominik and Tielens, 1997; Geretshauser et al., 2010) and semi-analytical models (Kataoka et al., 2013; Yamamoto et al., 2014).

1.6.2 *Grain-grain interactions*

Grain-grain interactions play a fundamental role for planet formation. Grains can stick at contact under the effect of local electrostatic forces and form larger aggregates (Blum, 2018). Dust growth strongly affects dust dynamics since Stokes number is proportional to the grain size. Dynamics may in return concentrate solid particles, increasing collisional rates. Dust distributions are the result of a complex interplay between growth and dynamics. Dust growth strongly affects the dust distributions from which observational parameters are evaluated, such as dust opacity (Andrews, 2020). Therefore, dust growth has to be accounted for accurately. The so-called Smoluchowski coagulation equation

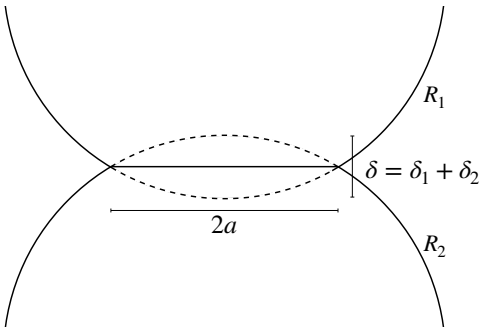

Figure 1.7: Geometry of the Hertz contact model. Deformations are small $\delta \ll a_0 \ll R_{1,2}$.

(Smoluchowski, 1916) describes the evolution of populations of grains due to grain-grain collision. Solving efficiently and accurately this non-linear integro-differential equation is a numerical challenge. In astrophysics community, several numerical schemes have been developed to solve this equation (e.g. Safronov (1972), Hayashi and Nakagawa (1975), Weidenschilling (1977a), Nakagawa et al. (1981), Ohtsuki et al. (1990), Wetherill (1990), Tanaka et al. (1996), Lee (2001), Dullemond and Dominik (2005b), Ormel et al. (2007), Estrada and Cuzzi (2008), Brauer et al. (2008), Okuzumi et al. (2009), Birnstiel et al. (2010), Kobayashi and Tanaka (2010), Charnoz and Taillifet (2012), Garaud et al. (2013), and Drążkowska et al. (2019)) to treat dust growth in simulations of discs.

1.6.3 *Bouncing barrier*

Blum and Münch (1993), Güttler et al. (2010), and Blum (2018) experimented grain-grain collisions in laboratory. A major result is that above a typical size of $\sim 1\,\mathrm{cm}$, growth is quenched as aggregates bounce onto each others. The initial growth starts by collisions of small leading to the formation of large grains. Grain sizes and impact velocities increase. Then, large grains stop to stick. They are only compacted by collisions and only bouncing collisions occurred.

1.6.4 *Fragmentation barrier*

Above a velocity threshold that depends on the material properties of the grains, the outcome of a collision between two grains can be the fragmentation. Colliding aggregates explode in several fragments that roughly follow a power-law in size. Blum and Wurm (2008) determined for a velocity $v \geq 1\,\mathrm{m} \cdot \mathrm{s}^{-1}$, the outcome of a collision is not sticking. This lead to a limitation in size during the dust growth.

1.7 NUMERICAL SIMULATIONS

Since the equations of motion of gas and dust are not solvable analytically, the use of numerical simulations is required. A consistent understanding of the evolution of protoplanetary discs requires contribution of spatially resolved observations of discs and numerical 3D simulations of discs. Two kinds of numerical methods have emerged to simulate the evolution of dusty discs. The first type of numerical methods are the grid-based methods which have been widely used since 90s. The major grid-based code to perform 3D simulations of dusty discs are the following: `RAMSES` (Teyssier, 2002) with

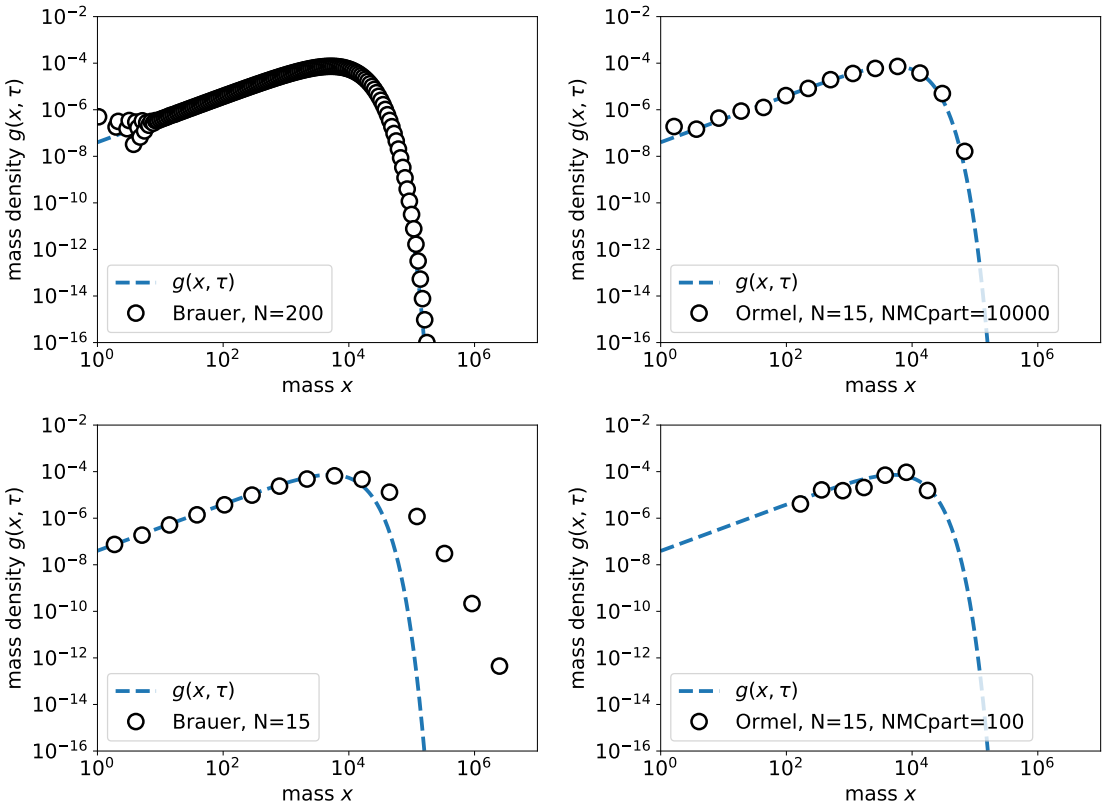

Figure 1.8: Numerical simulations of the mass density from methods presented in Brauer et al. (2008) and Ormel et al. (2007) codes are compared to the analytical solution for constant kernel $\mathcal{K} = 1$. Top Left: Numerical solution of the mass density versus masses of grains for the Brauer et al. (2008) code with $N = 200$ bins. The implementation of this code is confirmed by the convergence to the analytical solution with a large number of bins. Top Right: Numerical solution for the Ormel et al. (2007) code with $N = 15$ bins and 10000 Monte-Carlo particles. For a large number of Monte-Carlo particles, the scheme converge to the analytical solution. Bottom Left: Brauer et al. (2008) code with $N = 15$ bins. Strong numerical diffusion for grains of large masses. Bottom Right: Ormel et al. (2007) code with $N = 15$ bins and 100 Monte-Carlo particles. The analytical solution can not be approximated on all the mass range, specially for large masses.

the implementation of the dust dynamics by Lebreuilly et al. (2019), `PLUTO` (Mignone et al., 2012; Mignone et al., 2019), `FARGO3D` (Benítez-Llambay and Masset, 2016; Benítez-Llambay et al., 2019), `ATHENA` (Stone et al., 2008; Stone et al., 2020). The second type of numerical methods is the particle-based method such as Smoothed-Particle Hydrodynamics (SPH). These methods have the advantage to be grid-free. The most widely used code to perform 3D simulations of dusty discs is `PHANTOM` (Price et al., 2018).

1.8 SCIENTIFIC OBJECTIVES OF THE THESIS

According to the encountered barriers in the dust evolution, how grains can growth over 30 orders of magnitude in mass to form planet in less than 1 million years ? To answer this question, numerical models have to include a complete dust collision model described by the Smoluchowski coagulation equation (see Chapter 2). Solving efficiently and accurately this non-linear integro-differential equation is a critical numerical challenge that has not been achieved so far. Typically, we estimate that 3D simulations with

PHANTOM could handle ~ 15 dust bins. In astrophysics community, current algorithms require an important computational cost to solve accurately the Smoluchowski coagulation equation (e.g. Ormel et al. (2007), Brauer et al. (2008), Birnstiel et al. (2010), Kobayashi and Tanaka (2010), and Drążkowska et al. (2019)). During the first year of my Ph.D. thesis, I implemented two widely used algorithms presented in Ormel et al. (2007) and Brauer et al. (2008) to evaluate their performance. Figure 1.8 shows the performance of these two schemes. The numerical solution from the Ormel et al. (2007) code converges for a large number of Monte-Carlo particles (NMCpart). In the case of a small number of Monte-Carlo particles, the numerical solution from the Ormel et al. (2007) can not approximate the analytical solution in all the mass range, specially for large masses. The numerical solution from the Brauer et al. (2008) algorithm converges for a large number of bins $N = 200$. In the case of a small number of bins $N = 15$, the numerical solution from the Brauer et al. (2008) scheme strongly over-estimates the mass density for grains with large masses. These two codes require a large number of bins or a large number of Monte-Carlo particles to approximate accurately the analytical solution, leading to an important computational cost. Therefore, efficiency and accuracy are not achievable with these two codes in a tractable computational time for 3D simulations of dusty discs.

From the review of "*Protostars and Planets VI*" (Testi et al., 2014), the next stage, for the global models of dust evolution in discs, is however to account properly the dust growth in 3D. The work, presented in this thesis, was to figure out and develop a numerical scheme to do so. The first step was to implement the Ormel et al. (2007) and Brauer et al. (2008) codes. Then a bibliographical research in other scientific communities such as mathematics, chemistry and aerosols have been realised to develop our algorithm. The development of our high-order solver started with Filbet and Laurencot (2004) finite volume scheme, the first to solve the Smoluchowski equation in its conservative form. The cross references of Filbet and Laurencot (2004) led us to the work of Liu et al. (2019) for developing a high-order scheme based on the discontinuous Galerkin method in order to overcome this numerical challenge (see Chapter 3). This scheme solves efficiently and accurately the Smoluchowski coagulation equation and fulfils all the requirements to be coupled in a tractable manner to the code PHANTOM (see Chapter 4). 3D simulations of dusty discs will be performed by including this algorithm in the code PHANTOM.

1.9 OUTLINE OF THE THESIS

The manuscript is presented in 7 chapters starting with this introduction. Chapter 2 presents the Smoluchowski coagulation equation. Chapter 3 details the high-order scheme based on the discontinuous Galerkin scheme. Chapter 4 details the benchmarks and the performances of the scheme. Chapter 5 presents the first side project on the small grains evolution in the vertical direction. Chapter 6 presents the second side project on the analysis of observational data to detect exoplanets with the instrument SPHERE/VLT. Chapter 7 concludes the thesis and details the perspectives for further studies and developments.

2 DUST COAGULATION AND FRAGMENTATION

"Music washes away the dust of every day life"– Art Blakey

2.1 Introduction . . . 23
2.1.1 Dust coagulation . . . 23
2.1.2 Dust fragmentation . . . 24
2.2 Smoluchowski equation . . . 24
2.2.1 Analytic solutions . . . 28
2.2.2 Self-preserving solutions . . . 30
2.2.3 Physical coagulation kernels . . . 33
2.2.4 Conservative form . . . 33
2.3 Collisional fragmentation model . . . 34
2.3.1 Analytic solutions . . . 35
2.3.2 Conservative form . . . 37
2.4 Coagulation-fragmentation equation . . . 37
2.5 Summary . . . 38

2.1 INTRODUCTION

The first step towards planet formation consists of the dust coagulation. Observations reveal that protoplanetary discs contain dust grains of at least $0.1 - 1\mu m$ in size (Testi et al., 2014; Birnstiel et al., 2016; Blum, 2018; Andrews, 2020). To form planetesimals, small dust grains have to grow over thirty orders of magnitude in mass. Shall the core-accretion model be correct, spatially resolved observations of young stellar objects suggest that at least some planetesimals have to form in less than one million of years (Andrews (2020) and references therein). Therefore, the formation of planetesimals may be a relatively short stage of the planet formation process. The key challenge is to explain how such an effective formation while accounting for the complex dynamics of grains in discs. The processes of radial drift, vertical settling and turbulence stirring are the main contributors to the dynamics of dust grains in discs. This complex dynamics can lead grains of different sizes to have relative local differential velocities. In a simplified manner, two colliding grains can form a larger grain by coagulation, or several smaller grains by fragmentation according to the value of this relative velocity. More details about the result from the collision of two particles are in Blum (2018). To address the interplay between growth and dynamics, it is required to comprehensively study the coagulation and fragmentation processes. An interesting point of view is to come back to the description of the composition of protoplanetary discs. These discs are composed of a mixture of gas and dust. This mixture is a dispersed system composed of grains suspended in gas. Therefore, dust grains are dynamically equivalent to aerosols. The physics of aerosols developed at the beginning of 20th century can be used to analyse the evolution of dust in protoplanetary discs.

2.1.1 *Dust coagulation*

In aerosols science, the coagulation process has long been studied (Hidy and Brock (1972), Williams and Loyalka (1991), Friedlander et al. (2000), Ramkrishna (2000), Jacobson (2005),

Pruppacher and Klett (2010), Hidy (2012), and Khain and Pinsky (2018) and references in these reviews). Coagulation can be triggered by any mechanism which sustains relative velocity between particles (e.g. Brownian motion, turbulence, differential particle motion associated with external force fields). The mean-field theory of coagulation for binary collisions has been established by Smoluchowski (1916) to analyse the coagulation of particles due to Brownian motion. The Smoluchowski coagulation equation has been derived for a general collision mechanism involving a relative velocity between particles. This theory has been verified experimentally (Kruyt and Van Arkel, 1920; Turkevich, 1959; Higuchi et al., 1963; Devir (Weinstock), 1963; Devir (Weinstock), 1966; Delichatsios and Probstein, 1975; Davies, 1979; Lee and Chen, 1984; di Stasio et al., 2002). Therefore, as mentioned by Safronov (1972), it is natural to adopt the Smoluchowski coagulation theory in the case of dust coagulation in astrophysics. The Smoluchowski coagulation model will be described in Section 2.2.

2.1.2 *Dust fragmentation*

The first model in astrophysics for collisional fragmentation has been developed in the asteroids community by Piotrowski (1953), Dohnanyi (1969), Hellyer (1970), and Dohnanyi (1971). The same model is used by Safronov (1972) to describe dust fragmentation in protoplanetary discs. This model has been widely used in astrophysics community (Wilkins, 1982; Jones et al., 1994; Tanaka et al., 1996; Hirashita and Yan, 2009; Birnstiel et al., 2010; Kobayashi and Tanaka, 2010; Kobayashi et al., 2010; Gáspár et al., 2012; Brilliantov et al., 2015). The collisional fragmentation occurs in many other fields such as chemistry to describe the polymer degradation (Cheng and Redner, 1988; Cheng and Redner, 1990) or other chemical engineering applications (Kostoglou and Karabelas, 2000; Kostoglou and Karabelas, 2006), aerosols science (Brazier-Smith et al., 1972; Young, 1975; List and Gillespie, 1976; Gillespie and List, 1978; Srivastava, 1978; Tzivion (Tzitzvashvili) et al., 1989; Hu and Srivastava, 1995; Ramkrishna, 2000; Pruppacher and Klett, 2010; Khain and Pinsky, 2018). In parallel, the mathematical properties of this model have been studied (Laurençot and Wrzosek, 2001; Paul and Kumar, 2018). The collisional fragmentation model will be described in Section 2.3.

2.2 SMOLUCHOWSKI EQUATION

At the beginning of the 20th century, M. Smoluchowski studied the statistical problem of the collision of spherical particles thermally agitated in a gas, by applying the theory of Brownian motion. The potential of interaction between the molecules is neglected. He determined the rate of coagulation of aerosols in a static medium by considering only binary collisions. Smoluchowski's model assumes that coalescence occurs instantaneously after two particles collide, and a new spherical particle is formed. The spatially homogeneous system is initially composed of N_0 particles of equal mass m_0 (i.e. monomers) in a unit volume of the gas. These monomers can form polymers by collision of mass an integral multiple of m_0. The coagulation process lead to the reduction in the number of polymers in unit volume (i.e. number density), and therefore to the total number of polymers. The model derived by Smoluchowski (1916) follows the evolution of the number density of polymers. The illustration in Figure 2.1 explains the evolution of a group of polymers with similar mass m_i during a time dt. This group is named i^{th}-*group*. Two colliding polymers can form a new polymer with mass m_i. This new polymer populates the ith-*group* (left grey arrow in Figure 2.1). A collision between a polymer

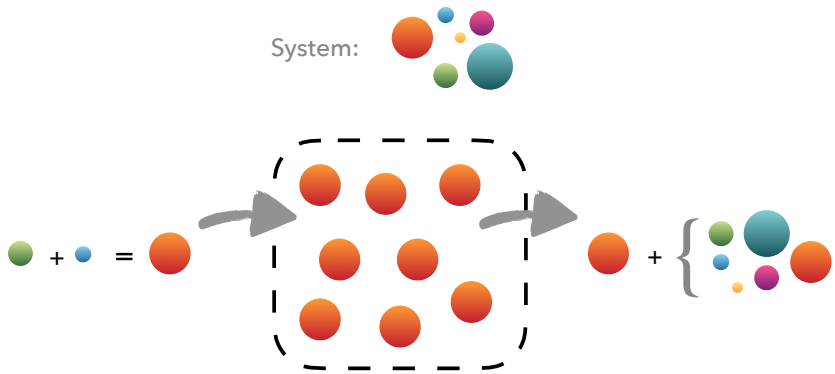

Figure 2.1: Illustration of the Smoluchowski coagulation equation for the group of polymers with mass m_i in orange. The green and blue polymers have a mass lower than m_i. The rainbow polymer represents any polymer in the system. The left, (respectively right) arrow represents the ingoing (respectively outgoing) polymers in the group.

from the ith-*group* and any polymers in the system empties the ith-*group* (right grey arrow in Figure 2.1). Figure 2.1 is a schematic representation of the Smoluchowski coagulation equation.

The Smoluchowski theory of coagulation results in the following set of non-linear differential equations on the number density of polymers in the system

$$\begin{cases} \forall i \in \mathbb{N}, \\ \dfrac{\mathrm{d}n_i}{\mathrm{d}t} = \dfrac{1}{2}\displaystyle\sum_{j=1}^{i-1} K_{j,i-j} n_j n_{i-j} - n_i \sum_{j=1}^{\infty} K_{i,j} n_j, \\ n_1(0) = N_0,\ \forall i > 1,\ n_i(0) = 0, \end{cases} \tag{2.1}$$

where n_i denotes the number density of polymers with mass m_i, t is the time in second and K is the collision frequency, also called kernel function. It describes the microphysics of the collision. K depends on the sizes of the colliding particles and on such properties of the gas such as temperatures and pressure.

The first term on the right-hand side of equation 2.1 is the gain term (left grey arrow in Figure 2.1). It describes the rate of generation of polymers with mass m_i by coalescence with polymers of mass m_j and m_{i-j}. The second term is the loss term (right grey arrow in Figure 2.1). It describes the decay rate of the number of polymers with mass m_i by coalescence with any other polymers. The coefficient $1/2$ is inserted to avoid double counting of pairwise collisions. equation 2.1 is known as the Smoluchowski equation, also known as population balance equation (PBE, Ramkrishna (2000)). It is assumed that Müller (1928) is the first to rewrite Equation 2.1 in its continuous form. The link between the discrete and the continuous form is straightforward (Hidy and Brock, 1972). Let denote n_i the number of polymers per unit volume at time t whose masses of polymers are between m_i and $m_i + \mathrm{d}m_i$,

$$n_i = n(m_i, t)\mathrm{d}m_i. \tag{2.2}$$

The quantity $n(m, t)$ is the continuous polymers number density function by mass interval $\mathrm{d}m$. Its unity is $\mathrm{g}^{-1}.\mathrm{cm}^{-3}$ in c.g.s. $K_{ij} = K(m_i, m_j)$ is the coagulation kernel for binary

collisions between polymers of volumes v_i and v_j. The unity of the kernel function is $\mathrm{cm}^3.\mathrm{s}^{-1}$ in c.g.s. Equation 2.1 becomes

$$\begin{aligned}\frac{\partial n(m_i,t)}{\partial t}\Delta m_i =& \frac{1}{2}\sum_{j=1}^{i-1} K(m_j, m_i - m_j)n(m_j,t)n(m_i - m_j,t)\Delta m_j \Delta(m_i - m_j) \\ &- n(m_i,t)\Delta m_i \sum_{j=1}^{\infty} K(m_i,m_j)n(m_j,t)\Delta m_j.\end{aligned} \tag{2.3}$$

Dividing by Δm_i and taking the limit $\Delta m_j \to 0$, the result is

Continuous form of the Smoluchowski coagulation equation

$$\begin{cases}\dfrac{\partial n(m,t)}{\partial t} = \dfrac{1}{2}\displaystyle\int_0^v K(m', m-m')n(m',t)n(m-m',t)\mathrm{d}m' \\ \qquad\qquad - n(m,t)\displaystyle\int_0^\infty K(m',m)n(m',t)\mathrm{d}m', \\ n(m,0) = n_0(m),\end{cases} \tag{2.4}$$

where $m_i = m$ and $m_j = m'$. Integrals are defined in the sense of Riemann. The first integral in equation 2.4 describes the formation of a polymer of mass m only by collision between polymers with masses m' and $m - m'$. The second integral handles the fact that each polymer of mass m disappears from the interval $m + \mathrm{d}m$ after collision with a polymer of mass m'. The expression of $K(m, m')$ depends on the physics of the collision. The Smoluchowski coagulation equation 2.4 is a mean-field deterministic integro-differential equation. It's an averaged equation over a certain volume of gas, meaning the existence of a great number of polymer pairs within the volume where collisions are analysed. The Smoluchowski coagulation equation 2.4 is also called stochastic collection equation (SCE, Pruppacher and Klett (2010) and Khain and Pinsky (2018)), due to the fact that coagulation process is a stochastic process.

The physical properties of equation 2.4 are the following

$$\forall (m,t) \in \mathbb{R}_+^2,\ n(m,t) \geq 0, \quad \forall (m,m') \in \mathbb{R}_+^2,\ 0 \leq K(m,m') = K(m',m). \tag{2.5}$$

K is a nonnegative symmetric function. Equation 2.4 is an equation of mass conservation. During each coagulation event, the total mass of particles $M_1(t)$ is conserved while the total number of particles $M_0(t)$ decreases. These two quantities are given by

$$M_0(t) = \int_0^\infty n(m,t)\mathrm{d}m, \quad M_1(t) = \int_0^\infty mn(m,t)\mathrm{d}m. \tag{2.6}$$

It is known that the total mass of particles might not remain constant throughout time evolution for some kernels. If K increases rapidly for large masses, the larger the particles are, the faster they merge. A runaway growth appears, where particles with "infinite" mass are formed in finite time. These particles are removed from the system. Therefore the total mass starts to decrease. This phenomenon is called occurrence of gelation (Leyvraz and Tschudi, 1981; Ernst et al., 1984; Dubovskiui, 1994; Aldous, 1999; Filbet and Laurencot, 2004).

Before analysing the solutions of the Smoluchowski coagulation equation, it is simpler to rewrite equation 2.4 in a dimensionless form. Relevant mass normalisation can be obtained by looking at the evolution of the first moment. Multiplying equation 2.4 by m and integrating from 0 to ∞, we have

$$\begin{aligned}\frac{\mathrm{d}M_1(t)}{\mathrm{d}t} =& \frac{1}{2}\int_0^\infty\int_0^m K(m',m-m')mn(m',t)n(m-m',t)\mathrm{d}m'\mathrm{d}m \\ &- n(m,t)\int_0^\infty\int_0^\infty K(m,m')mn(m',t)\mathrm{d}m'\mathrm{d}m.\end{aligned} \tag{2.7}$$

Following the idea from Estrada and Cuzzi (2008), a step function H is introduced to extent the limits of the integral over m' from $(0,m)$ to $(0,\infty)$. H is defined as $H=0$ for $m-m'<0$ and $H=1$ otherwise. With a change of variable $z=m-m'$ and using the Fubini theorem, the first double integral on the right-hand side writes

$$\begin{aligned}&\frac{1}{2}\int_0^\infty\int_0^\infty H(m-m')K(m',m-m')mn(m',t)n(m-m',t)\mathrm{d}m'\mathrm{d}m \\ &= \frac{1}{2}\int_0^\infty\int_0^\infty K(m',z)(z+m')n(m',t)n(z,t)\mathrm{d}z\mathrm{d}m'.\end{aligned} \tag{2.8}$$

With the property of symmetry for the kernel function, the second double integral writes

$$\begin{aligned}&\int_0^\infty\int_0^\infty K(m',m)mn(m',t)n(m,t)\mathrm{d}m'\mathrm{d}m \\ &= \frac{1}{2}\int_0^\infty\int_0^\infty K(m',m)(m+m')n(m',t)n(m,t)\mathrm{d}m'\mathrm{d}m.\end{aligned} \tag{2.9}$$

Then, z is substituted by m,

$$\frac{\mathrm{d}M_1(t)}{\mathrm{d}t} = \frac{1}{2}\int_0^\infty\int_0^\infty K(m,m')\left[(m+m')-(m+m')\right]n(m',t)n(m,t)\mathrm{d}m'\mathrm{d}m = 0. \tag{2.10}$$

Mass conservation ensures that $M_1 = const \equiv N_0 m_0$ where N_0 is the initial total number density of particles and m_0 is the initial mean mass of the particles. Equation 2.4 is made dimensionless with the use of the following expressions (Scott, 1968; Drake, 1972)

$$x \equiv m/m_0,\ y \equiv m'/m_0,\ \mathcal{K}(x,y) = K(m,m')/K_0,\ \tau = (K_0N_0)t,\ f(x,\tau) = m_0 n(m,t)/N_0, \tag{2.11}$$

where K_0 is a normalising constant with dimensions $[\text{length}]^3/\text{time}$. Equation 2.4 becomes

Dimensionless Smoluchowski coagulation equation in continuous form

$$\begin{cases} f(x,0) = f_0(x),\ 0 \leq \mathcal{K}(x,y) = \mathcal{K}(y,x),\ \int\limits_0^\infty x f(x,\tau) = 1, \\ \dfrac{\partial f(x,\tau)}{\partial \tau} = \dfrac{1}{2}\int\limits_0^x \mathcal{K}(y,x-y) f(y,\tau) f(x-y,\tau)\mathrm{d}y - f(x,\tau)\int\limits_0^\infty \mathcal{K}(y,x) f(y,\tau)\mathrm{d}y. \end{cases} \tag{2.12}$$

Melzak (1957) and McLeod (1962) proved the existence, uniqueness, nonnegativity and continuity properties of solutions of equation 2.12 in the case of bounded kernels and for some unbounded kernels. Equation 2.12 is an integro-differential equation strongly non-linear. Only numerical solution can be derived for general kernels. Analytical solutions have been derived for peculiar expressions of K.

2.2.1 *Analytic solutions*

Equation 2.12 have been solved exactly for three kernels: constant, additive and multiplicative.

2.2.1.1 *Constant kernel*

This solution has been first derived by Smoluchowski (1916) for the discrete equation and by Müller (1928), Schumann (1940), and Rajagopal (1959) for the continuous equation. I followed the work from Scott (1968) and Silk and Takahashi (1979) for the proofs. The kernel function writes $K(m,m') = K_0$, thus $\mathcal{K}(x,y) = 1$. Equation 2.12 becomes

$$\frac{\partial f(x,\tau)}{\partial \tau} = \frac{1}{2}\int\limits_0^x f(y,\tau) f(x-y,\tau)\mathrm{d}y - f(x,\tau) M_0(\tau). \tag{2.13}$$

Let us define the Laplace transform as

$$F(p,\tau) = \mathcal{L}[f](p,\tau) \equiv \int\limits_0^\infty \mathrm{e}^{-px} f(x,\tau)\mathrm{d}x. \tag{2.14}$$

By applying the Laplace transform to equation 2.13, we obtain

$$\frac{\partial F(p,\tau)}{\partial \tau} = \frac{1}{2}F^2(p,\tau) - M_0(\tau)F(p,\tau). \tag{2.15}$$

This step is derived by the same idea than in equation 2.8 with the step function and the change of variable. With $p = 0$, $F(0,\tau) = M_0(\tau)$, then equation 2.15 writes

$$\frac{\mathrm{d}M_0(\tau)}{\mathrm{d}\tau} = -\frac{1}{2}M_0^2(\tau) \quad \Rightarrow \quad M_0(\tau) = \frac{1}{1+\frac{\tau}{2}},\ \text{with}\ M_0(0) = 1. \tag{2.16}$$

The solution to equation 2.15 writes

$$F(p,\tau) = \frac{f_1(\tau)}{\frac{1}{F(0,\tau)} - f_2(\tau)}, \tag{2.17}$$

where

$$f_1(\tau) \equiv \exp\left(\int_0^\tau M_0(\tau')\mathrm{d}\tau'\right) = \frac{4}{(2+\tau)^2} \quad \text{and} \quad f_2(\tau) \equiv \frac{1}{2}\int_0^\tau f_1(\tau')\mathrm{d}\tau' = \frac{\tau}{2+\tau}. \tag{2.18}$$

At this stage, a general expression is obtained depending only on the Laplace transform of the initial condition. Let us choose an initial condition

$$n_0(m,0) = \frac{N_0}{m_0}\,\mathrm{e}^{-m/m_0} \quad \Rightarrow \quad f(x,0) = \mathrm{e}^{-x}\,. \tag{2.19}$$

The Laplace transform of the initial condition gives $F(p,0) = 1/(1+p)$. Then $F(p,\tau) = f_1(\tau)\left[1+p-f_2(\tau)\right]^{-1}$. To derive the number density, the inverse Laplace transform is obtained by comparing $F(p,\tau)$ with the usual Laplace transform expressions. Then, the solution is

Constant kernel

$$\begin{aligned}
&\mathcal{K}(x,y) = 1,\ f(x,0) = \mathrm{e}^{-x},\\
&f_1(\tau) \equiv \frac{4}{(2+\tau)^2},\ f_2(\tau) \equiv \frac{\tau}{2+\tau},\\
&f(x,\tau) = f_1(\tau)\,\mathrm{e}^{-(1-f_2(\tau))x}\,.
\end{aligned} \tag{2.20}$$

2.2.1.2 *Additive kernel*

The solution for the additive kernel $\mathcal{K}(x,y) = x+y$ with initial condition $f_0(x,0) = \mathrm{e}^{-x}$ has been derived by Golovin (1963) and Scott (1968) extended the derivation for a general initial condition. The solution is

Additive kernel

$$\begin{aligned}
&\mathcal{K}(x,y) = x+y,\ f(x,0) = \mathrm{e}^{-x},\\
&T \equiv 1-\mathrm{e}^{-\tau},\\
&f(x,\tau) = \frac{(1-T)\,\mathrm{e}^{-x(1+T)}}{xT^{1/2}} I_1\left(2xT^{1/2}\right),
\end{aligned} \tag{2.21}$$

with I_1 the modified Bessel function of first kind. The proofs of the solution are given in Golovin (1963) and Scott (1968).

2.2.1.3 *Multiplicative kernel*

McLeod (1962) derived the solution for multiplicative kernel $\mathcal{K}(x,y) = xy$ with initial condition $f_0(x,0) = x^{-1}\,\mathrm{e}^{-x}$ only for a small finite time interval. A new solution on all time interval has been derived by Ernst et al. (1984)

Multiplicative kernel

$$\begin{aligned} &\mathcal{K}(x,y) = xy,\ f(x,0) = x^{-1}\,\mathrm{e}^{-x}, \\ &T \equiv \begin{cases} 1+\tau & \text{if}\,(\tau \leq 1) \\ 2\tau^{1/2} & \text{otherwise} \end{cases}, \\ &f(x,\tau) = \frac{\mathrm{e}^{-Tx}\, I_1\left(2x\tau^{1/2}\right)}{x^2\tau^{1/2}}. \end{aligned} \tag{2.22}$$

The proofs of the solution are given in Ernst et al. (1984). The multiplicative kernel is a typical kernel to study the occurrence of gelation, since at $\tau = 1$ particles with infinite mass are formed and mass conservation is no longer satisfied.

2.2.2 *Self-preserving solutions*

In aerosol science, the size distribution of particles for a system after a long time is of great interest. Schumann (1940) found that for constant kernel, the exponential form of the size distribution might be the asymptotic solution for any initial distribution (Friedlander and Wang, 1966). A similarity theory has been developed by Friedlander (1960a), Friedlander (1960b), Swift and Friedlander (1964), Friedlander and Wang (1966), and Wang (1966) to account for similarities in the shapes of atmospheric aerosol spectra found experimentally (Junge, 1958). Solutions found in this way are asymptotic forms approached after long times, and they are independent of the initial size distribution. The similarity transformation is

$$\begin{aligned} &n(m,t) = \frac{M_0(t)^2}{M_1}\Psi(\eta), \\ &\eta \equiv \frac{M_0(t)m}{M_1}. \end{aligned} \tag{2.23}$$

The Smoluchowski coagulation equation 2.4 can be reduced to an ordinary integro-differential equation by the similarity transformation, if the kernel function $K(m,m')$ is a homogeneous function of order λ,

$$K(\alpha m, \alpha m') = \alpha^{\lambda} K(m,m'),\ \alpha > 0,\ \lambda \in [0,1). \tag{2.24}$$

Let us give an example by deriving the function Ψ with the Brownian kernel function following the work of Wang (1966), Lai et al. (1972), and Friedlander et al. (2000). The Brownian kernel function writes

$$K_B(m,m') = \left(\frac{3}{4\pi}\right)^{1/6}\left(\frac{6kT}{\rho_p}\right)^{1/2}\left[\frac{1}{m}+\frac{1}{m'}\right]\left(m^{1/3}+m'^{1/3}\right)^2, \tag{2.25}$$

where k is the Boltzmann constant, T the absolute temperature, and ρ_p the particle density. The Brownian kernel function is a homogeneous function of order 1/6 with respect to particle masses. Equation 2.4 writes

$$\begin{cases} \phi\left(2\Psi + \eta\dfrac{\mathrm{d}\Psi}{\mathrm{d}\eta}\right) + \displaystyle\int_0^\eta \left[\tilde{\eta}^{1/3} + (\eta-\tilde{\eta})^{1/3}\right]^2 \left(\frac{1}{\tilde{\eta}} + \frac{1}{\eta-\tilde{\eta}}\right)^{1/2} \Psi(\eta)\Psi(\tilde{\eta})\mathrm{d}\tilde{\eta} \\ -2\Psi(\eta)\displaystyle\int_0^\infty \left(\eta^{1/3} + \tilde{\eta}^{1/3}\right)^2 \left(\frac{1}{\eta} + \frac{1}{\tilde{\eta}}\right)^{1/2} \Psi(\tilde{\eta})\mathrm{d}\tilde{\eta} = 0, \\ \dfrac{\mathrm{d}M_0}{\mathrm{d}t} = -\dfrac{\phi}{2}\left(\dfrac{3}{4\pi}\right)^{1/6}\left(\dfrac{6kT}{\rho_p}\right)^{1/2} M_1^{1/6} M_0^{11/6}, \end{cases} \tag{2.26}$$

where

$$\phi = \int_0^\infty\int_0^\infty \left[\frac{1}{\eta} + \frac{1}{\tilde{\eta}}\right]^{1/2} \left(\eta^{1/3} + \tilde{\eta}^{1/3}\right)^2 \Psi(\eta)\Psi(\tilde{\eta})\mathrm{d}\eta\mathrm{d}\tilde{\eta}. \tag{2.27}$$

Equation 2.26 has the constraints

$$\int_0^\infty \Psi(\eta)\mathrm{d}\eta = 1, \int_0^\infty \eta\Psi(\eta)\mathrm{d}\eta = 1. \tag{2.28}$$

These constraints correspond to the definition of the total number of particles and to the conservation of mass. A solution for the lower end of the spectrum can be derived by assuming $\eta \to 0$. The first integral term in equation 2.26 vanishes faster than other terms. Physically, the gain of particles resulting from the coagulation at the lower end of the spectrum is negligible because the number density of the smallest particle is close to zero. The second integral is approximated by

$$\int_0^\infty \left(\eta^{1/3} + \tilde{\eta}^{1/3}\right)^2 \left(\frac{1}{\eta} + \frac{1}{\tilde{\eta}}\right)^{1/2} \Psi(\tilde{\eta})\mathrm{d}\tilde{\eta} = \mu_{2/3}\eta^{-1/2} + 2\mu_{1/3}\eta^{-1/6} + \eta^{1/6} + \mathcal{O}(\eta^{1/3}), \tag{2.29}$$

where μ_i is the i-th moment of Ψ, defined as

$$\mu_i = \int_0^\infty \eta^i \Psi(\eta)\mathrm{d}\eta. \tag{2.30}$$

Therefore, at the lower end of the spectrum equation 2.26 is approximated by

$$\phi\left(2\Psi + \eta\frac{\mathrm{d}\Psi}{\mathrm{d}\eta}\right) - 2\Psi(\eta)\left[\mu_{2/3}\eta^{-1/2} + 2\mu_{1/3}\eta^{-1/6} + \eta^{1/6}\right] = 0. \tag{2.31}$$

The solution to this equation writes

Self-similar solution at lower end of the spectrum for Brownian kernel

$$\Psi(\eta) = \frac{C_1}{\eta^2}\exp\left[\frac{1}{\phi}\left(-4\mu_{2/3}\eta^{-1/2} - 24\mu_{1/3}\eta^{2/3} + 12\eta^{1/6}\right)\right], \tag{2.32}$$

where C_1 is an integration constant. It is shown numerically that this solution is valid for $\eta < 10^{-2}$ (Lai et al., 1972). The undetermined constants α, $\mu_{1/3}$ and $\mu_{2/3}$ are evaluated by using the numerical solution to the discrete Smoluchowski coagulation equation written in dimensionless form (Lai et al., 1972)

$$\begin{cases} \forall i \in \mathbb{N},\ m_i = i \cdot m_0,\ K_B(m_i, m_j) = \left(\dfrac{6kTr_1}{\rho_p}\right)^{1/2} \left[\dfrac{1}{i} + \dfrac{1}{j}\right]^{1/2} \left(i^{1/3} + j^{1/3}\right)^2, \\ \sigma_{i,j} = \left[\dfrac{1}{i} + \dfrac{1}{j}\right]^{1/2} \left(i^{1/3} + j^{1/3}\right)^2,\ X = \dfrac{t}{\tau},\ Y_k = \dfrac{N_k}{N(0)},\ \tau = \dfrac{1}{\left(\frac{6kTr_1}{\rho_p}\right)^{1/2} N(0)} \\ \dfrac{\mathrm{d}Y_i}{\mathrm{d}X} = \dfrac{1}{2}\displaystyle\sum_{j=1}^{i-1} \sigma_{j,i-j} Y_j Y_{i-j} - \sum_{j=1}^{\infty} \sigma_{i,j} Y_i Y_j, \end{cases} \tag{2.33}$$

where r_1 is the radius of the smallest particle, N_i is the number density of particles of mass m_i, $N(0) = \sum_{i=1}^{\infty} N_i(0)$ is the total initial number density and τ a characteristic coagulation time.

For the upper end of the spectrum, $\eta \to \infty$, the second integral of equation 2.26 is approximated by

$$\int_0^{\infty} \left(\eta^{1/3} + \tilde{\eta}^{1/3}\right)^2 \left(\frac{1}{\eta} + \frac{1}{\tilde{\eta}}\right)^{1/2} \Psi(\tilde{\eta}) \mathrm{d}\tilde{\eta} = \mu_{-1/2} \eta^{2/3} + \mathcal{O}(\eta^{1/3}), \tag{2.34}$$

where only the highest-order term is kept. Equation 2.26 becomes

$$\begin{aligned} &\phi \left(2\Psi + \eta \frac{\mathrm{d}\Psi}{\mathrm{d}\eta}\right) + \int_0^{\eta} \left[\tilde{\eta}^{1/3} + (\eta - \tilde{\eta})^{1/3}\right]^2 \left(\frac{1}{\tilde{\eta}} + \frac{1}{\eta - \tilde{\eta}}\right)^{1/2} \Psi(\eta)\Psi(\tilde{\eta}) \mathrm{d}\tilde{\eta} \\ &- 2\Psi \eta^{2/3} \mu_{-1/2} = 0. \end{aligned} \tag{2.35}$$

By setting $\Psi(\eta) = C_3\, \mathrm{e}^{-C_2 \eta}\, g(\eta)$, the result is

$$\begin{aligned} &\phi \left(\eta g'(\eta) - C_2 \eta g(\eta)\right) + C_3 \int_0^{\eta} \left[\tilde{\eta}^{1/3} + (\eta - \tilde{\eta})^{1/3}\right]^2 \left(\frac{1}{\tilde{\eta}} + \frac{1}{\eta - \tilde{\eta}}\right)^{1/2} g(\tilde{\eta}) g(\eta - \tilde{\eta}) \mathrm{d}\tilde{\eta} \\ &- 2g(\eta) \eta^{2/3} \mu_{-1/2} = 0. \end{aligned} \tag{2.36}$$

Assuming $g(\eta) = C_4 \eta^p$ for large values of η, the previous equation becomes, with only highest-order terms

$$-\phi C_2 \eta^{p+1} + C_4^2 C_3 \left(6 + 2B\left(\frac{2}{3}, \frac{2}{3}\right)\right) \eta^{2p+7/6}, \tag{2.37}$$

where B is the Beta function. The solution exists only if $p = -1/6$ and $C_4^2 C_3 = \frac{\phi C_2}{\left(6 + 2B\left(\frac{2}{3}, \frac{2}{3}\right)\right)}$. This solution implies that the loss of particles by coagulation is not important in the upper end of the spectrum where $\Psi(\eta) \to 0$, $\eta \to \infty$. Therefore, the approximate solution of the upper end of the spectrum writes

Self-similar solution at upper end of the spectrum for Brownian kernel

$$\Psi(\eta) = C_5 \left(\eta^{-1/6}\, \mathrm{e}^{-C_2 \eta}\right), \tag{2.38}$$

where the constants are evaluated from a numerical calculation with the discrete Smoluchowski coagulation equation 2.33.

Since the development of the self-similar theory, several authors such as van Dongen and Ernst (1985), van Dongen and Ernst (1988), Aldous (1999), Leyvraz (2003), Escobedo et al. (2005), Escobedo and Mischler (2006), Menon and Pego (2006), Pruppacher and Klett (2010), Niethammer and Velázquez (2013), Niethammer et al. (2016a), Niethammer et al. (2016b), and Laurençot (2018) extended the work on the self-preserving distribution (i.e. scaling theory) with the mathematical proofs for existence and uniqueness for such solutions.

2.2.3 *Physical coagulation kernels*

In the Smoluchowski theory, it is assumed that coalescence occurs instantaneously after collision of two particles. The probability that two particles coalesce is unity. In astrophysics, the probability of coalescence is different than one, because the main results of two colliding particles can be: coalescence, bouncing or fragmentation (Blum, 2018). The key kernel of importance for the early stages of planet formation is the Ballistic kernel which writes

$$K\left(m,m'\right) \leftrightarrow \beta\left(m,m',\Delta v\right) K\left(m,m'\right) = \beta\left(m,m',\Delta v\right) \Delta v\left(m,m'\right) \sigma\left(m,m'\right), \tag{2.39}$$

where Δv is the mean relative velocity between two colliding particles of masses m and m', σ is the effective cross section of the collision and β denotes the averaged probability for these particles to stick during such a collision. β depends on the shape and the structures of the grains and their relative velocity. σ is simply the geometric cross-section of the colliding grains (gravitational and electrostatic focusing can be neglected). The coagulation kernel encodes the microphysics of the collision such as the range of sizes considered of the colliding particles or the kinetic and thermodynamical parameters of an eventual surrounding flow.

The main difficulty is to determinate the appropriate probability β for the studied system. Without considering fragmentation, the main result of two colliding grains is coalescence or bouncing (Blum, 2018). The criteria to differentiate coalescence and bouncing is based on the value of the relative velocity and relies on experimental results (Blum and Wurm, 2008; Güttler et al., 2010; Blum, 2018) and theory (Chokshi et al., 1993; Dominik and Tielens, 1997; Wada et al., 2007; Wada et al., 2008; Paszun and Dominik, 2009). More complex models have been derived to determine the coagulation kernel. In these models, the coagulation kernel depends on a probability density function of the relative velocity (Okuzumi et al., 2011; Windmark et al., 2012; Garaud et al., 2013).

2.2.4 *Conservative form*

The mass conservation law governs the Smoluchowski coagulation equation. Tanaka et al. (1996) and Makino et al. (1998) rewrote the equation in its conservative form, meaning as conservation law equation

$$\begin{cases} \dfrac{\partial g\left(x,\tau\right)}{\partial \tau} + \dfrac{\partial F_{\text{coag}}\left[g\right]\left(x,\tau\right)}{\partial x} = 0, \\ F_{\text{coag}}\left[g\right]\left(x,\tau\right) = \displaystyle\int_0^x \int_{x-u}^{\infty} \mathcal{K}\left(u,v\right) g\left(u,\tau\right) \frac{g\left(v,\tau\right)}{v} \mathrm{d}v\mathrm{d}u, \end{cases} \tag{2.40}$$

Figure 2.2: Left: Scheme of the spontaneous (or linear) fragmentation process of a particle of mass x into several smaller particles of mass $y < x$. Right: Scheme of the collisional (or non-linear) fragmentation process. Two particles of mass x and y collide and form several smaller particles of mass $z < x + y$.

where $g(x, \tau) \equiv x f(x, \tau)$ is the dimensionless density of mass of particles, i.e. the mass encompassed in elementary mass bins, and $F_{\text{coag}}[g](x, \tau)$ is the flux of mass density across masses x triggered by coagulation (Filbet and Laurencot, 2004). The demonstration of the conservative form is given in Appendix a. Equation 2.40 is of particular interest for numerical aspects. Under such a form, this equation can be solved by finite volume methods or finite element method contrary to equation 2.12. These methods ensure an exact mass conservation. In equation 2.40, the first step is to reduce the computation to a finite interval since mass is positive. The infinite upper bound of the second integral in F_{coag} can simply be replaced by $x_{\max} - u$ to ensure mass flux across the mass $x_{\max}$ is null (no particle of mass larger than $x_{\max}$ is allowed to form). This formalism enforces genuinely mass conservation over a finite interval of masses.

2.3 COLLISIONAL FRAGMENTATION MODEL

Fragmentation is a phenomenon of breakup of particles into a range of smaller particles. This physical process is found in a wide variety of systems such as polymer degradation (Ziff and McGrady, 1985; Ziff and McGrady, 1986), breakup of grains (Safronov, 1972; Jones et al., 1996; Tanaka et al., 1996; Kobayashi et al., 2010; Birnstiel et al., 2010; Blum, 2018), breakup of droplets (Ramkrishna, 2000; Pruppacher and Klett, 2010; Khain and Pinsky, 2018), breakup of asteroids (Hellyer, 1970; Dohnanyi, 1969), comminution systems (Fuerstenau et al., 2004). Fragmentation may occurs through external forces, spontaneously, also called linear fragmentation (see Figure 2.2 on left), or through collisions between particles (see Figure 2.2 on right). Linear fragmentation has been widely studied (Simha, 1941; Melzak, 1957; Saito, 1958; Hidy and Brock, 1972; Ziff and McGrady, 1985; Hill and Ng, 1996; Ramkrishna, 2000; Filbet, 2008; Pruppacher and Klett, 2010; Rajesh Kumar, 2014; Liu et al., 2019) . Collisional fragmentation, also called the non-linear fragmentation has also been widely studied but with a recent mathematical development (Dohnanyi, 1969; Safronov, 1972; List and Gillespie, 1976; Cheng and Redner, 1988; Tanaka et al., 1996; Jones et al., 1996; Kostoglou and Karabelas, 2000; Laurençot and Wrzosek, 2001; Paul and Kumar, 2018; Bodrova et al., 2019). A review on both models can be found in Ernst and Pagonabarraga (2007), Villermaux (2007), and Da Costa (2015)

This Ph.D. Thesis is concerned only by collisional fragmentation since solid grains do not break spontaneously. The collisional fragmentation process can be described by the

following nonlinear partial integro-differential equation in dimensionless form (Safronov, 1972; Wilkins, 1982; Cheng and Redner, 1990; Kostoglou and Karabelas, 2000)

$$\begin{aligned}\frac{\partial f(x,\tau)}{\partial \tau} =& \frac{1}{2}\int_0^\infty\int_x^\infty b(x,y,z)\mathcal{K}_{\text{frag}}(y,z)f(y,\tau)f(z,\tau)\mathrm{d}y\mathrm{d}z \\ &- f(x,\tau)\int_0^\infty \mathcal{K}_{\text{frag}}(x,y)f(y,\tau)\mathrm{d}y,\end{aligned} \tag{2.41}$$

where τ, x, y and z are time and masses. f is the number density distribution, $\mathcal{K}_{\text{frag}}(x,y)$ is the fragmentation kernel, the rate of successful collision for breakage between two particles of masses x and y. In general, $\mathcal{K}_{\text{frag}}(x,y) = [1-\beta(x,y,\Delta v)]\,\mathcal{K}_{\text{coag}}(x,y)$ where $\beta(x,y,\Delta v)$ is the averaged probability that masses x,y stick together during collision (see Section 2.2.3). The factor $1-\beta(x,y,\Delta v)$ gives the probability that x and y fragment after their collision. The first term on the right-hand describes the gain of particles of mass x due to collisions of particles of masses y and z. The second term accounts for the loss of particles of mass x because of collisions between particles of mass x with the remaining particles in the system. $b(x,y,z)$ is the distribution function of particles of mass x resulting from a breakup of a particle of mass y due to collision with a particle of mass z. The function b has to satisfy the following requirements

$$\begin{aligned}&(i)\ \int_0^y xb(x,y,z)\mathrm{d}x = y,\\ &(ii)\ \int_0^k xb(x,y,z)\mathrm{d}x \geq \int_{y-k}^y (y-x)b(x,y,z)\mathrm{d}x,\\ &(iii)\ v(y,z) = \int_0^y b(x,y,z)\mathrm{d}x,\end{aligned} \tag{2.42}$$

where $k < y/2$. The requirement (i) is the mass conservation. The requirement (ii) states that when fragmentation occurs such that a particle of mass $x \geq y/2$ is formed, the mass contained in the smaller fragments $y-x$ must contribute to the total mass of the fragments smaller than $y-x$. In (iii), v is the number of particles resulting from fragmentation of a single particle of volume y after collision with a particle of mass z.

2.3.1 *Analytic solutions*

Analytical solutions to the nonlinear fragmentation equation 2.41 can be derived only for simple expression of fragmentation kernel and function b. The case of a homogeneous function b independent of z of the form $b(x,y,z) = b(x/y)/y$ and $\beta = 0$ are considered.

2.3.1.1 *Constant coagulation kernel*

An analytic solution has been derived for the constant coagulation kernel $\mathcal{K}_{\text{frag}}(x,y) = 1$ (Kostoglou and Karabelas, 2000). The equation 2.41 writes

$$\frac{\partial f(x,\tau)}{\partial \tau} = -M_0(\tau)f(x,\tau) + M_0(\tau)\int_x^\infty \frac{b(x/y)}{y}f(y,\tau)\mathrm{d}y, \tag{2.43}$$

where $M_0(\tau) = \int_0^\infty f(x,\tau)\mathrm{d}x$ is the dimensionless total number of particles. By integrating equation 2.43 with respect to x from 0 to ∞, the equation on M_0 writes

$$\frac{\mathrm{d}M_0(\tau)}{\mathrm{d}\tau} = (b_0 - 1)M_0^2(\tau), \quad \text{with} \quad b_0 = \int_0^\infty b(x)\mathrm{d}x. \tag{2.44}$$

The solution to this equation is $M_0(\tau) = (1 - (b_0 - 1)\,\tau)^{-1}$. By a change of variable

$$T \equiv \int_0^\tau M_0(\tau)\mathrm{d}\tau = \frac{\ln(1 - (b_0 - 1)\tau)}{1 - b_0}, \tag{2.45}$$

Equation 2.43 writes

$$\frac{\partial f(x,T)}{\partial T} = -f(x,T) + \int_x^\infty \frac{b(x/y)}{y} f(y,T)\mathrm{d}y, \tag{2.46}$$

Equation 2.46 is known as the linear fragmentation equation with constant fragmentation rate. The solution of equation 2.46 for monodisperse initial distribution $f(x,0) = \delta(x-1)$ and a power law fragments distribution $b(x/y) = (\nu+2)\left(\frac{x}{y}\right)^\nu$ with $-2 \leq \nu \leq 0$ (requirements (i) and (ii)) writes (McGrady and Ziff, 1987; Kostoglou and Karabelas, 2000)

Constant coagulation kernel and power law fragments distribution

$$\begin{aligned}
&\mathcal{K}_{\text{frag}}(x,y) = 1,\ f(x,0) = \delta(x-1),\ b(x/y) = (\nu+2)\left(\frac{x}{y}\right)^\nu,\ -2 \leq \nu \leq 0,\\
&T \equiv \frac{\ln(1-(b_0-1)\tau)}{1-b_0},\ b_0 = \int_0^\infty b(x)\mathrm{d}x,\\
&f(x,T) = \mathrm{e}^{-T}\, x^\nu \left(\frac{(\nu+2)T}{-\ln(x)}\right) I_1\left[2\left(T(\nu+2)\ln(1/x)\right)^{1/2}\right] + \delta(x-1)\,\mathrm{e}^{-T}.
\end{aligned} \tag{2.47}$$

2.3.1.2 *Multiplicative coagulation kernel*

A solution for the multiplicative coagulation kernel $\mathcal{K}_{\text{frag}}(x,y) = xy$ has been derived by Ziff and McGrady (1985), McGrady and Ziff (1987), Krapivsky (1992), and Kostoglou and Karabelas (2000). With the multiplicative coagulation kernel, $b(x,y,z) = b(x/y)/y$ and $\beta = 0$, equation 2.41 writes

$$\frac{\partial f(x,\tau)}{\partial \tau} = -xf(x,\tau) + \int_x^\infty b(x/y)f(y,\tau)\mathrm{d}y, \tag{2.48}$$

where the mass conservation relation is used $\int_0^\infty xf(x,\tau)\mathrm{d}x = 1$. The solution for a power law fragments distribution and a monodisperse initial condition writes (McGrady and Ziff, 1987)

Multiplicative coagulation kernel and power law fragments distribution

$$\begin{aligned} &\mathcal{K}_{\text{frag}}(x,y) = xy,\ f(x,0) = \delta(x-1),\ b(x/y) = (\nu+2)\left(\frac{x}{y}\right)^{\nu},\ -2 \leq \nu \leq 0, \\ &f(x,\tau) = \mathrm{e}^{-\tau}\left[\delta(x-1) + (\nu+2)\tau x^{\nu}\mathcal{M}\left(-(\nu+1),2,(x-1)\tau\right)\right], \end{aligned} \tag{2.49}$$

where $\mathcal{M}$ is the Kummer's function defined as

$$\mathcal{M}(a,b,z) = \sum_{n=0}^{\infty} \frac{a^{(n)}z^n}{b^{(n)}n!},\ \text{with}\, a^{(0)} = 1,\ a^{(n)} = a(a+1)(a+2)...(a+n-1). \tag{2.50}$$

2.3.2 *Conservative form*

Similarly to the Smoluchowski coagulation equation, the collision fragmentation equation can be written in its conservative form (Paul and Kumar, 2018)

$$\begin{cases} \dfrac{\partial g\,(x,\tau)}{\partial \tau} + \dfrac{\partial F_{\text{frag}}\,[g]\,(x,\tau)}{\partial x} = 0, \\ F_{\text{frag}}\,[g]\,(x,\tau) = \displaystyle\int_0^{\infty}\int_x^{\infty}\int_0^{x} \frac{w}{yz} b(w,y,z)\mathcal{K}_{\text{frag}}(y,z)g(y,\tau)g(z,\tau)\mathrm{d}w\mathrm{d}y\mathrm{d}z, \end{cases} \tag{2.51}$$

where $g\,(x,\tau) \equiv xf\,(x,\tau)$ is the dimensionless mass density of particles and $F_{\text{frag}}\,[g]\,(x,\tau)$ is the flux of mass density across mass x triggered by fragmentation. The expression of the flux is obtained using the Leibniz integral rules. As mentioned in Section 2.2.4, equation 2.51 can be efficiently solved by finite volume methods or finite element methods.

2.4 COAGULATION-FRAGMENTATION EQUATION

In general, collisional fragmentation is studied simultaneously with the coagulation process (Melzak, 1957; Safronov, 1972; Hidy and Brock, 1972; List and Gillespie, 1976; Tanaka et al., 1996; Ramkrishna, 2000; Laurençot and Wrzosek, 2001; Birnstiel et al., 2010; Pruppacher and Klett, 2010; Da Costa, 2015; Khain and Pinsky, 2018; Liu et al., 2019). To obtain the coagulation-fragmentation equation, equations 2.12 and 2.41 are mixed. The loss term of particles of mass x is present in the coagulation equation 2.4 and in the collisional fragmentation equation 2.41. In a system where coagulation and fragmentation are considered, the loss term is used only one time. Meaning, the loss of particles of mass x is due to collision between particles of mass x with the remaining particles in the system leading to coalescence or fragmentation. The coagulation-fragmentation writes (Safronov, 1972; Tanaka et al., 1996; Laurençot and Wrzosek, 2001; Birnstiel et al., 2010)

Dimensionless coagulation-fragmentation equation in continuous form

$$\begin{aligned}\frac{\partial f(x,\tau)}{\partial \tau} =& \frac{1}{2}\int_0^x \mathcal{K}_{\text{coag}}(y, x-y) f(y,\tau) f(x-y,\tau)\mathrm{d}y \\ &- f(x,\tau)\int_0^\infty \mathcal{K}_{\text{coag}}(y,x) f(y,\tau)\mathrm{d}y \\ &+ \frac{1}{2}\int_0^\infty\int_x^\infty \mathcal{K}_{\text{frag}}(y,z) f(y,\tau) f(z,\tau)\mathrm{d}y\mathrm{d}z \\ &- f(x,\tau)\int_0^\infty \mathcal{K}_{\text{frag}}(y,x) f(y,\tau)\mathrm{d}y,\end{aligned} \tag{2.52}$$

where f is the number density of particles, x, y, z the masses, $\mathcal{K}$ the coagulation kernel, b the fragment distribution function and β the average probability that masses y, z coalesce after collision. In a more general way,

$$\frac{\partial g(x,\tau)}{\partial \tau} + \frac{\partial}{\partial x}\left(F_{\text{coag}}[g](x,\tau) + F_{\text{frag}}[g](x,\tau)\right) = 0. \tag{2.53}$$

Key is to find a solver for F_{coag}, and then apply it to F_{frag}.

2.5 SUMMARY

Dust coagulation can be described by the Smoluchowski equation 2.4. The Smoluchowski coagulation theory has long been studied leading to the derivation of analytic solutions for constant, additive and multiplicative kernels. The self-similarity theory allowed to study the behaviour of the solution of Smoluchowski equation for long times. A fundamental property of the Smoluchowski coagulation equation consists of mass conservation for non-multiplication kernels. Therefore, the equation can be written in its conservative form 2.40. The collisional fragmentation model is similar to the Smoluchowski equation. Analytic solutions have been derived for simple fragmentation kernels. The fragmentation equation can also be written in its conservative form similar to equation 2.40. In astrophysics, the kernel of interest for dust coagulation is the ballistic kernel, for which no analytic solution exists. The dust coagulation equation 2.40 has to be solved numerically. Solving efficiently and accurately this non-linear integro-differential equation is a critical numerical challenge, since it may lead to strong numerical diffusion towards large masses. Taking advantage of the conservative form of the dust coagulation equation, high-order schemes can be developed to overcome the numerical challenge (see Chapter 3).

3 NUMERICAL SOLUTION OF THE SMOLUCHOWSKI EQUATION

"Nature laughs at the difficulties of integration"– Pierre-Simon Laplace

3.1 Introduction . . . 39
3.1.1 Method of moments . . . 39
3.1.2 Point-based methods . . . 40
3.1.3 Finite element methods . . . 41
3.1.4 Requirements from hydrodynamical simulations . . . 42
3.1.5 Code PHANTOM . . . 43
3.1.6 Scientific objectives of the Ph.D. Thesis . . . 45
3.2 High-order solver for Smoluchowski equation . . . 45
3.2.1 Discontinuous Galerkin method . . . 45
3.2.2 Evaluation of the flux . . . 48
3.2.3 Evaluation of the integral of the flux . . . 56
3.2.4 Slope limiter . . . 56
3.2.5 High-order time solver . . . 57
3.2.6 Algorithm flowchart . . . 59
3.2.7 Design . . . 59
3.3 Summary . . . 59

This work led to the publication of the article M. Lombart and G. Laibe, "Grain growth for astrophysics with Discontinuous Galerkin schemes", *Monthly Notices of the Royal Astronomical Society*, staa3682 (2020).

3.1 INTRODUCTION

No analytic solution exists for the Smoluchowski coagulation equation with physical kernels, implying a numerical resolution. Various numerical schemes have been developed for this purpose. Two classes of algorithms have been developed. A first class of solvers consists of Monte-Carlo simulations (e.g. Gillespie (1975), Liffman (1992), Smith and Matsoukas (1998), Lee and Matsoukas (2000), Debry et al. (2003), Sheng and Shen (2006), Ormel et al. (2007), and Zsom and Dullemond (2008)). Although convenient, these methods have two principal drawbacks. Firstly, a large number of particles is required to ensure appropriate accuracy of the number density distribution f. Secondly, the scheme is non deterministic and simulations can be reproduced only in a statistical sense. To be coupled with a hydrodynamic solver, the numerical scheme has to be deterministic. The second class of numerical algorithms consist of deterministic numerical solvers. The methods have been summarized in Kostoglou and Karabelas (1994), Kumar and Ramkrishna (1996), Ramkrishna (2000), Pruppacher and Klett (2010), and Khain and Pinsky (2018). A short but comprehensive summary is given hereafter.

3.1.1 *Method of moments*

The method of moments seems to be the first numerical method proposed to solve the Smoluchowski equation (Hulburt and Katz, 1964). A system of ordinary differential equations is written over the kth moments $M_k \equiv \int_0^\infty x^k f(x,\tau)\mathrm{d}x$ of the number density function. Approximations either for the reconstruction of f (Hulburt and Katz, 1964) or

for the derivation of fractional moments (Estrada and Cuzzi, 2008) are then required to close this system of ordinary differential equations. The Standard Moment Method (SMM) requires an analytical integration of the kernel. To avoid this difficulty, Quadrature Moment Methods (QMM), where integrals are approximated by Gaussian quadrature methods, have been developed. Solutions of moments can be used directly to derive the total number of particles M_0, the total mass M_1 or other physical quantity such as dust opacities (Marchisio et al., 2003; Estrada and Cuzzi, 2008). Number densities f are reconstructed using polynomials (Pruppacher and Klett, 1980; Piskunov and Golubev, 2002).

3.1.2 *Point-based methods*

The number density function f is sampled on discrete mass grids. The main difficulty is to represent the continuous distribution f as accurately as possible using the values of f at discrete points. Different algorithms have been developed using this approach.

3.1.2.1 *Interpolation method*

This method was developed by Berry (1967) and Berry and Reinhardt (1974). The continuous Smoluchowski equation is written in terms of $g(x,\tau) \equiv xf(x,\tau)$, the mass density function. The mass interval is discretised using a logarithmic grid. A system of ordinary differential equations is derived with respect to the variable g evaluated on the grid points. Gain and loss terms are evaluated separately, and integrals are calculated by using high-order Lagrangian interpolations. Middleton and Brock (1976) and Suck and Brock (1979) improved this method by using Simpson's rules for the integrals and cubic splines interpolations.

3.1.2.2 *Method of orthogonal collocation*

The method of weighted residuals (Finlayson, 1972) is a general method for obtaining numerical solutions to differential equations. The unknown solution is tested over a set of weight functions and is adapted to give the best approximated solution to the differential equation. The Smoluchowski equation is multiplied by the weight function ϕ and integrated over all the mass domain to form the residual

$$\begin{aligned} R \equiv \int_0^\infty \Bigg(\frac{\partial f(x,\tau)}{\partial \tau} - \int_0^x \mathcal{K}(x-y,y) f(x-y,\tau) f(x,\tau) \mathrm{d}y \\ + \int_0^\infty \mathcal{K}(x,y) f(x,\tau) f(y,\tau) \mathrm{d}y \Bigg) \phi(x) \mathrm{d}x = 0. \end{aligned} \tag{3.1}$$

The number density f is approximated by polynomials. The collocation method corresponds to the case where $\phi(x) = \delta(x - x_0)$. The coagulation equation is evaluated at the collocation points x_0. This gives a set of ordinary differential equations equal to the degree of freedom of the polynomials used. Integrals are usually performed using Gaussian quadrature rules (Eyre et al., 1988).

3.1.2.3 *Pair interaction methods*

Numerical integration of the Smoluchowski equation consists of summing contributions of pairwise collisions between all grid points of different masses. For non-regular mass samplings, aggregates do usually not have masses corresponding to an existing grid point. To ensure mass conservation, the mass of the aggregate is distributed over the

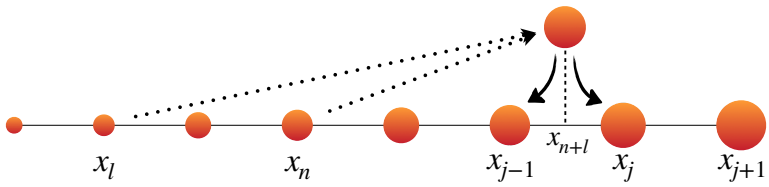

Figure 3.1: Illustration of the pair interaction methods. A particle of mass $x_{n+l} = x_n + x_l$ forms from collision between particles of masses x_l and x_n. The resulting mass x_{n+l} is distributed onto adjacent bins, generating numerical over-diffusion towards large masses.

two relevant adjacent grid points (Figure 3.1). The first pair-interaction solver has been developed by Kovetz and Olund (1969). In this algorithm, a system of ordinary differential equations is obtained over the quantities $N(x_i) = \int_{a_i}^{b_i} f(x)\mathrm{d}x$ where x_i denotes the mass of individual particles of the i-th point, and $a_i \equiv (x_{i+1} - x_i)/2$ and $b_i \equiv (x_i - x_{i-1})/2$. In practice, logarithmic grids are used to cover wide ranges of masses. In the context of planet formation, widely used solvers follow this approach (e.g. Brauer et al. (2008) and Birnstiel et al. (2010)). The principal drawback of this method is that redistribution of mass towards large grains tend to over-predict the number of large aggregates, triggering artificial formation of large bodies (Figure 1.8). A large number of grid points is therefore required to avoid an artificial broadening of number density of particles f (Berry and Reinhardt, 1974; Soong, 1974; Khain and Pinsky, 2018). Moreover, a sufficient number of grid points is also needed to avoid difficulties related to collisions that form aggregates of masses larger than the largest mass point. Jacobson (2005) extended the Kovetz and Olund (1969) algorithm by distributing the mass between grid points and writing the scheme in a semi-implicit form. This solver ensures mass conservation to machine precision. Bott (1998), Simmel et al. (2002), and Wang et al. (2007) developed also binary-pairs interaction methods. Mass is advected towards adjacent grid points by a mass flux expressed with a high-order scheme. These methods do not introduce a significant numerical broadening. Other methods have been developed by Hounslow et al. (1988) and Lister et al. (1995) where four binary interaction mechanisms of gain and loss of particles are considered to deal correctly the rate of change of particle and mass.

3.1.3 *Finite element methods*

In these methods, the continuous mass distribution is discretised by a finite number of mass elements (intervals, cells, bins).

3.1.3.1 *Method with finite elements*

The first finite element scheme for coagulation was developed by Bleck (1970) by discretising mass distributions over logarithmic bins. f is approximated by its moment of order zero over each bin to obtain a system of ordinary differential equations. Over-diffusion for large grains is observed with this piecewise constant approximation. A change of variable $x \to x^{-3}$ is operated to reduce diffusivity at large masses. The method of Soong (1974) follows Bleck (1970). The Smoluchowski equation is written in terms of mass density distributions g and approximated by piecewise exponential functions. This allows to reduce drastically the diffusive effect at large masses. Gelbard et al. (1980) and Landgrebe

and Pratsinis (1990) proposed a similar method, where the Smoluchowski equation is decomposed over bins of indices j in terms of $Q_j = \int_{I_j} x f(x,\tau) \mathrm{d}x$. A precise account of gain and loss of particles in terms of fluxes of Q is performed. Trautmann and Wanner (1999) extends the work of Gelbard et al. (1980), also finding numerical diffusion when using piecewise constant approximation, and addressing it by using piecewise exponential approximations. Another moment method that involves polynomial approximations for the first two moments M_0 and M_1 of f has been proposed by Enukashvily (1980), Kumar and Ramkrishna (1996), and Tzivion et al. (1999).

3.1.3.2 *Discontinuous Galerkin method*

The discontinuous Galerkin method is a weighted residual method where the weight $\phi(x)$ consists of orthogonal polynomials (Lagrange polynomials, Legendre polynomials, cubic splines). The numerical solution of the Smoluchowski equation is decomposed on each bin over this basis and a system of ordinary differential equations is obtained for the coefficients (e.g. Pilinis (1990), Erasmus et al. (1994), and Mahoney and Ramkrishna (2002), see Section 3.2.1). Generally, the integrals are performed by Gaussian quadrature rules (Gelbard and Seinfeld, 1978; Rigopoulos and Jones, 2003; Sandu, 2006).

3.1.3.3 *Finite element scheme in the conservative form*

Deterministic methods described above solve the Smoluchowski equation 2.12 written in its original form. The conservative form equation 2.40 has been exploited for numerical simulations only lately. Filbet and Laurencot (2004) derived a finite volume scheme of order zero where volume integrals over flux divergences are replaced by flux terms at the interfaces by the mean of the divergence theorem. This scheme conserves mass exactly and has been further extended by Filbet (2008), Bourgade and Filbet (2008), and Forestier-Coste and Mancini (2012). The mass interval can be sampled uniformly or non-uniformly. Finite volume schemes of higher orders solving for the conservative form have been investigated recently (Gabriel and Tine, 2010; Liu et al., 2019). Gabriel and Tine (2010) used WENO reconstruction (Jiang and Peng, 2000) to approximate the coagulation flux at interfaces. Liu et al. (2019) developed a numerical scheme based on the discontinuous Galerkin method. This method provides the further advantage to choose the order of the scheme in a flexible manner. Integrals are calculated using Gaussian Quadrature rules, which implies sub-sampling of the mass intervals.

3.1.4 *Requirements from hydrodynamical simulations*

Densities must remain strictly positive and total mass conserved rigorously to ensure the stability of hydrodynamical simulations. These two properties are genuinely ensured by finite volume methods based on the conservative form equation 2.40. The double-integral formulation allows to simply quench the formation of aggregates with unphysical masses, by setting for the integral bound the maximum mass allowed. These constrains may not always be satisfied with simple integral formulations.

On the other hand, observational constraints on young stellar objects are essentially provided by high-contrast spectro-polarimetry at infrared wavelengths (SPHERE/VLT, GPI, Subaru/HiCIAO) and millimetre interferometry (ALMA). These observations probe (sub)micron-to-millimetre-in-size dust distributions in discs, which corresponds to 4 orders of magnitude in size, i.e. 12 orders of magnitude in mass for compact grains.

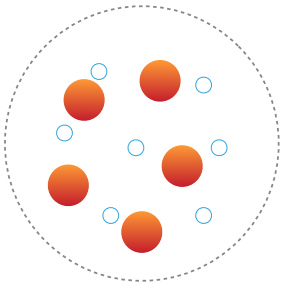

Figure 3.2: Scheme of the monofluid approach. Gas (blue circle) and dust (orange) are gathered into a single continuous fluid.

With current computational capacities, 3D dust/gas simulations of dusty discs can handle $\sim 10 - 20$ dust species simultaneously (e.g. PHANTOM, Price et al. (2018) or RAMSES, Lebreuilly et al. (2020)). The global accuracy of second-order hydrodynamical solvers is of order $\sim 10^{-3}$. We aim therefore to design a versatile algorithm for coagulation of accuracy $\sim 10^{-3}$ with ~ 15 dust bins distributed over 12 orders of magnitude in mass that allows tractable simulations. We therefore face the issue of over-diffusion associated to piecewise constant reconstructions with few mass bins, and high-order schemes appear as a natural way to overcome this difficulty. It is much preferable for hydrodynamics to handle a fix grid of sizes, to avoid interpolations when updating forces. We seek therefore for a growth algorithm that works efficiently with a fixed grid.

Additionally, we seek for an algorithm which allows for convergence analysis in 3D hydrodynamical simulations. As explained above, multiplying the number of dust bins provides prohibitive computational costs. Instead, the order of the scheme may be varied, should it be parametrised in a flexible manner. This requirement tends to favour Discontinuous Galerkin schemes with respect to WENO schemes, although they provide in theory equivalent accuracies. Compared to regular Galerkin schemes, discontinuous Galerkin solvers decompose the solution over several mass bins. This helps to better capture the exponential decay of the solution at large masses and avoid over-diffusion biases. For these reasons, we have chosen to focus on the Discontinuous Galerkin method to solve for the Smoluchowski equation in astrophysical contexts, an approach recently pioneered by Liu et al. (2019).

3.1.5 *Code PHANTOM*

For the purpose of simulating the early stages of planet formation, we decided to choose the code PHANTOM. It is an efficient 3D non-ideal magnetohydrodynamics Lagrangian code (Smooth Particle Hydrodynamic) developed in the purpose to study high-energy, galaxy, stellar and planetary astrophysics (Price et al., 2018). Particularly, this code is well designed for the 3D simulations of protoplanetary discs. PHANTOM integrates the monofluid approach which consists of grouping gas and dust into a single continuous fluid of density $\rho = \rho_g + \rho_d$ and velocity $\rho v = \rho_g v_g + \rho_d v_d$ (see Figure 3.2). In this approach, barycentric quantities arise naturally since they are fundamentally associated to mass conservation. The physical quantities are advected at a single velocity v. The description of the mixture of gas and dust involves two quantities, the dust mass

concentration $\epsilon \equiv \rho_{\rm d}/\rho$ and the differential velocity $\Delta \boldsymbol{v} = \boldsymbol{v}_{\rm d} - \boldsymbol{v}_{\rm g}$. The monofluid set of equations expresses (Laibe and Price, 2014b; Lebreuilly et al., 2019)

$$\begin{aligned}
\frac{{\rm d}\rho}{{\rm d}t} &= -\rho\left(\nabla\cdot\boldsymbol{v}\right),\\
\frac{{\rm d}\boldsymbol{v}}{{\rm d}t} &= \boldsymbol{f} - \frac{\nabla P_{\rm g}}{\rho} - \frac{1}{\rho}\nabla\cdot\left(\epsilon\left(1-\epsilon\right)\rho\Delta\boldsymbol{v}\otimes\Delta\boldsymbol{v}\right),\\
\frac{{\rm d}\epsilon}{{\rm d}t} &= -\frac{1}{\rho}\nabla\cdot\left(\epsilon\left(1-\epsilon\right)\rho\Delta\boldsymbol{v}\right),\\
\frac{{\rm d}\Delta\boldsymbol{v}}{{\rm d}t} &= -\frac{\Delta\boldsymbol{v}}{t_{\rm S}} + \frac{\nabla P_{\rm g}}{\left(1-\epsilon\right)\rho} - \left(\Delta\boldsymbol{v}\cdot\nabla\right)\boldsymbol{v} + \frac{1}{2}\nabla\left(\left(2\epsilon-1\right)\Delta\boldsymbol{v}\cdot\Delta\boldsymbol{v}\right)\\
&\quad + \left(1-\epsilon\right)\Delta\boldsymbol{v}\times\left(\nabla\times\left(1-\epsilon\right)\Delta\boldsymbol{v}\right) - \epsilon\Delta\boldsymbol{v}\times\left(\nabla\times\epsilon\Delta\boldsymbol{v}\right),\\
\frac{{\rm d}e_{\rm g}}{{\rm d}t} &= -\frac{P_{\rm g}}{\rho\left(1-\epsilon\right)}\nabla\cdot\left(\boldsymbol{v}-\epsilon\Delta\boldsymbol{v}\right) + \left(\epsilon\Delta\boldsymbol{v}\cdot\nabla\right)e_{\rm g} + \epsilon\frac{\Delta\boldsymbol{v}\cdot\Delta\boldsymbol{v}}{t_{\rm S}},
\end{aligned} \tag{3.2}$$

where $t_{\rm S}$ is the stopping time of the mixture, i.e. the typical time for the drag to damp $\Delta\boldsymbol{v}$. $\boldsymbol{f}$ represents forces that act on fluid such as gravity. $e_{\rm g}$ is the gas specific internal energy. This set of equations is complex to solve, therefore the terminal velocity approximation can used for grains with $\mathrm{St} \ll 1$.

3.1.5.1 *Terminal velocity approximation*

The terminal velocity approximation (Youdin and Goodman, 2005; Chiang, 2008; Laibe and Price, 2014b) is used when $\mathrm{St} \ll 1$. The following terms $\left\|\Delta\boldsymbol{v}^2/\boldsymbol{v}^2\right\|$, $\left\|\Delta\boldsymbol{v}\otimes\Delta\boldsymbol{v}/\boldsymbol{v}^2\right\|$, $\left\|\Delta\boldsymbol{v}\times\left(\nabla\times\left(1-\epsilon\right)\Delta\boldsymbol{v}\right)\boldsymbol{v}^2\right\|$ and $\left\|\Delta\boldsymbol{v}\left(\nabla\times\epsilon\Delta\boldsymbol{v}\right)/\boldsymbol{v}^2\right\|$ are second order in St, therefore they can be neglected. In these conditions, $\left\|\frac{{\rm d}\Delta\boldsymbol{v}}{{\rm d}t}/\left(\frac{\Delta\boldsymbol{v}}{t_{\rm S}}\right)\right\|$ and $\left\|\left(\Delta\boldsymbol{v}\cdot\nabla\right)\boldsymbol{v}/\left(\frac{\Delta\boldsymbol{v}}{t_{\rm S}}\right)\right\|$ are transitory terms, they can be neglected. After a few stopping times, differential velocity has relax to the terminal velocity

$$\Delta\boldsymbol{v}_{\rm f} \equiv t_{\rm S}\frac{\nabla P_{\rm g}}{(1-\epsilon)\rho}. \tag{3.3}$$

The steady value for $\Delta\boldsymbol{v}$ results from drag balancing the differential forces between gas and dust. With this approximation the set of equations 3.2 reduces to

$$\begin{aligned}
\frac{{\rm d}\rho}{{\rm d}t} &= -\rho\left(\nabla\cdot\boldsymbol{v}\right),\\
\frac{{\rm d}\boldsymbol{v}}{{\rm d}t} &= -\frac{\nabla P_{\rm g}}{\rho} + \boldsymbol{f},\\
\frac{{\rm d}\epsilon}{{\rm d}t} &= -\frac{1}{\rho}\nabla\cdot\left(\epsilon t_{\rm S}\nabla P_{\rm g}\right),\\
\frac{{\rm d}e_{\rm g}}{{\rm d}t} &= -\frac{P_{\rm g}}{\rho\left(1-\epsilon\right)}\nabla\cdot\boldsymbol{v} + \left(\epsilon t_{\rm S}\frac{\nabla P_{\rm g}}{\left(1-\epsilon\right)\rho}\cdot\nabla\right)e_{\rm g}.
\end{aligned} \tag{3.4}$$

This set of equations works for one dust species. Hutchison et al. (2018) developed the MULTIGRAIN formalism to take into account several dust species in the set of equations 3.4. For $\mathcal{N}$ dust populations, the terminal velocities writes $\Delta\boldsymbol{v}_{{\rm f},k} \equiv T_{{\rm S},k}\frac{\nabla P_{\rm g}}{(1-\mathcal{E})\rho}$. $\mathcal{E} \equiv \sum_{l=1}^{\mathcal{N}}\epsilon_l$ is the total dust fraction such as $\rho_{{\rm d},k} = \epsilon_k\rho$ and $\rho_{\rm g} = \left(1-\mathcal{E}\right)\rho$. $T_{{\rm S},k} \equiv \frac{t_{{\rm S},k}}{1-\epsilon_k} - \sum_{l=1}^{\mathcal{N}}\frac{\epsilon_l}{1-\epsilon_l}t_{{\rm S},l}$ is the effective stopping time of the k-th species (Lebreuilly et al., 2019). The MULTIGRAIN formalism is essential to couple coagulation to the code `PHANTOM`.

Monofluid dust/gas hydrodynamical solvers provide a natural architecture to include a coagulation equation. Indeed, relative drifts between grains of different sizes are genuinely computed, eventually in the terminal velocity approximation (e.g. Laibe and Price (2014b), Hutchison et al. (2018), and Lebreuilly et al. (2019)). Monofluid formalism also ensures exact conservation of momentum, i.e. no thrust due to mass transfers propel the mixture. Sub-grid fluctuations should be prescribed by an accurate model that describes local turbulence or Brownian motion. The Smoluchowski coagulation equation is a mass conservation equation and, therefore, can be used in the monofluid formalism in PHANTOM.

3.1.6 *Scientific objectives of the Ph.D. Thesis*

The aim of my Ph.D. Thesis is to elaborate an efficient algorithm solving the conservative form of the Smoluhcowski coagulation equation in the purpose to be used in a 3D hydrodynamic dust and gas code such as PHANTOM.

To design the algorithm, constraints has to be respected:

1. exact mass conservation,
2. positivity of the mass density,
3. discretizing masses over 12 orders of magnitudes which roughly corresponds to grains of sizes $1\mu\text{m} - 1\text{mm}$ relevant for observations,
4. an accuracy of order $\sim 0.1 - 1\%$ to be consistent with hydrodynamics solvers (here PHANTOM),
5. having a minimal number of bins to maintain global simulations of discs computationally tractable.

The coagulation solver is coupled to the MULTIGRAIN monofluid dust/gas hydrodynamical solver, ensuring exact momentum conservation. A typical number of $10 - 20$ bins is targeted compared to the $10^2 - 10^3$ bins used so far in current algorithms (Ormel et al., 2007; Brauer et al., 2008; Birnstiel et al., 2010). To fulfil the requirements we figured out after a literature review that the discontinuous Galerkin method is well adapted to design the algorithm. In the following, the high-order solver for the Smoluchowski equation is presented. The solver is based on the discontinuous Galerkin method combined with a high-order time solver.

3.2 HIGH-ORDER SOLVER FOR SMOLUCHOWSKI EQUATION

3.2.1 *Discontinuous Galerkin method*

The discontinuous Galerkin method is presented for the general scalar hyperbolic conservative equation

$$\begin{cases} \dfrac{\partial g(x,t)}{\partial t} + \dfrac{\partial F[g](x,t)}{\partial x} = 0, \\ (x,t) \in \mathbb{R}_+, \end{cases} \tag{3.5}$$

where g is a density of a conservative quantity and $F[g]$ the associated flux.

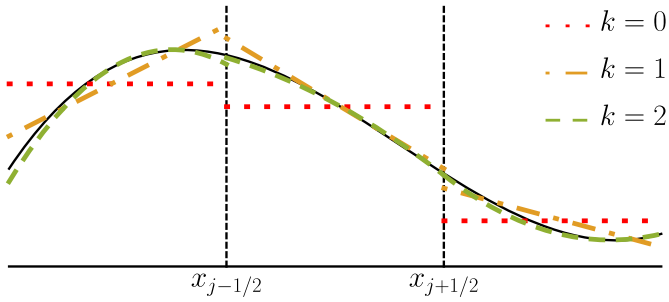

Figure 3.3: Schematic representation of the discontinuous Galerkin method. In each cell, the solution can be approximated by high-order polynomials to increase accuracy.

Let us partition the domain of interest $[x_{\min}, x_{\max}] \in \mathbb{R}$ in N subintervals (alternatively, cells or bins), not necessarily of equal size. Each cell is defined by $I_j = (x_{j-1/2}, x_{j+1/2}], j \in [\![1, N]\!]$. The size of the j-th cell is defined as $h_j = x_{j+1/2} - x_{j-1/2}$. The cell is centred around the position $x_j = \left(x_{j+1/2} + x_{j-1/2}\right)/2$. We define $\mathcal{V}^k$ the space of polynomials of degree k in each cell I_j

$$\mathcal{V}^k = \left\{ v : v|_{I_j} \in P^k\left(I_j\right), j \in [\![1, N]\!] \right\}. \tag{3.6}$$

We denote $g_j \in \mathcal{V}^k$ the approximate solution of g in the bin I_j. The terminology discontinuous Galerkin (DG) comes from the fact that in $\mathcal{V}^k$, the functions are allowed to have jumps at the interfaces $x_{j+1/2}$. One obtains a weak formulation of equation 3.5 by multiplying by a test function $\phi \in \mathcal{V}^k$, integrating over I_j and finally integrating by parts (Cockburn and Shu, 1989)

$$\begin{aligned} \int_{I_j} \frac{\partial g_j}{\partial t} \phi \mathrm{d}x - \int_{I_j} F[g]\left(x, t\right) \frac{\partial \phi}{\partial x} \mathrm{d}x + F[g]\left(x_{j+1/2}, t\right) \phi(x_{j+1/2}) \\ - F[g]\left(x_{j-1/2}, t\right) \phi(x_{j-1/2}) = 0. \end{aligned} \tag{3.7}$$

Equation 3.7 allows to fix unequivocally the degrees of freedom of the function g_j. The DG method is a particular case of the method of the weighted residual (Finlayson, 1972). The residual of equation 3.5 on bin I_j is defined as

$$\begin{aligned} R_j \equiv \int_{I_j} \frac{\partial g_j}{\partial t} \phi \mathrm{d}x - \int_{I_j} F[g]\left(x, t\right) \frac{\partial \phi}{\partial x} \mathrm{d}x + F[g]\left(x_{j+1/2}, t\right) \phi(x_{j+1/2}) \\ - F[g]\left(x_{j-1/2}, t\right) \phi(x_{j-1/2}). \end{aligned} \tag{3.8}$$

DG schemes consist of choosing a local orthogonal polynomials basis on I_j to replace the test function and to approximate the solution. Residuals R_j are therefore null in the sense of orthogonalisation on the basis. In practice, Legendre polynomials are used (Cockburn and Shu, 1989). We denote hereafter the i-th Legendre polynomial by $\phi_i\left(\xi\right)$, where $\xi \in [-1, 1]$. Polynomial functions $\phi_i\left(\xi\right)$ are orthogonal in $L^2\left([-1, 1]\right)$ with respect to the inner product with weight unity. The prime interest of the DG method is to approximate the function g in cell I_j by a Legendre polynomial of arbitrary chosen order. DG method allows to approximate the function g by a piecewise polynomial function

instead of a constant polynomial function. Figure 3.3 shows a schematic representation of the DG method. In each cell, the function g is approximated by Legendre polynomials. The accuracy of the approximation increases with respect to the order of polynomials. The approximation of g in cell I_j writes

$$\begin{aligned}
&\forall x \in I_j,\ g(x) \approx g_j(x,t) = \sum_{i=0}^{k} g_j^i(t)\,\phi_i(\xi_j(x)),\\
&g_j(x,t) = \boldsymbol{g}_j^T(t)\cdot\boldsymbol{\phi}(\xi_j(x)),\ \text{with } \boldsymbol{g}_j = \begin{bmatrix} g_j^0 \\ \vdots \\ g_j^k \end{bmatrix} \text{ and } \boldsymbol{\phi} = \begin{bmatrix} \phi_0 \\ \vdots \\ \phi_k \end{bmatrix},
\end{aligned} \tag{3.9}$$

where g_j^i is the component of g_j on the Legendre polynomials basis. The function $\xi_j(x) \equiv \frac{2}{h_j}(x - x_j)$ is used to map the interval I_j onto the interval $[-1,1]$. Normalising the Legendre basis gives

$$\int_{-1}^{1} \boldsymbol{\phi}(\xi)\boldsymbol{\phi}^T(\xi)\mathrm{d}\xi = d_i\delta_{ik} \text{ with } d_i \equiv \frac{2}{2i+1}, \tag{3.10}$$

where d_i is the coefficient normalisation. By combining equations 3.7, 3.9 and 3.10 one obtains

$$\begin{aligned}
&\frac{\mathrm{d}\boldsymbol{g}_j(t)}{\mathrm{d}t} = \boldsymbol{L}[g] \text{ with}\\
&\boldsymbol{L}[g] \equiv \frac{2}{h_j}\begin{bmatrix} 1/d_0 & & \\ & \ddots & \\ & & 1/d_k \end{bmatrix}\\
&\quad\Bigg(\int_{I_j} F[g](x,t)\,\partial_x\boldsymbol{\phi}(\xi_j(x))\,\mathrm{d}x\\
&\qquad - \Big[F[g](x_{j+1/2},t)\,\boldsymbol{\phi}(\xi_j(x_{j+1/2}))\\
&\qquad\quad - F[g](x_{j-1/2},t)\,\boldsymbol{\phi}(\xi_j(x_{j-1/2}))\Big]\Bigg),
\end{aligned} \tag{3.11}$$

where $\boldsymbol{L}$ is the operator that results from applying the DG procedure to equation 3.5 with a Legendre polynomials basis. With the procedure described above, the original system of partial differential equations (PDE) equation 3.7 is transformed into a system of ordinary differential equations (ODE) equation 3.11 onto the coefficients $g_j^i(t)$. The initial condition $g_j(x,0)$ is generated by the piecewise L^2 projection of an initial mass density distribution $g_0(x)$ on each bin, that is

$$\begin{aligned}
&\forall j \in [\![1,N]\!],\\
&\int_{I_j} \left(g_j(x,0) - g_0(x)\right)\boldsymbol{\phi}^T(\xi_j(x))\mathrm{d}x = \mathbf{0}.
\end{aligned} \tag{3.12}$$

Orthogonality of the Legendre polynomials ensures

$$\begin{aligned}
\int_{I_j} g_j\boldsymbol{\phi}^T\mathrm{d}x &= \frac{h_j}{2}\int_{-1}^{1}\boldsymbol{\phi}(\xi)\boldsymbol{\phi}^T(\xi)\mathrm{d}\xi\boldsymbol{g}_j(t)\\
&= \frac{h_j}{2}\mathrm{diag}[d_0,\ldots,d_k]\boldsymbol{g}_j(t).
\end{aligned} \tag{3.13}$$

Then, the components of $\boldsymbol{g}_j$ are given by

$$\begin{aligned}&\forall j \in [\![1, N]\!], \forall i \in [\![0, k]\!],\\ &g_j^i(0) = \frac{2}{h_j d_i} \int_{-1}^{1} g_0\left(\frac{h_j}{2}\xi_j + x_j\right) \phi_i(\xi_j) \mathrm{d}\xi_j.\end{aligned} \tag{3.14}$$

To summarize, the DG method consists in solving the following Cauchy problem

DG method applied to a conservative law equation

$$\begin{cases}\forall j \in [\![1, N]\!], \forall i \in [\![0, k]\!],\\ \dfrac{\mathrm{d}\boldsymbol{g}_j(t)}{\mathrm{d}t} = \boldsymbol{L}[g],\\ g_j^i(0) = \dfrac{2}{h_j d_i} \displaystyle\int_{-1}^{1} g_0\left(\frac{h_j}{2}\xi_j + x_j\right) \phi_i(\xi_j) \mathrm{d}\xi_j,\end{cases} \tag{3.15}$$

where $\boldsymbol{L}$ is detailed in equation 3.11.

3.2.2 *Evaluation of the flux*

3.2.2.1 *Regularised flux*

The continuous Smoluchowski coagulation equation 2.40 is defined over an unbounded interval of masses $x \in \mathbb{R}_+$. Before applying DG procedure, equation 2.40 is restrained to a more physical interval of masses. Moreover, growth from a gaseous reservoir is excluded, meaning that $x > 0$. The mass interval is therefore reduced to the interval $[x_{\min}, x_{\max}]$ (Filbet and Laurencot, 2004; Liu et al., 2019). The coagulation flux can be truncated according to two procedures (Filbet and Laurencot, 2004). On the one hand

$$F_{\text{coag}}^{\text{c}}[g](x, \tau) = \int_{x_{\min}}^{x} \int_{x-u+x_{\min}}^{x_{\max}-u+x_{\min}} \mathcal{K}(u, v)\, g(u, \tau) \frac{g(v, \tau)}{v} \mathrm{d}v \mathrm{d}u, \tag{3.16}$$

where $F_{\text{coag}}^{\text{c}}$ is the conservative flux, meaning that no particle of mass larger than $x_{\max}$ is allowed to form. On the other hand

$$F_{\text{coag}}^{\text{nc}}[g](x, \tau) = \int_{x_{\min}}^{x} \int_{x-u+x_{\min}}^{x_{\max}} \mathcal{K}(u, v)\, g(u, \tau) \frac{g(v, \tau)}{v} \mathrm{d}v \mathrm{d}u, \tag{3.17}$$

where $F_{\text{coag}}^{\text{nc}}$ is the non-conservative flux which allows formation of particles of mass $x > x_{\max}$. $F_{\text{coag}}^{\text{c}}$ is useful in realistic simulations of growth, whereas $F_{\text{coag}}^{\text{nc}}$ should be used to compare numerical solution to analytic solutions of equation 2.4.

3.2.2.2 *Method of evaluating the flux*

A crucial difference between this scheme and usual DG solvers is that the coagulation flux $F_{\text{coag}}^{\text{nc}}$ is non local. The evaluation of the numerical flux $F_{\text{coag}}^{\text{nc}}[g]$ at the interface $x_{j+1/2}$ depends on the evaluation of g_j in all cells. Mathematically, $F_{\text{coag}}^{\text{nc}}$ is a double integral of a product of polynomials. Then the flux is a continuous function of mass x. At the

interface $x_{j+1/2}$, the numerical flux reduces to $F^{\text{nc}}_{\text{coag}}[g] = F^{\text{nc}}_{\text{coag}}[g](x_{j+1/2}, t)$. In usual DG solvers, the numerical flux is a discontinuous function and must be reconstructed at the interfaces (e.g. the Lax-Friedrichs flux in Cockburn and Shu (1989) and Zhang and Shu (2010)). The principal difficulty lies in carefully evaluating the flux at interfaces. This relies on handling the numerical integration of the polynomials g_j in every relevant cell. Liu et al. (2019) uses a Gaussian quadrature method with a Legendre polynomials basis to approximate the flux. The lower bound of the inner integral $x - u$ does usually not correspond to a grid point. To accurately perform the Gauss quadrature, some grid elements must be sub-divided, increasing drastically the cost of the numerical procedure, especially for high-order polynomials. To avoid prohibitive computational costs due to cell oversampling, we take advantage of the polynomial approximation by calculating integrals analytically. This requires integrable kernels, which is the case for the four kernels presented in this study. This approach maintains a reasonable computational cost by not multiplying the number of sampling points. This also avoid to add errors due to the numerical integration and to approximate kernels by piecewise constant functions.

3.2.2.3 *Mathematical procedure*

To integrate analytically the numerical flux $F^{\text{nc}}_{\text{coag}}$, let define the function $\tilde{g}$ that approximates the function g over the entire mass interval. To gather all the g_j polynomials defined in each bin, we take advantage of the Heaviside θ function as following

$$\forall x \in [x_{\min}, x_{\max}],\ \tilde{g}(x,t) \equiv \sum_{l=1}^{N}\sum_{i=0}^{k} g_l^i(t)\,\phi_i(\xi_l(x))[\theta(x - x_{l-1/2}) - \theta(x - x_{l+1/2})]. \quad (3.18)$$

We assume that the kernel function is polynomials and can be written as $\mathcal{K}(u,v) = \mathcal{K}_1(u)\mathcal{K}_2(v)$, which is effectively the case forthe three simple kernels and the ballistic kernel (see Chapter 2). For instance, the additive kernel writes $\mathcal{K}_{\text{add}}(u,v) = u + v = \mathcal{K}_1^1(u)\mathcal{K}_2^1(v) + \mathcal{K}_1^2(u)\mathcal{K}_2^2(v)$, where $\mathcal{K}_1^1(u) = u$, $\mathcal{K}_2^1(v) = 1$, $\mathcal{K}_1^2(u) = 1$ and $\mathcal{K}_2^2(v) = v$. The numerical flux is split in two terms. The numerical flux writes

$$\begin{aligned} &F^{\text{nc}}_{\text{coag}}[\tilde{g}](x,t) = \\ &\sum_{l'=1}^{N}\sum_{i'=0}^{k}\sum_{l=1}^{N}\sum_{i=0}^{k} g_{l'}^{i'}(t) g_l^i(t) \\ &\int_{x_{\min}}^{x}\int_{x-u+x_{\min}}^{x_{\max}} \frac{\mathcal{K}(u,v)}{v}\phi_{i'}(\xi_{l'}(u))[\theta(u - x_{l'-1/2}) - \theta(u - x_{l'+1/2})] \\ &\qquad \phi_i(\xi_l(v))[\theta(v - x_{l-1/2}) - \theta(v - x_{l+1/2})]\mathrm{d}v\mathrm{d}u. \end{aligned} \quad (3.19)$$

In the DG equation 3.7, the numerical flux is evaluated on grid points $x_{j+1/2}$ and $x_{j-1/2}$ with $j \in [\![1, N]\!]$. k is the order of the Legendre polynomials to approximate the solution.

Therefore, $F^{\text{nc}}_{\text{coag}}$ depends on j and k. The flux is sampled over a 2D array $(N, k+1)$ in order to use vectorial operations to reduce the computational time. The numerical flux is

$$\begin{cases} F^{\text{nc}}_{\text{coag}}[\tilde{g}](x,t) = \sum_{l'=1}^{N}\sum_{i'=0}^{k}\sum_{l=1}^{N}\sum_{i=0}^{k} g^{i'}_{l'}(t) g^{i}_{l}(t) T(x, x_{\min}, x_{\max}, i', i, l', l), \\ T(x, x_{\min}, x_{\max}, i', i, l', l) \equiv \\ \int_{x_{\min}}^{x} \mathcal{K}_1(u)\phi_{i'}(\xi_{l'}(u))[\theta(u - x_{l'-1/2}) - \theta(u - x_{l'+1/2})] \\ \int_{x-u+x_{\min}}^{x_{\max}} \frac{\mathcal{K}_2(v)}{v}\phi_i(\xi_l(v))[\theta(v - x_{l-1/2}) - \theta(v - x_{l+1/2})]\mathrm{d}v\mathrm{d}u. \end{cases} \tag{3.20}$$

A priori, the boundaries for the intervals of integration can be very large. We therefore rescale these intervals over the values, we choose to write the term T in $\xi_{l'}$ and ξ_l variables to avoid any numerical issues with large numbers. To avoid critical typos, the term T is derived with MATHEMATICA by starting with the inner integral on ξ_l and then injecting it in the integral on $\xi_{l'}$.

3.2.2.4 *Inner integral*

With the change of variable $\xi_l = \frac{2}{h_l}(x - x_l)$, the inner integral of equation 3.20 writes

$$\begin{aligned} &T_{\text{inner}}(x, x_{\min}, x_{\max}, i, l) = \\ &\int_{x-u+x_{\min}}^{x_{\max}} f_2(\xi_l)\left[\theta\left(\xi_l - \frac{2}{h_l}(x_{l-1/2} - x_l)\right) - \theta\left(\xi_l - \frac{2}{h_l}(x_{l+1/2} - x_l)\right)\right]\mathrm{d}\xi_l, \end{aligned} \tag{3.21}$$

with

$$f_2(\xi_l) \equiv K_2\left(\frac{h_l}{2}\xi_l + x_l\right)\frac{\phi_i(\xi_i)}{\frac{h_l}{2}\xi_l + x_l}. \tag{3.22}$$

We take advantage of the following identity

$$\begin{cases} a < b, c < b, d \leq b, c < d \\ \int_a^b f(x)[\theta(x-c) - \theta(x-d)]\mathrm{d}x = \\ \int_c^b f(x)\mathrm{d}x + \theta(a-c)\int_a^c f(x)\mathrm{d}x - \theta(b-d)\int_d^b f(x)\mathrm{d}x - \theta(b-d)\theta(a-d)\int_a^d f(x)\mathrm{d}x. \end{cases} \tag{3.23}$$

Therefore, T_{inner} writes

$$
\begin{aligned}
&T_{\text{inner}}\left(x, x_{\min}, x_{\max}, i, l\right) = \\
&\int_{\frac{2}{h_l}\left(x_{l-1/2}-x_l\right)}^{\frac{2}{h_l}\left(x_{\max}-x_l\right)} f_2(\xi_l)\mathrm{d}\xi_l + \theta\left(x - \frac{h_{l'}}{2}\xi_{l'} - x_{l'} + x_{\min} - x_{l-1/2}\right) \int_{\frac{2}{h_l}\left(x-\frac{h_{l'}}{2}\xi_{l'}-x_{l'}+x_{\min}-x_l\right)}^{\frac{2}{h_l}\left(x_{l-1/2}-x_l\right)} f_2(\xi_l)\mathrm{d}\xi_l \\
&- \theta\left(x_{\max} - x_{l+1/2}\right) \left\{ \int_{\frac{2}{h_l}\left(x_{l+1/2}-x_l\right)}^{\frac{2}{h_l}\left(x_{\max}-x_l\right)} f_2(\xi_l)\mathrm{d}\xi_l \right. \\
&\qquad \left. +\theta\left(x - \frac{h_{l'}}{2}\xi_{l'} - x_{l'} + x_{\min} - x_{l+1/2}\right) \int_{\frac{2}{h_l}\left(x-\frac{h_{l'}}{2}\xi_{l'}-x_{l'}+x_{\min}-x_l\right)}^{\frac{2}{h_l}\left(x_{l+1/2}-x_l\right)} f_2(\xi_l)\mathrm{d}\xi_l \right\}.
\end{aligned}
\tag{3.24}
$$

3.2.2.5 *Outer integral*

By applying the outer integral to T_{inner}, the term T writes

$$
\begin{aligned}
&T(x, x_{\min}, x_{\max}, i', i, l', l) = \frac{h_l}{2}\frac{h_{l'}}{2} \\
&\Bigg[\int_{\frac{2}{h_l}\left(x_{l-1/2}-x_l\right)}^{\frac{2}{h_l}\left(x_{l+1/2}-x_l\right)} f_2(\xi_l)\mathrm{d}\xi_l \times \\
&\quad \left\{ \int_{\frac{2}{h_{l'}}\left(x_{\min}-x_{l'}\right)}^{\frac{2}{h_{l'}}\left(x-x_{l'}\right)} f_1(\xi_{l'}) \left[\theta\left(\xi_{l'} - \frac{2}{h_{l'}}\left(x_{l'-1/2} - x_{l'}\right)\right) - \theta\left(\xi_{l'} - \frac{2}{h_{l'}}\left(x_{l'+1/2} - x_{l'}\right)\right)\right] \mathrm{d}\xi_{l'} \right\} \\
&\quad + \int_{\frac{2}{h_{l'}}\left(x_{\min}-x_{l'}\right)}^{\frac{2}{h_{l'}}\left(x-x_{l'}\right)} \int_{\frac{2}{h_l}\left(x-\frac{h_{l'}}{2}\xi_{l'}-x_{l'}+x_{\min}-x_l\right)}^{\frac{2}{h_{l'}}\left(x_{l-1/2}-x_l\right)} f_1(\xi_{l'}) f_2(\xi_l) \\
&\qquad \left[\theta\left(\xi_{l'} - \frac{2}{h_{l'}}\left(x_{l'-1/2} - x_{l'}\right)\right) - \theta\left(\xi_{l'} - \frac{2}{h_{l'}}\left(x_{l'+1/2} - x_{l'}\right)\right)\right] \\
&\qquad\qquad \theta\left(\frac{2}{h_{l'}}\left(x - x_{l-1/2} + x_{\min} - x_{l'}\right) - \xi_{l'}\right) \mathrm{d}\xi_l \mathrm{d}\xi_{l'} \\
&\quad - \int_{\frac{2}{h_{l'}}\left(x_{\min}-x_{l'}\right)}^{\frac{2}{h_{l'}}\left(x-x_{l'}\right)} \int_{\frac{2}{h_l}\left(x-\frac{h_{l'}}{2}\xi_{l'}-x_{l'}+x_{\min}-x_l\right)}^{\frac{2}{h_{l'}}\left(x_{l+1/2}-x_l\right)} f_1(\xi_{l'}) f_2(\xi_l) \\
&\qquad \left[\theta\left(\xi_{l'} - \frac{2}{h_{l'}}\left(x_{l'-1/2} - x_{l'}\right)\right) - \theta\left(\xi_{l'} - \frac{2}{h_{l'}}\left(x_{l'+1/2} - x_{l'}\right)\right)\right] \\
&\qquad\qquad \theta\left(\frac{2}{h_{l'}}\left(x - x_{l+1/2} + x_{\min} - x_{l'}\right) - \xi_{l'}\right) \mathrm{d}\xi_l \mathrm{d}\xi_{l'} \\
&\Bigg],
\end{aligned}
$$

(3.25)

with $f_1(\xi_{l'}) \equiv \mathcal{K}_1(\xi_{l'})\phi_{i'}(\xi_{l'})$. We now use the following identities

$$\begin{cases} a < b, a \leq c, a < d, c < d \\ \int_a^b f(x)\left[\theta(x-c) - \theta(x-d)\right] \mathrm{d}x \\ = \theta(b-c)\left[\int_c^b f(x)\mathrm{d}x + \theta(a-c)\int_a^c f(x)\mathrm{d}x\right] - \theta(b-d)\int_d^b f(x)\mathrm{d}x \end{cases}$$

$$\begin{cases} a < b, a \leq c, a < d, c < d, e < b \\ \int_a^b f(x)\left[\theta(x-c) - \theta(x-d)\right]\theta(e-x)\mathrm{d}x \\ = \theta(b-d)\theta(e-d)\int_e^d f(x)\mathrm{d}x \\ \quad + \theta(b-c)\left[(\theta(a-c)-1)\theta(b-c)\theta(e-c)\int_e^c f(x)\mathrm{d}x + \theta(a-c)\theta(e-a)\int_a^e f(x)\mathrm{d}x\right], \end{cases}$$

$$\begin{cases} a < b, a \leq c, a < d, c < d, e \leq b \\ \int_a^b f(x)\left[\theta(x-c) - \theta(x-d)\right]\theta(e-x)\mathrm{d}x \\ = \theta(b-c)\left[-\theta(a-c)\theta(e-a)\left\{\int_e^a f(x)\mathrm{d}x + \theta(e-b)\int_b^e f(x)\mathrm{d}x\right\}\right. \\ \quad + (1-\theta(a-c))\left[\theta(b-c)\theta(e-c)\left\{\int_c^e f(x)\mathrm{d}x + \theta(e-b)\int_e^b f(x)\mathrm{d}x\right\}\right. \\ \qquad \left.\left. +\theta(c-b)\theta(e-b)\left\{\int_e^b f(x)\mathrm{d}x + \theta(e-c)\int_c^e f(x)\mathrm{d}x\right\}\right]\right] \\ \quad - \theta(b-d)\left[\theta(b-d)\theta(e-d)\left\{\int_d^e f(x)\mathrm{d}x + \theta(e-b)\int_e^b f(x)\mathrm{d}x\right\}\right. \\ \qquad \left. +\theta(d-b)\theta(e-b)\left\{\int_e^b f(x)\mathrm{d}x + \theta(e-d)\int_d^e f(x)\mathrm{d}x\right\}\right], \end{cases}$$

(3.26)

The outer integrals write

- $$\int_{\frac{2}{h_{l'}}(x_{\min}-x_{l'})}^{\frac{2}{h_{l'}}(x-x_{l'})} f_1(\xi_{l'})\left[\theta\left(\xi_{l'} - \frac{2}{h_{l'}}(x_{l'-1/2}-x_{l'})\right) - \theta\left(\xi_{l'} - \frac{2}{h_{l'}}(x_{l'+1/2}-x_{l'})\right)\right]\mathrm{d}\xi_{l'}$$

$$= \theta(x-x_{l'-1/2})\int_{\frac{2}{h_{l'}}(x_{l'-1/2}-x_{l'})}^{\frac{2}{h_{l'}}(x-x_{l'})} f_1(\xi_{l'})\mathrm{d}\xi_{l'} - \theta(x-x_{l'+1/2})\int_{\frac{2}{h_{l'}}(x_{l'+1/2}-x_{l'})}^{\frac{2}{h_{l'}}(x-x_{l'})} f_1(\xi_{l'})\mathrm{d}\xi_{l'},$$

(3.27)

$$
\begin{aligned}
\bullet \int_{\frac{2}{h_{l'}}(x_{\min}-x_{l'})}^{\frac{2}{h_{l'}}(x-x_{l'})} & f_1(\xi_{l'})F_{2,1}(\xi_{l'})\left[\theta\left(\xi_{l'}-\frac{2}{h_{l'}}\left(x_{l'-1/2}-x_{l'}\right)\right)-\theta\left(\xi_{l'}-\frac{2}{h_{l'}}\left(x_{l'+1/2}-x_{l'}\right)\right)\right] \\
& \theta\left(\frac{2}{h_{l'}}\left(x-x_{l-1/2}+x_{\min}-x_{l'}\right)-\xi_{l'}\right)\mathrm{d}\xi_l\mathrm{d}\xi_{l'} \\
= \theta(x-x_{l'-1/2})\theta(x-x_{l-1/2}+x_{min}-x_{l'-1/2}) & \int_{\frac{2}{h_{l'}}\left(x_{l'-1/2}-x_{l'}\right)}^{\frac{2}{h_{l'}}(x-x_{l-1/2}+x_{\min}-x_{l'})} f_1(\xi_{l'})F_{2,1}(\xi_{l'})\mathrm{d}\xi_{l'} \\
+\theta(x-x_{l'+1/2})\theta(x-x_{l-1/2}+x_{\min}-x_{l'+1/2}) & \int_{\frac{2}{h_{l'}}(x-x_{l-1/2}+x_{\min}-x_{l'})}^{\frac{2}{h_{l'}}\left(x_{l'+1/2}-x_{l'}\right)} f_1(\xi_{l'})F_{2,1}(\xi_{l'})\mathrm{d}\xi_{l'},
\end{aligned}
\tag{3.28}
$$

$$
\begin{aligned}
\bullet \int_{\frac{2}{h_{l'}}(x_{\min}-x_{l'})}^{\frac{2}{h_{l'}}(x-x_{l'})} & f_1(\xi_{l'})F_{2,2}(\xi_{l'})\left[\theta\left(\xi_{l'}-\frac{2}{h_{l'}}\left(x_{l'-1/2}-x_{l'}\right)\right)-\theta\left(\xi_{l'}-\frac{2}{h_{l'}}\left(x_{l'+1/2}-x_{l'}\right)\right)\right] \\
& \theta\left(\frac{2}{h_{l'}}(x-x_{l+1/2}+x_{\min}-x_{l'})-\xi_{l'}\right)\mathrm{d}\xi_l\mathrm{d}\xi_{l'} \\
=\theta(x-x_{l'+1/2})\theta(x-x_{l+1/2}+x_{\min}-x_{l'+1/2}) & \int_{\frac{2}{h_{l'}}(x-x_{l+1/2}+x_{\min}-x_{l'})}^{\frac{2}{h_{l'}}\left(x_{l'+1/2}-x_{l'}\right)} f_1(\xi_{l'})F_{2,2}(\xi_{l'})\mathrm{d}\xi_{l'} \\
+\theta(x-x_{l'-1/2})\theta(x-x_{l+1/2}+x_{\min}-x_{l'-1/2}) & \int_{\frac{2}{h_{l'}}\left(x_{l'-1/2}-x_{l'}\right)}^{\frac{2}{h_{l'}}(x-x_{l+1/2}+x_{\min}-x_{l'})} f_1(\xi_{l'})F_{2,2}(\xi_{l'})\mathrm{d}\xi_{l'}\Bigg],
\end{aligned}
\tag{3.29}
$$

with

$$
F_{2,1}(\xi_{l'}) \equiv \int_{\frac{2}{h_l}\left(x-\frac{h_{l'}}{2}\xi_{l'}-x_{l'}+x_{\min}-x_l\right)}^{\frac{2}{h_l}(x_{l-1/2}-x_l)} f_2(\xi_l)\mathrm{d}\xi_l,\ F_{2,2}(\xi_{l'}) \equiv \int_{\frac{2}{h_l}\left(x-\frac{h_{l'}}{2}\xi_{l'}-x_{l'}+x_{\min}-x_l\right)}^{\frac{2}{h_l}(x_{l+1/2}-x_l)} f_2(\xi_l)\mathrm{d}\xi_l.
\tag{3.30}
$$

All details about the derivation are given in Appendix b.1. Therefore, the term T writes

$$
\begin{aligned}
T(x, x_{\min}, x_{\max}, i', i, l', l) = \frac{h_l}{2}\frac{h_{l'}}{2} \\
\Bigg[\int_{\frac{2}{h_l}(x_{l-1/2}-x_l)}^{\frac{2}{h_l}(x_{l+1/2}-x_l)} f_2(\xi_l)\mathrm{d}\xi_l \\
\left(\theta(x - x_{l'-1/2}) \int_{\frac{2}{h_{l'}}(x_{l'-1/2}-x_{l'})}^{\frac{2}{h_{l'}}(x-x_{l'})} f_1(\xi_{l'})\mathrm{d}\xi_{l'} - \theta(x - x_{l'+1/2}) \int_{\frac{2}{h_{l'}}(x_{l'+1/2}-x_{l'})}^{\frac{2}{h_{l'}}(x-x_{l'})} f_1(\xi_{l'})\mathrm{d}\xi_{l'} \right) \\
+ \theta(x - x_{l'-1/2}) \\
\Bigg[\theta(x - x_{l-1/2} + x_{\min} - x_{l'-1/2}) \\
\int_{\frac{2}{h_{l'}}(x_{l'-1/2}-x_{l'})}^{\frac{2}{h_{l'}}(x-x_{l-1/2}+x_{\min}-x_{l'})} \int_{\frac{2}{h_l}(x-\frac{h_{l'}}{2}\xi_{l'}-x_{l'}+x_{\min}-x_l)}^{\frac{2}{h_l}(x_{l-1/2}-x_l)} f_1(\xi_{l'})f_2(\xi_l)\mathrm{d}\xi_l\mathrm{d}\xi_{l'} \\
- \theta(x_{\max} - x_{l+1/2})\theta(x - x_{l+1/2} + x_{\min} - x_{l'-1/2}) \\
\int_{\frac{2}{h_{l'}}(x_{l'-1/2}-x_{l'})}^{\frac{2}{h_{l'}}(x-x_{l+1/2}+x_{\min}-x_{l'})} \int_{\frac{2}{h_l}(x-\frac{h_{l'}}{2}\xi_{l'}-x_{l'}+x_{\min}-x_l)}^{\frac{2}{h_l}(x_{l+1/2}-x_l)} f_1(\xi_{l'})f_2(\xi_l)\mathrm{d}\xi_l\mathrm{d}\xi_{l'} \Bigg] \\
+ \theta(x - x_{l'+1/2}) \\
\Bigg[\theta(x - x_{l-1/2} + x_{\min} - x_{l'+1/2}) \\
\int_{\frac{2}{h_{l'}}(x-x_{l-1/2}+x_{\min}-x_{l'})}^{\frac{2}{h_{l'}}(x_{l'+1/2}-x_{l'})} \int_{\frac{2}{h_l}(x-\frac{h_{l'}}{2}\xi_{l'}-x_{l'}+x_{\min}-x_l)}^{\frac{2}{h_l}(x_{l-1/2}-x_l)} f_1(\xi_{l'})f_2(\xi_l)\mathrm{d}\xi_l\mathrm{d}\xi_{l'} \\
- \theta(x_{\max} - x_{l+1/2})\theta(x - x_{l+1/2} + x_{\min} - x_{l'+1/2}) \\
\int_{\frac{2}{h_{l'}}(x-x_{l+1/2}+x_{\min}-x_{l'})}^{\frac{2}{h_{l'}}(x_{l'+1/2}-x_{l'})} \int_{\frac{2}{h_l}(x-\frac{h_{l'}}{2}\xi_{l'}-x_{l'}+x_{\min}-x_l)}^{\frac{2}{h_l}(x_{l+1/2}-x_l)} f_1(\xi_{l'})f_2(\xi_l)\mathrm{d}\xi_l\mathrm{d}\xi_{l'} \Bigg] \Bigg] .
\end{aligned}
\tag{3.31}
$$

The high-order solver is written in `Fortran`. Reducing the number of integrals is key to avoid numerical issues with differences of large numbers. In this purpose the expression of T is split in several terms

$$
\begin{aligned}
T_{\phi_i} &\equiv \int_{\frac{2}{h_l}(x_{l-1/2}-x_l)}^{\frac{2}{h_l}(x_{l+1/2}-x_l)} f_2(\xi_l)\mathrm{d}\xi_l, \\
T_{\phi_{i'},\mathrm{mix}} &\equiv \int_{\frac{2}{h_{l'}}(x_{l'-1/2}-x_{l'})}^{\frac{2}{h_{l'}}(x_{l'+1/2}-x_{l'})} f_1(\xi_{l'})\mathrm{d}\xi_{l'}, \\
T_{\phi_{i'},\mathrm{term1}} &\equiv \int_{\frac{2}{h_{l'}}(x_{l'-1/2}-x_{l'})}^{\frac{2}{h_{l'}}(x-x_{l'})} f_1(\xi_{l'})\mathrm{d}\xi_{l'}, \\
T_{\phi_{i'},\phi_i,\mathrm{allmix}} &\equiv \int_{\frac{2}{h_{l'}}(x_{l'-1/2}-x_{l'})}^{\frac{2}{h_{l'}}(x_{l'+1/2}-x_{l'})} \int_{\frac{2}{h_l}(x_{l+1/2}-x_l)}^{\frac{2}{h_l}(x_{l-1/2}-x_l)} f_1(\xi_{l'})f_2(\xi_l)\mathrm{d}\xi_l\mathrm{d}\xi_{l'}, \\
T_{\phi_{i'},\phi_i,\mathrm{mix_P1term1_P2term1}} &\equiv \int_{\frac{2}{h_{l'}}(x_{l'-1/2}-x_{l'})}^{\frac{2}{h_{l'}}(x_{l'+1/2}-x_{l'})} \int_{\frac{2}{h_l}(x-\frac{h_{l'}}{2}\xi_{l'}-x_{l'}+x_{\min}-x_l)}^{\frac{2}{h_l}(x_{l-1/2}-x_l)} f_1(\xi_{l'})f_2(\xi_l)\mathrm{d}\xi_l\mathrm{d}\xi_{l'} \\
T_{\phi_{i'},\phi_i,\mathrm{P1term1}} &\equiv \int_{\frac{2}{h_{l'}}(x_{l'-1/2}-x_{l'})}^{\frac{2}{h_{l'}}(x-x_{l-1/2}+x_{\min}-x_{l'})} \int_{\frac{2}{h_l}(x-\frac{h_{l'}}{2}\xi_{l'}-x_{l'}+x_{\min}-x_l)}^{\frac{2}{h_l}(x_{l-1/2}-x_l)} f_1(\xi_{l'})f_2(\xi_l)\mathrm{d}\xi_l\mathrm{d}\xi_{l'} \\
T_{\phi_{i'},\phi_i,\mathrm{P1term2}} &\equiv \int_{\frac{2}{h_{l'}}(x_{l'-1/2}-x_{l'})}^{\frac{2}{h_{l'}}(x-x_{l+1/2}+x_{\min}-x_{l'})} \int_{\frac{2}{h_l}(x-\frac{h_{l'}}{2}\xi_{l'}-x_{l'}+x_{\min}-x_l)}^{\frac{2}{h_l}(x_{l+1/2}-x_l)} f_1(\xi_{l'})f_2(\xi_l)\mathrm{d}\xi_l\mathrm{d}\xi_{l'}.
\end{aligned}
\tag{3.32}
$$

For robustness, all these integrals are calculated with MATHEMATICA. The function `FortranForm` in MATHEMATICA is used to translate integral expression of integrals to `Fortran`. For large expressions, it is necessary to split them with the function `MonomialList`. Each part is then translated with `FortranForm`. The scheme to evaluate $T(x, x_{\min}, x_{\max}, i', i, l', l)$, in `Fortran`, is given in Appendix b.1.4.
To summarize, a 4D array with element $T(x, x_{\min}, x_{\max}, i', i, l', l)$ and a 4D array with element $g_{l'}^{i'}(t)g_l^i(t)$ are computed. The element (j,k) of the 2D array corresponding to the flux is obtained by multiplying these two 4D arrays and summing over of all elements. $F_{\mathrm{coag}}^{\mathrm{nc}}[\tilde{g}]$ is then evaluated in $x_{j-1/2}$ and $x_{j+1/2}$ for all j.

The numerical flux $F_{\mathrm{coag}}^{\mathrm{nc}}[\tilde{g}]$ is now evaluated in $x_{j-1/2}$ and $x_{j+1/2}$ for all j. In the DG equation, it remains the evaluation of the term containing the integral of the flux $F_{\mathrm{coag}}^{\mathrm{nc}}[\tilde{g}]$.

3.2.3 *Evaluation of the integral of the flux*

Let denote $\mathcal{F}^{\text{nc}}_{\text{coag}}$ the term of equation 3.7 corresponding to the integral of the numerical flux. $\mathcal{F}^{\text{nc}}_{\text{coag}}$ writes

$$\begin{cases} \mathcal{F}^{\text{nc}}_{\text{coag}}[\tilde{g}, j, k](t) = \sum_{l'=1}^{N} \sum_{i'=0}^{k} \sum_{l=1}^{N} \sum_{i=0}^{k} g^{i'}_{l'}(t)\, g^{i}_{l}(t) \mathcal{T}\left(x_{\min}, x_{\max}, j, k, i', i, l', l\right) \\ \mathcal{T}\left(x_{\min}, x_{\max}, j, k, i', i, l', l\right) \equiv \\ \int_{I_j} \int_{x_{\min}}^{x} \int_{x-u+x_{\min}}^{x_{\max}} \dfrac{\mathcal{K}(u,v)}{v} \partial_x \phi_k(\xi_j(x)) \\ \qquad \phi_{i'}(\xi_{l'}(u))[\theta(u - x_{l'-1/2}) - \theta(u - x_{l'+1/2})] \\ \qquad \phi_i(\xi_l(v))[\theta(v - x_{l-1/2}) - \theta(v - x_{l+1/2})] \mathrm{d}v\, \mathrm{d}u\, \mathrm{d}x. \end{cases} \tag{3.33}$$

$\mathcal{F}^{\text{nc}}_{\text{coag}}[\tilde{g}]$ is evaluated similarly to the flux term. A triple integral is derived with MATHEMATICA with the changes of variables

$$\xi_l \equiv \frac{2}{h_l}\left(v - x_l\right), \xi_{l'} \equiv \frac{2}{h_{l'}}\left(u - x_{l'}\right), \xi_j \equiv \frac{2}{h_j}\left(x - x_j\right). \tag{3.34}$$

To derive tractable equations for the integrals involving Heaviside distributions, we start to compute integrals over the variable ξ_l, then calculating the integral over $\xi_{l'}$ and finally, over x. All details of the calculations are given in Appendix b.2. The integrals cannot be switched. Therefore, the computational time can take a couple of hours to derive one triple integral with MATHEMATICA. The obtained expressions are very large. As for the numerical flux, `FortranForm` and `MonomialList` are used to split large expressions and translate them in `Fortran`. The scheme in `Fortran` to evaluate $\mathcal{T}\left(x_{\min}, x_{\max}, j, k, i', i, l', l\right)$ is given in Appendix b.2.3. $\mathcal{F}^{\text{nc}}_{\text{coag}}$ is computed as a product of 4D arrays similarly to $F^{\text{nc}}_{\text{coag}}$.

Accuracy on T and $\mathcal{T}$ depends only the quality of the polynomial approximation of g by $\tilde{g}$, since the integrals corresponding to $F^{\text{nc}}_{\text{coag}}[\tilde{g}]$ and $\mathcal{F}^{\text{nc}}_{\text{coag}}[\tilde{g}]$ are calculated analytically.

3.2.4 *Slope limiter*

In Chapter 2, the self-similarity theory shows that the solution of the Smoluchowski coagulation equation has been mathematically shown to decay with an exponential at large masses, for most of astrophysical kernels. This part is challenging to approximate with polynomials, and numerical estimates g_j of g in the bin I_j can lead to negative values, which is not acceptable physically.

To preserve the positivity of solution, the requirement $g_j(x,t) \geq 0$ for $x \in I_j$ needs to be enforced. The idea is to use a scaling limiter (Liu and Osher, 1996; Zhang and Shu, 2010; Liu et al., 2019) which controls the maximum/minimum of the reconstruction polynomials. This is achieved by a reconstruction step using cell averages as a reference. Let us consider the polynomials $g_j(x)$ of order k that approximates $g(x)$ on I_j. Let us

denote m and M two positive reals and $M_j = \max_{x \in I_j} g_j(x)$, $m_j = \min_{x \in I_j} g_j(x)$ and define the scaled polynomials

$$\begin{aligned} p_j(x) &\equiv \gamma_j \left(g_j(x) - \overline{g}_j \right) + \overline{g}_j, \\ \gamma_j &= \min \left\{ \left| \frac{M - \overline{g}_j}{M_j - \overline{g}_j} \right|, \left| \frac{m - \overline{g}_j}{m_j - \overline{g}_j} \right|, 1 \right\}, \end{aligned} \tag{3.35}$$

For all j, we assume $\overline{g}_j \in [m, M]$. $p_j(x)$ is a polynomial of order k such as $\overline{p}_j = \overline{g}_j$. Liu and Osher (1996) proved that $\forall x \in I_j,\ p_j(x) \in [m, M]$. This scaling limiter allows to build a maximum-principle-satisfying DG scheme, in the sense that the numerical solution never goes out of the range $[m, M]$ of the initial condition. The main difficulty is to ensure the property $\overline{g}_j \in [m, M]$ during the time evolution without loosing high accuracy.

In the DG scheme given by equation 3.11, polynomials $g_j(x)$ are replaced by the scaled polynomials $p_j(x)$ that write

$$\begin{aligned} p_j(x) &= \gamma_j \left(g_j(x) - \overline{g}_j \right) + \overline{g}_j \\ &= \sum_{i=0}^{k} \gamma_j g_j^i(t) \phi_{1,i}(\xi_j(x)) + \sum_{i=0}^{k} g_j^i(t) \phi_{2,i}(\xi_j(x)) \end{aligned} \tag{3.36}$$

with

$$\begin{aligned} \phi_{1,i}(\xi_j(x)) &\equiv \left(\phi_i(\xi_j(x)) - \frac{1}{2} \int_{I_j} \phi_i(\xi_j(x)) \mathrm{d}x \right), \\ \phi_{2,i}(\xi_j(x)) &\equiv \frac{1}{2} \int_{I_j} \phi_i(\xi_j(x)) \mathrm{d}x. \end{aligned} \tag{3.37}$$

Replacing g_j by p_j in equation 3.20 gives four terms for the function T: $T_{11}[\phi_{1,i'}\phi_{1,i}]$, $T_{12}[\phi_{1,i'}\phi_{2,i}]$, $T_{21}[\phi_{2,i'}\phi_{1,i}]$ and $T_{22}[\phi_{2,i'}\phi_{2,i}]$. For each term, a corresponding coefficient $g_{l',i'}(t) g_{l,i}(t)$ is associated, namely $\gamma_{l'} g_{l',i'}(t) g_{l,i}(t)$, $\gamma_{l'} g_{l',i'}(t) g_{l,i}(t)$, $\gamma_l g_{l',i'}(t) g_{l,i}(t)$ and $g_{l',i'}(t) g_{l,i}(t)$ (no γ in the last term). $F^{\mathrm{nc}}_{\mathrm{coag}}$ is evaluated by summing over those four terms. The same procedure is applied for $\mathcal{F}^{\mathrm{nc}}_{\mathrm{coag}}$. Therefore, the positivity of $\tilde{g}$ is ensured in each cell.

To complete the DG scheme equation 3.11, a high-order time solver is required.

3.2.5 *High-order time solver*

3.2.5.1 *Timestepping*

Forward Euler discretisation of equation 3.7 gives

$$\overline{g}_j^{n+1} = \overline{g}_j^n - \frac{\Delta t}{\Delta x_j} \left[F^{\mathrm{nc}}_{\mathrm{coag}} \left[g_j \right] \left(x_{j+1/2}, t \right) - F^{\mathrm{nc}}_{\mathrm{coag}} \left[g_j \right] \left(x_{j-1/2}, t \right) \right], \tag{3.38}$$

for the n-th time step. Equation 3.38 is also equivalent to the ordinary differential equation 3.11 for the component g_j^0. The numerical scheme have to fulfil a criterion on the timestep to be stable and to converge to a physical solution. This so-called Courant-Friedrichs-Lewy condition (CFL) is chosen to guarantee the positivity of the cell average $\overline{g}_j^{n+1} > 0$ (Filbet and Laurencot, 2004), i.e.

$$\Delta t < \frac{\Delta x_j \overline{g}_j^n}{\left| F^{\mathrm{nc}}_{\mathrm{coag}} \left[g_j \right] \left(x_{j+1/2}, t \right) - F^{\mathrm{nc}}_{\mathrm{coag}} \left[g_j \right] \left(x_{j-1/2}, t \right) \right|}. \tag{3.39}$$

This CFL condition associated with the slope limiter (see Section. 3.2.4) ensures the positivity of the high-order scheme. The CFL condition is initially dominated by small grains and softens as grains grow.

3.2.5.2 *Strong Stability Preserving Runge-Kutta method*

In equation 2.40, the spatial derivative $\partial_x F_{\text{coag}}[g]$ is approximated by $-L[g]$ given in equation 3.11. The expression of $L[g]$ depends on the finite element method (DG method in our case). $L[g]$ is a nonlinearly stable approximation. For hyperbolic conservation laws, nonlinear stability property is characterised by the total variation diminishing (TVD) semi-norm

$$TV\left(g\right) \equiv \sum_j |\overline{g}_{j+1} - \overline{g}_j|. \tag{3.40}$$

The spatial discretisation $-L[g]$ has the property that the total variation of the numerical solution does not increase for a forward Euler integration

$$g^{n+1} = g^n + \Delta t L[g],\ \Delta t \leq \Delta t_{\text{FE}}, \tag{3.41}$$

where Δt_{FE} is the CFL condition determined in equation 3.39, i.e. $TV\left(g^{n+1}\right) \leq TV\left(g^n\right)$. In this case the coupling between DG method and forward Euler method has the TVD property, meaning a nonlinear stability. There is no guarantee that any linear stable high-order time discretisation method will preserve this nonlinear stability. A new high-order time discretisation method called Strong Stability Preserving (SSP) has been developed in the purpose to maintain the nonlinear stability under the same semi norm TV with a probable different timestep restriction (Shu and Osher, 1988; Gottlieb et al., 2001; Zhang and Shu, 2010; Liu et al., 2019). The method is SSP if the following condition holds

$$TV\left(g^{n+1}\right) \leq TV\left(g^n\right), \tag{3.42}$$

and the timestep satisfies

$$\Delta t_{\text{SSP}} \leq c\Delta t_{\text{FE}}, \tag{3.43}$$

where c is a positive coefficient. Stability arguments are based on convex decomposition of high-order methods in term of the first-order Euler elements. This ensures that SSP preserves high-order accuracy in time for any convex functional (e.g. TV). In practice, errors are dominated by mass discretisation. We use a SSP Runge-Kutta (SSPRK) third-order method (Gottlieb et al., 2009; Zhang and Shu, 2010; Liu et al., 2019) which writes, with $c = 1$,

$$\begin{aligned}
\boldsymbol{g}_j^{(1)} &= \boldsymbol{g}_j^n + \Delta t_{\text{SSP}} \boldsymbol{L}[g_j^n], \\
\boldsymbol{g}_j^{(2)} &= \frac{3}{4}\boldsymbol{g}_j^n + \frac{1}{4}\left(\boldsymbol{g}_j^{(1)} + \Delta t_{\text{SSP}} \boldsymbol{L}[g_j^{(1)}]\right), \\
\boldsymbol{g}_j^{n+1} &= \frac{1}{3}\boldsymbol{g}_j^n + \frac{2}{3}\left(\boldsymbol{g}_j^{(2)} + \Delta t_{\text{SSP}} \boldsymbol{L}[g_j^{(2)}]\right).
\end{aligned} \tag{3.44}$$

This SSPRK third-order method ensures that $\overline{g}_j \in [m, M]$ for $(m, M) \in \mathbb{R}_+$ for all time. Hence, under a suitable CFL condition, SSP high-order time discretisation preserves the property $\overline{g}_j \in [m, M]$ of the DG scheme and the linear scaling presented in Section 3.2.4 satisfies a maximum principle.

3.2.6 *Algorithm flowchart*

Associating SSPRK with a DG scheme provides overall an high-order scheme that maintains overall a uniform high-order accuracy of the solution (Zhang and Shu, 2010). We use the SSPRK of third order given by equation 3.44. Splitting the algorithm into the following steps ensures positivity:

1. Initialisation: From the initial data $g_0(x)$,
   a) generate $\forall j \in [\![1, N]\!],\ g_j(x, 0) \in \mathcal{V}^k$ by piecewise L^2 projection and get the components on Legendre basis equation 3.14,
   b) define $[m, M]$ for which $\overline{g}_j(x, 0) \in [m, M]$,
   c) replace g_j by p_j
2. Evolution: Use the scheme 3.44 to compute $\forall j \in [\![1, N]\!], \forall i \in [\![1, k]\!],\ (g_j^i)^{n+1}$
3. Reconstruction: Use 3.36 to reconstruct $p_j(x, t)$

3.2.7 *Design*

During my Ph.D. Thesis, I visited the Monash Centre of Astrophysics (MoCA) at Monash University (Melbourne, Australia) to work on the high-order solver in collaboration with Pr. D. J. Price and D. Mentiplay. I spent in total 4 months at MoCA. We worked on the interface of the high-order solver and the code `PHANTOM`. Thanks to their advices, the high-order solver is designed in a modular way to be user friendly. The code is compiled as a static library. The `submodule` procedure in `Fortran` allows to define the routine which calls the high-order solver in the library. This `submodule` interfaces the library with any other code requiring to solve the Smoluchowski coagulation equation.

3.3 SUMMARY

A high-order solver has been developed with the aim of solving efficiently and accurately the Smoluchowski coagulation equation with a small number of bins and a low impact on time computation. The high-order solver is based on the discontinuous Galerkin method (see equation 3.7) associated with a linear slope limiter (see Section 3.2.4) and on a positivity-preserving high-order time scheme (see Section 3.2.5). This scheme, developed in this Ph.D. thesis, relies on an analytic integration of numerical fluxes in order to make the solver efficient. Analytic solutions for different kernels are provided to benchmark coagulation algorithms. This solver is designed to solve the collisional fragmentation equation 2.51 and be straightforwardly extended to the coagulation-fragmentation equation 2.52.

4

BENCHMARKS OF THE HIGH-ORDER SOLVER

4.1 Introduction . . . 61
4.2 Error measurements . . . 61
4.3 Benchmark for coagulation . . . 62
4.3.1 Constant kernel . . . 63
4.3.2 Additive kernel . . . 67
4.3.3 Multiplicative kernel . . . 72
4.4 Future developments for the Discontinuous Galerkin scheme . . . 72
4.4.1 Ballistic kernel . . . 76
4.5 Summary . . . 79

"The benchmark of quality I go for is pretty high" – Jimmy Page

This work led to the publication of the article M. Lombart and G. Laibe, "Grain growth for astrophysics with Discontinuous Galerkin schemes", *Monthly Notices of the Royal Astronomical Society*, staa3682 (2020).

4.1 INTRODUCTION

We benchmarked our numerical solver presented in Chapter 3 against the analytical solutions presented in Chapter 2. Numerical tests for the proposed high-order positivity-preserving solver are applied to pure coagulation. For comparison purpose, we perform similar tests than in Liu et al. (2019). The accuracy and the computational time are compared to the DG method from Liu et al. (2019) where Gauss quadrature method is used to approximate the integrals. As mentioned in Section 3.1.6, accuracy with a minimal number of bins is required to couple the high-order solver to the code `PHANTOM`. Hence, accuracy tests are performed with a small number of bins.

4.2 ERROR MEASUREMENTS

Numerical simulations are carried out to: i) investigate the *experimental order of convergence* (EOC, Rajesh Kumar (2014) and Liu et al. (2019)), and ii) determine the performances of the algorithm. Relative errors are measured using a continuous norm and a discrete norm. The L^1 norm is a natural choice for equations of conservation. The continuous L^1 norm can be approximated by using a high order Gaussian quadrature rule

$$\|f\|_1 \equiv \int_{x_{\min}}^{x_{\max}} |f(x)|\mathrm{d}x = \sum_{j=1}^{N} \int_{I_j} |f(x)|\mathrm{d}x \approx \sum_{j=1}^{N} \frac{h_j}{2} \sum_{\alpha=1}^{R} \omega_\alpha |f(x_j^\alpha)|, \tag{4.1}$$

where N is the number of bins, h_j is the size of bin I_j, ω_α are the weights and x_j^α are the corresponding Gauss points in cell I_j. We use $R = 16$ for sufficient accuracy. The numerical error $e_{c,N}$ is measured with the continuous L^1 norm as

$$e_{c,N}(\tau) \equiv \sum_{j=1}^{N} \frac{h_j}{2} \sum_{\alpha=1}^{R} \omega_\alpha |g_j(x_j^\alpha, \tau) - g(x_j^\alpha, \tau)|, \tag{4.2}$$

where g and g_j are the analytic and the numerical solution of the Smoluchowski equation. Equation 4.2 computed with MATHEMATICA with 16 digits for sufficient precision. The dis-

crete L^1 norm is defined by evaluating g_j and g at the geometric mean $\hat{x}_j \equiv \sqrt{x_{j-1/2}x_{j+1/2}}$ of the bin I_j. The numerical error measured with this discrete L^1 norm is

$$e_{\mathrm{d},N}(\tau) \equiv \sum_{j=1}^{N} h_j |g_j(\hat{x}_j, \tau) - g(\hat{x}_j, \tau)|. \tag{4.3}$$

We follow Liu et al. (2019) to calculate the *experimental order of convergence* (EOC)

$$\mathrm{EOC} \equiv \frac{\ln\left(\frac{e_N(\tau)}{e_{2N}(\tau)}\right)}{\ln(2)}, \tag{4.4}$$

where e_N is the error evaluated for N bins and e_{2N} for $2N$ bins. For the calculation of the EOC, the numerical errors are calculated at time $\tau = 0.01$ for the order of convergence of the DG scheme not to be altered by time stepping errors.
The moments of the numerical solutions are defined by

$$M_{p,N}(\tau) = \int_{x_{\min}}^{x_{\max}} x^{p-1}\tilde{g}(x,\tau)\mathrm{d}x = \sum_{j=1}^{N}\int_{I_j} x^{p-1} g_j(x,\tau)\mathrm{d}x = \sum_{j=1}^{N}\sum_{i=0}^{k} g_j^i(\tau)\int_{I_j} x^{p-1}\phi_i\left(\xi_j(x)\right)\mathrm{d}x. \tag{4.5}$$

The total mass of the system writes

$$M_{1,N}(\tau) = \sum_{j=1}^{N}\sum_{i=0}^{k} g_j^i(\tau)\frac{h_j}{2}\underbrace{\int_{-1}^{1}\phi_i\left(\xi_j\right)\mathrm{d}\xi_j}_{=\delta_{00}=2} = \sum_{j=1}^{N} h_j g_j^0(\tau). \tag{4.6}$$

Absolute errors on the moments are given by

$$e_{M_{p,N}}(\tau) \equiv \frac{|M_{p,N}(\tau) - M_p(\tau)|}{M_p(\tau)}, \tag{4.7}$$

where $M_p(\tau)$ is the moment of order p at time τ for the exact solution. In usual convergence tests, errors are normalised with respect to the number of degrees of freedom of the algorithm. This is not the case here, since we compare absolute gains for the purpose interfacing it with an hydrodynamical solver.

4.3 BENCHMARK FOR COAGULATION

Numerical tests are performed by comparing numerical solutions the constant, additive and multiplicative kernels to the solutions given in equations 2.20, 2.2.1.2 and 2.22. Solutions are integrated over the intervals $x \in [10^{-3}, 10^{6}]$ for the constant and the additive kernels, and $x \in [10^{-3}, 10^{3}]$ for the multiplicative kernel. Tests are performed with FORTRAN, errors are calculated with MATHEMATICA at machine precision. Quadruple precision is required for the additive kernel with $k = 2$, and for all kernels with $k = 3$. The results are shown for Legendre polynomials of order $k = 0, 1, 2, 3$. Above order 3, numerical errors due to arithmetics of large numbers are not negligible anymore. A safety coefficient of $1/2$ is applied on the CFL condition, i.e. the coagulation time-step used in practice is $\mathrm{d}\tau_{\mathrm{coag}} = 1/2\,\mathrm{d}\tau_{\mathrm{CFL}}$ (see Section 3.2.5.1 in Chapter 3). Initial conditions are set to satisfy the analytic solution at initial time $\tau = 0$. The analytical and numerical solutions are compared when particles of large masses are formed at final times τ that depend

on the kernels. Simulations are performed by dividing τ into constant dumps of value $d\tau$ (300 for the constant and the additive kernels, 10000 for the multiplicative kernel). Each dump is subdivided in several coagulation steps satisfying the CFL condition. The analytical derivation of the coagulation flux allows the algorithm to be efficient, i.e. to reach desired accuracy with a low computational time. To quantify efficiency, the computational time is compared to the one obtained with the scheme of Liu et al. (2019) with a number of Gauss points $Q = k + 1$ on a simulation in double precision with $N = 20$ bins, $k = 1$ for the additive kernel and $k = 2$ for the constant and multiplicative kernels. The Liu scheme is implemented by following the description of Liu et al. (2019) step-by-step, without additional optimisations. Simulations are performed in sequential on an Intel Core i7 2.8GHz. We use the `gfortran v9.2.0` compiler. Such a comparison is delicate to perform and interpret, since it is implementation-dependant. Should the number of Gauss points in the Liu algorithm be increased to better approximate the integral terms calculated here analytically, this may result in an increase of computational time by several orders of magnitudes, giving the false impression that the Liu algorithm is not performant. Hence the choice $Q = k + 1$. Qualitatively, our scheme is more effective by a factor of several unities for same precision and without requiring sub-binning, except for the additive kernel for which the Liu scheme exhibits serendipitous super-convergence (Liu et al., 2019).

4.3.1 *Constant kernel*

4.3.1.1 *Positivity and mass conservation*

Physically, the constant kernel $\mathcal{K} = 1$ means the frequency of collisions between two particles is independent of their size. All particles are formed at the same frequency. The solution keeps the same shape during time. Figure 4.1 shows the numerical solutions obtained for $N = 20$ bins, varying the order of the polynomials k. The analytical and numerical solutions are compared at time $\tau = 30000$. As expected, the solution remains positive, as a result from combining the slope limiter (see Section 3.2.4) and the SSP Runge-Kutta time stepping (see Section 3.2.5.2 in Chapter 3). The piecewise linear solution ($k = 1$) appears curved due to the logarithmic scale of the x-axis. Figure 4.2 shows the numerical absolute error $e_{M_1,N}$ on the moment $M_{1,N}$ for $N = 20$ bins from $\tau = 0$ to $\tau = 30000$. The total mass remains conserved to machine precision until $\tau = 10^4$.

4.3.1.2 *Accuracy of the numerical solution*

As expected, the accuracy of the numerical solution improves with the order of the scheme. Figure 4.3 shows the numerical solution obtained at $\tau = 30000$ (note the 16 *orders of magnitude in mass* on the y axis in log). The major part of the total mass of the system is located around the maximum of the curve. Figure 4.3 shows that around this maximum, schemes of order $k = 1, 2, 3$ provide errors of order $\sim 0.1 - 1\%$ when $k = 0$ generates errors of order $\sim 30\%$. Figure 4.3 also shows that numerical diffusion is drastically reduced in the exponential tail as the order of the scheme increases, since a gain of a factor ~ 100 is obtained with order 3 compared to order 0.

4.3.1.3 *Convergence analysis*

Numerical errors introduced in Section 4.2 are shown on Figure 4.4 at $\tau = 0.01$. $e_{c,N}$ and $e_{d,N}$ are plotted as a functions of the number of bins per decade $N_{\text{bin/dec}}$, to infer the EOC independently from the global mass interval. With the continuous L^1 norm, the

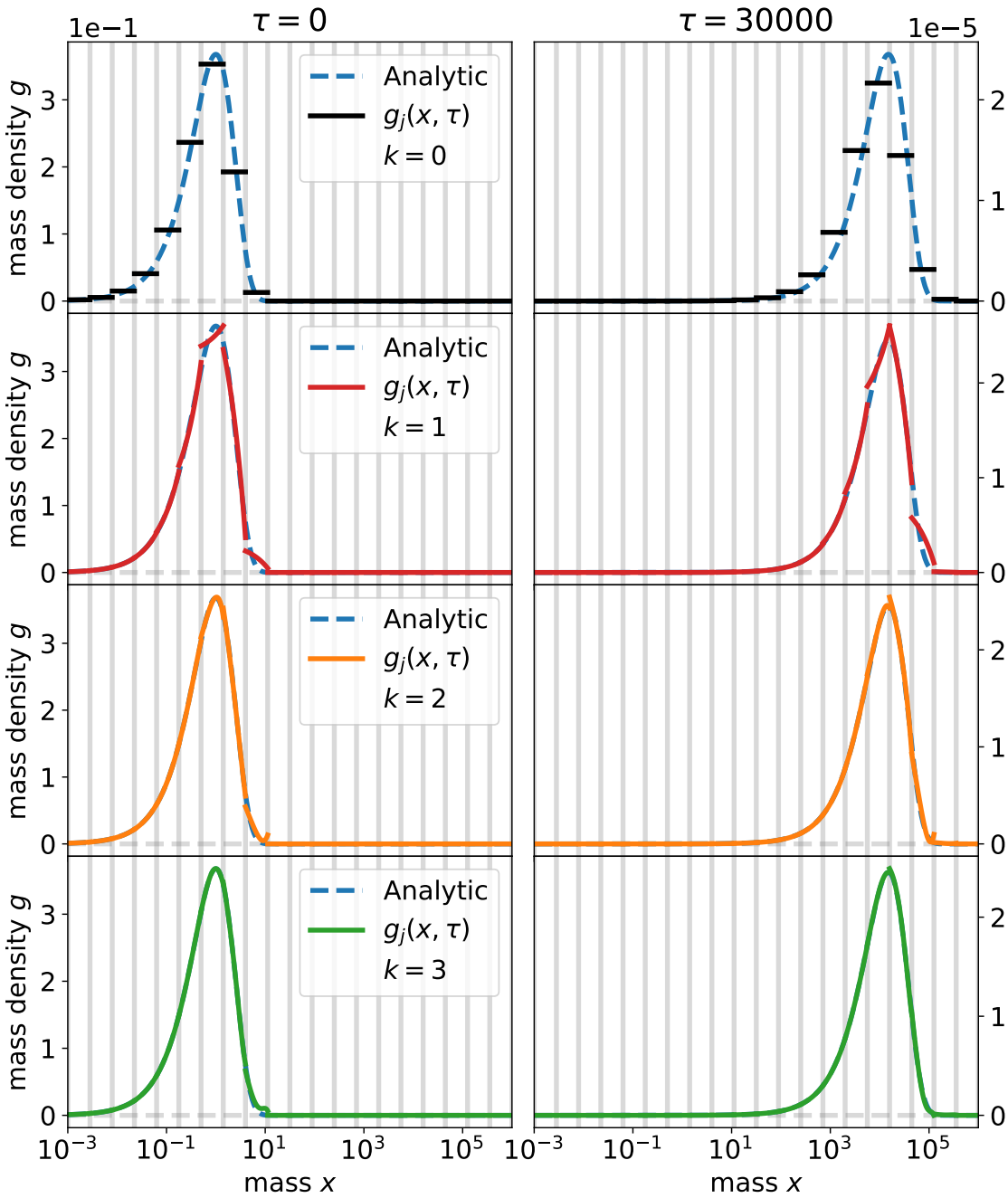

Figure 4.1: Test case, constant kernel: the numerical solution $g_j(x, \tau)$ is plotted for $N = 20$ bins and $k = 0, 1, 2, 3$ from $\tau = 0$ to $\tau = 30000$, and compared to the analytic solution $g(x, \tau)$. Vertical grey lines delimit the bins. The accuracy improves for a higher-order polynomials. Order 3 approximates the bump where the major part of the total mass is concentrated with accuracy of order $\sim 0.1\%$.

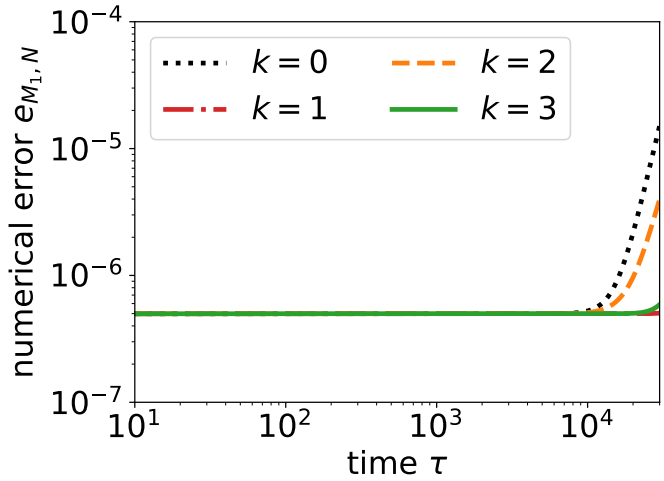

Figure 4.2: Test case, constant kernel: evolution of the numerical absolute error $e_{M_{1,N}}$ on the moment $M_{1,N}$ for $N = 20$ bins. The divergence at long time is explained by accumulation of errors due to numerical diffusion for even orders $k = 0$ and $k = 2$. The total mass is conserved at machine precision so far $\tau = 10^4$.

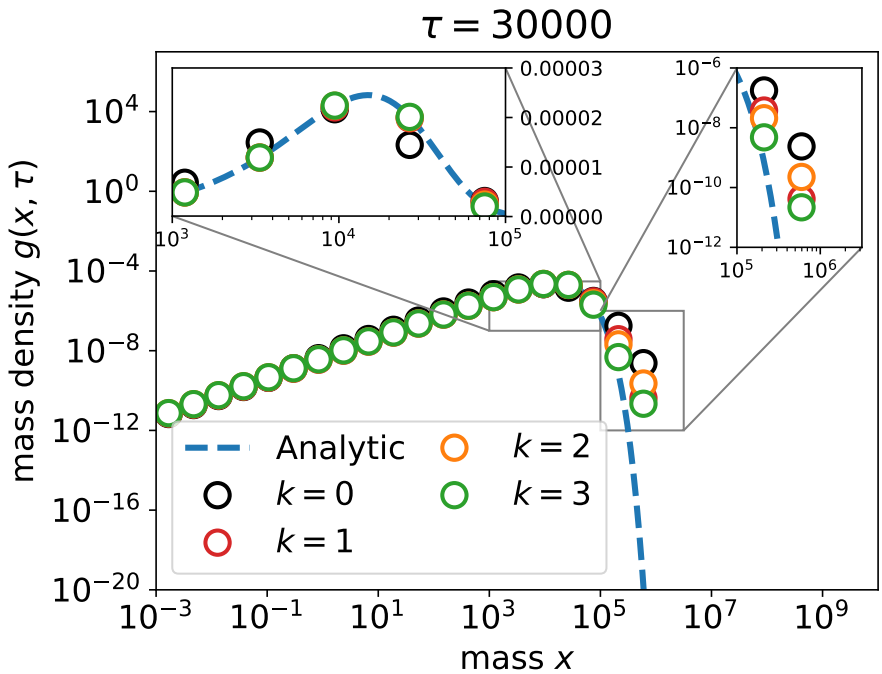

Figure 4.3: Test case, constant kernel: the numerical solution $g_j(x,\tau)$ is evaluated at the geometric mean $\hat{x}_j$ of each bin I_j.At the location of the maximum, orders $k = 1, 2, 3$ achieve an absolute error of $\sim 0.1 - 1\%$, to be compared with 30% obtained with $k = 0$. Accuracy in the exponential tail is improved by a factor 100 with $k = 3$ compared to $k = 0$.

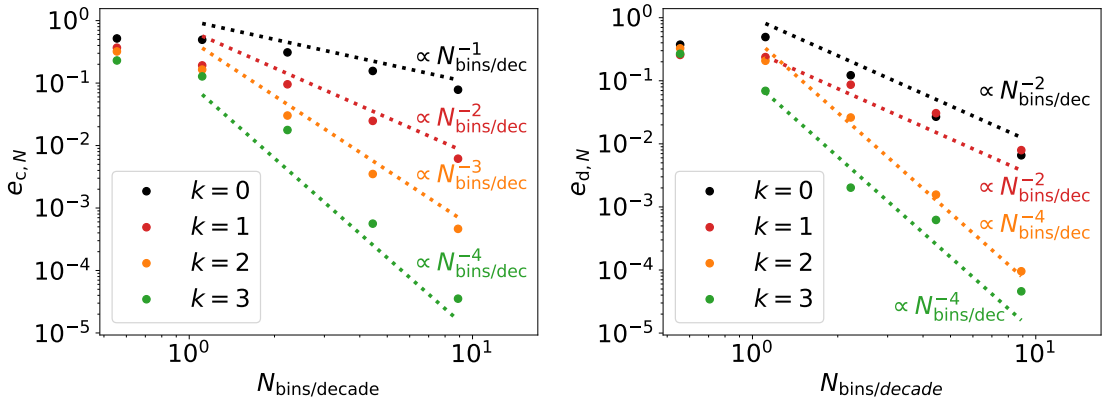

Figure 4.4: Test case, constant kernel: the continuous L^1 error $e_{c,N}$ and the discrete L^1 error $e_{d,N}$ are plotted as functions of the number of bins per decade. With $e_{c,N}$, the experimental order of convergence is EOC = $k+1$. With $e_{d,N}$, EOC = $k+1$ for polynomials of odd orders and EOC = $k+2$ for polynomials of even orders. The DG scheme achieves on $e_{d,N}$ an accuracy of 0.1% with more than 10 bins/decade for $k = 0, 1$, with ~ 9 bins/decade for $k = 2$ and with ~ 5 bins/decade for $k = 3$. An accuracy of 1% is achieved with ~ 9 bins/decade for $k = 0, 1$, with ~ 5 bins/decade for $k = 2$ and ~ 2 bins/decade for $k = 3$.

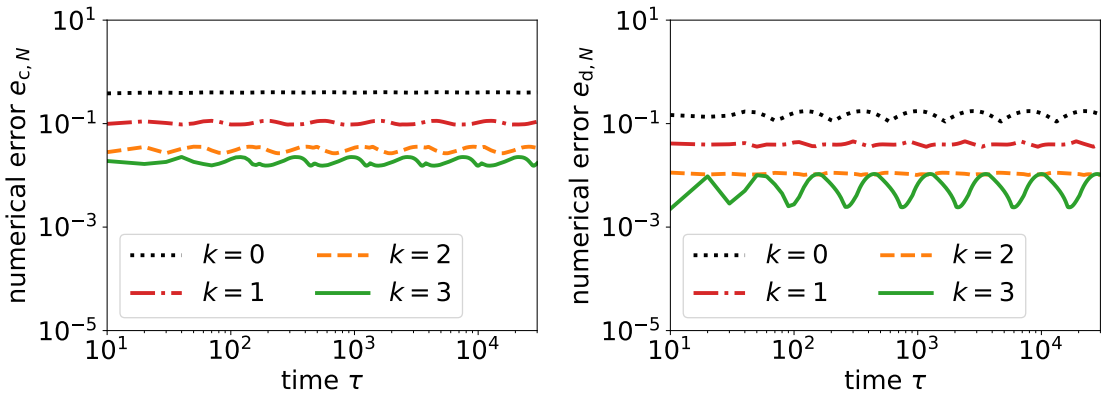

Figure 4.5: Test case, constant kernel: numerical errors $e_{c,N}$ with the L^1 continuous norm, $e_{d,N}$ with the discrete L^1 norm and. All these errors are calculated for $N = 20$. Errors remain bounded at large times.

EOC is of order $k+1$ on a geometric grid, similarly to Liu et al. (2019). With the discrete L^1 norm, the EOC is of order $k+2$ for odd polynomials, and $k+1$ for even polynomials. We recover second order of convergence (EOC=2) for the finite volume scheme with $k = 0$ that was predicted by Filbet and Laurencot (2004). Figure 4.4 shows that the expected accuracy of order $\sim 0.1\%$ on $e_{d,N}$ is achieved with more than 10 bins/decade for orders 0 and 1, with ~ 9 bins/decade for order 2 and with ~ 5 bins/decade for order 3. Accuracy of order $\sim 1\%$ is achieved with ~ 9 bins/decade for orders 0 and 1, with ~ 5 bins/decade for order 2, and with ~ 2 bins/decade for order 3.

4.3.1.4 *Stability in time*

Time evolution of the numerical errors $e_{c,N}$ and $e_{d,N}$ are shown in Figure 4.5. The results are shown for $N = 20$ bins for $k = 0, 1, 2, 3$ at time $\tau = 30000$, when particles of large masses have formed. We verify that $e_{c,N}$ and $e_{d,N}$ remain bounded.

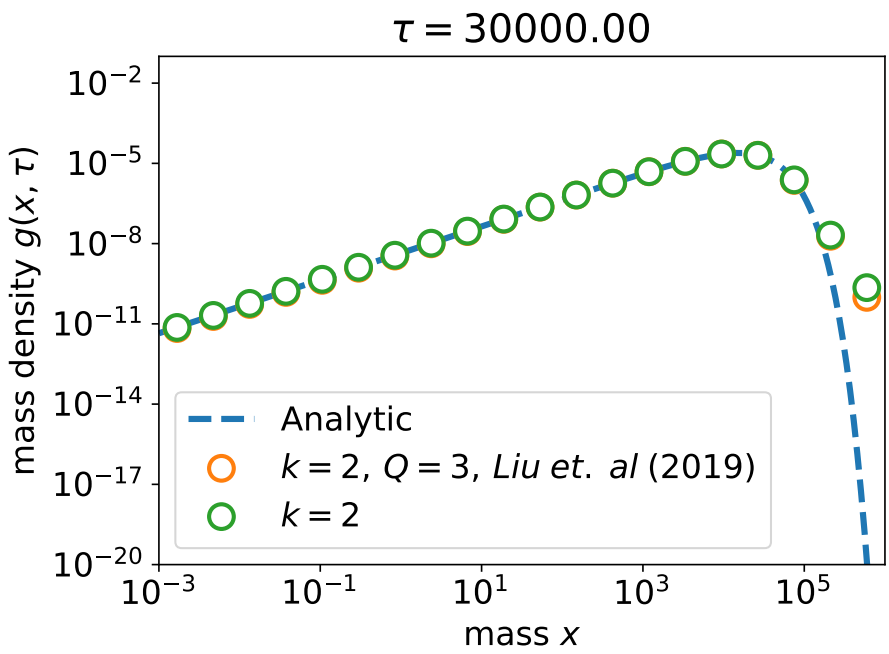

Figure 4.6: Test case, constant kernel: comparison with the scheme of Liu et al. (2019). Similar accuracies are reached, but being $\sim 4\times$ more effective due to numerical integration.

4.3.1.5 *Computational performance*

Figure 4.6 shows that similar accuracies are obtained with this scheme and the scheme described in Liu et al. (2019). Computational time is compared on a simulation with $N = 20$ bins, $k = 2$ and a final time $\tau = 30000$ after $\sim 10^3$ timesteps. The computational time for the Liu et al. (2019) scheme is around 16 seconds (real time). The computational time for this scheme is around 4 seconds (real time). An improvement of factor 4 is therefore achieved for the computational time by estimating integrals analytically.

4.3.2 *Additive kernel*

4.3.2.1 *Positivity and mass conservation*

Physically, the additive kernel means the frequency of collisions increases according to the size of particles. Massive particles are formed faster compared with constant kernel leading to greater values of mass density g_j for particles of large masses. The exponential decay is smoother during the time evolution compared to the constant kernel case. Figure 4.7 shows numerical solutions obtained for $N = 20$ bins and $k = 0, 1, 2, 3$ at time $\tau = 3$. The numerical solutions remains positive as grains grow. Figure 4.8 shows the evolution of the numerical absolute error $e_{M_1,N}$ on the first moment $M_{1,N}$. The total mass remains conserved to machine precision until $\tau = 1$.

4.3.2.2 *Accuracy of the numerical solution*

Figure 4.9 shows numerical solutions obtained at $\tau = 3$ on a logarithmic scale. Figure 4.9 reveals a strong numerical diffusion for order 0. Numerical errors are indeed integrated and diffused extremely efficiently towards large masses by the additive kernel. In this case, the mass density for large-masses particles is over-estimated by several orders of magnitude. High-order schemes reduce this numerical diffusion as expected. Figure 4.9 shows that around the maximum, schemes of order $k = 1, 2, 3$ provide errors of order

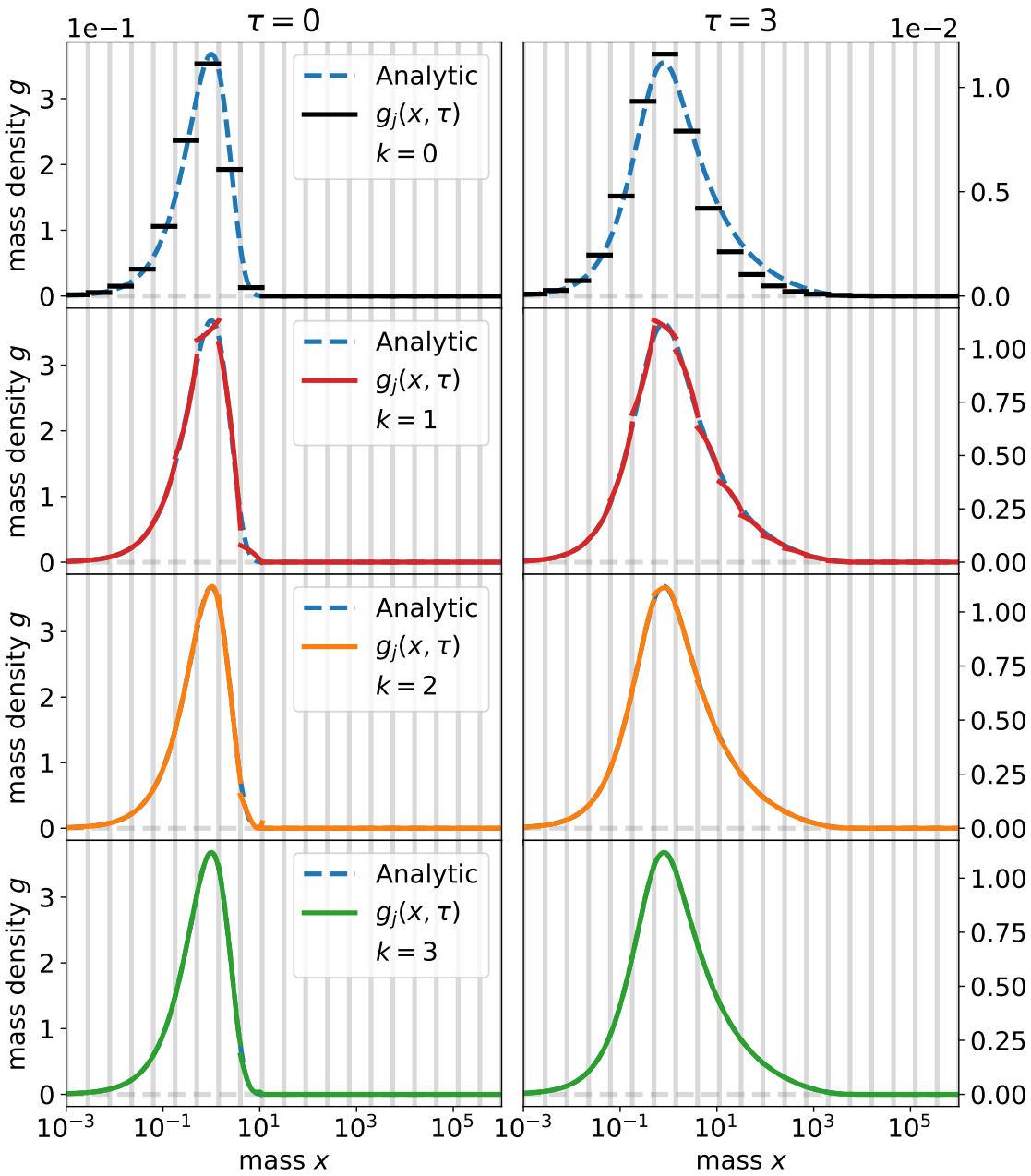

Figure 4.7: Test case, additive kernel: the numerical solution $g_j(x, \tau)$ is plotted for $N = 20$ bins and $k = 0, 1, 2, 3$ from $\tau = 0$ to $\tau = 3$, and compared to the analytic solution $g(x, \tau)$. Vertical grey lines delimit the bins. The accuracy improves for larger values of k. Order 3 approximates the bump where the major part of the mass is concentrated with accuracy of order $\sim 0.1\%$.

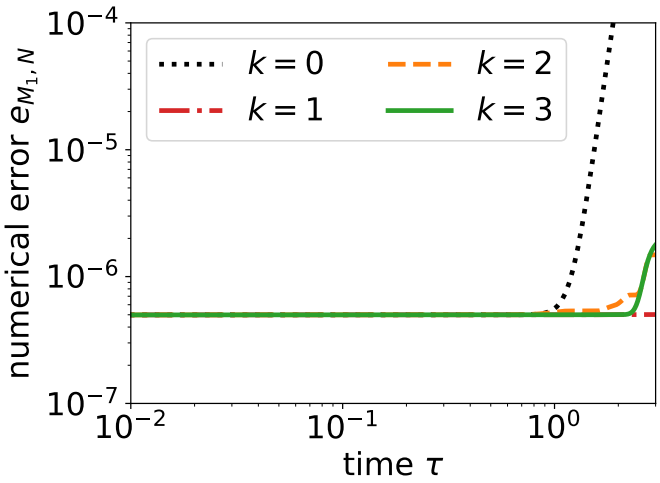

Figure 4.8: Test case, additive kernel: evolution of the numerical absolute error $e_{M_1,N}$ on the moment $M_{1,N}$ for $N = 20$ bins. The divergence at long times is explained by accumulation of errors due to numerical diffusion for orders $k = 0$, $k = 2$ and $k = 3$. Total mass is conserved at machine precision until $\tau = 1$.

$\sim 0.1 - 1\%$ when $k = 0$ generates errors of order $\sim 10\%$. Numerical diffusion is reduced in the exponential tail as the order of the scheme increases, up to reaching a gain of a factor ~ 10000 with order 3 compared to order 0.

4.3.2.3 *Convergence analysis*

Numerical errors are shown on Figure 4.10 at $\tau = 0.01$. With the continuous L^1 norm, the EOC is $k+1$ on a geometric grid with similar to Liu et al. (2019). With the discrete L^1 norm, the EOC is $k+2$ for odd polynomials and $k+1$ for even polynomials. Accuracy of order $\sim 0.1\%$ on $e_{d,N}$ errors are achieved with more than 10 bins/decade for order 0 and 1, with ~ 9 bins/decade for orders 2 and 3. Accuracy of order $\sim 1\%$ is achieved with ~ 9 bins/decade for orders 0 and 1, with ~ 5 bins/decade for order 2 and ~ 2 bins/decade for order 3.

4.3.2.4 *Stability in time*

Evolution of the numerical errors $e_{c,N}$ and $e_{d,N}$ are shown in Figure 4.11. The results are shown for $N = 20$ bins for $k = 0, 1, 2, 3$ at $\tau = 3$, when particles with large masses have formed. At order 0, $e_{c,N}$ (resp. $e_{d,N}$) increases significantly after $\tau \approx 5 \cdot 10^{-1}$ (resp. $\tau \approx 10^{-1}$). On the contrary, $e_{c,N}$ and $e_{d,N}$ remain bounded for longer times at orders 1, 2 and 3.

4.3.2.5 *Computational performance*

Computational time is compared to Liu et al. (2019) on a simulation with $N = 20$ bins, $k = 1$ and a final time $\tau = 3$. Figure 4.6 shows similar accuracy for both schemes. The computational time for the Liu et al. (2019) scheme is around 3 seconds (real time) for a number of Gauss quadrature points $Q = 2$. The computational time for this scheme is 1 second, providing an improvement by a factor 3. Figure 4.12 also shows that for the additive kernel, the Liu scheme with $Q = 2$ is counter-intuitively more accurate than for $Q = 16$ and the DG scheme. This result can be explained by a serendipitous compensation of errors when approximating the integrals with a Gauss quadrature of low order.

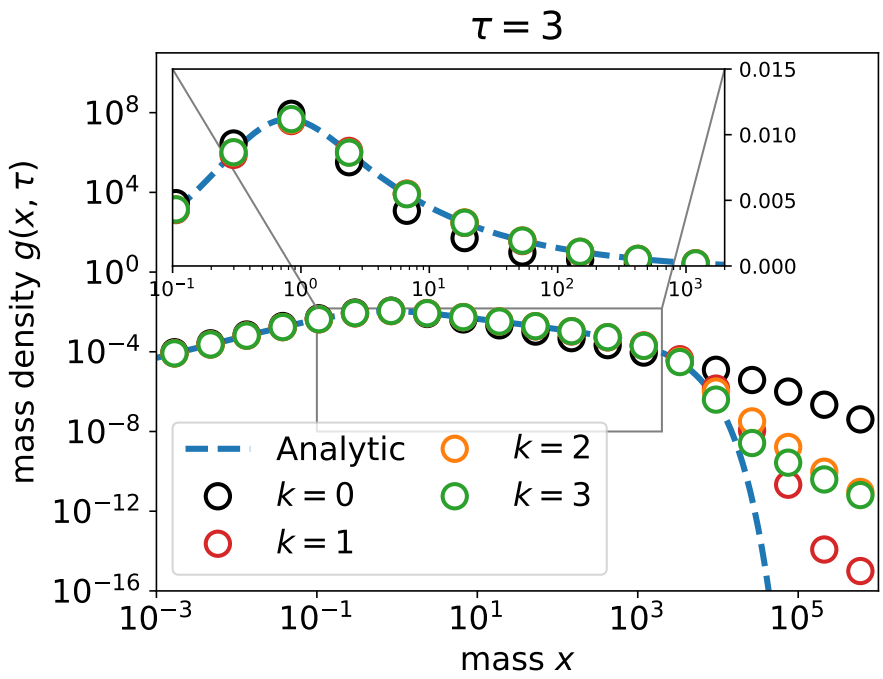

Figure 4.9: Test case, additive kernel: At the location of the maximum, orders $k = 1, 2, 3$ achieve an absolute error of $\sim 0.1 - 1\%$, to be compared with 10% obtained with $k = 0$. Accuracy in the exponential tail is improved by a factor 10000 by $k = 3$ compared to $k = 0$.

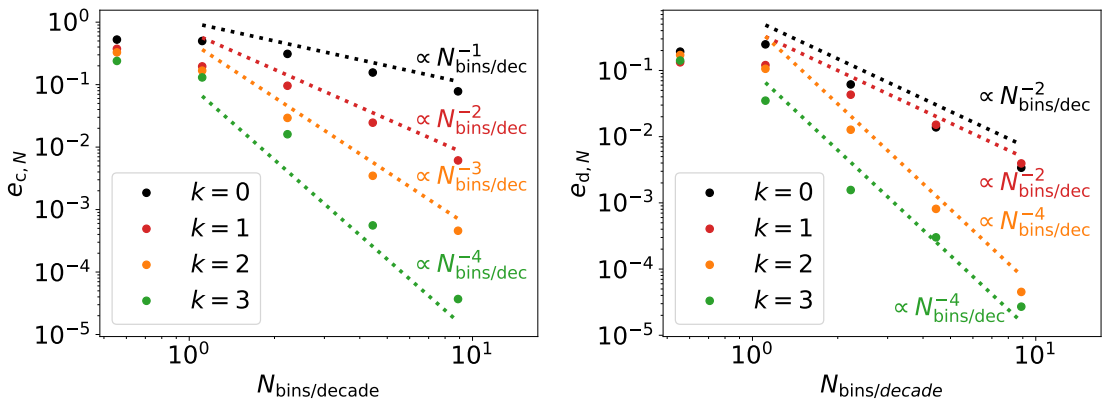

Figure 4.10: Test case, additive kernel: similar to Figure 4.4. The DG scheme achieves on $e_{d,N}$ an accuracy of order 0.1% with more than 10 bins/decade for $k = 0, 1$, with ~ 5 bins/decade for $k = 2, 3$. An accuracy of order 1% is achieved with ~ 9 bins/decade for $k = 0, 1$, with ~ 5 bins/decade for $k = 2$ and with ~ 2 bins/decade for $k = 3$.

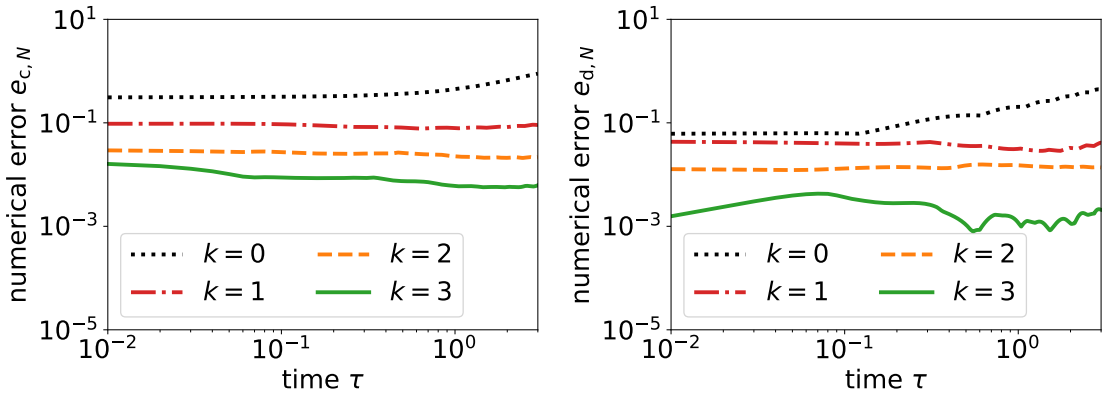

Figure 4.11: Test case, additive kernel: numerical errors $e_{c,N}$ with the L^1 continuous norm, $e_{d,N}$ with the discrete L^1 norm. All these errors are calculated for $N = 20$. Errors remain bounded at large times for orders $k = 1, 2, 3$.

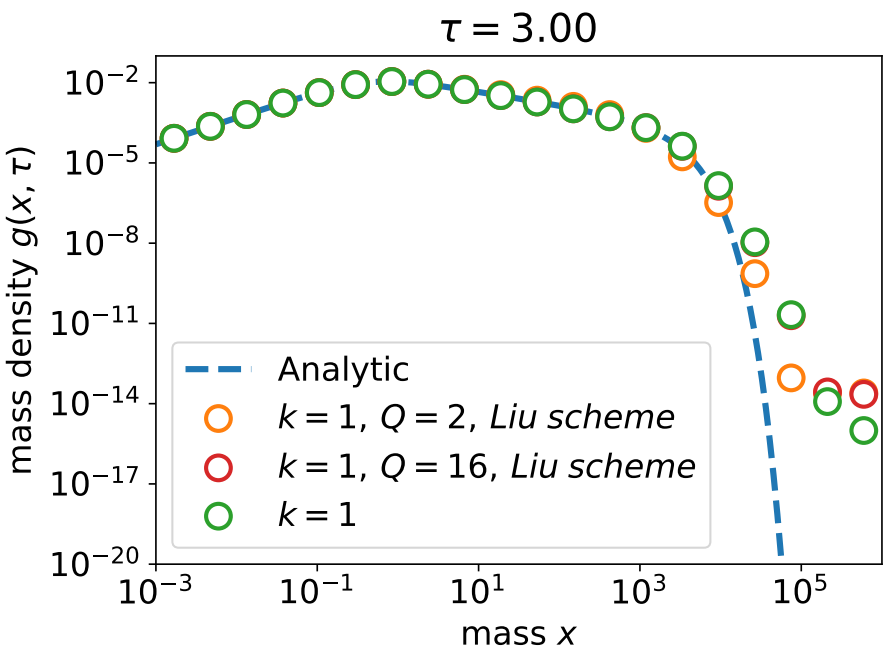

Figure 4.12: Test case, additive kernel: comparison with the scheme of Liu et al. (2019). Unexpected accuracy occurs for integral estimates with $Q = 2$ Gauss points due to serendipitous error compensations. Our algorithm is $\sim 3\times$ more effective due to analytical integration compared to the Liu scheme with $Q = 2$.

4.3.3 *Multiplicative kernel*

4.3.3.1 *Positivity and mass conservation*

Physically, the multiplicative kernel means the frequency of collisions increases according to the size of particles. Massive particles are formed faster compared with additive kernel leading to greater values of mass density g_j for particles of large masses. The mass density for lighter particles decreases quickly during time. The exponential decay is slower during the time evolution. Figure 4.13 shows the numerical solutions obtained for $N = 20$ bins and $k = 0, 1, 2, 3$ after $\tau = 100$. The numerical solutions remain positive as grain grow. Figure 4.14 shows the evolution of $e_{M_1,N}$. Total mass remains conserved to machine precision until $\tau < 1$. At $\tau = 1$, gelation occurs, particles with infinite mass are formed (McLeod, 1962; Ernst et al., 1984; Filbet and Laurencot, 2004) and total mass is no longer conserved anymore.

4.3.3.2 *Accuracy of the numerical solution*

Figure 4.15 shows the numerical solution for the multiplicative kernel at $\tau = 100$. Accuracy of order $\sim 0.1\%$ is obtained at all orders, even $k = 0$. Physically, growth is effective enough for advection in the mass space to be more efficient than numerical diffusion.

4.3.3.3 *Convergence analysis*

Numerical errors are shown on Figure 4.16 at $\tau = 0.01$. With the continuous L^1 norm, the EOC is $k + 1$ on a geometric grid with similar to Liu et al. (2019). With the discrete L^1 norm, the EOC is $k + 2$ for odd polynomials and $k + 1$ for even polynomials. Accuracy of order $\sim 0.1\%$ on $e_{d,N}$ errors are achieved with ~ 15 bins/decade for $k = 0, 1$, with ~ 7 bins/decade for $k = 2$, and with ~ 4 bins/decade for $k = 3$. Accuracy of order $\sim 1\%$ is achieved with ~ 7 bins/decade for $k = 0, 1$, with ~ 2 bins/decade for $k = 2$, and with ~ 1 bins/decade for $k = 3$.

4.3.3.4 *Stability in time*

The evolution of the numerical errors $e_{c,N}$ and $e_{d,N}$ are shown in Figure 4.17. The results are shown for $N = 20$ bins fo $k = 0, 1, 2, 3$ at time $\tau = 100$, when particles with large masses have formed. We observe that $e_{c,N}$ and $e_{d,N}$ remain bounded, even after the occurence of gelation at $\tau = 1$.

4.3.3.5 *Computational performance*

Figure 4.18 shows similar accuracies for the Liu et al. (2019) scheme and our implementation. With $k = 2$, the computational time for the Liu et al. (2019) scheme is around 8 minutes for a number of Gauss quadrature points $Q = 3$. The computational time is for this scheme 1 minute and 40 seconds, providing an improvement by a factor 5.

4.4 FUTURE DEVELOPMENTS FOR THE DISCONTINUOUS GALERKIN SCHEME

Benchmarks shown that our DG scheme is able to estimate accurately the analytic solutions for constant, additive and multiplicative kernels. The DG scheme presented in Section 3.2.1 involves polynomials of high-order, implying issues with differences of large real numbers. Order $k = 3$ appears as a maximum limit for the order of the scheme

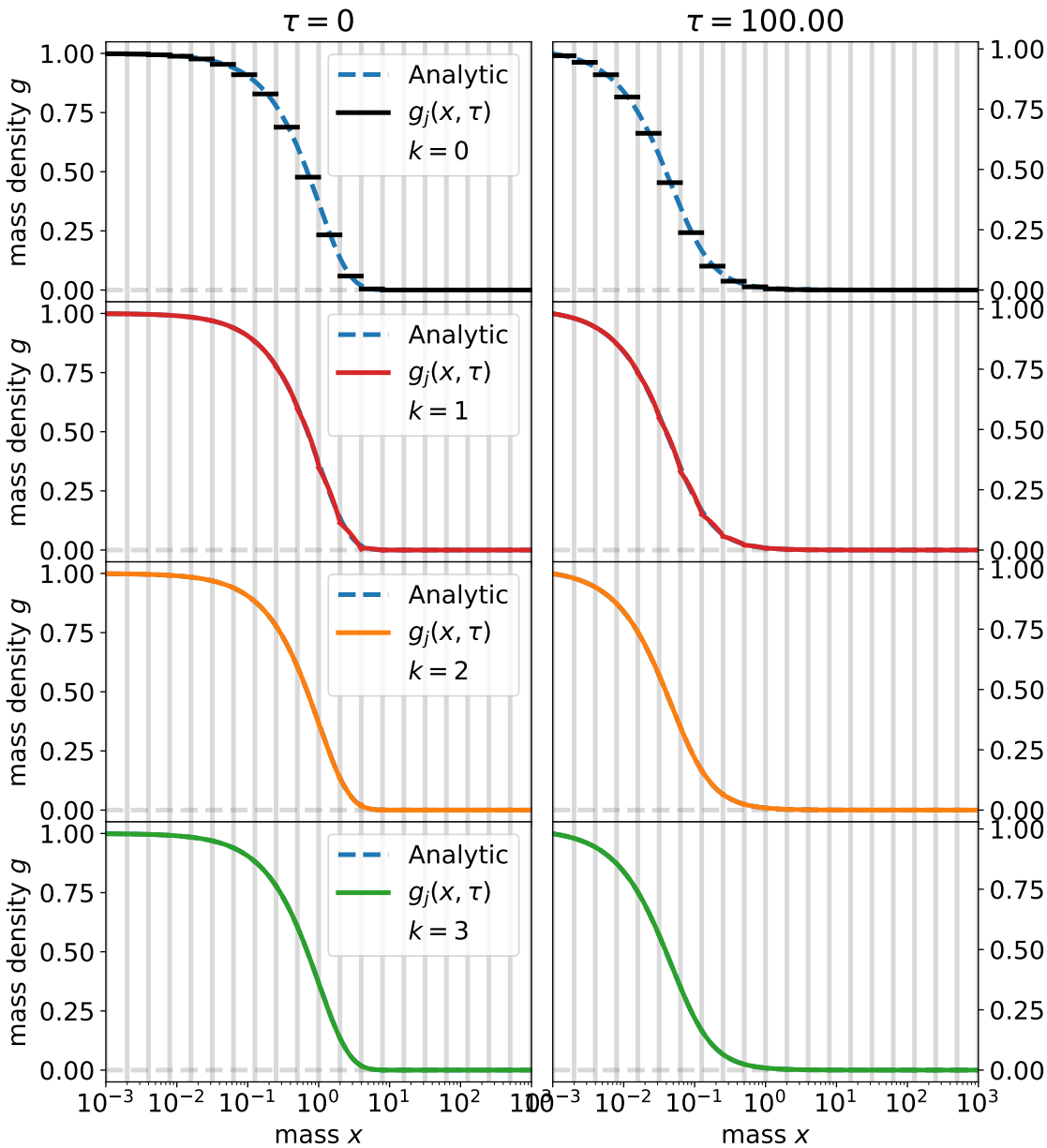

Figure 4.13: Test case, multiplicative kernel: numerical solution $g_j(x, \tau)$ is plotted for $N = 20$ bins for $k = 0, 1, 2, 3$ from $\tau = 0$ to $\tau = 100$ and compared to the analytic solution $g(x, \tau)$. Vertical grey lines delimit the bins. Accuracy of order $\sim 0.1\%$ is achieved at all orders.

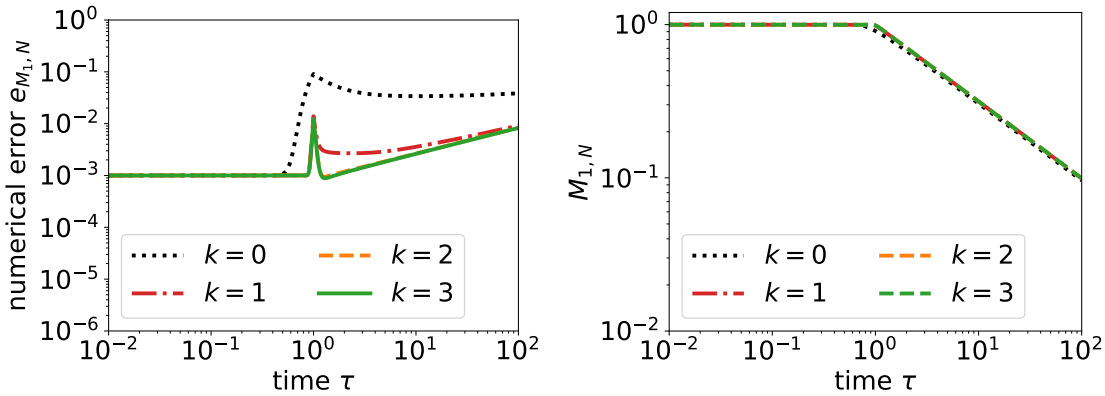

Figure 4.14: Test case, multiplicative kernel: evolution of the numerical absolute error $e_{M_1,N}$ on the moment $M_{1,N}$ for $N = 20$ bins. Mass is conserved anymore when gelation occurs at $\tau = 1$.

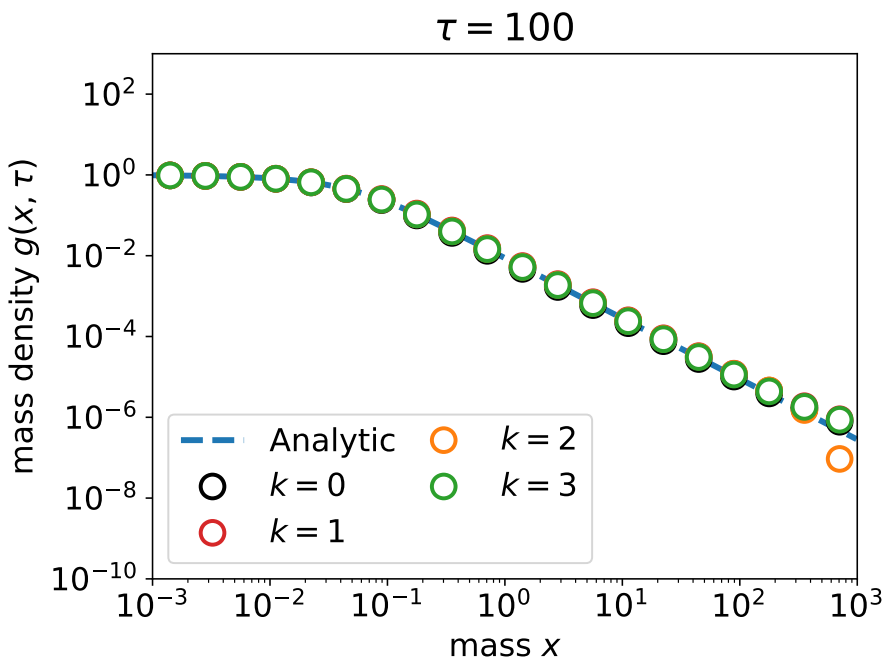

Figure 4.15: Test case, multiplicative kernel: Accuracy of order $\sim 0.1\%$ is achieved at any order. Growth is so efficient than it overtakes numerical diffusion.

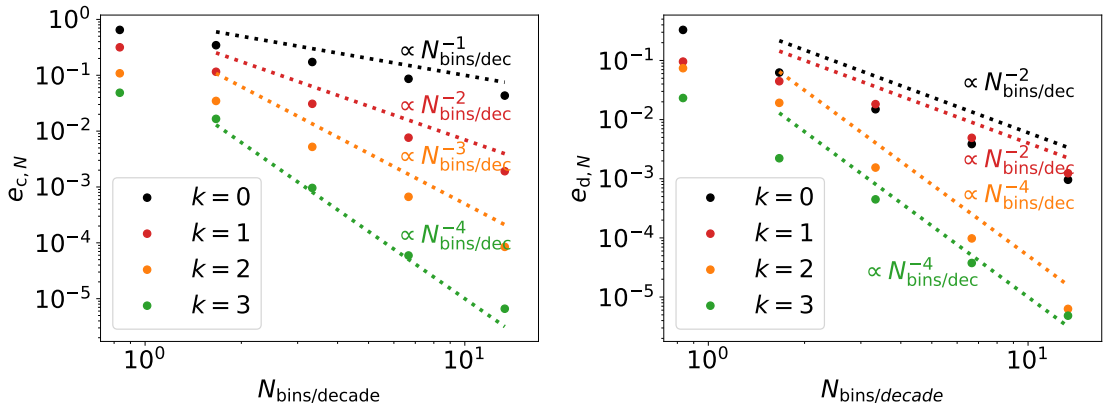

Figure 4.16: Test case, multiplicative kernel: the continuous L^1 error $e_{c,N}$ and the discrete L^1 error $e_{d,N}$ are plotted as functions of the number of bins per decade. With $e_{c,N}$, the experimental order of convergence is EOC $= k+1$. With $e_{d,N}$, EOC $= k+1$ for polynomials of odd orders and EOC $= k+2$ for polynomials of even orders. The DG scheme achieves on $e_{d,N}$ an accuracy of 0.1% with ~ 15 bins/decade for $k = 0, 1$, with ~ 7 bins/decade for $k = 2$ and with ~ 4 bins/decade for $k = 3$. An accuracy of 1% is achieved with ~ 7 bins/decade for $k = 0, 1$, with ~ 2 bins/decade for $k = 2$ and with ~ 1 bins/decade for $k = 3$.

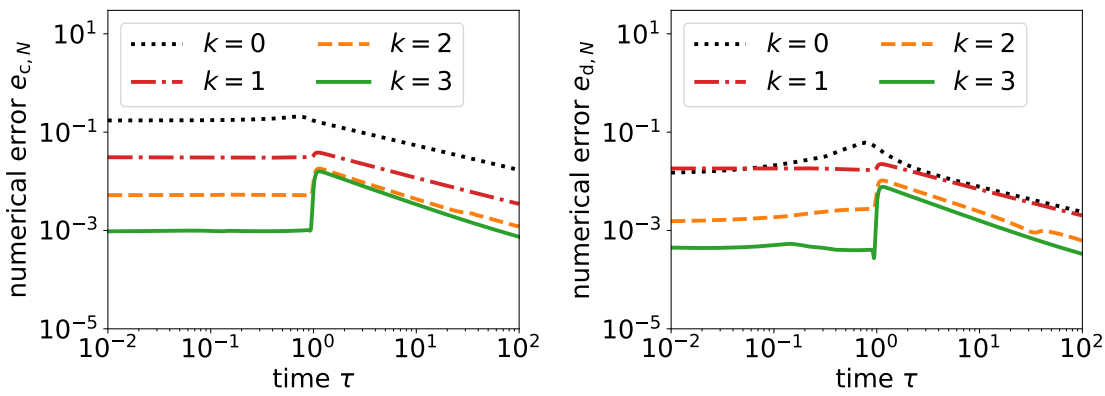

Figure 4.17: Test case, multiplicative kernel: numerical errors $e_{c,N}$ with the L^1 continuous norm, $e_{d,N}$ with the discrete L^1 norm. All these errors are calculated for $N = 20$. Errors remain bounded at large times.

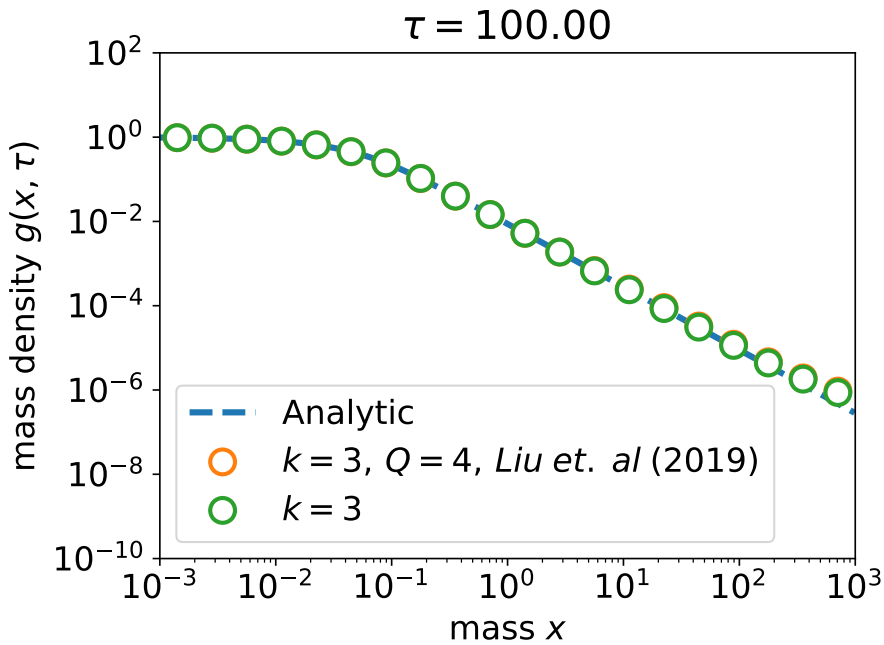

Figure 4.18: Test case, multiplicative kernel: comparison between the numerical solutions provided by this scheme and the scheme of Liu et al. (2019). Similar accuracies are reached, but being $\sim 5\times$ more effective due to analytical integration.

in its current form in practice. The derivation of the analytic expressions for the ballistic kernel are in progress. In a next step, the first 3D simulation of a dusty disc will be performed by interfacing our algorithm with the code `PHANTOM`.

In a short future, we plan to extend the scheme to further add relevant physics and gain in accuracy and computational efficiency: i) the ballistic kernel, ii) the fragmentation flux, iii) taking advantage of more ingenious time-stepping (e.g. Carrillo and Goudon (2004) and Goudon et al. (2013), iv) adopt a more relevant choice for the basis (e.g. Soong (1974)), v) an adapted distribution of bins, vi) the coagulation among grains of different composition, vii) the agglomerate size distribution. Only the ballistic kernel is presented here, the other developments are detailed in Chapter 7.

4.4.1 *Ballistic kernel*

The most relevant kernel for astrophysics is the ballistic kernel (Section 2.2.3). The analytic derivation of the flux follows the same procedure explained in Section 3.2.2. The conservative formulation of the flux, i.e. $F^{\mathrm{c}}_{\mathrm{coag}}$, is used. The numerical flux writes

$$\begin{aligned} &F^{\mathrm{c}}_{\mathrm{coag}}[\tilde{g}](x,t) = \\ &\sum_{l'=1}^{N}\sum_{i'=0}^{k}\sum_{l=1}^{N}\sum_{i=0}^{k} g^{i'}_{l'}(t) g^{i}_{l}(t) \\ &\int_{x_{\min}}^{x}\int_{x-u+x_{\min}}^{x_{\max}-u+x_{\min}} \frac{\mathcal{K}_{\mathrm{B}}(u,v)}{v}\phi_{i'}(\xi_{l'}(u))[\theta(u-x_{l'-1/2})-\theta(u-x_{l'+1/2})] \\ &\qquad\qquad \phi_{i}(\xi_{l}(v))[\theta(v-x_{l-1/2})-\theta(v-x_{l+1/2})]\mathrm{d}v\mathrm{d}u, \end{aligned} \tag{4.8}$$

where $\mathcal{K}_{\mathrm{B}}(u,v) = \sigma(u,v)\Delta v(u,v)$ is the ballistic kernel (see Section **??**). In equation 4.8, the probability of sticking collision β is taken equal to 1. The ballistic kernel writes in detail

$$\mathcal{K}_{\mathrm{B}}(u,v) \sim (u^{1/3}+v^{1/3})^2\Delta v(u,v) = (u^{2/3}+2u^{1/3}v^{1/3}+v^{2/3})\Delta v(u,v). \tag{4.9}$$

For the analytical derivations, the ballistic kernel is written in the following form

$$\begin{cases} \mathcal{K}_{\mathrm{B}}(u,v) \sim \left(\sigma_1^1(u)\sigma_2^1(v)+\sigma_1^2(u)\sigma_2^2(v)+\sigma_1^3(u)\sigma_2^3(v)\right)\Delta v(u,v), \\ \sigma_1^1(u) \equiv u^{2/3},\ \sigma_2^1(v) \equiv 1, \\ \sigma_1^2(u) \equiv 2u^{1/3},\ \sigma_2^2(v) \equiv v^{1/3}, \\ \sigma_1^3(u) \equiv 1,\ \sigma_2^3(v) \equiv v^{2/3}. \end{cases} \tag{4.10}$$

Large-scale values of Δv are provided by 2D piecewise constant functions from hydrodynamic codes. In discs, the Δv function encompasses radial drift, vertical settling and turbulence at large scales. $\Delta v(u,v)$ writes

$$\begin{aligned} &\forall (u,v) \in [x_{\min}, x_{\max}]^2, \\ &\Delta v(u,v) = \sum_{l'=1}^{N}\sum_{l=1}^{N} \Delta v_{l',l}\left[\theta(u-x_{l'-1/2})-\theta(u-x_{l'+1/2})\right]\left[\theta(v-x_{l-1/2})-\theta(v-x_{l+1/2})\right]. \end{aligned} \tag{4.11}$$

Models of differential velocities are also used to model sub-grid small-scale values of Δv (Brownian motion, dusty turbulence at small scales). Shall these kernels not be integrable, we will estimate them with an appropriate interpolation.
As such, the conservative flux writes

$$F^{\mathrm{c}}_{\mathrm{coag}}[\tilde{g}](x,t) = \sum_{l'=1}^{N}\sum_{i'=0}^{k}\sum_{l=1}^{N}\sum_{i=0}^{k} g_{l'}^{i'}(t)g_l^i(t)T(x,x_{\min},x_{\max},i',i,l',l), \tag{4.12}$$

with

$$\begin{aligned} &T(x,x_{\min},x_{\max},i',i,l',l) \equiv \Delta v_{l',l} \\ &\times\Bigg[\int_{x_{\min}}^{x}\int_{x-u+x_{\min}}^{x_{\max}-u+x_{\min}} \sigma_1^1(u)\sigma_2^1(v)\phi_{i'}(\xi_{l'}(u))[\theta(u-x_{l'-1/2})-\theta(u-x_{l'+1/2})] \\ &\qquad\qquad \frac{\phi_i(\xi_l(v))}{v}[\theta(v-x_{l-1/2})-\theta(v-x_{l+1/2})]\mathrm{d}v\mathrm{d}u \\ &\quad + \text{symmetric terms in } \sigma_1^2(u)\sigma_2^2(v) \\ &\quad + \text{symmetric terms in } \sigma_1^3(u)\sigma_2^3(v)\Bigg]. \end{aligned} \tag{4.13}$$

The procedure in Section 3.2.3 with the ballistic kernel is used to derive the expression of the integral of the flux $\mathcal{F}^{\mathrm{c}}_{\mathrm{coag}}[\tilde{g}]$. All the derivation are calculated with MATHEMATICA.

4.4.1.1 *First test with constant piecewise approximation*

First test has been performed with the ballistic kernel by using the expression of the flux from Filbet and Laurencot (2004). For constant piecewise approximation of g, the numerical scheme only need F^c_{coag} which writes

$$F^c_{\text{coag}}[g](x_{j+1/2},t) = \sum_{l'=1}^{j} \int_{I_{l'}} g(u,t) \int_{x_{j+1/2}-u+x_{\min}}^{x_{\max}-u+x_{\min}} \frac{\mathcal{K}(u,v)}{v} g(v,t)\mathrm{d}v\mathrm{d}u, \tag{4.14}$$

where $x_{min} = 0$. As $u \in [x_{l'-1/2}, x_{l'+1/2}]$, Δv writes

$$\Delta v(u,v) = \sum_{l=1}^{N} \Delta v_{l',l} \left[\theta(v - x_{l-1/2}) - \theta(v - x_{l+1/2})\right]. \tag{4.15}$$

By approximating g by $\tilde{g}$, the conservative flux writes

$$F^c_{\text{coag}}[\tilde{g}](x_{j+1/2},t) = \sum_{l'=1}^{j} \sum_{i'=0}^{k} \sum_{l=1}^{N} \sum_{i=0}^{k} g^{i'}_{l'}(t) g^{i}_{l}(t) T(x_{j+1/2}, x_{\min}, x_{\max}, i', i, l', l), \tag{4.16}$$

with

$$\begin{aligned} &T(x_{j+1/2}, x_{\min}, x_{\max}, i', i, l', l) \equiv \Delta v_{l',l} \\ &\Bigg[\int_{I_{l'}} \int_{x_{j+1/2}-u+x_{\min}}^{x_{\max}-u+x_{\min}} \sigma^1_1(u)\sigma^1_2(v)\phi_{i'}\left(\xi_{l'}(u)\right) \frac{\phi_i\left(\xi_l(v)\right)}{v} \left[\theta(v - x_{l-1/2}) - \theta(v - x_{l+1/2})\right] \mathrm{d}v\mathrm{d}u \\ &\qquad + \text{symmetric terms in } \sigma^2_1(u)\sigma^2_2(v) \\ &\qquad + \text{symmetric terms in } \sigma^3_1(u)\sigma^3_2(v) \Bigg]. \end{aligned} \tag{4.17}$$

The development of term T and the flux are detailed in Appendix c.1.

The test is performed for a typical dusty disc (Laibe et al., 2008) where micron-in-size silicate grains are located at 1 AU for the initial condition. The parameters of the discs are $\alpha = 0.003$, $\epsilon_0 = 0.01$ and $H/r = 0.05$. The differential velocity between grains is obtain from turbulence (Stepinski and Valageas, 1997),

$$\Delta v_{i,j} = \sqrt{\alpha c_s^2 \left(\frac{1}{\mathrm{Sc}_i} + \frac{1}{\mathrm{Sc}_j} - \frac{2}{\mathrm{Sc}_i \mathrm{Sc}_j}\right)}, \tag{4.18}$$

where i and j denote grains and Sc is the Schmidt number of the flow which estimates the effect of gas turbulence on the grains. The Schmidt number is defined as

$$\mathrm{Sc} \approx (1 + \Omega_k t_s). \tag{4.19}$$

Figure 4.19 shows grains of size 10cm are formed after 15120 years. Pebble formation is consistent with the results from in Laibe et al. (2008). These grains represent the majority of the dust mass. The formation of these grains is faster than in Laibe et al. (2008), as expected with growth only with 15 bins. Moreover, all the mass is transferred to the last bin, centimetre-in-size grains, due to the use of the conservative flux. This explains the rapid formation of centimetre-in-size grains. Over-diffusion is highlighted for simulations with 8 bins compared to the one with 30 bins. Orders 1, 2 and 3 are in progress. We expect to have similar result than $k = 0, N = 30$ but with $k = 3, N = 8$.

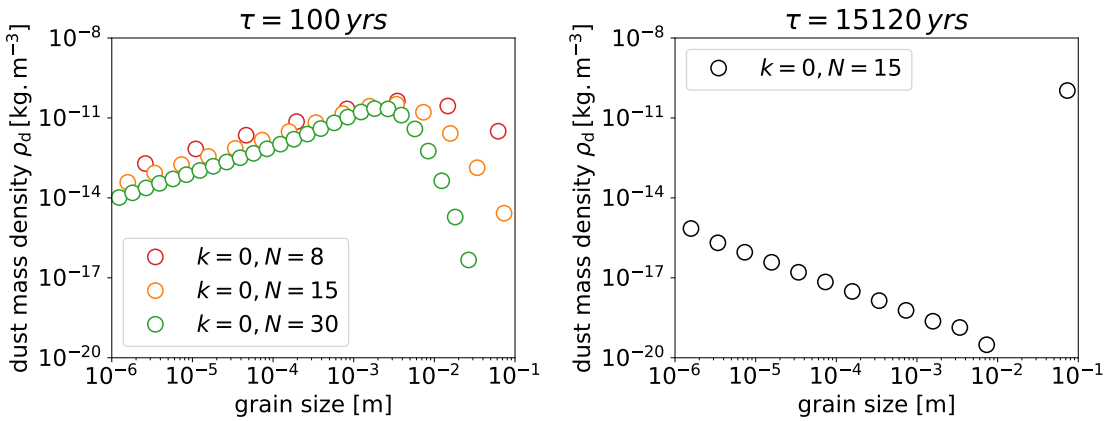

Figure 4.19: Test case for ballistic kernel with only growth and constant polynomial approximation. Left: Test of convergence in number of bins for order 0 at $\tau = 100$ years. A factor ~ 1000 is reached between 8 bins and 30 bins when centimetre-in-size grains form. Orders 1, 2 and 3 are in progress. Right: Simulation so far $\tau = 15120$ years where grains of size 10cm form. These grains represent almost all the dust mass at this time.

4.5 SUMMARY

We benchmark our high-order solver against the analytic solutions presented in Chapter 2. As expected accuracy increases with the order of the scheme (we tested orders 0, 1, 2 and 3). At all orders for every tests performed, positivity and mass conservation are satisfied rigorously. For the three kernels, the DG scheme of order 3 can achieve an improvement in accuracy of a factor at least 100. The additive kernel is a sensitive test case to analyse the performance of the code, since it behaves as astrophysical kernels. For this kernel, the required accuracy of 0.1% for polynomials of order 3 with ~ 5 bins/decade. An accuracy of 1% is achieved for order 3 with ~ 2 bins/decade. Generically, high accuracy is achieved with a low number of bins. We compare execution times with the ones found for the DG scheme proposed by Liu et al. (2019). An improvement of factor at least 3 is achieved for the computational time with the three kernels. Our high-order solver is able to solve efficiently and accurately the Smoluchowski coagulation equation with a small number of bins. Therefore, the dust growth over 30 orders in mass can be studied accurately and in a tractable computational time with our algorithm. This includes kernels relevant for astrophysics. A first test with the ballistic kernel has been performed with $k = 0$, the results are consistent with Laibe et al. (2008).

In a next future, ballistic kernel and fragmentation flux will be added in the algorithm to perform the first 3D simulation of a dusty disc including dust growth/fragmentation by interfacing our algorithm with the code `PHANTOM`. In parallel our solver will be optimised by adding such as an adapted polynomials basis, an adapted distribution of bins and by using a rescaling of the Smoluchowski equation in order to increase further the accuracy and the efficiency. Details on the future developments are given in Chapter 7.

5

DUST SETTLING FOR SMALL GRAINS IN PROTOPLANETARY DISCS

"Another one bites the dust" – Queen

5.1 Context . . . 81
5.2 Introduction . . . 82
5.3 Physical model . . . 83
  5.3.1 Balance of forces . . . 83
  5.3.2 Modelling dusty turbulence . . . 86
  5.3.3 Link with previous works . . . 89
5.4 Mathematical analysis . . . 93
  5.4.1 Rescaling . . . 93
  5.4.2 Asymptotic expansions . . . 94
  5.4.3 Steady-state dust distributions . . . 96
5.5 Numerical results . . . 97
  5.5.1 Numerical scheme . . . 97
  5.5.2 Numerical dust distributions . . . 100
5.6 Discussion . . . 101
5.7 Conclusion . . . 101

5.1 CONTEXT

Dust settling refers to the vertical motion of a grain towards the mid-plane of a disc in vertical hydrostatic equilibrium. This motion is due to a combination of the vertical component of the gravity from the central star and gas drag, see Figure 5.1. On top of these two forces is added a stochastic contribution from the turbulence of the gas, which stirs particles out of the mid-plane. Dust settling, therefore, fixes the vertical distribution of grains in disc. According to Mie theory, the size of the scattering particles is comparable to the wavelength of the emitted light. Critically, this distribution has a direct effect on the interaction between the radiation emitted by the star and the disc via the grains. The Dubrulle et al. (1995) model is considered as state-of-the-art to model dust settling in discs. In this model, the disc's turbulence is treated as a white noise and inertia of particles is neglected. This asssumption is correct in the mid-plane of the disc, but not in the top layers. The use of the Dubrulle et al. (1995) model has already been a strong improvement compared to a uniform distribution of grains in the disc. After a typical settling time, the grains converge to the mid-plane and change the amount of light intercepted by the disc at the different wavelengths. This is a key parametrisation for disc modelling.

During my M1 internship supervised by Dr. G. Laibe, we aimed to go beyond the Dubrulle et al. (1995) model. An improved model has been developed to take into account altogether the stratification in density of the disc and turbulent correlations. The purpose is to obtain the vertical distribution of dust grains, by including the stratification in density of the disc self-consistently. I studied the evolution of the grains numerically along the vertical axis from the new model. This study aimed at better constraining observationnal data provided by ALMA or SPHERE and the future James Webb Telescope

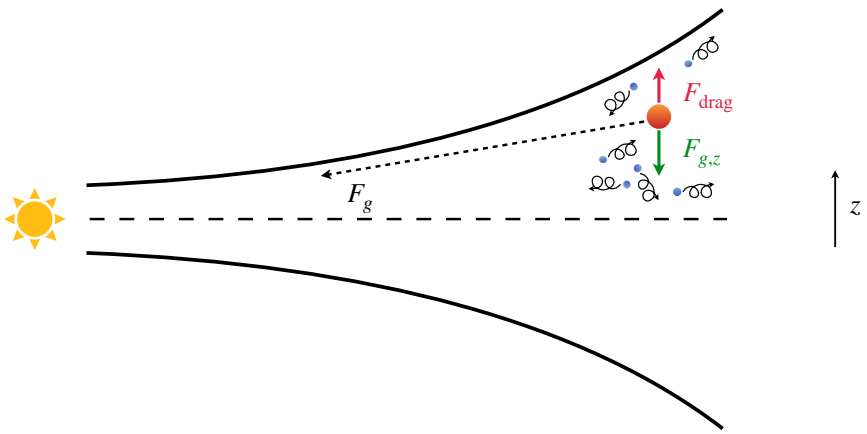

Figure 5.1: Illustration of dust settling of grains in discs. The vertical motion of grains (in orange) is due to the balance between the gas drag force and the vertical component of the gravity from the star. The blue spheres represent the stochastic fluctuation of the gas around the grain.

(JWST). However, we were limited by the existing analytical and numerical methods for stochastic systems to extract a definitive conclusion from this study.

During my Ph.D. Thesis, I collaborated with Dr. G. Laibe and Dr. C-E. Bréhier to follow-up the work from my M1 internship. The aim was to derived an analytic formula for the distribution of small grains that encompass gas stratification, dust inertia and finite correlation times. This analytic formula is then validated against numerical simulations. My contribution to this work was to develop the code to solve the system of stochastic differential equations and perform the convergence analysis of the simulations. The numerical scheme is the Monte-Carlo method coupled to a Strang splitting method. Moreover, I parallelized with `OpenMP` to achieve high accuracy with the Monte-Carlo method in a reasonable computational time.

This collaboration led to a publication Laibe et al. (2020). The content of this paper is transcribed below.

5.2 INTRODUCTION

Details of the structure of dusty discs are now accessible by the mean of instruments such as the Atacama Large (sub)Millimetre Array ALMA (e.g. van der Marel et al. (2013), ALMA Partnership et al. (2015), and Andrews et al. (2018)), the Spectro-Polarimetric High-contrast Exoplanet REsearch instrument SPHERE/VLT (e.g. Benisty et al. (2015) and Avenhaus et al. (2018)) or the Gemini Planet Imager Gemini/GPI (e.g. Laws et al. (2020)). Spatial differentiation between gas and dust grains is evidenced, both in the midplane of the disc (radial drift) or in the vertical direction (vertical settling). Centimetre-in-size pebbles have attracted lot of attention as they provide primordial material to form planetary cores (e.g. Chiang (2008) and Testi et al. (2014)). Small micron-in-size grains are as important (e.g. Apai et al. (2004), Furlan et al. (2006), Dent et al. (2013), Espaillat et al. (2014), and Maaskant et al. (2015)), since they are often used as a proxy for the gas. They also set the charge and thermal balances of the disc and radiate polarized

light. Hence the need of an accurate description of vertical distributions of small particles.

Primary theories of dust settling (e.g. Hoyle (1960), Kusaka et al. (1970), Cameron (1973), Adachi et al. (1976), Handbury and Williams (1977), and Coradini et al. (1980)) have emerged with the development of the planetary nebulae hypothesis (Mendoza V., 1966; Safronov, 1972). Further developments of the Minimum Mass Solar Nebulae models (e.g. Cameron and Pine (1973), Weidenschilling (1977b), and Hayashi (1981)) sparked models coupling settling to growth (Weidenschilling, 1980; Nakagawa et al., 1981). The idea that turbulence sustains dust stirring (Cuzzi et al., 1993) emanated from observations of Spectral Energy Distributions of T-Tauri objects (Kenyon and Hartmann, 1987) concomitant to the rediscovery of the magneto-rotational instability (Balbus and Hawley, 1991).

The seminal theory of dust settling was established by Dubrulle et al. (1995). Turbulence is treated by the mean of a Fokker-Planck equation, an approach that resulted in a widely-used model to estimate dust scale heights in discs. Soon after, Dullemond and Dominik (2004b) and Dullemond and Dominik (2005a) pioneered models of dust settling coupled to Monte-Carlo methods for radiative transfer, a technic extended to ray tracing by Pinte et al. (2006) and Pinte et al. (2007). Tanaka et al. (2005) modelled spectral energy distributions expected from the interplay between settling and coagulation. In parallel, several aspects of dust settling were quantified with (magneto)-hydrodynamical simulations: the role of dust feed-back (Barrière-Fouchet et al., 2005; Johansen and Klahr, 2005; Johansen et al., 2006), turbulence (Takeuchi and Lin, 2002; Carballido et al., 2006; Fromang and Papaloizou, 2006; Fromang and Nelson, 2009; Ciesla, 2010; Turner et al., 2010; Charnoz et al., 2011; Johansen et al., 2011; Carballido et al., 2011; Zhu et al., 2015; Stoll and Kley, 2016; Lin, 2019), and grain growth/fragmentation (Zsom et al., 2011). Analytic or semi-analytic models were refined to understand the role played by different drag regime (Garaud and Lin, 2004), refined models of turbulence (Schräpler and Henning, 2004; Jacquet, 2013; Ormel and Liu, 2018), turbulent dead zones (Ciesla, 2007), turbulent correlations (Youdin and Lithwick, 2007), grain growth (Laibe and Price, 2014a) or winds (Riols and Lesur, 2018). These models are widely used to infer the properties of the disc from observations (e.g. de Boer et al. (2017), Dullemond et al. (2018), Sengupta et al. (2019), Greenwood et al. (2019), and Liu et al. (2019)).

However, we still lack an analytic formula for the distribution of small dust grains that encompass gas stratification, dust inertia and finite correlation times. To obtain such a recipe, we depart from the historical Fokker-Planck approach and start directly from a balance of forces on a dust grain (Sect. 5.3). We obtain a system of stochastic differential equations that we analyse, in the spirit of Ormel and Liu (2018) (Sect. 5.4). Results are validated against numerical simulations in Sect. 5.5 and discussed in Sect. 5.6.

5.3 PHYSICAL MODEL

5.3.1 *Balance of forces*

We consider a non-magnetic non self-gravitating vertically isothermal disc made of gas and dust. We denote by r and z the radial and the vertical coordinates respectively. The

central star is modelled as a point mass $M_\star$, such that the vertical component g_z of its gravitational field is

$$g_z = -\frac{\mathcal{G} M_\star z}{\left(r^2 + z^2\right)^{3/2}}. \tag{5.1}$$

The gas is supposed to be inviscid and the disc to be at vertical hydrostatic equilibrium. Thus, at a distance r from the central star, the gas density is

$$\rho_{\mathrm{g}}\left(r, z\right) = \rho_{\mathrm{g0}}\left(r\right) \mathrm{e}^{-\frac{\mathcal{G} M_\star}{c_{\mathrm{s}}^2\left(r\right)} \int_0^z g\left(z'\right) \mathrm{d}z'}, \tag{5.2}$$

$$= \rho_{\mathrm{g0}}\left(r\right) \mathrm{e}^{-\frac{\mathcal{G} M_\star}{c_{\mathrm{s}}^2\left(r\right)} \left[\frac{1}{r} - \frac{1}{\sqrt{r^2 + z^2}}\right]}, \tag{5.3}$$

where ρ_{g0} and c_{s} denote the gas density in the midplane of the disc and the sound speed at a distance r from the star respectively (e.g. Laibe and Price (2012b)). In the limit $z \ll r$, g_z linearises into

$$g_z \simeq -\frac{\mathcal{G} M_\star z}{r^3} = -\Omega^2 z, \tag{5.4}$$

a spring-like force of frequency the orbital frequency of the disc. Under this approximation, Eq. 5.3 reduces to

$$\rho_{\mathrm{g}}\left(r, z\right) = \rho_{\mathrm{g0}}\left(r\right) \mathrm{e}^{-\frac{z^2}{2H^2}}, \tag{5.5}$$

where $H \equiv \Omega^{-1} c_{\mathrm{s}}$ denotes the pressure scale height of the gas. The typical aspect ratio H/r of observed discs is of order ~ 0.1. Close to the midplane of the disc ($z \ll H$), Eq. 5.5 becomes

$$\rho_{\mathrm{g}}\left(r, z\right) = \rho_{\mathrm{g0}} + \mathrm{O}\left(z^2/H^2\right). \tag{5.6}$$

Dust grains are assumed to be compact, homogeneous and of spherical shape with radius s. Grains are uncharged, although this assumption might not be correct anymore for $z \lesssim 3H$ (e.g. Bai and Goodman (2009)). The mass of the grain is therefore $m_{\mathrm{d}} = \frac{4}{3}\pi\rho s^3$, where ρ denotes the intrinsic density of the grain material – typically a few g.cm^{-1}. In typical classical T-Tauri star discs, the collisional mean free path of the gas is larger than the size of the grain. The drag force $\mathbf{f}_{\mathrm{d}}$ exerted by the gas on grains is

$$\mathbf{f}_{\mathrm{d}} = -m_{\mathrm{d}} \frac{\left(\mathbf{v}_{\mathrm{d}} - \mathbf{v}_{\mathrm{g}}\right)}{t_{\mathrm{s}}}, \tag{5.7}$$

where t_{s} denotes the drag stopping time, i.e. the typical time for dust grains to reach gas velocity. The stopping time depends on the gas and dust parameters according to

$$t_{\mathrm{s}} = \frac{\rho s}{\rho_{\mathrm{g}} c_s} \sqrt{\frac{\pi\gamma}{8}}, \tag{5.8}$$

where γ denotes the adiabatic index of the gas (Epstein, 1924; Baines et al., 1965; Whipple, 1972). Combining Eqs. 5.3 and 5.8,

$$t_{\mathrm{s}}\left(z\right) = t_{\mathrm{s0}}\, \mathrm{e}^{\frac{\mathcal{G} M_\star}{c_{\mathrm{s}}^2\left(r\right)} \left[\frac{1}{r} - \frac{1}{\sqrt{r^2 + z^2}}\right]} \simeq t_{\mathrm{s0}}\, \mathrm{e}^{\frac{z^2}{2H^2}}, \tag{5.9}$$

where t_{s0} denotes the stopping time in the midplane. Hence, grains decouple very efficiently in the high atmosphere of the disc where the gas density drops, and the stopping time is an increasing function of the vertical height inversely proportional to gas density.

Gravity from the star and gas drag are the two main relevant forces for this problem. Additional contributions such as radiation forces, magnetic forces or other hydrodynamical forces are negligible (Laibe and Price, 2012a). Quadratic corrections for supersonic drag are not expected to play any sensible contribution in this problem and are neglected (Kwok, 1975). The ratio of the timescales between the vertical and the radial timescale is of order $(H/r)^2 \sim 0.01$, justifying treating r as a constant (Laibe et al., 2014b). This assumption holds whenever z is small enough for the conservation of angular momentum to remain valid up to second order in z/r.

From the expression of the stopping time given by Eq. 5.9, the balance of forces for single dust grain provides

$$\ddot{z} + \frac{(\dot{z} - v_{g,z})}{t_{s,0}} e^{-\frac{\mathcal{G}M_\star}{c_s^2(r)}\left[\frac{1}{r} - \frac{1}{\sqrt{r^2+z^2}}\right]} + \frac{\mathcal{G}M_\star z}{(r^2+z^2)^{3/2}} = 0. \tag{5.10}$$

We now introduce the dimensionless quantities $Z \equiv z/H$, $T \equiv t/\Omega^{-1}$ and $\dot{Z} = \dot{z}/c_s$. Note that T denotes the time in units of the orbital period and *not* the temperature. We scale also the gas velocity by its sound speed, i.e. $V_g = v_g/c_s$. We denote by the constant $\phi = H/r$ the local aspect ratio of the disc. The Stokes number $S_t \equiv \Omega t_s$ measures the relative contribution between gas drag and gravity. From Eq. 5.9, it increases with vertical height as

$$S_t = S_{t0}\, e^{Z^2/2}, \tag{5.11}$$

where S_{t0} denotes the Stokes number in the midplane of the disc. We note that grains reach $S_t = 1$ for $Z = \sqrt{-2\ln S_{t0}}$, i.e. a few pressure scale heights even for tiny values of S_{t0}. Starting from Eq. 5.10 and rearranging the terms, one obtains the equation of motion for a single grain:

$$\ddot{Z} + S_{t0}^{-1} f_\phi(Z)\,\dot{Z} + g_\phi(Z) = S_{t0}^{-1} f_\phi(Z)\, V_g, \tag{5.12}$$

where

$$f_\phi(Z) \equiv e^{-\frac{1}{\phi^2}\left[1-\left(1+(\phi Z)^2\right)^{-1/2}\right]}, \tag{5.13}$$

$$g_\phi(Z) \equiv \frac{Z}{(1+\phi^2 Z^2)^{3/2}}. \tag{5.14}$$

Effects of vertical stratification are still encapsulated in the Taylor expansion of Eq. 5.12 with respect to the small parameter $\phi^2 \sim 0.01$

$$\ddot{Z} + S_{t0}^{-1} e^{-Z^2/2}\dot{Z} + Z = S_{t0}^{-1} e^{-Z^2/2} V_g. \tag{5.15}$$

The final step of the model consists of modelling the turbulent velocity of the gas V_g, which appears in the right-hand side of Eq. 5.12. In the limiting case of a laminar flow, $V_g = 0$ and Eq. 5.12 reduces to the well-known equation for vertical settling in laminar discs (e.g. Laibe and Price (2014a)).

5.3.2 *Modelling dusty turbulence*

5.3.2.1 *Lagrangian turbulence*

The gas velocity is unknown since no exact analytic solution for turbulence in a disc – and turbulence in general – are known. However, statistical properties of turbulence can be inferred from laboratory, numerical experiment or theory, and turbulent fluctuations can be modelled using stochastic processes, independently from the origin of the turbulence itself. In a seminal study, Thomson (1987) proved that the only expression of v_g that is consistent with Kolmogorov turbulence and the hydrodynamical equations is

$$\frac{\mathrm{d}v_\mathrm{g}}{\mathrm{d}t} = -\frac{v_\mathrm{g}}{t_\mathrm{e}} + \frac{\sqrt{D}}{t_\mathrm{e}}\dot{w}, \tag{5.16}$$

where t_e denotes the Lagrangian timescale of the turbulence, D is the turbulent diffusivity (in units $\mathrm{m^2s^{-1}}$). w is a Wiener process, such that its derivative is a white noise such that

$$\langle \dot{w}(t) \rangle = 0, \tag{5.17}$$

$$\langle \dot{w}(t)\, \dot{w}(t') \rangle = \delta(t - t'), \tag{5.18}$$

where δ denotes the Dirac distribution and the notation $\langle \cdot \rangle$ is the expectation operator (see also **WilsonSawford**; Sawford (1984)). Eq. 5.16 describes turbulent fluctuations from a Lagrangian point of view (Taylor, 1922). From Eq. 5.16, the gas velocity can be rewritten

$$v_\mathrm{g} = \zeta\left(t, t_\mathrm{e}, D\right), \tag{5.19}$$

where ζ is a stationary Ornstein-Uhlenbeck process defined by

$$\langle \zeta(t, t_\mathrm{e}, D) \rangle = 0, \tag{5.20}$$

$$\langle \zeta(t, t_\mathrm{e}, D)\, \zeta(t', t_\mathrm{e}, D) \rangle = \frac{D}{2t_\mathrm{e}} \mathrm{e}^{-\frac{|t-t'|}{t_\mathrm{e}}}. \tag{5.21}$$

Eq. 5.16 defines a model of turbulence with two parameters, D and t_e. In discs, t_e is typically of order one orbital period, since turbulent vortices are stretched out by differential rotation in a few orbits (e.g. Beckwith et al. (2011)). From Eq. 5.21, D is related to the auto-correlation of the turbulent noise according to

$$D = 2\int_0^{+\infty} \langle v_\mathrm{g}\left(0\right) v_\mathrm{g}\left(t\right) \rangle \, \mathrm{d}t. \tag{5.22}$$

Eq. 5.22 can alternatively be seen as a definition of the turbulent diffusivity, useful in practice to measure D in numerical simulations. The Wiener-Khinchin theorem ensures that the power spectrum of the turbulent velocity field $S(\omega)$ is the Fourier transform of this autocorrelation function, i.e.

$$S\left(\omega\right) = \frac{1}{2\pi}\int_{-\infty}^{+\infty} \mathrm{e}^{-i\omega t} \langle v_\mathrm{g}\left(0\right) v_\mathrm{g}\left(t\right) \rangle \, \mathrm{d}t = \frac{D}{2\pi\left(1 + \omega^2 t_\mathrm{e}^2\right)}. \tag{5.23}$$

Thus, in the inertial subrange ($\omega^2 t_\mathrm{e}^2 \gg 1$), we have $S(\omega) \propto \omega^{-2}$, whose equivalent in the wavelength space is $\tilde{S}(k) \propto k^{-5/3}$ (Batchelor, 1950). From Eq. 5.23, the standard deviation of the velocity fluctuation σ is

$$\sigma^2 \equiv \int_{-\infty}^{+\infty} S\left(\omega\right) \mathrm{d}\omega = \frac{D}{2t_\mathrm{e}}. \tag{5.24}$$

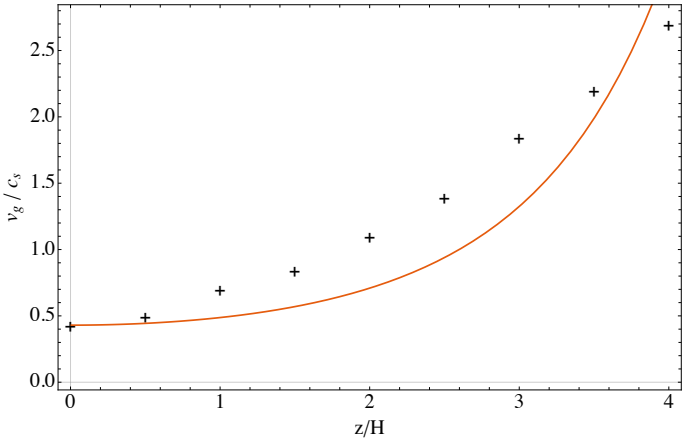

Figure 5.2: Comparison between the toy model $\alpha(z) = \alpha_0/\sqrt{\rho_g(z)/\rho_0}$ and values of α measured directly from the MHD numerical simulations of Fromang and Nelson (2009). The global trend is reproduced with maximum errors reaching $\simeq 50\%$, which is sufficient for this study.

Physically, Eq. 5.24 is a turbulent fluctuation-dissipation theorem.

In astrophysics, the turbulent activity of a disc is often parametrised by a constant denoted by α (Shakura and Sunyaev, 1973). In this work, we define α according to

$$\alpha \equiv \frac{D}{2c_s H}, \tag{5.25}$$

to be consistent with previous studies on dust diffusivity (e.g. Fromang and Papaloizou (2006)). Combining Eqs. 5.21 and 5.25, Eq. 5.19 can be rewritten as

$$v_g/c_s = \sqrt{2\alpha}\,\zeta\left(T, \tau_e, 1\right), \tag{5.26}$$

where $\tau_e \equiv t_e\Omega$. In the literature, the *same notation* α has been used to denote *different* dimensionless physical quantities, all related to the turbulent activity of the disc and being therefore of the same order of magnitude. The parameter α may be used e.g. for quantities measuring the efficiency of the transport of angular momentum, the intensity of the velocity fluctuations or the turbulent diffusivity (e.g. Arena and Gonzalez (2013)). For a quantitative use of our results, values of α should either be directly measured using Eq. 5.22 or deduced from an alternative measurement of the turbulent activity of the disc and a coefficient of proportionality which has been calibrated independently. The ratio between turbulent and thermal pressure is of order $\sqrt{\alpha}$. Hence, Eq. 5.3 remains a valid expression for the density profile of the disc.

The vertical dependency of α can be inferred from numerical simulations of magneto-hydrodynamical turbulence (e.g. Miller and Stone (2000), Fromang and Nelson (2009), and Fromang (2010)). For numerical tractability, simulations are performed in a local shearing-box that extends vertically over a few pressure scale heights. Fig. 5.2 displays values of α measured by Fromang and Nelson (2009). A generic feature is that α increases with z. No first-principle model exists so far to prescribe $\alpha(z)$. Alternative recipes have been proposed to mimic this behaviour (e.g. Ciesla (2010) and Ormel and Liu (2018)). In this study, we use for convenience and tractability a very crude but parameter-free parametrisation of $\alpha\,(z)$

$$\alpha = \alpha_0\left(\rho_0/\rho\right)^{1/2}. \tag{5.27}$$

This assumption ensures that the density of turbulent energy $\rho_g v_g^2$ remains finite and roughly constant in a vertical slab of the disc. The model is therefore compatible with

a steady-state, since no further turbulent processes are required to smooth out local energy gradients. The agreement between Eq. 5.27 and numerical simulations is quite reasonable (Fig. 5.2). Although errors may reach $\simeq 50\%$, the model is conservative for our study since it enhances slightly the eventual role played by a positive value of the vertical gradient of α. The prescription may probably be incorrect for $z \gtrsim 3H$ (Fromang and Nelson, 2009). This does not affect significantly our results since we find almost no grain at these heights. In dimensionless quantities, we denote

$$\alpha = \alpha_0 h^2 (Z) . \tag{5.28}$$

A value of $h = f^{-1/4}$ corresponds to Eq. 5.27.

Turbulence could have alternatively been described by the turbulent velocity σ_t and the mean rate of dissipation of turbulence kinetic energy ϵ_t, where $t_e = \frac{2\sigma_t^2}{C_0 \epsilon_t}$, $D = \frac{\left(2\sigma_t^2\right)^2}{C_0 \epsilon_t}$, and C_0 is a constant to be calibrated (Thomson, 1987). Thus, $\sigma_t = \mathrm{O}\left(\sqrt{\alpha} c_s\right)$ and $\epsilon_t = \mathrm{O}\left(\alpha c_s^3 / H\right)$. The turbulent viscosity ν scales like $\nu = \mathrm{O}\left(\sigma_t^2 / \epsilon_t\right) = \mathrm{O}\left(\alpha c_s H\right)$, consistently with a Sakura and Sunyaev prescription, for which $\nu = \alpha_{SS} c_s H$. It is found in numerical simulations that in protoplanetary discs, $\alpha \simeq \alpha_{SS} \simeq 10^{-4} - 10^{-2}$. Further refined stochastic models including multiple turbulent timescales have been used in the context of aerosols and suspensions (e.g. Shao (1995) and Pope (2002)). Effects of anisotropy may also be described by other turbulent parameters (e.g. Balbus and Papaloizou (1999), Ogilvie (2001), Lodato (2008), and Balbus (2011)). These refinements are not expected to have any significant impact in our study.

5.3.2.2 *Equations of motion*

Combining Eqs. 5.12 – 5.14, Eq. 5.16 and Eq. 5.28 in a dimensionless form, one obtains the system

$$\begin{aligned} \mathrm{d}Z &= V \mathrm{d}T, & (5.29)\\ \mathrm{d}V + S_{t0}^{-1} f_\phi(Z) V \mathrm{d}T + g_\phi(Z) \mathrm{d}T &= S_{t0}^{-1} f_\phi(Z) h(Z) \sqrt{2\alpha_0}\, \xi \mathrm{d}T & (5.30)\\ \mathrm{d}\xi &= -\frac{\xi}{\tau_e} dT + \frac{\mathrm{d}w}{\tau_e}. & (5.31) \end{aligned}$$

The system of equations Eqs. 5.29 – 5.31 is stochastic and the dust scale height in steady-state is subsequently defined in a probabilistic way as the variance of the dust distribution at large times, i.e.

$$H_d \equiv \sqrt{\langle ZZ \rangle}_{T=+\infty}. \tag{5.32}$$

Gravity, which confines dust particle close to the midplane, is encompassed in the function g_ϕ. in In a real disc, this confinement is weaker than if it were operated by the osculating harmonic potential of the midplane. On the one hand, gas drag dissipates the mean kinetic energy of the grain through the second term of the left-hand side of Eq. 5.30. This makes grains settle to the midplane, which is the bottom of the potential well. On the other hand, gas drag couples the grain to the stirring turbulent fluctuations of the gas through the driving term of the right-hand side of Eq. 5.30.

Density stratification of the gas is encoded in the function f_ϕ. From Eqs. 5.29– 5.31, stratification affects the dynamics of the grain in two ways. Firstly, grains having small Stokes numbers $S_{t0} \ll 1$ in the midplane may have Stokes numbers $S_t = S_{t0}/f_\phi$ larger than unity in the top-layers of the disc. Thus, the dynamics of those grains may counter-intuitively be gravity-dominated. Secondly, grains couple and react more efficiently to

turbulent stirring close to the midplane of the disc. If the gradient of the product $f_\phi h$ is negative, grains receive stronger turbulent kicks from the bottom of the disc than from the top layers. For smooth vertical profiles of α, this differential effect is the strongest close to the inflection point of the density profile, i.e. one pressure scale height for the Gaussian profile. Hence, stratification affects the stirring of small grains ($S_{t0} \sim \alpha \ll 1$) and can not be neglected. Its effects are the strongest in the top layers of the disc, where the dynamics is gravity-dominated and submitted to a large differential driving.

5.3.3 *Link with previous works*

5.3.3.1 *Strong drag approximation*

A first approximation for Eqs. 5.29 – 5.31 consists of assuming that grains are small enough for the dynamics to be always drag dominated and that $\ddot{Z} \ll S_{t0} f_\phi(Z)\,\dot{Z}$ in Eq. 5.12. For the sake of clarity, we shall now use the approximations of Eqs. 5.4–5.5 for f_ϕ and g_ϕ and a constant viscosity ($h = 1$) to illustrate the effect of this approximation since it does not affect the nature of our conclusions. The evolution of dust grains is therefore governed by the equation

$$\mathrm{d}Z = -S_{t0} Z \mathrm{e}^{Z^2/2} \mathrm{d}T + \sqrt{2\alpha}\mathrm{d}\xi. \tag{5.33}$$

For a purely diffusive process ξ, Eq. 5.33 is equivalent to the following Fokker-Planck equation (e.g. Risken and Haken (1989))

$$\frac{\partial p}{\partial T} = \frac{\partial}{\partial Z}\left(S_{t0} Z \mathrm{e}^{Z^2/2} p\right) + \alpha \frac{\partial^2 p}{\partial Z^2}. \tag{5.34}$$

In the Fokker-Planck formalism, a definition of the dust scale height equivalent to Eq. 5.32 is

$$H_\mathrm{d} = \left(\int_{-\infty}^{+\infty}\int_{-\infty}^{+\infty} p(+\infty, Z, V) Z^2 \,\mathrm{d}V \mathrm{d}Z\right)^{1/2}. \tag{5.35}$$

Eq. 5.34 does not depend on the velocity V anymore, and its steady-state solution is (e.g. Wallis (1990) and Fromang and Nelson (2009))

$$p(z) \propto \mathrm{e}^{\int_0^z -\frac{Z' \mathrm{e}^{Z'^2/2}}{\alpha/S_{t0}} \mathrm{d}Z'} = \mathrm{e}^{-\frac{\mathrm{e}^{Z^2/2}}{\alpha/S_{t0}}}, \tag{5.36}$$

which gives the dust scale height on an integral form

$$H_\mathrm{d} = \left(\int_{-\infty}^{+\infty} Z^2 \mathrm{e}^{-\frac{\mathrm{e}^{Z^2/2}}{\alpha/S_{t0}}} \mathrm{d}Z \;\Big/ \int_{-\infty}^{+\infty} \mathrm{e}^{-\frac{\mathrm{e}^{Z^2/2}}{\alpha/S_{t0}}} \mathrm{d}Z\right)^{1/2} \tag{5.37}$$

The parameter α/S_{t0} appears naturally as the relevant quantity to measure whether dust grains are significantly sensitive to the turbulent activity of the gas or not.
In the dust distribution given by Eq. 5.36, small grains remain confined within almost three pressure scale heights around the midplane. Indeed, the low gas density in the top layers of the disc reduces drastically the efficiency of turbulent driving, preventing the particles to escape. Eq. 5.33 shows that gas stratification acts as a stiff effective potential

$\mathcal{V}_{\rm eff}(Z) \equiv S_{\rm t0} {\rm e}^{z^2/2}$ that confines the particles close to the midplane. As expected, the distribution Eq. 5.36 corresponds to the Boltzmann distribution

$$p(z) \propto {\rm e}^{-\mathcal{V}_{\rm eff}(Z)/\alpha}. \tag{5.38}$$

In Eq. 5.38, α is the dimensionless form of the turbulent energy $\alpha c_{\rm s}^2$. It is not possible to obtain a closed-form expression for the dust scale height in stationary regime from Eq. 5.36. When the particles are close enough to the midplane of the disc, i.e. when $\alpha/S_{\rm t0} \ll 1$, Eqs. 5.33 and 5.36 can be linearised, giving

$$p(+\infty, Z) = \sqrt{\frac{S_{\rm t0}}{2\pi\alpha}} {\rm e}^{-\dfrac{Z^2}{2\alpha/S_{\rm t0}}}. \tag{5.39}$$

From Eq. 5.32, and integrating over Z only in this case, the analytic expression of $H_{\rm d}$ is

$$H_{\rm d} = \sqrt{\alpha/S_{\rm t0}}. \tag{5.40}$$

Eq. 5.40 is the analytic estimate obtained by Dubrulle et al. (1995) for the dust scale height of particles close to the midplane. Physically, $H_{\rm d}$ is large when turbulence is intense and grains are small, since strong coupling with the gas ensure continuous stirring by the turbulent kicks. Importantly, for $S_{\rm t0} = \alpha$, dust reaches the pressure scale height of the gas ($H_{\rm d} = 1$). This corresponds to Stokes numbers of order $10^2 - 10^3$ in typical discs. Some numerical codes use the expression given by Eq. 5.40 since it is easily tractable. However, to overcome the divergence of $H_{\rm d}$ at large coupling parameters, cut-offs for large dust thicknesses need to be enforced, such as

$$\tilde{H}_{\rm d} \equiv \min\left(\sqrt{\frac{\alpha}{S_{\rm t0}}}, 1\right), \tag{5.41}$$

or the smoother variant (e.g. Riols and Lesur (2018))

$$\hat{H}_{\rm d} \equiv \left(1 + \frac{S_{\rm t0}}{\alpha}\right)^{-1/2}. \tag{5.42}$$

Although convenient, this approach brings the drawback of not reproducing the step-function aspect of the dust distribution for small grains predicted by Eq. 5.36.

5.3.3.2 *Linearisation*

Eqs. 5.29 – 5.30 have alternatively been studied by linearising the function f_ϕ and g_ϕ in the limit $Z \ll 1$ according to

$$\begin{aligned} {\rm d}Z &= Z{\rm d}T, & (5.43)\\ {\rm d}V + S_{\rm t0}^{-1} V {\rm d}T + Z{\rm d}T &= S_{\rm t0}^{-1}\sqrt{2\alpha}\,{\rm d}\xi. & (5.44) \end{aligned}$$

This approximation is valid when the dust evolution occurs close to the disc's midplane. Carballido et al. (2006) model turbulence by a white noise, i.e. ${\rm d}\xi$ is the Wiener process given by Eqs. 5.17 – 5.18. Eqs. 5.43–5.44 are equivalent to the Fokker-Planck equation

$$\frac{\partial p}{\partial T} + V\frac{\partial p}{\partial Z} + \frac{\partial}{\partial V}\left(\left[-S_{\rm t0}^{-1}V - Z\right]p\right) - \alpha S_{\rm t0}^{-2}\frac{\partial^2 p}{\partial V^2} = 0. \tag{5.45}$$

A rescaling of Eq. 5.45 by $\hat{Z} = Z/\sqrt{\alpha/S_{\rm t0}}$ shows that its solution depends only on the product $\alpha/S_{\rm t0}$. The probability density function of the grains converges to the Gaussian distribution

$$p(+\infty, Z, V) = \frac{S_{\rm t0}}{2\pi\alpha} {\rm e}^{-\frac{1}{\alpha/S_{\rm t0}}\left\{\frac{Z^2}{2} + \frac{V^2}{2}\right\}}, \tag{5.46}$$

after a typical time $T_{\rm sett} = S_{\rm t0} + S_{\rm t0}^{-1}$ that is the typical settling time in a laminar disc. From Eq. 5.32, the dust scale height at equilibrium is

$$H_{\rm d} = \sqrt{\alpha / S_{\rm t0}}. \tag{5.47}$$

Remarkably, Eq. 5.47 provides the same expression than the one obtained in the strong drag approximation (Eq. 5.40). Youdin and Lithwick (2007) have generalised Eq. 5.47 by including temporal correlations in the model of turbulence. In this case, $d\xi$ is the Ornstein-Uhlenbeck process given by Eqs. 5.20 - 5.21, and the dust scale height depends additionally on the correlation time $\tau_{\rm e}$ according to (Masoliver and Porrà, 1993; Wang and Masoliver, 1996)

$$H_{\rm d} = \sqrt{\alpha / S_{\rm t0}} \sqrt{\frac{1 + \tau_{\rm e}/S_{\rm t0}}{1 + \tau_{\rm e}/S_{\rm t0} + \tau_{\rm e}^2}}. \tag{5.48}$$

In the limit $\tau_{\rm e} = 0$, Eq. 5.48 reduces to Eq. 5.47. For a typical $\tau_{\rm e} = 1$, $H_{\rm d} = \sqrt{\alpha / S_{\rm t0}} \sqrt{\frac{S_{\rm t0}+1}{2S_{\rm t0}+1}}$. Hence, in real discs, the qualitative discrepancy between Eq. 5.47 and Eq. 5.48 is not significant. Moreover, the two models are rigorously equivalent in the small grains limit. Indeed, $H_{\rm d} \simeq \sqrt{\alpha / S_{\rm t0}}$ with an approximation better than one per cent for $S_{\rm t0} < 0.02$. In the limit $\tau_{\rm e} \to +\infty$, the disc is laminar and $H_{\rm d} \to 0$. This case is not relevant in practice.

Importantly, linearised models predict dust scale heights larger than the pressure scale height of the gas for $S_{\rm t0} \lesssim \alpha$ even if physically, there is almost no gas in these layers and thus, almost no turbulent driving. To understand this feature, let us examine closely how equations including stratification behaves against linearisation (i.e. Eqs. 5.12 and 5.15). The limit of a "spring-like" restoring force is obtained by letting the parameter ϕ go to zero. This corresponds to the thin cold disc limit. However, the limit of constant damping (Eq. 5.6) can *not* be obtained as an asymptotic behaviour of the equations of evolution with respect to any continuous parameter. Hence, the linearised system of equations models dust particles embedded in an infinite homogeneous vertical slab of gas, whose density is the one of the midplane. Small grains are therefore always scattered efficiently by turbulence wherever their location in the disc, explaining why they are ultimately reaching infinitely high regions. When including stratification, small particles decouple from the gas when they reach a sufficient height and fall back into the minimum of gravitational potential located in the midplane of the disc.

5.3.3.3 *Diffusion equations*

In Dubrulle et al. (1995), the dust density is obtained from the Fokker-Planck equation

$$\frac{\partial \rho_{\rm d}}{\partial t} = \frac{\partial}{\partial z}\left[z\Omega^2 t_{\rm s}(z)\rho_{\rm d}\right] + \frac{\partial}{\partial z}\left[\rho_{\rm g}(z)\kappa_{\rm T}(z)\frac{\partial}{\partial z}\left(\frac{\rho_{\rm d}}{\rho_{\rm g}(z)}\right)\right], \tag{5.49}$$

where $\kappa_{\rm T}(z)$ is an effective half-diffusivity (to be consistent with Eq. 5.25). For particles with small Stokes numbers, $\kappa_{\rm T}(z) = \alpha c_{\rm s} H$ and $\kappa_{\rm T}(z) \propto z^{-1/2}$ for particles with large Stokes numbers (see Riols and Lesur (2018) for a detailed discussion of the origin of this equation). In essence, the Dubrulle et al. (1995) model is build on the strong drag approximation and Eq. 5.49 is equivalent to our Eq. 5.34 in dimensionless quantities. The discrepancies between the two models can be understood the following way:

1. The diffusion operator of Eq. 5.49, originally introduced by Morfill and Voelk (1984), acts on the quantity $\rho_{\rm d}/\rho_{\rm g}$ and not on the quantity $\rho_{\rm d}$. For independent and non-interacting particles, diffusion fluxes smooths gradients of chemical potentials

that are proportional to densities. The extrapolation to concentrations is valid only for homogeneous solvent/gas densities. It looks therefore that Eqs. 5.29–5.31 rely on more robust physical bases. We also note that Eq. 5.49 can not be derived from a balance of forces with stochastic driving. However, the difference between the two equations is only minor, since Eq. 5.49 writes with our notations

$$\frac{\partial p}{\partial T} = \frac{\partial}{\partial Z}\left(Z\left[S_{t0}e^{Z^2/2} + \alpha\right]p\right) + \alpha\frac{\partial^2 p}{\partial Z^2}. \tag{5.50}$$

We note the appearance of an extra drift-term for the grains which does not depend on S_{t0}. This terms can not be of physical origin, since dust coupled to gas only through gas drag. Anyhow, the extra stir provided by this additional term would affect only tiny grains close to the mid-plane, which are lifted up by turbulence anyway.

2. The variable diffusivity $\kappa_T(z)$ is inherited from an *ad-hoc* concept of eddy classes invoked originally in Voelk et al. (1980), seven years *before* the work of Thomson. Riols and Lesur (2018) provide a interpretation for the origin of this term through Reynolds averaging of the dust/gas equations of motion. On the other hand, Thomson (1987) demonstrated that a rigorous way to account eddies of different lifetimes in a Lagrangian descriptions of turbulence is to introduce a finite correlation time t_e. Eq. 5.23 ensures that the correct spectrum of lifetimes for the turbulent structures in reproduced. In the strong drag approximation, the generalisation of Eq. 5.50 for finite turbulent times is

$$\frac{\partial p}{\partial T} = \frac{\partial}{\partial Z}\left(S_{t0}Ze^{Z^2/2}\right) + \sqrt{\alpha/2}\frac{\partial^2}{\partial Z^2}\left[H\left(T,Z\right)p\right], \tag{5.51}$$

where $\tilde{H}(Z) = H\left(+\infty, Z\right)$ satisfies

$$\tilde{H} + \tau_e\left(\tilde{H}\frac{\partial S_{t0}Ze^{Z^2/2}}{\partial Z} - \frac{\partial \tilde{H}}{\partial Z}S_{t0}Ze^{Z^2/2}\right) = \sqrt{2\alpha}. \tag{5.52}$$

The general expression for $H\left(Z,t\right)$ is given in Hernandez-Machado et al. (1983). Eqs. 5.51 – 5.52 reduce to Eq. 5.34 when $\tau_e = 0$. Interestingly, Eqs. 5.51 – 5.52 reduce to

$$\frac{\partial p}{\partial T} = -\frac{\partial}{\partial Z}\left(S_{t0}Zp\right) + \frac{\alpha}{1+S_{t0}\tau_e}\left(1 - e^{-\left[\tau_e^{-1}+S_{t0}\right]T}\right)\frac{\partial^2 p}{\partial Z^2}, \tag{5.53}$$

when the equations of evolution are linearised. The equivalent dimensionless diffusivity is $2\alpha/\left(1+S_{t0}\tau_e\right)$ and does not depend on Z. In the limit $T \to +\infty$, the dust scale height obtained from Eq. 5.53 is

$$H_d = \sqrt{\frac{\alpha/S_{t0}}{1+S_{t0}\tau_e}}. \tag{5.54}$$

5.3.3.4 *Conclusion*

So far, no analytic model predicts steady distributions of small grains that can become gravity-dominated in the top layers in stratified discs, where turbulence develops on finite correlation times. Those effects have however been shown to play an important role in structuring the dust layers and are expected to be the most important for the smallest grains. Obtaining a formula which integrates these effects altogether is the goal of the following derivation.

5.4 MATHEMATICAL ANALYSIS

5.4.1 *Rescaling*

For the mathematical analysis, introduce the parameters

$$\epsilon = S_{t0}\ , \quad \delta = \sqrt{\tau_e S_{t0}}\ , \quad \sigma = \sqrt{\alpha_0 / S_{t0}}. \tag{5.55}$$

For convenience, we also introduce the parameter λ such as

$$\lambda = \delta/\epsilon = \sqrt{\tau_e / S_{t0}}. \tag{5.56}$$

Asymptotic analysis is performed in the regime

$$\epsilon \ll 1\ , \quad \delta \ll 1, \quad \sigma \sim 1, \tag{5.57}$$

i.e. the parameters ϵ and δ go to 0 whereas σ remains of order 1. As will be clear below, depending on whether $\delta \ll \epsilon$, $\epsilon \ll \delta$, or $\epsilon \sim \delta$, the limiting equations for Z will be different.

The physical parameters are recovered in terms of the mathematical ones as follows:

$$S_{t0} = \epsilon\ , \quad \tau_e = \frac{\delta^2}{\epsilon}\ , \quad \alpha_0 = \sigma^2 \epsilon. \tag{5.58}$$

Define $Z'(T) = Z(\epsilon^{-1}T)$, $V'(T) = V(\epsilon^{-1}T)$, $\xi'(T) = \xi(\epsilon^{-1}T)$ and $\zeta'(T) = \delta\epsilon^{-\frac{1}{2}}\xi'(T)$. Note that the Stochastic Differential Equation for ξ' is written as

$$d\xi' = -\frac{\xi'}{\tau_e \epsilon}\mathrm{d}T + \frac{\mathrm{d}w}{\sqrt{\epsilon}\tau_e}, \tag{5.59}$$

since in distribution $\big(w(\epsilon^{-1}T)\big)_{T\geq 0} = \big(\epsilon^{-\frac{1}{2}} w(T)\big)_{T\geq 0}$.

As a consequence, the Stochastic Differential for $\zeta' = \delta\epsilon^{-\frac{1}{2}}\xi'$ is written as

$$d\zeta' = -\frac{\zeta'}{\tau_e \epsilon}\mathrm{d}T + \frac{\delta \mathrm{d}w}{\epsilon \tau_e} = -\frac{\zeta'}{\delta^2}\mathrm{d}T + \frac{\mathrm{d}w}{\delta}. \tag{5.60}$$

Writing $\xi' = \delta^{-1}\epsilon^{\frac{1}{2}}\zeta'$ and using the relations between the parameters, one obtains the system (where the notation $f = f_\phi$ is used)

$$\begin{cases} \mathrm{d}Z^{\epsilon,\delta} = \frac{V^{\epsilon,\delta}}{\epsilon}\mathrm{d}t \\ \mathrm{d}V^{\epsilon,\delta} + \frac{f(Z^{\epsilon,\delta})V^{\epsilon,\delta}}{\epsilon^2}\mathrm{d}t + \frac{g(Z^{\epsilon,\delta})}{\epsilon}\mathrm{d}t = \frac{\sigma\sqrt{2}}{\epsilon\delta} f(Z^{\epsilon,\delta}) h(Z^{\epsilon,\delta}) \zeta^\delta \mathrm{d}t \\ \mathrm{d}\zeta^\delta = -\frac{\zeta^\delta}{\delta^2}\mathrm{d}t + \frac{1}{\delta}\mathrm{d}\beta(t), \end{cases} \tag{5.61}$$

where $\big(\beta(t)\big)_{t\geq 0}$ is a standard real-valued Wiener process (Brownian Motion). For simplicity of the presentation, it is assumed that the initial conditions $Z^{\epsilon,\delta}(0) = z$ and $V^{\epsilon,\delta}(0) = v$ are independent of the parameters ϵ and δ.

In addition, it is assumed that $\zeta^\delta(0) \sim \mathcal{N}(0,1)$ is a centered Gaussian random variable with variance 1, and is independent of the Wiener process β. As a consequence, $\big(\zeta^\delta(t)\big)_{t\geq 0}$ is a stationary Ornstein-Uhlenbeck process: for all $t \geq 0$, $\zeta^\delta(t) \sim \mathcal{N}(0,1)$, and for all $t_1, t_2 \geq 0$, the covariance is written as $\mathbb{E}\big[\zeta^\delta(t_1)\zeta^\delta(t_2)\big] = \frac{1}{2}\exp\big(-\frac{|t_2 - t_1|}{\delta^2}\big)$. When $\delta \to 0$, the process ζ^δ converges to a white noise, in fact more precisely $\big(\frac{1}{\delta}\int_0^t \zeta^\delta(s)\mathrm{d}s\big)_{t\geq 0}$ converges (in distribution) to a Brownian Motion $\big(W(t)\big)_{t\geq 0}$. However, as will be clear below, one needs to be careful when taking the limit $\delta \to 0$ (in particular concerning the interpretation of the stochastic integral in either Itô or Stratonovich sense at the limit).

5.4.2 *Asymptotic expansions*

The goal of this section is to derive limiting Stochastic Differential Equations for the component $Z^{\epsilon,\delta}$ where the other components are eliminated, when $\epsilon, \delta \to 0$. We will only focus on the derivation of the limiting model, the full rigorous proof of convergence is out of the scope of this work. In this section, the functions f, g and h are arbitrary real-valued smooth functions, such that $f(z) > 0$ for all $z \in \mathbb{R}$, and with appropriate growth conditions at infinity to ensure global well-posedness of all the SDEs considered below.

5.4.2.1 *Tools*

A convenient approach (Pavliotis and Stuart, 2008) to perform asymptotic analysis in SDEs such as (5.61) consists in analyzing the behaviour of the associated infinitesimal generator:

$$\mathcal{L}^{\epsilon,\delta} = \frac{1}{\epsilon}\mathcal{A}_1 + \frac{1}{\epsilon\delta}\mathcal{A}_2 + \frac{1}{\epsilon^2}\mathcal{A}_3 + \frac{1}{\delta^2}\mathcal{A}_4, \tag{5.62}$$

where, for any smooth function $\varphi : (z, v, \zeta) \in \mathbb{R}^3 \mapsto \varphi(z, v, \zeta) \in \mathbb{R}$,

$$\begin{aligned}
\mathcal{A}_1\varphi(z,v,\zeta) &= v\partial_z\varphi(z,v,\zeta) - g(z)\partial_v\varphi(z,v,\zeta),\\
\mathcal{A}_2\varphi(z,v,\zeta) &= \sigma\sqrt{2}h(z)f(z)\zeta\partial_v\varphi(z,v,\zeta),\\
\mathcal{A}_3\varphi(z,v,\zeta) &= -f(z)v\partial_v\varphi(z,v,\zeta)\\
\mathcal{A}_4\varphi(z,v,\zeta) &= -\zeta\partial_\zeta\varphi(z,v,\zeta) + \frac{1}{2}\partial^2_{\zeta\zeta}\varphi(z,v,\zeta).
\end{aligned} \tag{5.63}$$

The second-order differential operator $\mathcal{L}^{\epsilon,\delta}$ appears on the right-hand side of the backward Kolmogorov equation:

$$\begin{cases}
\dfrac{\partial u^{\epsilon,\delta}(t,z,v,\zeta)}{\partial t} = \mathcal{L}^{\epsilon,\delta}u^{\epsilon,\delta}(t,z,v,\zeta), \quad t > 0,\\
u^{\epsilon,\delta}(0,z,v,\zeta) = u_0(z,v,\eta)
\end{cases} \tag{5.64}$$

for which the solution is given by

$$u^{\epsilon,\delta}(t,z,v,\zeta) = \mathbb{E}_{z,v,\zeta}\Big[u_0\Big(Z^{\epsilon,\delta}(t), V^{\epsilon,\delta}(t), \zeta^{\epsilon,\delta}(t)\Big)\Big], \tag{5.65}$$

where the notation $\mathbb{E}_{z,v,\zeta}$ means that the initial conditions are given by $Z^{\epsilon,\delta}(0) = z, V^{\epsilon,\delta}(0) = v, \zeta^{\epsilon,\delta}(0) = \zeta$. By duality, one obtains that the adjoint of the infinitesimal generator $\mathcal{L}^{\epsilon,\delta}$ is the Fokker-Planck operator, which governs the evolution of the probability density function of the process (Fokker-Planck equation).

The strategy to obtain a limiting SDE for $Z^{\epsilon,\delta}$ consists in the following two steps. First, one identifies the limit of the solution $u^{\epsilon,\delta}$ of the backward Kolmogorov equation (5.64), for any initial condition u_0 which depends only on the z variable. This requires to construct an appropriate asymptotic expansion, to deal with the singular perturbations when $\epsilon, \delta \to 0$. Second, one interprets the limit as the solution of the backward Kolmogorov equation associated with a well-posed SDE. Then one concludes that the limiting model is given by this SDE.

5.4.2.2 *Limiting Equations*

In the case of small physical parameters, the system of equations Eq. 5.61 converges to a *single* limiting SDE. Three regimes will be studied below:

Regime 1: $\epsilon \to 0$, then $\delta \to 0$,

Regime 2: $\delta \to 0$, then $\epsilon \to 0$,

Regime 3: $\delta = \lambda\epsilon$, with $\lambda \in (0, \infty)$.

Physically, Regime 1 can be interpreted as $\epsilon \ll \delta \ll 1$, Regime 2 can be interpreted as $\delta \ll \epsilon \ll 1$ and in Regime 3, $\epsilon \sim \delta \ll 1$.

Recall that for Stochastic Differential Equations, the noise may be interpreted either with the Itô or the Stratonovich convention, and that formulations are equivalent when taking into account a correction term: the Itô SDE

$$\mathrm{d}X = b(X)\mathrm{d}t + a(X)\mathrm{d}W(t) \tag{5.66}$$

is equivalent to the Stratonovich SDE

$$\mathrm{d}X = \Big(b(X) + \frac{1}{2}a(X)a'(X)\Big)\mathrm{d}t + a(X) \circ \mathrm{d}W(t), \tag{5.67}$$

where the notation $a(X) \circ \mathrm{d}W(t)$ is used to precise that the Stratonovich convention is used. The Stratonovich formulation is convenient since it respects the chain rule, whereas for the Itô formulation one needs to use Itô's formula. However, the link between an infinitesimal generator, a SDE, and Kolmogorov or Fokker-Planck equations is more clearly seen when using the Itô formulation. Below, depending on the situation, the most convenient interpretation is chosen.

Below, we prove that the limiting equations are given by the following SDEs:

Regime 1: $\mathrm{d}Z = -\frac{g(Z)}{f(Z)}\mathrm{d}t + \sigma\sqrt{2}h(Z) \circ \mathrm{d}W(t)$

Regime 2: $\mathrm{d}Z = -\frac{g(Z)}{f(Z)}\mathrm{d}t - \frac{\sigma^2 h(Z)^2 f'(Z)}{f(Z)}\mathrm{d}t + \sigma\sqrt{2}h(Z)\mathrm{d}W(t)$

Regime 3: $\mathrm{d}Z = -\frac{g(Z)}{f(Z)}\mathrm{d}t - \frac{\sigma^2 h(Z)(hf)'(Z)}{(1+\lambda^2 f(Z))f(Z)}\mathrm{d}t + \sigma\sqrt{2}h(Z) \circ \mathrm{d}W(t)$

where $\big(W(t)\big)_{t\geq 0}$ is a standard real-valued Wiener process.

Importantly, taking limits $\epsilon \to 0$ then $\delta \to 0$ or $\delta \to 0$ then $\epsilon \to 0$ provides different limiting SDEs. This property originates from stratification. It is not surprising, since if f is a constant function, then the Itô formulation of the SDE of Regime 2 gives $\mathrm{d}Z = -\frac{g(Z)}{f(Z)}\mathrm{d}t + \sigma\sqrt{2}\frac{h(Z)}{f(Z)}\mathrm{d}W(t)$: the SDEs of Regime 1 and Regime 2 differ by an Itô-Stratonovich correction term. However, this observation does not hold if f is not constant: indeed the Itô formulation of the SDE of Regime 2 is

$$\mathrm{d}Z = -\frac{g(Z)}{f(Z)}\mathrm{d}t - \frac{\sigma^2 h^2(Z) f'(Z)}{f^3(Z)}\mathrm{d}t + \sigma\sqrt{2}h(Z)\mathrm{d}W(t). \tag{5.68}$$

More precisely, consider the case $h = 1$, with a non-constant f (this is the most important case in this study). Whereas Itô and Stratonovich interpretations coincide, the limiting SDEs differ by the presence of an additional *noise-induced drift* term (Hottovy et al. (2012), Hottovy et al. (2015), Herzog et al. (2016), and Freidlin and Hu (2011)) Observe that, formally, Regime 1 (resp. Regime 2) corresponds to Regime 3 when $\lambda = \infty$ (resp. $\lambda = 0$).

The physical consequence of this result is that one has to be extremely careful when choosing the Regime to interpret the dynamics of the system (see Appendix d.1 for detailed calculations).

5.4.3 *Steady-state dust distributions*

5.4.3.1 *Constant diffusivity*

In this section, it is assumed that $h = 1$ is a constant. As a consequence, Itô and Stratonovich interpretations of the limiting SDEs coincide, since the diffusion coefficient is constant. However, stratification means that f is not constant, thus a noise-induced drift term appears. With the convention that Regime 1 (resp. Regime 2) is obtained with $\lambda = \infty$ (resp. $\lambda = 0$), the limiting SDE is written as

$$\mathrm{d}Z = -\frac{g(Z)}{f(Z)}\mathrm{d}t - \frac{\sigma^2 f'(Z)}{(1+\lambda^2 f(Z))f(Z)}\mathrm{d}t + \sigma\sqrt{2}\mathrm{d}W(t). \tag{5.69}$$

This SDE is rewritten as the overdamped Langevin equation

$$\mathrm{d}Z = -\nabla\mathcal{V}_\lambda^\sigma(Z)\mathrm{d}t + \sigma\sqrt{2}\mathrm{d}W(t), \tag{5.70}$$

where the potential energy function $\mathcal{V}_\lambda^\sigma$ is defined as

$$\mathcal{V}_\lambda(z) = \mathcal{V}_\infty(z) + \mathcal{V}_{\mathrm{corr}}(z).$$

$\mathcal{V}_\infty$ denotes the antiderivative of g/f and $\mathcal{V}_{\mathrm{corr}}$ the antiderivative of $\sigma^2 f'/\left(\left[1+\lambda^2 f\right] f\right)$, i.e.

$$\mathcal{V}_{\mathrm{corr}} = \sigma^2 \log\left(\frac{f(z)}{1+\lambda^2 f(z)}\right).$$

As a consequence, under appropriate conditions on the growth at infinity of $\mathcal{V}_\lambda^\sigma$ (which are satisfied in the example considered below), the limiting SDE defines an ergodic dynamics, with unique invariant distribution having the density

$$\rho_\lambda^\sigma(z) = \frac{1}{Z_\lambda^\sigma}\exp\left(-\frac{\mathcal{V}_\lambda^\sigma(z)}{\sigma^2}\right), \tag{5.71}$$

with normalization constant $Z_\lambda^\sigma = \int_{-\infty}^{+\infty} e^{-\frac{\mathcal{V}_\lambda^\sigma(z)}{\sigma^2}}\mathrm{d}z$.

The parameters λ and σ may considerably change the qualitative properties of the potential energy function $\mathcal{V}_\lambda^\sigma$. For instance, choose the functions f and g as follows:

$$f(z) = e^{-\frac{z^2}{2}}\,, \quad g(z) = z,$$

which gives $\mathcal{V}_\infty(z) = e^{\frac{z^2}{2}}$. Observe that this potential energy function is convex, with a unique global minimum located at $z = 0$. However, straightforward computations give

$$\nabla\mathcal{V}_\lambda^\sigma(0) = 0\,, \quad \nabla^2\mathcal{V}_\lambda^\sigma(0) = \frac{1}{2} - \frac{\sigma^2}{1+\lambda^2},$$

thus 0 is not a minimum of $\mathcal{V}_\lambda^\sigma$ if $\sigma^2 > 1+\lambda^2$. Hence, the steady dust density can either be single- or double-hump shaped. For eddy times of order unity and typical disc parameters, the asymptotic distribution obtained from Eq. 5.71 does not differ much from the model of Fromang and Nelson (2009). This is not the case anymore in the diffusive limit $t_e \to 0$.

5.4.3.2 *Stratified diffusivity*

We address vertical gradients of the diffusivity α via the simple parametrisation $h(z) = f(z)^{-1/4}$ discussed in Sect. 5.3.2.1. We obtain

$$\mathcal{V}_{\rm corr}(z) = \sigma^2 \int \frac{h\,(fh)'}{(1+\lambda^2 f)\,f} \tag{5.72}$$

$$= -\frac{3\sigma^2}{4}\left\{\frac{2}{\sqrt{f}} + 2\lambda\tan^{-1}\left(\lambda\sqrt{f}\right).\right\}. \tag{5.73}$$

Hence,

$$\nabla\mathcal{V}_\lambda^\sigma(0) = 0\,, \quad \nabla^2\mathcal{V}_\lambda^\sigma(0) = \frac{1}{2} - \frac{3\sigma^2}{8\,(1+\lambda^2)}.$$

0 is therefore not a minimum of $\mathcal{V}_\lambda^\sigma$ if $\sigma^2 > \frac{4\left(1+\lambda^2\right)}{3}$. Except for a marginal set of nonphysical parameters, dust distributions that account form the vertical dependency of the diffusivity are almost similar to the one obtained for constant values of α. Stochastic turbulent driving scales as $\sqrt{\alpha}/\rho_{\rm g} \propto hf = f^{3/4}$ for our model, hence preserving the essential of the $h = 1$ settling mechanism.

5.4.3.3 *On the development of bumps in the diffusive limit*

A striking feature of the asymptotic distributions obtained in Sect. 5.4.3 is the development of dust over-concentrations above the midplane in the limit $t_{\rm e} \to 0$. Fig. 5.3 corroborates this finding by comparing the evolution of the two following oscillators

$$\ddot{z} + S_{\rm t0}^{-1}{\rm e}^{-z^2/2}\dot{z} + z = G\,S_{\rm t0}^{-1}{\rm e}^{-z^2/2}\sin(\omega t)\,, \tag{5.74}$$

and its linearised version

$$\ddot{z} + S_{\rm t0}^{-1}\dot{z} + z = G\,S_{\rm t0}^{-1}\sin(\omega t)\,, \tag{5.75}$$

for $S_{\rm t0} = 0.1$, $G = 2$, $\omega = 4.4$ and $z_0 = \dot{z}_0 = 0$ (those parameters are chosen to make the figure clear). G and ω parametrise the intensity and the frequency of the driving and play the role of α and $\tau_{\rm e}$ in the stochastic model. Fig. 5.3 shows spontaneous symmetry breaking between the top and the bottom layers of the stratified disc. Physically, the lift-up of small grains results from i) an important inertia when grains reach the top layers of the disc, ii) a modulated intensity of the turbulent driving by stratification that sets the maximum gradient of turbulent driving at one pressure scale height, and iii) a driving frequency that is large enough for this differential effect to cumulate. This is always the case when $\omega \to \infty$, which corresponds to $\tau_{\rm e} \to 0$. Hence, grains are constantly kicked from below by the differential driving and are lifted up above the midplane, explaining the formation of the dusty bumps.

5.5 NUMERICAL RESULTS

5.5.1 *Numerical scheme*

We now aim to validate Eq. 5.71, i.e. the formula obtained for the invariant distribution of the limiting SDE by direct numerical simulation of Eqs. 5.29,5.30,5.31. When changing

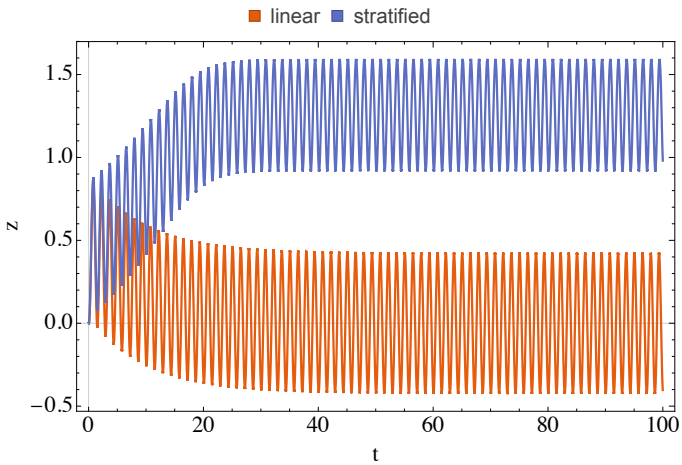

Figure 5.3: Evolution of dust grains driven by toy sinusoidal gas velocities. Lift-up of small grains resulting from the differential driving that originates form stratification (solid blue line). For an homogeneous disc, grains relax and oscillate around the midplane (solid red line). We adopt $S_{t0} = 0.1$, $G = 2$, $\omega = 4.4$ and $z_0 = \dot{z}_0 = 0$.

the parameters, we illustrate the apparition of double-humped shaped instead of single-humped distributions. Eqs. 5.29,5.30,5.31 are solved numerically with a Strang splitting method, observing that the sub-systems

$$\begin{aligned} \mathrm{d}Z &= 0, && (5.76)\\ \mathrm{d}V + S_{t0}^{-1} f_\phi(Z) V \mathrm{d}T + g_\phi(Z)\mathrm{d}T &= S_{t0}^{-1} f_\phi(Z) h(Z)\sqrt{2\alpha_0}\,\xi \mathrm{d}T, && (5.77)\\ \mathrm{d}\xi &= 0, && (5.78) \end{aligned}$$

and

$$\begin{aligned} \mathrm{d}Z &= V\mathrm{d}T, && (5.79)\\ \mathrm{d}V &= 0, && (5.80)\\ \mathrm{d}\xi &= -\frac{\xi}{\tau_e}\mathrm{d}T + \frac{\mathrm{d}w}{\tau_e}, && (5.81) \end{aligned}$$

can be solved exactly. On the one hand, the solution at any time $T > 0$ of the system of Eqs. 5.76,5.77,5.78 is given by

$$\Psi_t^{(1)}(Z_0, V_0, \xi_0) = \begin{cases} Z_0, \\ e^{-\frac{f_\phi(Z_0)T}{S_{t0}}} V_0 + \\ \left(1 - \mathrm{e}^{-\frac{f_\phi(Z_0)T}{S_{t0}}}\right)\left(h(Z_0)\sqrt{2\alpha_0}\,\xi_0 - \frac{S_{t0}}{f_\phi(Z_0)} g_\phi(Z_0)\right), \\ \xi_0. \end{cases} \tag{5.82}$$

On the other hand, the solution at any time $T > 0$ of the system of Eqs. 5.79,5.80,5.81 is given by

$$\Psi_t^{(2)}(Z_0, V_0, \xi_0) = \begin{cases} Z_0 + TV_0, \\ V_0, \\ \mathrm{e}^{-\frac{T}{\tau_e}}\xi_0 + \frac{1}{\tau_e}\int_0^T \mathrm{e}^{-\frac{T-T'}{\tau_e}}\mathrm{d}w(T'), \end{cases} \tag{5.83}$$

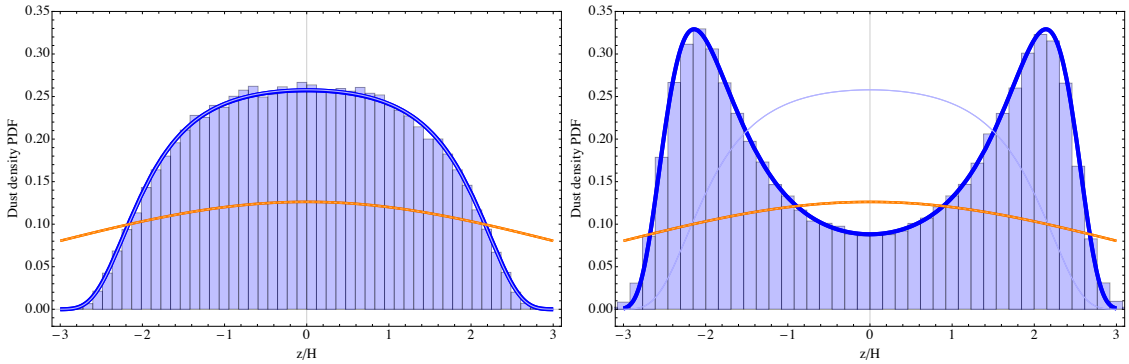

Figure 5.4: Left: Histogram obtained for 10^5 particles in a configuration where $\alpha = 0.01$, $S_{t,0} = 0.001$ and $\tau_e = 1$ after a time $t = 10^3$. The asymptotic solution obtained in Sect. 5.4.2 is represented by the solid thick blue line. Other curves represent predictions from the Dubrulle et al. (1995) model (dashed light blue line), the Youdin and Lithwick (2007) model (dot-dashed lighter blue line) and the Fromang and Nelson (2009) model (solid lightest blue line). The steady-state distribution is single-humped and is flatter than a Gaussian, as predicted by our model and the one of Fromang and Nelson (2009). Right: Similar plot, but for $\alpha = 0.1$, $S_{t,0} = 0.01$ and $\tau_e = 0.001$. This case corresponds to the purely diffusive limit, and grains are found to over-concentrate well above the midplane of the disc. This double-hump shape is recovered only by our asymptotic expansion.

where $\frac{1}{\tau_e}\int_0^t e^{-\frac{t-s}{\tau_e}} dw(s) \sim \mathcal{N}\left(0, \frac{1}{2\tau_e}(1 - e^{-\frac{2T}{\tau_e}})\right)$ follows a Gaussian distribution. Given a time-step size $\Delta T > 0$, then the Strang splitting scheme is defined by the recursion

$$(Z_{n+1}, V_{n+1}, \xi_{n+1}) = \left(\Psi^{(2)}_{\frac{\Delta T}{2}} \circ \Psi^{(1)}_{\Delta t} \circ \Psi^{(2)}_{\frac{\Delta T}{2}}\right)(Z_n, V_n, \xi_n)\,, \tag{5.84}$$

and each step is made of three succesive updates. Let $\gamma_{0,1}, \gamma_{0,2}, \ldots, \gamma_{n,1}, \gamma_{n,2}, \ldots$ be independent $\mathcal{N}(0,1)$ standard Gaussian random variables. First, using the definition of $\Psi^{(2)}_{\frac{\Delta T}{2}}$, and a random variable $\gamma_{n,1} \sim \mathcal{N}(0,1)$, let

$$\begin{cases} Z_n \leftarrow Z_n + \frac{\Delta T}{2} V_n, \\ V_n \leftarrow V_n, \\ \xi_n \leftarrow e^{-\frac{\Delta T}{2\tau_e}} \xi_n + \frac{1}{\sqrt{2\tau_e}} \sqrt{1 - e^{-\frac{\Delta T}{\tau_e}}}\, \gamma_{n,1}. \end{cases} \tag{5.85}$$

Second, using the definition of $\Psi^{(1)}_{\Delta T}$, let

$$\begin{cases} Z_n \leftarrow Z_n, \\ V_n \leftarrow e^{-\frac{f_\phi(Z_n)\Delta T}{S_{t0}}} V_n + \left(1 - e^{-\frac{f_\phi(Z_n)\Delta T}{S_{t0}}}\right)\left(h(Z_n)\sqrt{2\alpha_0}\,\xi_n - \frac{S_{t0}}{f_\phi(Z_n)} g_\phi(Z_n)\right), \\ \zeta_n \leftarrow \zeta_n. \end{cases} \tag{5.86}$$

Using the definition of $\Psi^{(1)}_{\frac{\Delta T}{2}}$ and a random variable $\gamma_{n,2} \sim \mathcal{N}(0,1)$,

$$\begin{cases} Z_n \leftarrow Z_n + \frac{\Delta T}{2} V_n, \\ V_n \leftarrow V_n, \\ \xi_n \leftarrow e^{-\frac{\Delta T}{2\tau_e}} \xi_n + \frac{1}{\sqrt{2\tau_e}} \sqrt{1 - e^{-\frac{\Delta T}{\tau_e}}}\, \gamma_{n,2}, \end{cases} \tag{5.87}$$

and one sets

$$Z_{n+1} \leftarrow Z_n\,, \quad V_{n+1} \leftarrow V_n\,, \quad \xi_{n+1} \leftarrow \xi_n. \tag{5.88}$$

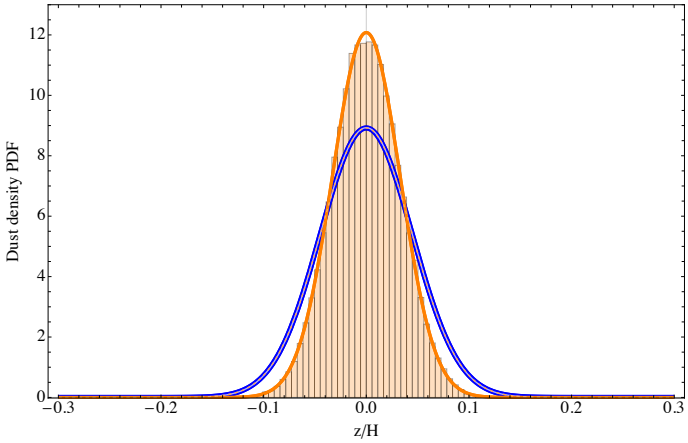

Figure 5.5: Similar to Fig. 5.4, but with $\alpha = 0.01$, $S_{t,0} = 5$ and $\tau_e = 1$, a regime where our asymptotic expansion is not valid. The model of Youdin and Lithwick (2007) is the most accurate in this regime.

5.5.2 *Numerical dust distributions*

We adopt a Courant-Friedrich-Levy condition of $\Delta t \propto S_{t0} \ll 1$ and use a safety factor of 0.1 gathered from a numerical convergence analysis. The probability density distributions reach steady-state for $t \sim S_{t0}^{-1}$, the settling time of small dust grains. Fig. 5.4 shows histograms obtained for 10^5 particles initially placed in the midplane with no velocity. In this configuration, sufficient accuracy is obtained to validate the model. Our first simulation consists of a seminal disc with $\alpha = 0.01$ and $\tau_e = 1$, populated with small grains with Stokes number in the midplane $S_{t,0} = 10^{-3}$. Fig. 5.4 (left) shows that the steady-state distribution is correctly reproduced by our asymptotic description and the Fromang and Nelson (2009) model, the two curves being nearly superimposed in this regime. In particular, flatter distributions than Gaussian are obtained. Stratification gradients push more grains from the midplane to the top layers of the disc than in an homogeneous configuration. Almost no grains above $z = 3$ are found. This is expected as there is almost no gas at this height and dust grains settle back to the midplane until they got stuck again. Our second simulation is designed to demonstrate the accuracy of our asymptotic expansion. We setup an academic configuration where $\alpha = 0.1$, $S_{t,0} = 10^{-2}$ and $\tau_e = 10^{-3}$ to reach the purely diffusive limit while preserving numerical tractability. Fig. 5.4 (right) shows that again, the steady-state distribution is correctly reproduced by our asymptotic expansion. In an obvious manner, the double-hump shape with strong over-concentrations of dust at $z \simeq 2$ is correctly captured. Alternative models predict incorrect bell-shaped distributions in this regime. In this regime, the rate of differential kicks received by the grains is extremely important and the cumulative contribution powers up the lift-up of the particles.

Importantly, these peaks can arise as a parasitic effect when equations of motion are integrated with stratification, inertia, but in the diffusive limit with zero eddy-time. Hence the necessity of integrating the settling equations including a finite turbulent timescales. Finally, it should be noted that our asymptotic expansion does not hold for large grains $S_{t,0} \gtrsim 1$ that remain close to the midplane. Fig. 5.5 shows that in that case, best accuracy is obtained by the Youdin and Lithwick (2007) model. Interestingly, finite eddy time terms gives noticeable corrections in this case as well.

5.6 DISCUSSION

The model of disc considered in this study remains fiducial. Gas does not undergo any dynamical evolution such as outflows, winds, viscous spreading or evaporation. We did not consider gravitating bodies embedded in the disc and have restrained the study to grains of constant size that neither grow nor fragment. We also focused on steady-state distributions, since they are widely used in as practical recipes for dust densities. As a short remark on this point, we note that steady-state is reached after a few settling times (Eqs. 5.29,5.30). For small grains, this time is orders of magnitude longer than other dynamical times in the disc. We put therefore a strong warning against using these formulae in vertically integrated models, to estimate instantaneous volume concentrations from surface densities. Finally, we note that dust lift-up may become significant in stratified objects that are trans- or supersonic and contain small grains, such as molecular clouds. In this case, dust may be lifted up easily by turbulence even when it develops on large integral timescales, as long as the cloud remains stable over a time that is sufficiently long for the grains to differentiate spatially.

5.7 CONCLUSION

In the context of better understanding observations of small dust grains in young discs, we derived refined analytic prescriptions for the distributions of small grains that populate their top layers. Our model includes gas stratification, dust inertia and finite correlation times for the turbulence. It is derived from first principles, by writing a balance of forces on a grain where stochastic driving mimics rigorously the statistical properties of homogeneous isotropic turbulence. The role of the vertical gradient of α is investigated using the scaling $\alpha \propto \rho^{-1/2}$, which ensures a constant density of turbulent energy through the disc. From rigorous asymptotic expansions, we obtained steady-state distributions for small grains scattered through the stratified disc by turbulence. Unexpected technicalities arise to handle small Stokes numbers in the diffusive limit. These novel distributions are validated against a direct numerical integration of the stochastic system via a Strang-splitting scheme. The main results of this study are summarised below.

1. Let consider a disc orbiting with frequency Ω and gas scale height H, for which the turbulent activity and the lifetime of the largest eddies are parametrised by α and t_e. We consider grains that have Stokes numbers in the midplane smaller than unity, i.e. $S_{t0} \ll 1$. Dust density a steady-state is given by

$$\rho_d(z) \propto \left(\frac{t_e \Omega}{S_{t0}} + e^{\frac{z^2}{2H^2}} \right) \exp\left(- \frac{e^{\frac{z^2}{2H^2}}}{\alpha / S_{t0}} \right), \tag{5.89}$$

   which corresponds to Eq. 5.71 expressed in physical quantities.

2. For $t_e \sim \Omega^{-1}$, dust distributions are single-humped and flattened. In the purely diffusive limit $t_e \ll \Omega^{-1}$, dust distributions become bumpy and develop non-physical strong peaks at $z \geq H$. As such, turbulent correlations must be handled with care in settling models.

3. Observations support the absence of dust over-concentrations above the scale height of young disc, hence corroborating numerical experiments predicting $t_e \sim \Omega^{-1}$.

Trans- or supersonic stratified systems such as molecular clouds may enter the regime of parameters where dust lift-up may becomes important and should deserve further investigations.

6

VLT/SPHERE SURVEY FOR EXOPLANETS AROUND YOUNG EARLY-TYPE STARS

6.1 Context 103
6.2 Introduction 105
6.3 Target Properties 106
6.4 Observations 106
6.5 Data reduction and analysis 109
6.6 Companion candidate detection and characterization 112
6.7 Detection limits and survey completeness 115
6.8 Discussion 116
6.9 Conclusions 119

"I am from the planet of elegance." – Ron Carter

6.1 CONTEXT

Two decades ago, the only planets we knew were the ones of our Solar System. Nowadays, with the important development of space and ground based telescopes, dedicated instrumentation and observing technics, thousands of exoplanets have been discovered, which is a significant step toward the search for other worlds and exo-Life. In this context, the role of observations to detect and characterize exoplanets and planetary architectures is essential to improve our understanding of planetary formation and evolution, as well as of the physics of exoplanets. Since the first exoplanet discovery around the main-sequence star 51 Peg in 1995 Mayor and Queloz (1995), key discoveries were obtained in exoplanetary science with: i/ the detection and confirmation of about 4500 exoplanets today (http://exoplanet.eu), ii/ the discovery of the Hot-Jupiter family, composed of gaseous giants similar to Jupiter but located at a few stellar radii from the star, iii/ the first glimpse of planetary atmosphere characterization, iv/ the direct images of Super-Jupiters around their host stars, v/ the discovery of Super-Earths in the Habitable Zone, where water should be at the liquid state.

Today, the five main techniques currently used to detect exoplanets are: radial velocity, transit, micro-lensing, direct-imaging and astrometry. They are complementary and can be combined to constrain the planet properties like density (with radial velocity and transit) or the internal energy (combining radial velocity/astrometry and imaging). Fig. 6.1 shows today's confirmed exoplanets detected by those different methods. Radial velocity, transit, micro-lensing and astrometry are mostly sensitive to the internal part of exoplanetary systems, at less than typically $5-10$ au. Direct imaging is here unique to explore the outer regions beyond $5-10$ au to complete our view of planetary system architectures. Moreover, direct imaging enables to resolve the photons of exoplanets and thus to probe the planet's luminosity and atmospheric properties. All exoplanets currently imaged are young, as they are hotter, brighter, and thus easier to detect than their old counterparts. As a consequence, their atmospheres reveal low-gravity features, as well as the presence of thick cloud layers, and non-equilibrium chemistry processes. These physical observations are very different and complementary to the ones observed in the atmospheres of irradiated Hot Jupiters studied with transit techniques. Finally,

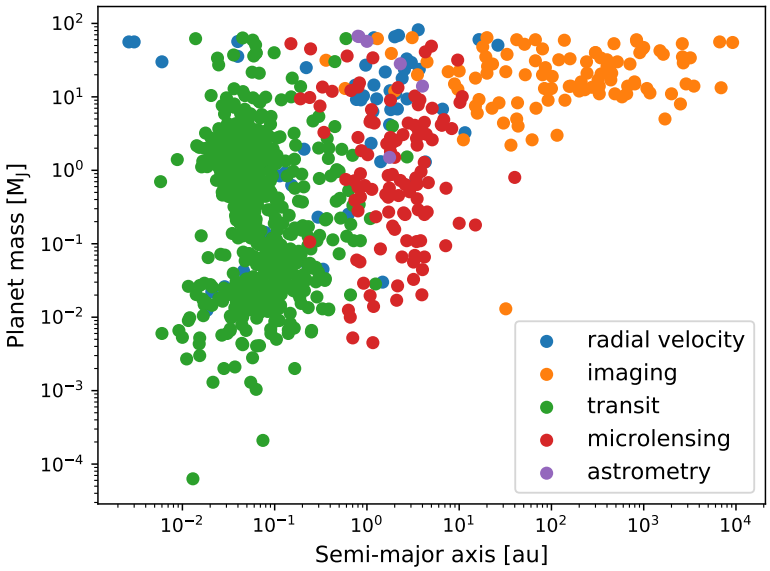

Figure 6.1: Exoplanets discoveries nowadays considering the different planet hunting techniques (from http://exoplanet.eu). The exoplanets masses are reported as a function of their distances to the star.

direct imaging (DI) enables to directly probe the presence of planets in their birth environment within circumstellar disks to study the formation and evolution processes in action (Keppler et al., 2018; Christiaens et al., 2019; Keppler et al., 2019; Boccaletti et al., 2020a).

During my M2 internship supervised by Dr. G. Chauvin at the Franco-Chilean Laboratory for Astronomy in Santiago, I carried out the complete analysis of a direct imaging survey to search for young, giant planets. I analysed data from the VLT/SPHERE extreme Adaptive Optics (xAO) planet imager obtained in the course of the Open Time program DUSTIES (Dusty, yoUng and early-type Star Imaging for ExoplanetS). This program is dedicated to the search for and the characterization of giant planets around young, nearby stars hosting multi-belt system to maximize the chances of discoveries. Key questions studied are the physical properties of young Jupiters and their interaction with belt architecture. I used the SPHERE Data Reduction and Handling automated pipeline to perform the data reduction (Pavlov et al., 2008). During that period, I had the chance to participate to a SPHERE observing run from June 3th to June 7th, 2017 to witness in real time performances and limitations of xAO imagers.

Companion candidates have been detected after the data reduction process. Follow-up observations of these candidates were automatically scheduled, during 2018 and 2019. These new observations were performed in J_2J_3 bands to distinguish bound companions from background star. No new exoplanets were found that could be in addition connected to the multi-belt architectures known for these systems. I could however set robust constraints on the presence of giant planets in these systems, paving the way to future characterization with new generation for planet imagers at VLT and ELT. This study was completed during my Ph.D leading to a publication of the paper Lombart, M. et al. (2020). The details of this paper is presented in the following parts.

6.2 INTRODUCTION

How giant planets form and evolve is one of the biggest challenges of modern astronomy and remains a subject of heated debate. This major goal is directly connected to the ultimate search for life over the horizon 2030 to 2040, although several astrophysical (formation, evolution, dynamics, structure, and atmosphere), biological (bio-markers), and technical (new technologies developed for next generation of instrumentation) steps must be carried out in that perspective. Understanding how giant planets are formed and structured, how they evolve and interact, is critical as they completely shape the planetary system architectures and therefore the possibility of forming telluric planets capable of hosting life. More than two decades ago, the only planets we knew were the ones of our Solar System. With the manna of exoplanet discoveries since the 51 Peg discovery (Mayor and Queloz, 1995), the diversities of systems found (hot Jupiters, irradiated and evaporating planets, misaligned planets with stellar spin, planets in binaries, telluric planets in habitable zones, discovery of Mars-sized planets...), the theories of planetary formation have drastically evolved to digest these observing constraints. However, we are still missing the full picture, and some key fundamental questions still lack answers. For example: i/ the physical processes at play to pass the km-size barrier to form planetary cores, ii/ the physics of accretion to form planetary atmospheres, iii/ the formation mechanisms to explain the existence of giant planets at wide orbits, iv/ the physical properties of young Jupiters, v/ the impact of planet-planet and planet-disk interaction in the final planetary system architecture, or vi/ the influence of the stellar mass and stellar environment in the planetary formation processes. Neither core accretion plus gas capture (CA; Pollack et al. (1996)) nor disk fragmentation driven by gravitational instabilities (GI; Cameron (1978)) can globally explain all current observables from planet hunting techniques. Alternative mechanisms are then proposed, such as pebbles accretion to enable core accretion to operate at wide orbits (Lambrechts and Johansen, 2012), inward/outward migration or planet-planet (Crida et al., 2009; Bromley and Kenyon, 2014) or simply the possibility to have several mechanisms forming giant planets (Boley, 2009). In this context, each individual discovery of a giant planet and young planetary system using direct imaging is rich in terms of scientific exploitation and characterization, as these systems offer the possibility of i/ directly probing the presence of planets in their birth environments, ii/ enabling the orbital, physical, and spectral characterization of young massive Jupiters, iii/ characterizing the population of giant planets at all separations in synergy with complementary techniques such as astrometry (*GAIA*) and radial velocity adapted to filter stellar activity.

Dusty debris disks around pre- and main-sequence stars are possible signposts for the existence of planetesimals and exoplanets (Matthews et al., 2014). Numerous T Tauri and Herbig stars indicate that the characteristic timescale for the dispersal of a surrounding dusty, gaseous disk is a few million years (Kennedy and Kenyon, 2008). Giant planet formation is therefore expected to play a key role in the evolution of disk. This is indirectly confirmed by extant submillimeter and near-infrared images of cool dusty debris disks around main-sequence stars usually showing substantial spatial structure (e.g., ϵ Eri, Vega, Fomalhaut, β Pic; see Schneider et al. (2014)). It is striking to note that a majority of recent discoveries of imaged giant planets have been obtained around young, dusty, early-type stars. It includes the breakthrough discoveries of Fomalhaut b (3 $M_{\rm Jup}$ at 110 AU, A4V star; Kalas et al. (2008)), HR 8799 bcde (5-10 $M_{\rm Jup}$ at 10-64 au, FoV star; Marois et al. (2010)), β Pictoris b (8-13 $M_{\rm Jup}$ at 9 au, A5V star; Lagrange et al. (2010)), HD 95086 b (3-5 $M_{\rm Jup}$ at 56 au, A8V star; Rameau et al. (2013)), and more recently

51 Eri b (2 $M_{\rm Jup}$ at 14 au, FoV star; Macintosh et al. (2015)). The presence of dust and the spatial substructure (ring, gap, warp, and other asymmetries) are possible indirect indicators of the presence of giant planets (Mouillet et al., 1997; Dipierro et al., 2015; Pinte et al., 2020). Direct imaging is here a unique and viable technique to complete our view of planetary system characteristics at wide orbits ($\geq$ 5 au). This technique enables us to directly study the planet-disk connection to constrain the planet's and disk's physical properties, evolution, and formation. In the case of β Pictoris, Lagrange et al. (2012) confirmed that β Pic b was actually responsible for the disk inner warp geometry, perturbing the planetesimals field and shaping the warp up to 40-60 au. The stars HD 95086 and HR 8799 share a common two-component architecture consisting of a warm inner belt ($\leq$ 5 au) and a cold outer disk (100 $-$ 200 au) (see Su et al. (2015)). Kennedy and Wyatt (2014) actually showed that the spectral energy distributions of both systems are consistent with two-temperature components compatible with dust emission arising from two distinct radial locations. Such an architecture would be analogous to the outer Solar System's configuration of asteroid and Kuiper belts separated by giant planets. Therefore, following the strategy of our NaCo DUSTIES (Dusty, yoUng, and early-type STar Imaging for ExoplanetS) survey (Rameau et al., 2013) that led to the discovery of HD 95086 b, we initiated a searching for giant planets with SPHERE at VLT around an newly identified sample of young early-type stars with indication for some cases of multi-belt architecture to maximize the chances of discoveries. The sample, the observations, and the data reduction and analysis are presented in Sections 6.3, 6.4 and 6.5, respectively. The results are reported in Section 6.6 and discussed in Section 6.7.

6.3 TARGET PROPERTIES

The target selection of the survey was obtained from a large sample of young, nearby early-type stars according to the following criteria: declination ($\delta \leq 25^o$), age ($\leq$ 100 Myr), distance ($\leq$ 100 pc), and R-band brightness ($\leq$ 9.5) to favor good adaptive optics performances. Age selection criteria were applied based on different youth diagnostics (kinematics, isochrones, Lithium, H_α emission, X-ray activity, stellar rotation, and chromospheric activity). We also used, as selection criteria, the presence of significant 60 $-$ 70 μm excess from the *IRAS* and *Spitzer* missions in the spectral energy distributions (Zuckerman et al., 1995; Zuckerman, 2001; Rhee et al., 2007; Zuckerman and Song, 2004a; Zuckerman and Song, 2004b; Zuckerman et al., 2011; Zuckerman et al., 2013; David and Hillenbrand, 2015; Moór et al., 2016) or the existence of multi-belt component analysis from Kennedy and Wyatt (2014). A final total of 30 late-B-, A-, and early-F-type young stars, observable from the southern hemisphere, were then kept, 22 of which were observed between October 2016 and August 2019. Their stellar properties are reported in Table 1. The age, distance, spectral type, and IR excess properties are shown in Figure 6.2.

6.4 OBSERVATIONS

The SPHERE planet-finder instrument installed at the VLT (Beuzit et al., 2019) is a highly specialized instrument, dedicated to high-contrast imaging and spectroscopy of young giant exoplanets. It is based on the SAXO extreme adaptive optics (XAO) system (Fusco et al., 2006; Sauvage et al., 2010; Petit et al., 2014), which controls a deformable mirror with 41 $\times$ 41 actuators, and four control loops (fast visible tip-tilt, high-orders, near-infrared differential tip-tilt, and pupil stabilization). The common path optics employ several stress-polished toric mirrors (Hugot et al., 2012) to transport the beam to the

Target	RA(2000)	DEC(2000)	μ_α (mas/yr)	$\mu_\delta.\cos(\delta)$ (mas/yr)	H (mag)	SpT	Dist. (pc)	Age (Myr)	Exc.	References
HIP3277	00 41 46.3	-56 30 04.73	90.79	57.19	5.6	A3V	67	93^{+283}_{-76}	/	D15
HIP7345	01 34 37.7	-15 40 34.89	94.84	-3.14	5.5	A1V	61	35^{+5}_{-5}	Y	Z95; Z12; G16
HIP7805	01 40 24.0	-60 59 53.62	61.94	-10.50	6.7	F2V	66	30^{+15}_{-15}	Y	Z01; Z04; M17
HIP8832	01 53 31.8	+19 17 37.87	79.20	-97.63	2.8	A0	50	87^{+195}_{-71}	/	D15
HIP9902	02 07 26.1	-59 40 45.942	91.11	-18.29	6.2	F7V	44	45^{+4}_{-4}	Y	K14; B15
HIP13141	02 49 01.4	-62 48 23.47	94.02	29.10	5.2	A2V	50	100^{+200}_{-70}	Y	R07; G16
HIP16095	03 27 18.6	+12 44 07.03	10.36	-7.56	6.3	A0V	88	194^{+171}_{-138}	/	Z13; D15
HIP18437	03 56 29.3	-38 57 43.80	29.46	0.10	6.8	A0V	100	187^{+150}_{-177}	Y	R07; M17
HIP19990	04 17 15.6	+20 34 42.93	-39.41	-60.79	4.6	A3	29	70^{+30}_{-40}	/	Z13; G16
HIP22192	04 46 25.7	-28 05 14.8	-3.82	17.58	5.7	A3V	56	12^{+5}_{-5}	/	Z13; G16
HIP22226	04 46 49.5	-26 18 08.84	34.52	-4.13	6.9	F3V	78	30^{+20}_{-20}	Y	R07; G16
HIP22845	04 54 53.7	+10 09 02.99	41.49	-128.73	4.5	A3V	34	100^{+200}_{-70}	Y	Z04b; G16
HIP26309	05 36 10.2	-28 42 28.847	25.80	-3.04	5.9	A2V	56	30^{+20}_{-10}	/	Z11; G16
HIP26990	05 43 35.8	-39 55 24.7145	25.82	15.08	6.8	G0V	55	42^{+8}_{-7}	Y	M16; V17
HIP34276	07 06 20.9	-43 36 38.69	5.80	13.20	6.5	A0V	102	185^{+120}_{-170}	Y	R07; M17
HIP41307	08 25 39.6	-03 54 23.11	-66.43	-23.41	3.9	A0V	37	203^{+100}_{-100}	Y	R07; M17
HIP93542	19 03 06.8	-42 05 42.38	56.41	-46.43	5.0	B9V	59	76^{+148}_{-62}	Y	R07; D15
HIP95619	19 26 56.4	-29 44 35.617	18.63	-50.13	5.7	B8.5	70	86^{+138}_{-69}	Y	D15
HIP97749	19 51 50.6	-39 52 27.7	18.42	-11.27	5.4	A	100	82^{+177}_{-67}	/	D15
HIP101800	20 37 49.1	+11 22 39.63	39.15	-8.26	5.4	A1V	57	225^{+311}_{-43}	Y	R07; D15
HIP101958	20 39 38.2	+15 54 43.46	53.82	8.47	3.9	B9V	77	60^{+164}_{-49}	/	D15
HIP117452	23 48 55.5	-28 07 48.97	100.80	-105.34	4.6	A0V	42	70^{+30}_{-40}	Y	Z11; D15

Table 6.1: Description and properties of the sample. The Exc. column indicates the presence of an IR excess. The symbol "/" means no IR excess, and "Y" means with IR excess. References: (B15) Bell et al. (2015); (D15) David and Hillenbrand (2015); (G16) Galicher et al. (2016); (K14) Kennedy and Wyatt (2014); (M16) Moór et al. (2016); (M17) Meshkat et al. (2017); (R07) Rhee et al. (2007); (V17) Vigan et al. (2017); (Z95) Zuckerman et al. (1995); (Z01) Zuckerman (2001); (Z04) Zuckerman and Song (2004a);(Z04b) Zuckerman and Song (2004b); (Z11) Zuckerman et al. (2011); (Z12) Zuckerman and Song (2012); (Z13) Zuckerman et al. (2013).

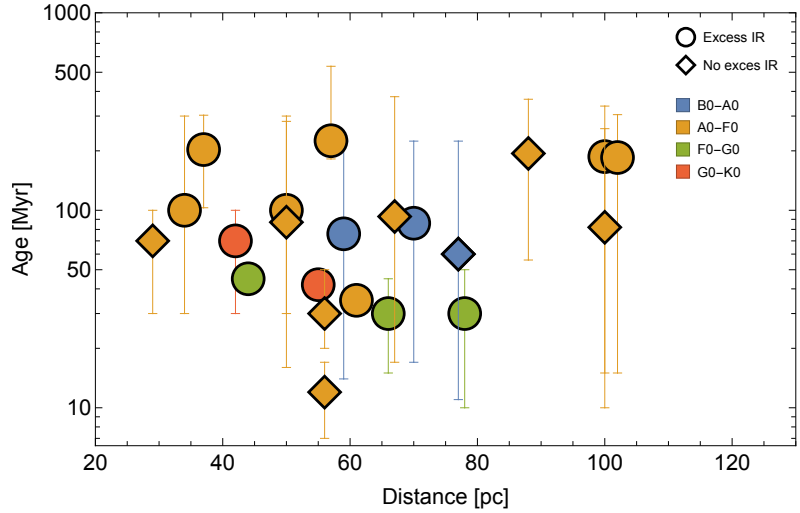

Figure 6.2: Diagram of target properties taking into account age with error bars, distance, spectral type, and excess in infrared.

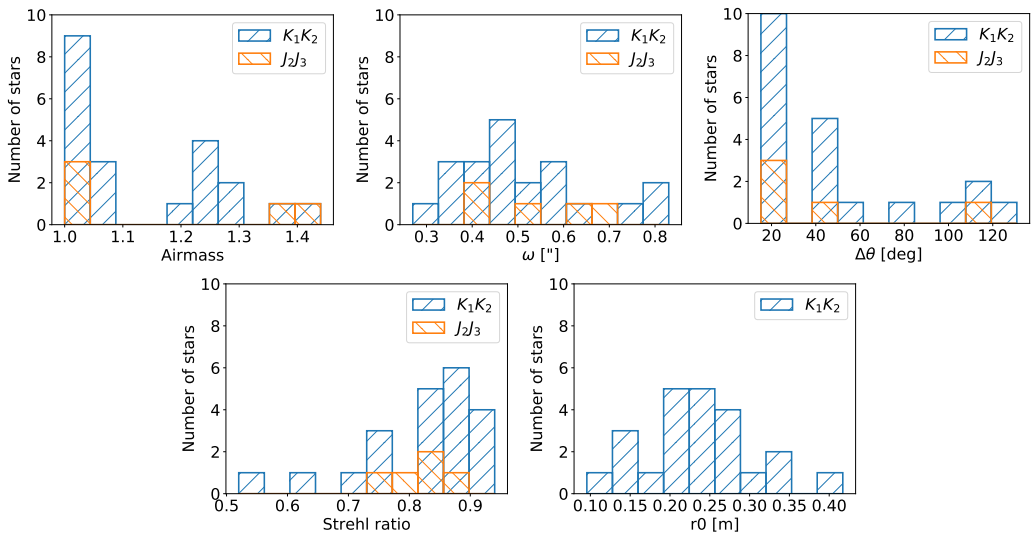

Figure 6.3: Distribution of the SAXO real-time parameters, averaged over each observing sequence, for the complete survey: airmass, DIMM seeing (ω), parallactic angle variation ($\Delta\theta$), the Strehl ratio at 1.6 μm, and the Fried parameter of the atmosphere (r_0).

coronagraphs and scientific instruments. Several types of coronagraphic devices for stellar diffraction suppression are provided, including apodized pupil Lyot coronagraphs (Soummer, 2005) and achromatic four-quadrant phase masks (Boccaletti et al., 2008). The instrument has three science subsystems: the infrared dual-band imager and spectrograph (IRDIS, Dohlen et al. (2008)), an integral field spectrograph (IFS; Claudi et al. (2008)), and the Zimpol rapid-switching imaging polarimeter (ZIMPOL; Thalmann et al. (2008)).

The sample of young early-type stars was observed using the IRDIFS-EXT mode, with IRDIS in the dual-band imaging (DBI, Vigan et al. (2010)) mode with K_1K_2 filters ($\lambda_{K_1} = 2.1025 \pm 0.1020, \mu$m - $\lambda_{K_2} = 2.2550 \pm 0.1090, \mu$m), and IFS in the $Y - H$ ($0.97 - 1.66\,\mu$m) mode in pupil-tracking. This combination enables the use of angular and/or spectral differential imaging techniques to improve the contrast performances at the subarcsecond level (Racine et al., 1999; Marois et al., 2006). The choice between IRDIFS mode and

IRDIFS-EXT mode is critical to optimizing the detection of young, early-T, or warm, mid-L dwarfs planets, considering the primary age and distance. Indeed, it was crucial in the cases of the β Pic b (Lagrange et al., 2009) and HD 95086 b (Rameau et al., 2013) discoveries to properly remove quasi-static speckles that dominate performance detection at close inner angles ($0.1 - 2.0''$, i.e., $3 - 60$ au at 30 pc), but to also maximize the emitted flux by the giant planets. For young ages ($10 - 50$ Myr), as the potential planets to which we are mostly sensitive are warm and dusty L-type planets with no methane absorption, the choice of the IRDIFS-EXT mode is more appropriate and was chosen for this observing campaign. For the follow-up, as candidates were only detected in the IRDIS field of view, we opted for the use of the IRDIS the DBI mode with J_2J_3 filters ($\lambda_{J_2} = 2.1025 \pm 0.1020\,\mu$m - $\lambda_{J_3} = 2.2550 \pm 0.1090\,\mu$m) in pupil-tracking. Thus, this second epoch provides, in addition to the possibility of checking for common proper motion of the candidates relative to the primary star, the possibility to better discriminate background stars from physically young, early-T, or warm mid-L dwarfs planets in the color-magnitude diagram (Bonnefoy et al., 2018).

The observing sequence used for the survey is as follows; PSF flux reference, coronographic centering using the waffle spots, deep coronographic observation of about 70 min in total on target, new coronographic centering using the waffle spots, PSF flux reference, and sky. The PSF flux references were used to estimate the relative photometry of the companion candidates detected in the IRDIS and IFS field of view, as well as the detection limits. The coronographic centering sequence using the waffle spots sequence is critical to obtaining the position of the star behind the coronograph and the relative astrometry of the companion candidates. The deep coronographic observation was obtained close to meridian to maximize the field rotation. Finally, the sky background was used to optimize the background subtraction and the flat field correction. The typical observing sequence lasts approximately 90 min, including pointing and overheads. The detail of the observations per target is reported in Table 6.2. As a by-product of the SPHERE observation, one can access the evolution of the different atmospheric parameters seen and registered by the SPHERE XAO system (SAXO). These real-time parameters are good diagnostics of the turbulence conditions (τ_0, r_0, integrated wind over the line of sight) and of the XAO correction (Strehl at 1.6 μm) during the observing sequence. The summary of these SAXO parameters over the full survey is reported in Table 6.2 and shown in Figure 6.3. Given the brightness of our targets, about 70 % of the survey was obtained under median or good conditions for Paranal, with a typical Strehl ratio larger than 80 %. Prior to the UT3 intervention at VLT in 2017, a few cases were affected by the low-wind effect, despite good atmospheric conditions.

6.5 DATA REDUCTION AND ANALYSIS

In order to calibrate the IRDIS and IFS dataset on sky, the platescale and true north solution at each epoch were corrected based on the long-term analysis of the SPHERE Guaranteed Time Observation astrometric calibration described by Maire et al. (2016). The rotation correction considered to align images to the detector vertical in pupil-tracking observations is $-135.99 \pm 0.11°$. Anamorphism correction was obtained by stretching the image Y-direction with a factor of 1.0060 ± 0.0002. All IRDIS and IFS datasets were reduced using the SPHERE Data Reduction and Handling (DRH) automated pipeline (Pavlov et al., 2008) and additional IDL routines for the IFS data reduction (Mesa et al., 2015) at the SPHERE Data Center (Delorme et al., 2017) to correct each data cube for bad pixels, dark current, flat field, and sky background. After combining all data cubes with an adequate calculation of the parallactic angle for each individual frame of the deep

UT Date	Target	Instru.	Mode	Filter	NDIT × DIT (s)	N_{exp}	$\Delta\theta$ (^{o})	ω (")	Strehl 1.6μm	Airmass
				Survey						
05-10-2016	HIP9902	IRDIS	DBI	K_1K_2	3×64	46	20.7	0.62	0.75	1.22
		IFS	$R_\lambda = 30$	YJH	1×64					
	HIP18437	IRDIS	DBI	K_1K_2	3×64	46	44.2	0.47	0.77	1.03
		IFS	$R_\lambda = 30$	YJH	1×64					
07-10-2016	HIP7805	IRDIS	DBI	K_1K_2	3×64	46	20.0	0.53	0.83	1.24
		IFS	$R_\lambda = 30$	YJH	1×64					
	HIP16095	IRDIS	DBI	K_1K_2	3×64	46	19.0	0.46	0.87	1.26
		IFS	$R_\lambda = 30$	YJH	1×64					
08-10-2016	HIP13141	IRDIS	DBI	K_1K_2	3×64	46	20.8	0.41	0.83	1.30
		IFS	$R_\lambda = 30$	YJH	1×64					
10-11-2016	HIP19990	IRDIS	DBI	K_1K_2	3×64	46	22.6	0.27	0.94	1.30
		IFS	$R_\lambda = 30$	YJH	1×32					
12-11-2016	HIP26309	IRDIS	DBI	K_1K_2	3×64	46	107.4	0.41	0.87	1.01
		IFS	$R_\lambda = 30$	YJH	1×64					
13-11-2016	HIP22192	IRDIS	DBI	K_1K_2	7×32	46	130.9	0.33	0.86	1.01
		IFS	$R_\lambda = 30$	YJH	1×32					
04-12-2016	HIP7345	IRDIS	DBI	K_1K_2	3×64	17	81.4	0.44	0.90	1.02
		IFS	$R_\lambda = 30$	YJH	1×64					
05-12-2016	HIP22226	IRDIS	DBI	K_1K_2	3×64	46	15.2	0.42	0.82	1.00
		IFS	$R_\lambda = 30$	YJH	1×64					
07-12-2016	HIP22845	IRDIS	DBI	K_1K_2	3×64	46	19.3	0.44	0.82	1.27
		IFS	$R_\lambda = 30$	YJH	1×32					
13-12-2016	HIP34276	IRDIS	DBI	K_1K_2	8×32	46	39.5	0.55	0.84	1.06
		IFS	$R_\lambda = 30$	YJH	1×64					
15-12-2016	HIP26990	IRDIS	DBI	K_1K_2	3×64	46	42.6	0.55	0.76	1.04
		IFS	$R_\lambda = 30$	YJH	1×64					
	HIP41307	IRDIS	DBI	K_1K_2	17×16	46	43.0	0.35	0.92	1.03
		IFS	$R_\lambda = 30$	YJH	1×16					
17-06-2017	HIP93542	IRDIS	DBI	K_1K_2	7×32	46	59.5	0.83	0.69	1.05
		IFS	$R_\lambda = 30$	YJH	1×32					
	HIP97749	IRDIS	DBI	K_1K_2	7×32	46	43.3	0.81	0.52	1.06
		IFS	$R_\lambda = 30$	YJH	1×32					
06-07-2017	HIP101800	IRDIS	DBI	K_1K_2	7×32	42	22.1	0.58	0.86	1.24
		IFS	$R_\lambda = 30$	YJH	1×32					
15-07-2017	HIP117452	IRDIS	DBI	K_1K_2	6×32	46	117.1	0.45	0.87	1.01
		IFS	$R_\lambda = 30$	YJH	1×32					

Table 6.2: Observing Log

UT Date	Target	Instru.	Mode	Filter	NDIT × DIT (s)	N_{exp}	$\Delta\theta$ (^{o})	ω (")	Strehl 1.6μm	Airmass
				Survey						
20-07-2017	HIP101958	IRDIS	DBI	K_1K_2	15×16	46	23.4	0.45	0.90	1.36
		IFS	$R_\lambda = 30$	YJH	1×16					
31-07-2017	HIP95619	IRDIS	DBI	K_1K_2	7×32	46	110.0	0.77	0.62	1.01
		IFS	$R_\lambda = 30$	YJH	1×32					
09-08-2017	HIP8832	IRDIS	DBI	K_1K_2	15×16	46	22.5	0.35	0.89	1.40
		IFS	$R_\lambda = 30$	YJH	1×16					
10-09-2017	HIP3277	IRDIS	DBI	K_1K_2	7×32	46	26.5	0.54	0.83	1.20
		IFS	$R_\lambda = 30$	YJH	1×32					
				Follow-up						
27-09-2018	HIP117452	IRDIS	DBI	J_2J_3	6×32	22	112.7	0.41	0.88	1.00
10-10-2018	HIP8832	IRDIS	DBI	J_2J_3	4×48	23	20.4	0.61	0.78	1.00
22-11-2018	HIP34276	IRDIS	DBI	J_2J_3	4×64	23	46.3	0.39	0.82	1.44
09-05-2019	HIP95619	IRDIS	DBI	J_2J_3	7×32	23	22.3	0.51	0.75	1.02
18-06-2019	HIP101800	IRDIS	DBI	J_2J_3	7×32	23	20.2	0.68	0.83	1.36

Table 6.2: Observing Log (cont.)

coronagraphic sequence, all frames were shifted at the position of the stellar centroid calculated from the initial star center position.

For an independent check, two pipelines were then used to process the data in angular differential imaging (ADI), and in combined spectral and angular differential imaging (ASDI): the IPAG-ADI pipeline (Chauvin et al., 2012), and the SpeCal (Galicher et al., 2018). These routines allowed us to reduce the data cubes with almost the same set of algorithms (classical ADI, Marois et al. (2006); LOCI, Lafrenière et al. (2007); PCA,Soummer et al. (2012); Andromeda, Cantalloube et al. (2015)), and to exploit the spectral diversity of the IRDIS and IFS observations using ASDI techniques in addition to ADI only. Following the principles described in Galicher et al. (2018), SpeCal (and IPAG-ADI) delivers, for various algorithms and observing techniques (ADI, ASDI), contrast curves, signal-to-noise ratio (S/N) maps, and the possibility to locally characterize the astrometric, photometric, and spectroscopic signal of any companion candidate using either a template or negative fake planet injection approach. As consistent results were found with both pipelines, the full set of observations was reduced with SpeCal (routinely used with the SPHERE GTO) using the TLOCI algorithm (in ADI and ASDI) for IRDIS, and the PCA algorithm (in ASDI) for IFS. A spatial filtering for each data cube was automatically applied to the deep coronographic observations and the reference PSFs before the use of SpeCal.

The TLOCI algorithm is implemented in SpeCal, to attenuate the background signal. The TLOCI algorithm locally subtracts the stellar speckle pattern for each frame in annuli of $1.5 \times FWHM$ further divided into sectors. The subtraction is based on a linear combination of the best 20 (N parameter) correlated reference images calculated in the optimization region and selected to minimize the self-subtraction at a maximum of 20% (τ parameter), see Galicher et al. (2011) and Marois et al. (2014) for a further description

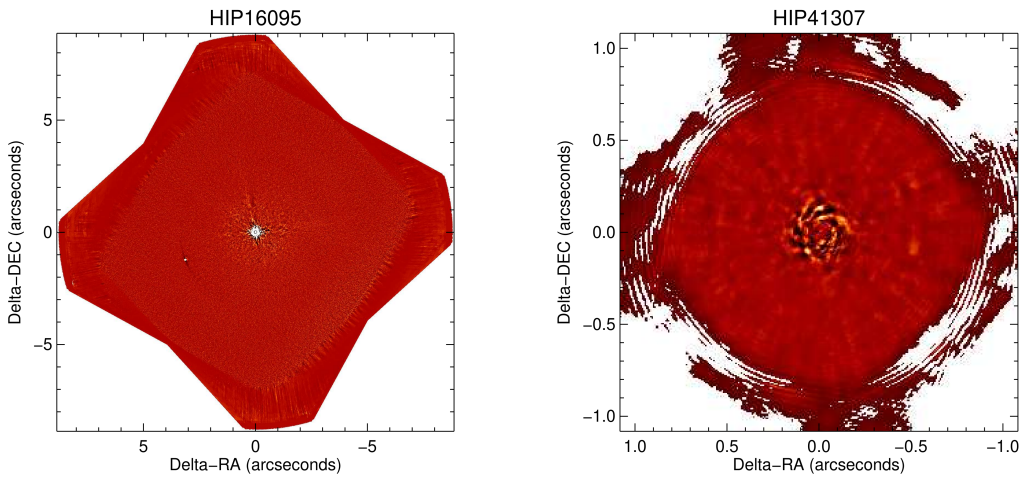

Figure 6.4: Left: IRDIS reduced full-frame image of HIP 16095 in the K_1 and K_2 combined filters using SpeCal with the TLOCI algorithm (Galicher et al., 2011). A bright companion candidate is well identified at a few arcseconds to the east of the star. North is up, and east is left. Right: IFS image reduced in PCA ASDI of HIP 41307.

of the reference frame selection and the subtraction and optimization regions. For IFS, in the PCA version, each frame we used is subtracted from its average over the field of view to estimate the principal components. The spectral diversity is exploited after proper rescaling and renormalization of the IFS data cubes as detailed by (Mesa et al., 2015). Considering the significant field rotation of our observations, the first 100 principal components were subtracted.

6.6 COMPANION CANDIDATE DETECTION AND CHARACTERIZATION

Using the IRDIS and IFS S/N maps provided by SpeCal, we identified a total of eight companion candidates by eye at relatively large separation ($\geq$ 3.0″) in the IRDIS fields of view of six targets (HIP 16095, HIP 95619, HIP 101800, HIP 34276, HIP 117452, and HIP 8832) of the complete survey. One companion candidate was identified at relatively close separation in the IFS field of view of HIP 41307, but later flagged as a bright quasi-static speckle through various processing tests, and was therefore discarded.

Figure 6.4 shows the IRDIS image reduced in TLOCI ADI of HIP 16095 (bright companion located at 3.3″ in the K_1 and K_2 combined filters), and the IFS image reduced in PCA ASDI of HIP 41307 (quasi-static speckle discarded located at 0.5″ in the combined *YJH*-bands) as an illustration of the detection process. All companion candidates were then characterized using SpeCal with the TLOCI algorithm in ADI only, and according to a template approach. The relative astrometry and photometry are reported in Table 6.3. As first diagnostics, in Figure 6.5 (*Left*), we reported the location of all our companion candidates in the K_1-band- and K_2-band-based color-magnitude diagram (CMD). Details on the diagrams are given in Mesa et al. (2016), Samland et al. (2017), Chauvin et al. (2018), and Bonnefoy et al. (2018). We used the most recent parallaxes of the young objects from Greco and Brandt (2016), and added additional companions (Gauza et al., 2015; Stone et al., 2016; De Rosa et al., 2014) at the L/T transition. At first glance, we see that all detected companion candidates fall on the expected sequence of possible bound companions from the early-M spectral type for the candidates around HIP 117452, late-L spectral types for HIP 95619, HIP 16095 and HIP 8832, to early-T for HIP 34276. The

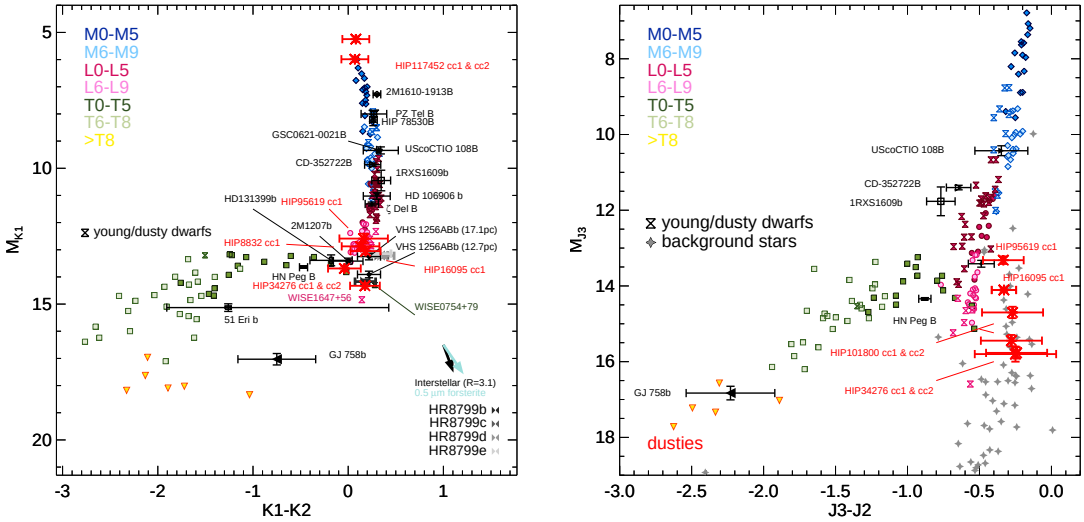

Figure 6.5: Left: absolute magnitude in K_1-band versus K_1-K_2 color for brown dwarfs with discovered companions. Right: same, but for absolute magnitude in J_3-band versus $J_3 - J_2$ color. The targets from our survey are noted in red.

companion around HIP 101800 was detected only in K_1-band during the first epoch. After a verification of the public archive, the companion candidates around HIP 34276 (cc1 and cc2) and HIP 101800 (cc1 and cc2) were previously known and characterized as stationary background sources by Wahhaj et al. (2013) as part of the NICI campaign concerning debris disk stars. Both companion candidates around HIP 117452 were earlier identified by De Rosa et al. (2011) in the course of the Volume-limited A-Star (VAST) survey as a candidate binary companion. They were later confirmed by Matthews et al. (2018) as physically bound, confirming that this system was actually a quadruple system with an A0 primary (HIP 117452 A), orbited by a close binary pair Ba and Bb also resolved in this survey, and additionally by a K-type star at about 75″.

Follow-up observations of the candidates were automatically scheduled and obtained using the DBI mode with J_2J_3 filters of IRDIS, which is well adapted to distinguish background stars from physically young, early-T, or warm mid-L dwarf planets, and offers an additional epoch for a proper motion test. Follow-up observations were then processed using SpeCal with the TLOCI algorithm in ADI only and a template approach as before. All companion candidates were re-detected, except the one around HIP 8832 falling outside the IRDIS field, given its large separation and an observing sequence that was not perfectly centered with the meridian passage. The results are reported in Table 6.3. The use of a different pair of filters enabled us to explore the companion candidate photometric properties in the J_2-band- and J_3-band-based CMD, for which we also report the distribution of background stars observed in previous crowded fields (see Figure 6.5, *Right*). One can directly see that most of our late-L to early-T potential companion candidates, including the previous ones identified as stationary background stars around HIP 34276 (cc1 and cc2) and HIP 101800 (cc1 and cc2), fall onto the background contaminant sequence indicating that they are most likely background stars. As a further check, we used the relative astrometry obtained at two epochs to estimate the proper motion of the companion candidates relative to their primary stars. Figure 6.6 shows the proper motion plots of each candidate and confirms that the companion candidates around HIP 34276, HIP 101800, and HIP 95619 are not co-moving with their primary stars. The distance and proper motion of the stars, with their

Target	UT Date	CC	Filter	Separation (mas)	Position angle (deg)	$\Delta_{\text{Filter}-1}$ (mag)	$\Delta_{\text{Filter}-2}$ (mag)
HIP16095	57669.2937186	cc-1	DK12	3368 ± 2	111.38 ± 0.04	11.46 ± 0.12	11.28 ± 0.12
	58092.1556576	cc-1	DJ23	3385 ± 2	111.21 ± 0.02	12.88 ± 0.08	12.55 ± 0.09
HIP95619	57965.1627630	cc-1	DK12	4564 ± 3	254.25 ± 0.03	11.11 ± 0.51	10.94 ± 0.54
	58613.3454076	cc-1	DJ23	4597 ± 2	255.23 ± 0.01	12.17 ± 0.24	11.83 ± 0.29
HIP101800	57940.3125070	cc-1	DK12	4513 ± 4	89.84 ± 0.037	12.42 ± 0.12	-
	58653.3759935	cc-1	DJ23	4418 ± 2	89.82 ± 0.01	13.34 ± 0.17	13.07 ± 0.15
	58653.3759935	cc-2	DJ23	4021 ± 2	89.83 ± 0.01	14.42 ± 0.19	14.17 ± 0.17
HIP34276	57736.2557381	cc-1	DK12	3108 ± 7	132.55 ± 0.11	12.90 ± 0.12	12.72 ± 0.13
	57736.2557381	cc-2	DK12	4407 ± 4	138.56 ± 0.06	12.26 ± 0.12	12.30 ± 0.12
	58445.3349875	cc-1	DJ23	3124 ± 4	133.01 ± 0.06	14.58 ± 0.29	14.34 ± 0.12
	58445.3349875	cc-2	DJ23	4421 ± 5	138.95 ± 0.06	14.30 ± 0.29	14.02 ± 0.13
HIP117452	57949.3975893	Ba	DK12	3708 ± 9	238.09 ± 0.15	3.84 ± 0.05	3.76 ± 0.05
		Bb	DK12	3318 ± 10	239.13 ± 0.17	4.58 ± 0.05	4.51 ± 0.05
HIP8832	57974.3996411	cc-1	DK12	5674 ± 3	213.71 ± 0.04	11.47 ± 0.50	11.54 ± 0.51

Table 6.3: Companion candidate (CC) characterization and identification. Target name and observing date (modified Julian day) are given, as well as the different sources identified with their relative position and relative flux.

uncertainties, are taken from the *Gaia* Data Release 2 catalog (Gaia Collaboration et al., 2018). For HIP 16095, given the relatively low proper motion of the star, the status of the companion candidate HIP 16095-cc1 remains ambiguous. However, the J_2-band- and J_3-band-based CMD still supports a background contamination. If bound, this candidate would have an estimated mass between 7 and 12 M_{Jup} at the system age ($\leq$ 100 Myr) and distance (88 pc) illustrative of the SPHERE detection performances around young nearby stars beyond 10 au.

For HIP 117452 Ba and Bb, the colors and magnitudes in K_1 and K_2 compared to the predictions of the evolutionary models of Siess et al. (2000) suggest that Ba and Bb are a pair of M1 and M2 low-mass stars, considering an age of 40 Myr at a distance of 42 pc. Combining our relative astrometry with the one reported by Matthews et al. (2018) and shown in Table 6.3, we performed a first orbit fitting of the pair. Following the method developed by Chauvin et al. (2012), we used a Markov chain Monte Carlo (MCMC) Bayesian analysis technique (Ford and Gregory, 2007), which is well suited for observations covering a small part of the whole orbit (for large orbital periods). We did not consider any prior information using the proximity of the primary star. The results are reported in Figure e.1 and favor a relatively inclined orbit $i \sim 98^{+8}_{-5}$ deg, a longitude of ascending node fairly well-constrained at $\Omega = 20 \pm 2$ deg, tight semi-major axis $a \sim 14^{+7}_{-4}$ au, but surprisingly large eccentricities $e \geq 0.4$. These large values of eccentricity are not dynamically expected, given the proximity of the primary star located at a physical projected separation of $\sim$ 150 au, although the orbit of the binary companion around HIP 117452 is not known. Fitting solutions using a least squares Levenberg-Marquardt (LSLM) algorithm (Press et al., 1992) to search for the model with the minimal reduced chi^2 are also reported for comparison. Further dynamical study of

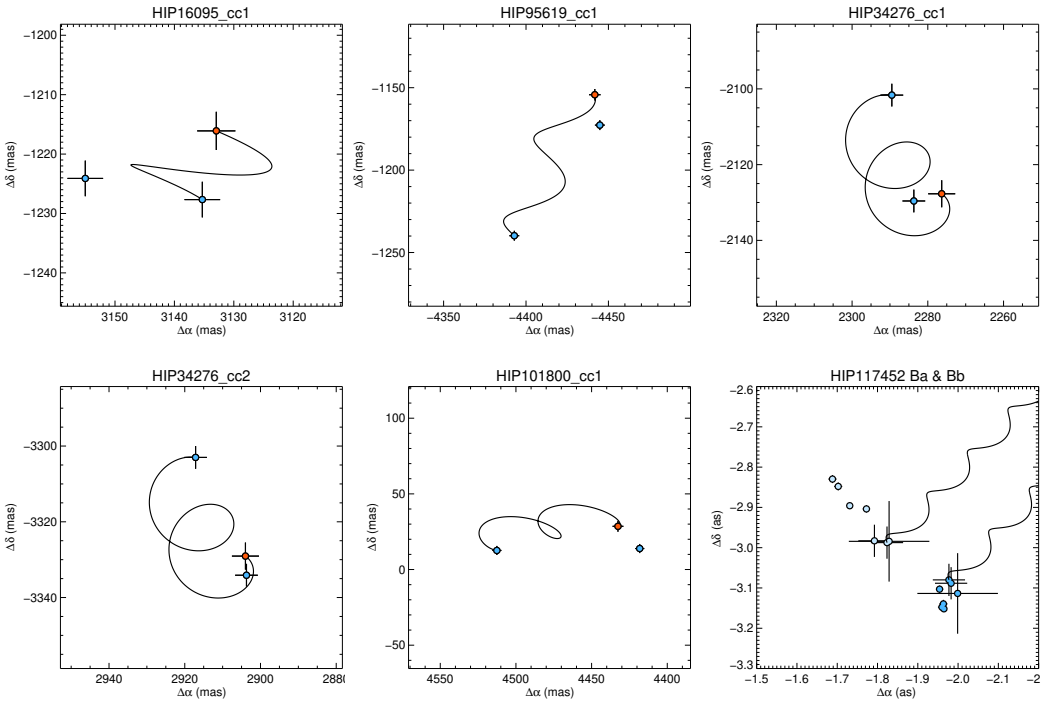

Figure 6.6: SPHERE measurements (in blue) of the offset positions of the companion candidates relative to their primary stars. For each diagram, if the candidate is a stationary background object, the expected variation of offset positions is shown (solid line). This is based on a distance and on a primary proper motion, as well as the initial offset position of the candidate relative to the primary. The predicted offset positions of a stationary background object for the second epoch is shown in red with uncertainties. For HIP117452, measurements of both components Ba and Bb at various epochs are plotted in dark and light blue, respectively.

the global system considering the debris disk architecture around HIP 117452 and the binary companion HIP 117452 BaBb configuration is be needed.

6.7 DETECTION LIMITS AND SURVEY COMPLETENESS

To exploit the information from the actual nondetection in IFS and IRDIS observations of the survey, the detection limits of each individual observations were then estimated. Based on SpeCal results, we derived a standard pixel-to-pixel noise map for each observing sequence corrected from the flux loss related to the ADI or ASDI processing by injecting fake planets. The detection limit maps at 5σ were then obtained using the pixel-to-pixel noise map divided by the flux loss and normalized by the relative calibration with the primary star (considering the different exposure times, the neutral density, and the coronograph transmission). These detection limits were finally corrected from small number statistics following the prescription of Mawet et al. (2014) to adapt our 5σ confidence level at small angles with IRDIS and IFS. The 5σ contrast curves, resulting from the azimuthal average of the detection maps, are reported for IFS and IRDIS in Figure 6.7.

To convert the detection limits in terms of the mass and semi-major axis parameter space explored with SPHERE, we used the multi-purpose exoplanet simulation system (MESS) code, a Monte Carlo tool for the statistical analysis and prediction of exoplanet search results (Bonavita et al., 2012). This code has been used extensively in previous

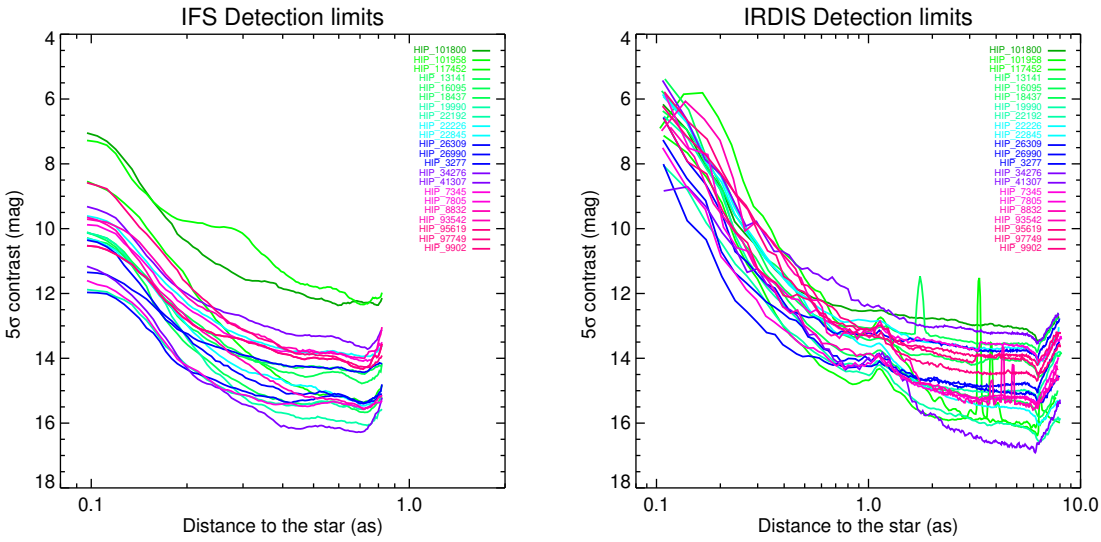

Figure 6.7: Magnitude contrast limit curves for all targets with TLOCI algorithm.

direct imaging surveys for that same purpose (Chauvin et al., 2010; Chauvin et al., 2015; Chauvin et al., 2018; Vigan et al., 2012; Vigan et al., 2017; Rameau et al., 2013; Lannier et al., 2016). With MESS, we then generated a uniform grid of mass and semi-major axis in the interval [1, 80] M_{Jup} and [1, 1000] au with a sampling of 0.5 M_{Jup} and 1 au, respectively.

For each point in the grids, 100 orbits were generated, randomly oriented in space from uniform distributions in cos(i), ω, Ω, $e \leq 0.8$, and T_p. We built detection probability maps by counting the number of detected planets over the number of generated ones and simply comparing the on-sky projected position (separation and position angle) of each synthetic planet with the SPHERE 2D detection limit maps at 5σ converted in masses based on the COND (hot-start) model predictions (Baraffe et al., 2003). The primary age, distance, and magnitude reported in Table 6.1 are considered for the luminosity-mass conversion.

The resulting detection probability map of the complete survey is reported in Figure 6.8. This result shows that, despite the relatively wide age range (20 to 120 Myr) and distance (10 to 102 pc) of our sample, we achieved a relatively good detection probability larger than 50 % for giant planets with masses larger than 5 M_{Jup} and semi-major axes between 10 and 500 au, sufficient for the detection of system analogs to HR 8799 or HD 95086. In principle, the degeneracy between mass and initial entropy could change these limits considerably (e.g., Marleau and Cumming (2014) and Brandt et al. (2014)). In practice, however, taking more realistic post-formation entropies into account strongly mitigates this problem, as shown for instance in the case of HIP 65426 b by Marleau et al. (2019).

6.8 DISCUSSION

Our survey is composed of relatively old gas-free systems. Therefore, some of these systems contain debris disks. We assumed that planets are a valid explanation for the formation of debris structure, as shown in the case of the Solar System where planets are known to reside between two belts of debris, and in the case of HR 8799 and HD 95086 where planets are known to reside in two-temperature debris disks. The analysis of our survey follows the work by Matthews et al. (2018). The temperature values of debris

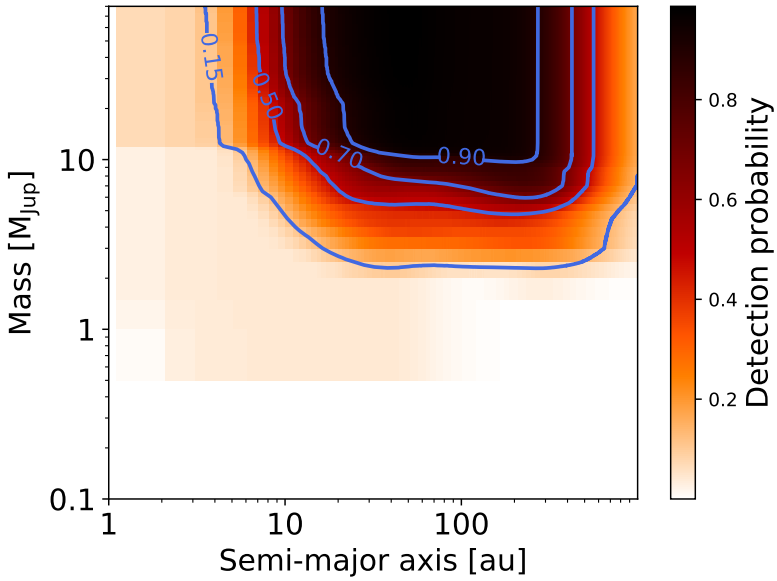

Figure 6.8: Combined mean detection probability map for the whole survey.

belts are found in Chen et al. (2014), where these temperatures were estimated using a two-temperature black-body model and a Bayesian parameter estimation to select the best model to fit the SED. The disk radii were calculated following Pawellek and Krivov (2015), assuming that dust are composed of 50% astrosilicate and 50% ice. In addition, we constrained our SPHERE/IRDIS observations with dynamical arguments on the possible planetary systems hiding within the debris gaps (Shannon et al., 2016).

Mass limits were calculated with the MESS code as described in Section 6.7 and shown in Figure 6.9. The theoretical mass for a single planet to clear the observed gap is large $\geq 25M_J$ (Nesvold and Kuchner, 2015). Therefore, in our cases, we infer that the systems must be in multi-planet configuration, as in HR8799, in which several planets with lower masses clear the gap. In Figure 6.9, we plot the minimum masses of planets required to clear the debris gaps, as well as their location and their "Np" number based on the N-body simulations of Shannon et al. (2016). This model considers only planets with low eccentricities. The mass and the Np number change if the eccentricity is larger. The mass, shown in green in Figure 6.9, is the minimum mass per planet, with uncertainties based on the age of the system and on the belts radius. The minimum mass calculation assumes that planets are spaced by a typical value of $\sim$ 20 mutual Hill radius (R_H), which is consistent with the value of $21.7 \pm 9.5 R_H$ predicted by Fang and Margot (2013).

By combining the observational upper and theoretical lower mass constrains, only a small region of parameter space is unconstrained. For 12 targets in our survey of which the temperature values are found in Chen et al. (2014), we infer a multi-planet system based on the large theoretical clearing masses. In such a multi-planet system, the widest separation planet would have a physical separation close to that of the outer debris belt, where our direct imaging limits are relatively tight. In main cases, planets must be at least $\sim 0.1M_J$ to clear the observed gap based on dynamical arguments, and in some cases the dynamical mass limit exceeds $1M_J$. In Figure 6.9, for the target HIP7345, the mass limit, $\sim 1.3M_J$ at 90% in the gap, is close to the dynamical mass limit $\sim$ 0.9.

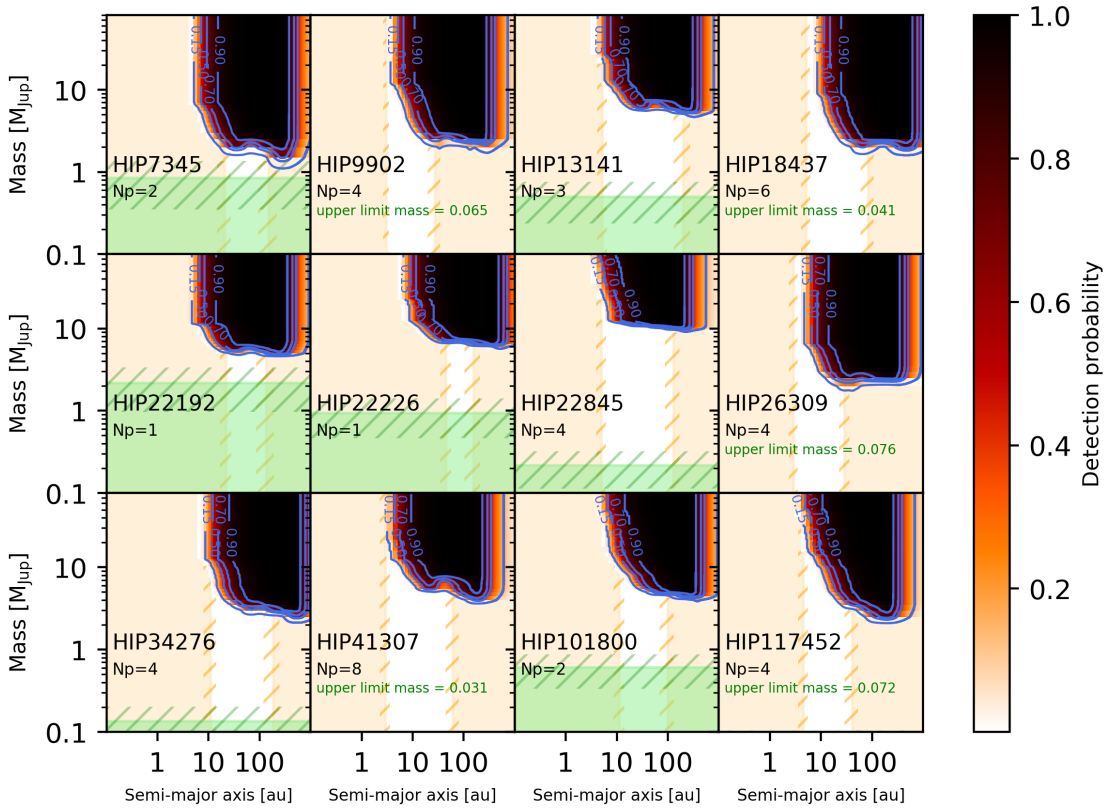

Figure 6.9: Constraints on planetary systems for 12 targets in our survey. The positions of the inner and the outer debris belts are shown in orange by shading the regions inside the inner and beyond the outer. Our mass contrast limits are based on SPHERE/IRDIS and COND model predictions. Dynamical mass constraints for a slightly closer planet spacing of 20 mutual Hill radii from Shannon et al. (2016) are shown in green with masses below this value shaded. Np is the number of planets with the mass (indicated in green) required to open the gap. The uncertainties for debris belt position and dynamical mass limit are calculated based on the uncertainty in debris belt temperature, and indicated with hatching.

Among our 12 targets for which we note the presence of two debris belts, no exoplanetary mass companions were detected. Our sample is too small for a detailed statistical analysis. However, a nondetection in a sample of 12 stars is not inconsistent with the debris disk occurrence rate of 6.27% in a debris disk sample of planets between $5-20M_J$ and 10-1000 au (Meshkat et al., 2017), since we would expect that some companions might be below our detection limits. Our nondetections are also consistent with the lower occurrence rate of $\sim 1\%$ found in Bowler (2016) and Galicher et al. (2016). The results of this 12 target sample are not incompatible with the theory that planets are carving wide debris gaps, since in each case our direct imaging mass limits are higher than the theoretical mass limits that we calculate.

The existence of the planetary perturbers beyond 5 au, and potentially these architectures will be explored in futur observations: i/ observations combining radial velocity, astrometry with *GAIA* for the inner parts (≤ 5 au), ii/ observations with the next generation of planet imagers from the ground (SCExAO, KPIC, SPHERE+, GPI2.0 on 10m-class Telescopes, then with the ELTs) and space (*JWST*, *WFIRST*).

6.9 CONCLUSIONS

We reported the observations and analysis of a survey of 22 stars with VLT/SPHERE with IRDIS in the DBI mode with K_1K_2 filters and J_2J_3 for the follow-up observations, and IFS in the $Y - H$ filters, with the goal of detecting and characterizing giant planets on wide orbits. The selected sample favors young, that is to say$\leq$ 100 Myr, nearby, $\leq$ 100 pc, dusty, and early-type stars to maximize the range of mass and separation, over which the observations are sensitive. The optimized observation strategy with the angular differential imaging in thermal bands and a dedicated data reduction using various algorithms allow us to reach a typical contrast 12.5 mag at 0.25″ and 14 mag at 1.0″ in IRDIS. These contrasts are converted to mass limits for each target. Despite the good sensitivity of our survey, we did not detect any new giant planets. We confirmed that the sources detected around HIP 34276, HIP 101800, HIP 16095, and HIP 95619 are stationary background sources by analyzing K_1-band, K_2-band, J_2-band, and J_3-band images and their relative motions. The status of the candidate around HIP 8832 still requires further follow-up. HIP 117452 BaBb is resolved and confirmed as a binary companion (De Rosa et al., 2011; Matthews et al., 2018). For 12 targets of our survey, where we determined the radii of the debris belt, we derived upper and lower mass limits. We used Monte Carlo simulations to estimate the sensitivity survey performance in terms of planetary mass and semi-major axis to perform the upper limit. We additionally calculated the minimum required mass for planets in the system to have cleared the observed debris gap to perform the lower mass limit. Combining our upper and lower mass limits, we are able to tightly constrain the unexplored parameter space around these systems: typically, planets must be at least $\sim 0.1 M_J$ in main cases to clear the observed gap based on dynamical arguments, and in some cases the dynamical limit exceeds $1 M_J$. Direct imaging data from VLT/SPHERE are sensitive to planets of $\sim 3 M_J$ for a typical target in our survey. Several of the planetary systems will likely be detectable with the next generation of high-contrast imagers.

7 CONCLUSION AND FUTURE WORKS

"When you do something best in life, you don't really want to give that up - and for me it's tennis." – Roger Federer

7.1 SUMMARY OF THE PH.D WORKS

How grains can grow over 30 orders of magnitudes in mass to form planets in less than 1 million years ? To answer this outstanding question, numerical models of dusty discs require a comprehensive model of dust collisions described by the Smoluchowski coagulation equation (see Chapter 2). We adopt a deterministic mean-field approach and aim to solve for the Smoluchowski equation in a 3D dust/gas hydrodynamical simulation of a young stellar object. However, solving efficiently and accurately this non-linear integro-differential equation is one of the grand challenges of planet formation (Haworth et al., 2016). We have first shown that a proper understanding of the mathematical properties of the Smoluchowski equation is crucial to choose an appropriate numerical scheme to solve this equation. Tanaka et al. (1996) wrote the Smoluchowski equation in the conservative form

$$\begin{cases} \dfrac{\partial g(x,\tau)}{\partial \tau} + \dfrac{\partial F_{\text{coag}}[g](x,\tau)}{\partial x} = 0, \\ F_{\text{coag}}[g](x,\tau) = \displaystyle\int_0^x \int_{x-u}^{\infty} \mathcal{K}(u,v)\, g(u,\tau)\, \frac{g(v,\tau)}{v} \mathrm{d}v\mathrm{d}u. \end{cases} \tag{7.1}$$

Equation 7.1 led to the development of a novel family of numerical solvers based on the methods of finite volume (Filbet and Laurencot, 2004; Liu et al., 2019). The work presented in this Ph.D. Thesis presents the development of a high-order scheme based on the discontinuous Galerkin method in order to fulfil the stringent criteria set by the astrophysical constraints (see Chapter 3). In particular, an important analytic development has been performed to calculate the flux term F_{coag} accurately and efficiently. Our scheme is designed to satisfy the requirements based on astrophysical observations and simulations, i.e.

1. exact mass conservation,
2. positivity of the mass density,
3. discretizing masses over 12 orders of magnitudes, which roughly corresponds to grains of sizes $1\mu\text{m} - 1\text{mm}$ relevant for observations,
4. an accuracy of order $\sim 0.1 - 1\%$ to be consistent with hydrodynamics solvers (here `PHANTOM`),
5. having a minimal number of bins to maintain global simulations of discs computationally tractable.

Typically, we estimate that with current computational capacities 3D simulations of dusty discs with hydrodynamics solvers (e.g `PHANTOM`, `RAMSES`) could handle ~ 20 bins. Differential velocities between grains are calculated by the hydrodynamics solver and then used in the algorithm. Sub-grid process not included in hydrodynamics code such as Brownian motion could be treated in our algorithm. Our high-order scheme is benchmarked with the analytic solutions of the Smoluchowski coagulation equation for constant, additive

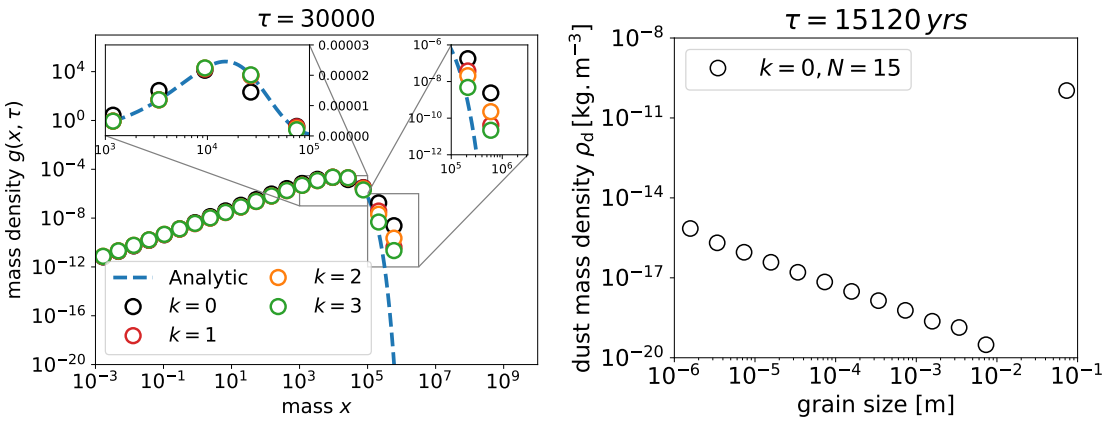

Figure 7.1: Left: Test case constant kernel: numerical solution $g_j(x, \tau)$ evaluated at the geometric mean $\hat{x}_j$ of each bin I_j. At the location of the maximum, order 0 can achieve an absolute error of 30% compared to order 1,2 and 3. Order 3 can achieve an improvement in accuracy of a factor 100 compared to order 0 in the exponential tail. Right: Test case for ballistic kernel with only growth and constant polynomial approximation. Simulation so far $\tau = 15120$ years where grains of size 10cm form. These grains represent almost all the dust mass at this time.

and multiplicative kernels (Figure 7.1, see Chapter 4). At the very end of this Ph.D. Thesis, a first test for a ballistic kernel has been performed with polynomials of order 0. Simulation of dust growth at 1 AU in a typical dusty discs shows the formation of pebbles from micron-in-size grains in 15120 years, consistent with the results from Laibe et al. (2008) in Figure 7.1. We worked in collaboration with Pr. D. J. Price and D. Mentiplay to design a modular and user friendly interface for the algorithm. In practice, the code is compiled as a library and interfaced with `PHANTOM`.

Two works have been carried out in parallel of the thesis work. Firstly, I continued the work from my M2 internship with Dr. G. Chauvin on the complete analysis of a direct imaging survey to determine the probability of detection for giant planets aroung young nearby stars hosting multi-belt system. I analysed data from the SPHERE/VLT extreme Adaptive Optics (xAO) planet imager obtained with the Open Time Program DUSTIES. No new exoplanets were found. I could however set robust constraints on the presence of giant planets around observed stars (Lombart, M. et al., 2020). This work paves the way to future observations of this survey with the next generation of instruments. The improvement of SPHERE called SPHERE+ (Boccaletti et al., 2020b) will detect planets with higher sensibility. SPHERE+ is designed to detect giant planets at snow lines location between 3-10 AU. The new instruments JWST and ELT will provide high resolution and sensibility. The JWST will be able to detect giant planet so far Neptune-sized and their atmosphere with high spectral resolution. The ELT will be able to detect planets close to the star (1-10 AU) and at very low masses (lower than $1M_{\rm Jup}$). Secondly, I collaborated with Dr. G. Laibe and Dr. C-E. Bréhier to derive an analytic formula for the distribution of small grains that encompass gas stratification, dust inertia and finite correlation times in protoplanetary discs (Laibe et al., 2020). My contribution to this work was to develop the code to solve the system of stochastic differential equations and perform the convergence analysis of the simulations. The numerical scheme is the Monte-Carlo method coupled to a Strang splitting method. The code is parallelized to achieve high-accuracy with the Monte-Carlo method in a tractable

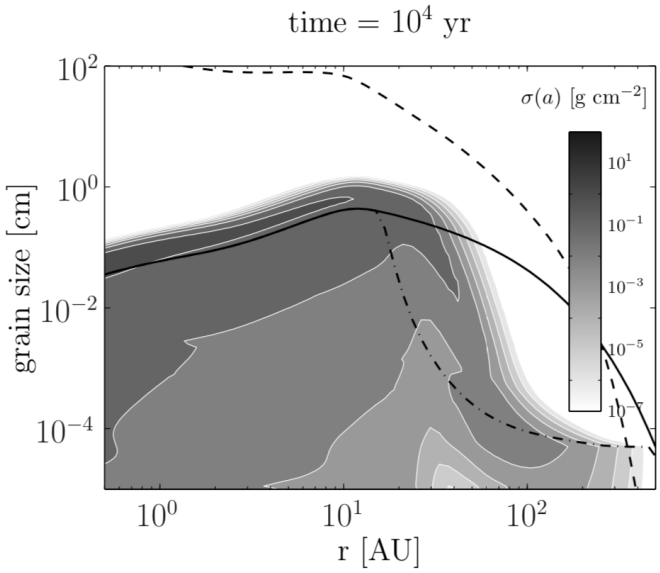

Figure 7.2: State-of-the-art dust surface density distributions as function of radius and grain size at 10^4 years from Birnstiel et al. (2012). The model is a 1D viscous disc evolution code and a dust evolution code taking into account radial drift, turbulent mixing, dust coagulation/fragmentation. We expect different result for 3D simulations.

computational time. The analytic formula is then validated against numerical simulations.

7.2 FUTURE WORKS

7.2.1 *Fragmentation*

Dust fragmentation will be implemented in the algorithm by adding the fragmentation flux presented in equation 2.51 since it does not affect the architecture of the solver. The fragmentation kernel depends on the mass distribution of fragments b, which is usually chosen as power law function (Petit and Farinella, 1993; Birnstiel et al., 2010; Kobayashi and Tanaka, 2010). We plan therefore to integrate the fragmentation flux in a similar manner than the coagulation flux, with analytical intermediates. Astrophysical mass distributions are expected to be dominated by large grains. Hence, the CFL condition for fragmentation should be similar to the one for growth (Vericel and Gonzalez, 2020). If so, numerical integration will be performed explicitly. If not, implicit time-stepping can be implemented in a manageable way since the number of dust bins has been kept minimal with analytic integrations (i.e. linear algebra with $\sim 15 \times 15$ matrices).

7.2.2 *3D simulations of dusty discs with dust growth/fragmentation*

Observations of discs such as HL Tau (ALMA Partnership et al., 2015), HD142527 (Avenhaus et al., 2017) or HD163296 (Isella et al., 2018) have revealed the presence of substructures (see Figure 7.3). Reproducing and understanding the physics under these observations is crucial to constrain models of discs, evolution of dust size distribution, masses of planets, physics of gas, the impact of dust grains on gas by back-reaction and on the physics of dust. In particular, can these structures be reproduced by 3D simulations of discs including dust growth/fragmentation ? So far, synthetic observations have

been produced with simulations evolving grains of constant sizes, over very short times (a few tens of orbits) compared to the lifetime of the disc (a few thousands of orbits). However, we expect grain growth to strongly affect the dynamics of the grains in a few tens of orbits as well, implying that the structures currently simulated are not stable. From these sensitive simulations, we hope to constrain important parameters such as fragmentation thresholds, gas densities or turbulent viscosities in the disc. Note that an incorrect estimate of the millimetre dust flux can lead to a large overestimation of the mass of the planet (Dipierro and Laibe, 2017). We also aim to ultimately constrain the detailed physics of the coagulation process. In particular, we expect for the model of dusty turbulence used to affect the results by favouring or not the formation of large grains (Ormel et al., 2007; Laibe, 2014). We plan to investigate whether some of these kernels can be discriminated from our numerical simulations. The shape of the grains, their composition and the value of the parameter β can also affect the growth timescales and can be investigated in a similar manner. We also note that β depends on the threshold velocity of fragmentation.

Birnstiel et al. (2010) model is a dust evolution code coupled to a 1D viscous gas disc evolution code. Radial drift, turbulent mixing, dust coagulation/fragmentation with $100 - 200$ different grain sizes are taken into account in this model. Figure 7.2 shows the evolution of dust surface density distributions as function of radius and grain size so far 10^4 years. We aim to perform 3D simulations of dusty discs with the code `PHANTOM` including our high-order scheme to test the validity of the model from Birnstiel et al. (2010). We expect to obtain different dust surface density distributions with 3D simulations for the same initial condition. Specifically, the evolution of dust size distribution strongly impacts the dust and gas dynamics in discs, which requires a precise account of the evolution of the dust size distribution obtained with our algorithm.

Planet formation results from a complex interplay between dynamics and growth of dust grains in discs. Metre-in-size barrier is thought to be overcome by the combination of two processes which concentrate grains: i) self-induced dust trap (Gonzalez et al., 2017), ii) streaming instability (Youdin and Goodman, 2005). Dust grains concentrate leading to a dust concentration of order $> 1\%$ due to the back-reaction on gas and grow to form grain with $\mathrm{St} \sim 0.1$. In Gonzalez et al. (2017), self-induced dust trap mechanism has been evidenced in 3D SPH simulations with the mono-disperse treatment of the growth and fragmentation. However, these traps have not been found in the simulations of Birnstiel et al. (2010). The model of Birnstiel et al. (2010) treat the dust growth/fragmentation by solving the Smoluchowski equation but with a $1 + 1$D code to simulate evolution of discs leading to a poor treatment of hydrodynamics. By performing 3D simulations with a comprehensive model of dust growth, we plan to disentangle between the two models and answer whether self-induced dust traps can form or not in young discs. Our algorithm which solves the Smoluchowski equation will be coupled to the code `PHANTOM` to study comprehensively dust growth/fragmentation in 3D hydrodynamics simulations of discs.

7.2.3 *3D simulations of dusty protostellar collapses*

Our algorithm is designed in a modular way, implying that it should be easily coupled to grid-based magneto-hydrodynamical codes such as `RAMSES` (Teyssier, 2002). A collaboration has been initiated with Dr. Ugo Lebreuilly to study dusty protostellar collapse with dust growth/fragmentation. Lebreuilly et al. (2020) found that dust grains of size 160μm

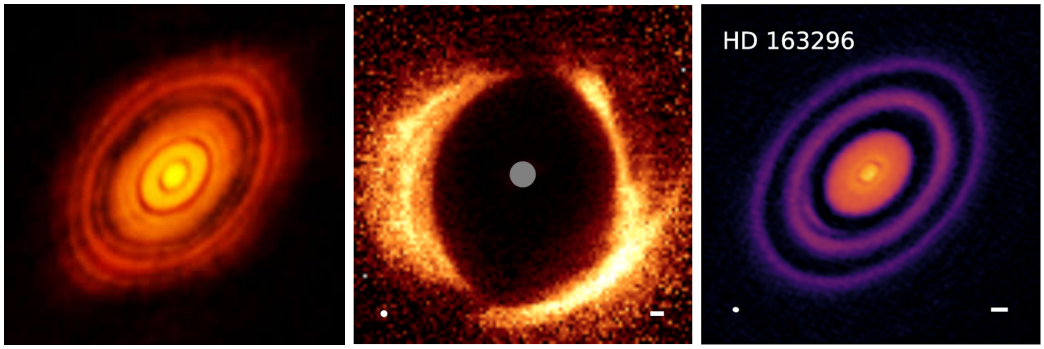

Figure 7.3: Sub-structures observed in dust in HL Tau (left, ALMA Partnership et al. (2015)), HD142527 (middle, Avenhaus et al. (2017)) and HD163296 (right, Isella et al. (2018)).

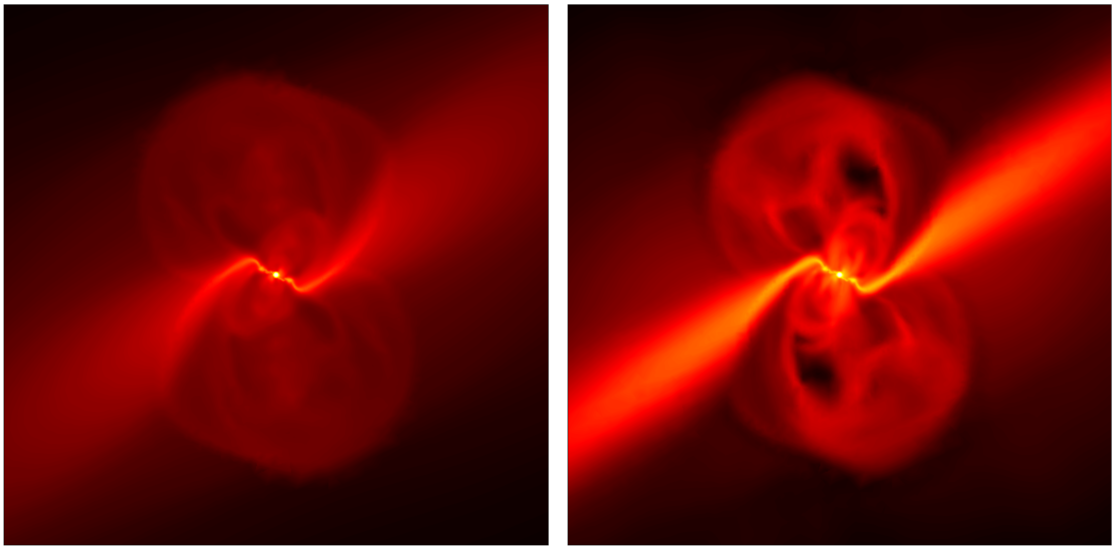

Figure 7.4: Simulation of protostellar collapse with gas and dust from Lebreuilly et al. (2020). Left: gas density during the collapse. Right: dust density during the collapse. Local enrichments of dust grains of size 160μm form.

start to decouple from the gas and concentrate in high density regions (see Figure 7.4). Indeed, at this critical size, the typical drag time becomes longer than the free-fall time which leads to dust enrichment in high density regions such as the disc. As such, one expects grains to decouple more or less from the gas during stellar collapses, and for the dust not to be a proxy for the gas even in this very young phase. A strong corollary is that star and disc formation should entirely be revisited ! Indeed, key processes (transfer of angular momentum, formation of the disc) are highly sensitive to the thermodynamics of the collapsing cloud, which itself depends on the dust opacities that can not be computed from the gas density profile. From the knowledge acquired on protoplanetary discs, we know that dust growth certainly play a key role in interplaying with the dust dynamics to set the dust distribution and thus, the local opacities. Dust opacity depends on grain sizes. Therefore, a precise account of the evolution of dust size distribution is required to obtain the right flux from dust to be compared with observations. Moreover, dust grains are charge carriers. They regulate the evolution of magnetic field during protostellar collapse which impact the formation of the disc (Hennebelle et al., 2020). We expect similarly that accounting for grain growth accurately will allow to compute the accurate dust charge for a realistic treatment of the magnetic effects during the collapse.

7.2.4 *Future developments for the DG scheme*

In parallel, the DG scheme will be extended with different developments. At the moment, one timestep with our DG scheme is executed in $\sim 10^{-3}$s (in real time). In a 3D numerical simulation, the hydrodynamical solver will call the coagulation algorithm in each SPH particles. To reproduce ALMA/SPHERE observations, a typical simulation uses ~ 1 million SPH particles. As is, it will take 10^3s to evolve the dust size distribution in all SPH particles for one hydrodynamics timestep. Optimisations are required to reduce the computational time as much as possible, ideally for not being the process dominating the global timestep. We plan to implement the following optimisations in our algorithm: i) modifying polynomial basis, ii) using an adapted distribution of bins, iii) rescaling of the Smoluchowski equation. Moreover GPU parallelisation is planned, since calls to the coagulation solver by the hydrodynamical code are independent.

7.2.4.1 *Adapted polynomials basis*

Figure 7.5 shows the approximation of the initial condition $g(x,0)$ with the Legendre polynomials of order 3 for $N = 3$ bins. This crude simulation highlights the main difficulty for the coagulation solver, that is to approximate the exponential tail on the right side of the curve with a third order polynomials. It is known that constant, additive and multiplicative kernels admit a self-similar solution with exponential decay (Menon and Pego, 2004). The idea is to include this expected exponential behaviour in the approximation g_j of g. In each bin I_j, g_j can be written as

$$\begin{aligned} g_j(x,\tau) &= \sum_{i=0}^{k} g_j^i(\tau)\psi_i(\xi_j(x)), \\ \psi(\xi_j) &\equiv \mathrm{e}^{-\xi_j/2}\, P_i(\xi_j), \end{aligned} \tag{7.2}$$

where P_i represents orthonormal basis of polynomials according to the inner product

$$\forall x \in [-1,1], \int_{-1}^{1} \mathrm{e}^{-x}\, P_i(x)P_j(x)\mathrm{d}x = \delta_{ij}. \tag{7.3}$$

This orthonormal basis is built with the Gram-Schmidt algorithm. This new orthonormal polynomials basis will allow to better approximate the function g in the exponential tail. Therefore, a good accuracy will be achieved for a small number of bins with low-order polynomials. Soong (1974) and Trautmann and Wanner (1999) shown the approximation of g by a decaying exponential reduces drastically the numerical diffusion. High accuracy reached with polynomials of low order will reduce drastically the computational time. We aim to reduce the computational time by a factor at least 10.

7.2.4.2 *Adapted distribution of bins*

Figure 7.5 shows that the left part of the curve is well approximated for one large bin with polynomial of order 3. Thus, only a few number of bins is required to approximate the left part of the curve. The exponential tail on the right side of the curve is better approximated with a large number of bins. Kumar and Ramkrishna (1996) shown a significant gain in accuracy for a non-uniform geometric grid. This non-uniform grid samples the exponential tail with a large number of bins. In practice, an adapted distribution of bins will allow to gain in accuracy with polynomials of low order. This will reduce the computational time.

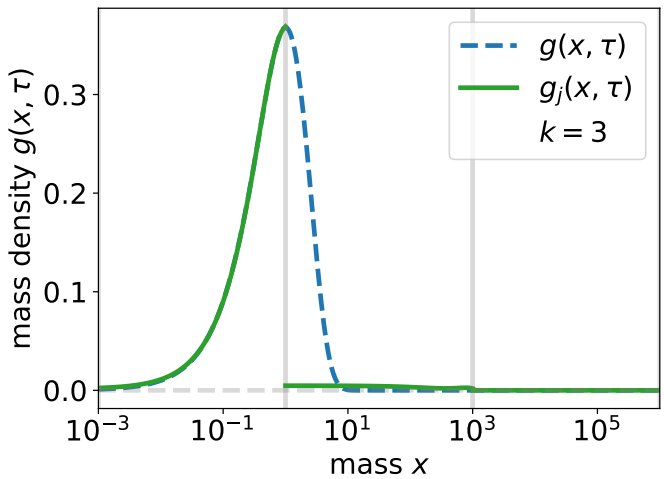

Figure 7.5: Initial projection of $g(x,0) = x\exp(-x)$ on Legendre polynomials of order 3 with $N = 3$ bins. The left side of the analytic solution is well approximated. The approximation of the exponential tail on the right side is poorly approximated.

7.2.4.3 *Rescaling*

In the aim to study the large time behaviour of the solutions of Smoluchowski coagulation equation, a rescaling can be applied (Carrillo and Goudon, 2004; Goudon et al., 2013)

$$\begin{aligned} &\tilde{\tau} \equiv \ln(1+\tau),\ y \equiv \frac{x}{1+\tau}, \\ &n(x,\tau) = \frac{1}{(1+\tau)^2} f\left(\ln(1+\tau), \frac{x}{1+\tau}\right), \end{aligned} \tag{7.4}$$

where n is the solution to the Smoluchowski equation 2.4. This rescaling is particularly important for numerics since it provides a natural way to reduce the computational domain. In practice, simulations are performed for smaller mass domain and a small evolution in time. The rescaling allows to obtain the numerical solution for large masses at larger evolution of time. Important reduction of the computational time will be achieved.

7.2.5 *Future physics developments*

The Smoluchowski equation can be adapted to integrate different aspects of the physics of coagulation such as the coagulation among grains of different composition and the coagulation between agglomerates.

7.2.5.1 *Ice condensation*

The coagulation of grains is not the only physical process to evolve the dust size distribution in discs. Condensation is an efficient mechanism that leads to growth of grains beyond decimetre-sized pebbles close to water ice line in protoplanetary discs (Ros and Johansen, 2013; Ros et al., 2019). Sublimation of icy particles at water ice line provides material in the form of vapour. Therefore, grains outside the ice line can grow by condensation of the vapour. Condensation has been widely studied in aerosol community (Gelbard and Seinfeld, 1978; Pratsinis, 1988; Ramkrishna, 2000; Friedlander et al., 2000; Sandu, 2006; Pruppacher and Klett, 2010; Khain and Pinsky, 2018). The condensation equation writes

$$\frac{\partial f}{\partial t} = -\frac{\partial I f}{\partial x}, \tag{7.5}$$

where I is the rate of grain growth from condensation. This equation of condensation is written as conservation law equation and can be directly solved by our algorithm and therefore included in PHANTOM simulations in mono-fluid by evolving the dust fraction.

7.2.5.2 *Coagulation among grains of different composition*

The Smoluchowski coagulation equation can be adapted to treat the coagulation of grains with different compositions (Gelbard and Seinfeld, 1980; Pilinis et al., 1987; Pilinis, 1990; Jacobson et al., 1994; Chen and Lamb, 1994; Trautmann and Wanner, 1999; Sandu, 2006; Matsoukas et al., 2006; Fernández-Díaz and Gómez-García, 2007; Yang et al., 2014). The mass density of species i is defined as $g_i(x,\tau)$, so that $g_i(x,\tau)\mathrm{d}x$ is the mass concentration of the species i in particles in the mass range $[x, x+\mathrm{d}x]$ at time τ. The total mass density $g(x,\tau)$ is given by

$$g(x,\tau) = \sum_{i=1}^{p} g_i(x,\tau), \tag{7.6}$$

where p is the total number of species. By definition, g_i and g are related by

$$g_i(x,\tau) = \frac{x_i}{x} g(x,\tau), \tag{7.7}$$

where x_i is the mass of species i in a particle of total mass x. Therefore, a system of Smoluchowski equations on g_i 2.40 is obtained and can be solved by our DG scheme. This future multicomponent DG solver would be adapted to analyse the coagulation of interstellar dust grains of different composition (Köhler et al., 2015; Ysard et al., 2019). The dust evolution in the interstellar medium (ISM) resulting from coagulation leads to significant changes in the optical properties of the grains. Therefore, it is crucial to follow accurately the dust evolution. The DG solver could be interfaced with the code THEMIS (Jones et al., 2017) to perform coagulation of interstellar dust grains with different compositions.

The water snow line located in protoplanetary discs is of particular interest for dust growth since it suggests the presence of wet icy grains. Icy grains tend to be less sensitive to fragmentation since the collisional energy necessary is much higher than for silicates (Blum and Wurm, 2008; Steinpilz et al., 2019). Therefore, a key question is the fragmentation barrier can be overcome by coagulation of icy grains ? Collisions between grains of multiple compositions such as silicate and water ice could be treated with our algorithm in 3D simulations of dusty discs. The system of Smoluchowski coagulation equations for each component of icy grains will be solved with our algorithm. The probability of sticking will be adapted for icy grains.

7.2.5.3 *Agglomerate size distribution*

The coagulation model from Smoluchowski considers that colliding spherical grains coalesce instantaneously to form larger spherical grains. In reality, dust growth is the growth of aggregates from small monomers (Chokshi et al., 1993; Dominik and Tielens, 1997; Blum and Wurm, 2000; Blum and Wurm, 2008; Blum, 2018). Figure 7.6 shows different kinds of aggregates formed in laboratory. Porous aggregates are found to be able to overcome the radial drift barrier (Okuzumi et al., 2012). Planetesimals can be formed by direct collisional growth of porous aggregates ?

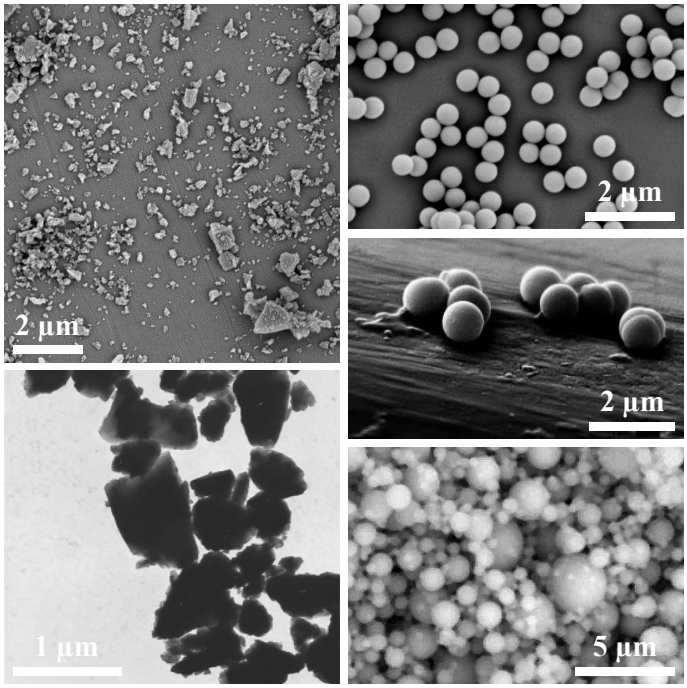

Figure 7.6: Example of aggregates from laboratory experiments. Credits: Güttler et al. (2019)

A dust agglomerate is composed of N monomer grains of radius $r_{\rm m}$. The agglomerate structure has a characteristic radius R. Experimentally, it is found that N and R are related by the following expression

$$N \sim R^{D_f}, \tag{7.8}$$

where the exponent D_f is called the fractal dimension of the aggregate. For instance, $D_f = 3$ for compact agglomerates, while for a chain-like structure $D_f = 1$ (Friedlander et al., 2000). Usually, the growth of aggregates from small monomers is treated in two ways: Particle-Cluster Aggregation (PCA) and Cluster-Cluster Aggregation (CCA) (Dominik and Tielens, 1997; Paszun and Dominik, 2009; Dominik et al., 2016). Agglomerate size distribution can also be calculated by solving the Smoluchowski coagulation equation using an appropriate expression of the kernel (Jullien and Meakin, 1989; Friedlander et al., 2000; Okuzumi et al., 2009). There is a fundamental difference between this approach and simulations with PCA or CCA. In general, the value of D_f is determined by the collision algorithm (PCA or CCA). The Smoluchowski equation requires an assumption on the value of D_f that appears in the collision kernel. For a ballistic kernel, only the cross-section depends on D_f,

$$\sigma(i,j) = (R_i + R_j)^2 \sim \left(mN_i^{1/D_f} + mN_j^{1/D_f}\right)^2, \tag{7.9}$$

where mN_i^{1/D_f} is the mass of agglomerate j. The impact of porous aggregates on dust dynamics and growth (Okuzumi et al., 2012; Garcia and Gonzalez, 2020) will be tested with the code `PHANTOM` and our algorithm solving the Smoluchowski coagulation equation with aggregates.

7.2.5.4 *Coagulation of charged grains*

An important aspect for the coagulation of micron-in-size grains is the electrostatic repulsion of charged grains (Simpson et al., 1979; Okuzumi et al., 2009; Akimkin, 2015;

Akimkin et al., 2020). Small dust can be charged positively in the layers of the discs due to the photoelectric emission caused by UV radiations. In disc, gas can be weakly ionised and plasma charging dominates. Therefore, grains are charged negatively inside the disc (Okuzumi et al., 2009; Okuzumi et al., 2011; Akimkin, 2015). How millimetre grains are formed from micron-in-size grains due to electrostatic barrier ?

Electrostatic interactions between charged grains affect their interaction and therefore their collisional cross section. Following the work from Spitzer (1941) and Okuzumi et al. (2009), the cross section is expressed as

$$\sigma = \pi(R_i + R_j)^2 \left(1 - \frac{E_{\rm el}}{E_{\rm kin}}\right), \quad E_{\rm kin} > E_{\rm el}, \tag{7.10}$$

where R_i and R_j are the radius of colliding grains. $E_{\rm kin}$ is the kinetic energy for relative motion of the two grains

$$E_{\rm kin} = \frac{1}{2}\tilde{m}(\Delta v)^2, \tag{7.11}$$

where $\tilde{m} = m_i m_j/(m_i + m_j)$ is the reduced mass and Δv the relative velocity between the two grains. The electrostatic energy between the grains just before contact expresses

$$E_{\rm el} = \frac{Z_i Z_j e^2}{R_i + R_j}, \tag{7.12}$$

where Z_i and Z_j are charges of grains. The condition for the grains to collide is

$$E_{\rm kin} > E_{\rm el}. \tag{7.13}$$

This modification of the cross section can be implemented in our algorithm to treat the coagulation of the charged grains. 3D simulations will be performed with the code `PHANTOM` to analyse the formation of millimetre grains from charged micron-in-size grains in discs.

Part II

APPENDIX

a

CHAPTER 2

A.1 CONSERVATIVE FORM OF THE SMOLUCHOWSKI EQUATION

The conservative form of the Smoluchowski equation is

$$\begin{cases} \dfrac{\partial g\left(x,\tau\right)}{\partial \tau} + \dfrac{\partial F_{\text{coag}}\left[g\right]\left(x,\tau\right)}{\partial x} = 0, \\ F_{\text{coag}}\left[g\right]\left(x,\tau\right) = \displaystyle\int_0^x \int_{x-u}^{\infty} \mathcal{K}\left(u,v\right) g\left(u,\tau\right) \frac{g\left(v,\tau\right)}{v} \mathrm{d}v\mathrm{d}u, \end{cases} \tag{a.1}$$

where $g(x,\tau) = xf(x,\tau)$. The proof is to develop the equation a.1 in order to obtain the classic Smoluchowski equation 2.4.
Let us define the Leibniz integral rule

$$\frac{\mathrm{d}}{\mathrm{d}x}\left(\int_{a(x)}^{b(x)} f(x,t\mathrm{d}t\right) = f(x,b(x)) \cdot \frac{\mathrm{d}b(x)}{\mathrm{d}} - f(x,a(x)) \cdot \frac{\mathrm{d}a(x)}{\mathrm{d}x} + \int_{a(x)}^{b(x)} \frac{\partial f}{\partial x}(x,t)\mathrm{d}t, \tag{a.2}$$

where $x \in \mathbb{R}_+$ and a, b two functions with values in $\mathbb{R}$. Let define

$$\Gamma(x,u,\tau) \equiv \int_{x-u}^{\infty} \mathcal{K}(u,v) f(u,\tau) f(v,\tau)\mathrm{d}v. \tag{a.3}$$

Applying the integral Leibniz rule the derivative of the flux, we obtain

$$\frac{\partial F_{\text{coag}}}{\partial x} = \Gamma(x,x,\tau) + \int_0^x \frac{\partial \Gamma(x,u,\tau)}{\partial x}\mathrm{d}u. \tag{a.4}$$

Now, let define the function Φ as

$$\Phi(u,v,\tau) \equiv \mathcal{K}(u,v) u f(u,\tau) f(v,\tau). \tag{a.5}$$

Integral Leibniz rule is applied to the derivative of Γ,

$$\frac{\partial \Gamma(x,u,\tau)}{\partial x} = -\Phi(u,x-u,\tau). \tag{a.6}$$

Therefore,

$$\begin{aligned} \frac{\partial F_{\text{coag}}}{\partial x} &= \Gamma(x,x,\tau) - \int_0^x \Phi(u,x-u,\tau)\mathrm{d}u \\ &= \int_0^{\infty} \mathcal{K}(x,v) x f(x,\tau) f(u,\tau)\mathrm{d}u - \int_0^x \mathcal{K}(u,x-u) u f(u,\tau) f(x-u,\tau)\mathrm{d}u. \end{aligned} \tag{a.7}$$

At this stage, the second integral on the right side of the equation has to be written by a change of variable. Let define $z \equiv x - u$,

$$\begin{aligned}\int_0^x \mathcal{K}(u, x-u) u f(u,\tau) f(x-u,\tau) \mathrm{d}u &= \int_0^x \mathcal{K}(x-z, z)(x-z) f(x-z,\tau) f(z,\tau) \mathrm{d}z \\ &= \int_0^x \mathcal{K}(x-z, z) x f(x-z,\tau) f(z,\tau) \mathrm{d}z \\ &\quad - \int_0^x \mathcal{K}(x-z, z) z f(x-z,\tau) f(z,\tau) \mathrm{d}z.\end{aligned} \tag{a.8}$$

The kernel is a symmetric function $\mathcal{K}(u, v) = \mathcal{K}(v, u)$, therefore equation a.8 writes with $z = u$

$$\int_0^x \mathcal{K}(u, x-u) u f(u,\tau) f(x-u,\tau) \mathrm{d}u = \frac{1}{2} \int_0^x \mathcal{K}(u, x-u) x f(u,\tau) f(x-u,\tau) \mathrm{d}u. \tag{a.9}$$

By combining equations a.8, a.7 and dividing by $x \neq 0$, the original Smoluchowski equation is obtained

$$\frac{\partial f(x,\tau)}{\partial \tau} = \frac{1}{2} \int_0^x \mathcal{K}(u, x-u) f(u,\tau) f(x-u,\tau) \mathrm{d}u - f(x,\tau) \int_0^\infty \mathcal{K}(u, x) f(u,\tau) \mathrm{d}u. \tag{a.10}$$

b

CHAPTER 3

B.1 DERIVATION OF THE FLUX

The expression of the numerical coagulation flux $F^{\mathrm{nc}}_{\mathrm{coag}}[\tilde{g}]$ is given in equation 3.20. After applying the rules for integrals with Heaviside function, T writes

$$
\begin{aligned}
&T(x, x_{\min}, x_{\max}, i', i, l', l) = \frac{h_l}{2}\frac{h_{l'}}{2} \\
&\Bigg[\\
&\int_{\frac{2}{h_l}(x_{l-1/2}-x_l)}^{\frac{2}{h_l}(x_{l+1/2}-x_l)} f_2(\xi_l)\mathrm{d}\xi_l \times \\
&\quad \left\{ \int_{\frac{2}{h_{l'}}(x_{\min}-x_{l'})}^{\frac{2}{h_{l'}}(x-x_{l'})} f_1(\xi_{l'}) \left[\theta\left(\xi_{l'} - \frac{2}{h_{l'}}\left(x_{l'-1/2} - x_{l'}\right)\right) - \theta\left(\xi_{l'} - \frac{2}{h_{l'}}\left(x_{l'+1/2} - x_{l'}\right)\right)\right] \mathrm{d}\xi_{l'} \right\} \\
&\quad + \int_{\frac{2}{h_{l'}}(x_{\min}-x_{l'})}^{\frac{2}{h_{l'}}(x-x_{l'})} \int_{\frac{2}{h_l}\left(x-\frac{h_{l'}}{2}\xi_{l'}-x_{l'}+x_{\min}-x_l\right)}^{\frac{2}{h_{l'}}(x_{l-1/2}-x_l)} f_1(\xi_{l'})f_2(\xi_l) \\
&\qquad \left[\theta\left(\xi_{l'} - \frac{2}{h_{l'}}\left(x_{l'-1/2} - x_{l'}\right)\right) - \theta\left(\xi_{l'} - \frac{2}{h_{l'}}\left(x_{l'+1/2} - x_{l'}\right)\right)\right] \\
&\qquad\qquad \theta\left(\frac{2}{h_{l'}}\left(x - x_{l-1/2} + x_{\min} - x_{l'}\right) - \xi_{l'}\right) \mathrm{d}\xi_l \mathrm{d}\xi_{l'} \\
&\quad - \int_{\frac{2}{h_{l'}}(x_{\min}-x_{l'})}^{\frac{2}{h_{l'}}(x-x_{l'})} \int_{\frac{2}{h_l}\left(x-\frac{h_{l'}}{2}\xi_{l'}-x_{l'}+x_{\min}-x_l\right)}^{\frac{2}{h_{l'}}(x_{l+1/2}-x_l)} f_1(\xi_{l'})f_2(\xi_l) \\
&\qquad \left[\theta\left(\xi_{l'} - \frac{2}{h_{l'}}\left(x_{l'-1/2} - x_{l'}\right)\right) - \theta\left(\xi_{l'} - \frac{2}{h_{l'}}\left(x_{l'+1/2} - x_{l'}\right)\right)\right] \\
&\qquad\qquad \theta\left(\frac{2}{h_{l'}}\left(x - x_{l+1/2} + x_{\min} - x_{l'}\right) - \xi_{l'}\right) \mathrm{d}\xi_l \mathrm{d}\xi_{l'} \\
&\Bigg],
\end{aligned}
\tag{b.1}
$$

with $f_1(\xi_{l'}) \equiv \mathcal{K}_1(\xi_{l'})\phi_{i'}(\xi_{l'})$ and $f_2(\xi_l) \equiv K_2\left(\frac{h_l}{2}\xi_l + x_l\right)\frac{\phi_i(\xi_i)}{\frac{h_l}{2}\xi_l + x_l}$.

B.1.1 *Simple integral*

The rule for the simple integral with the Heaviside function is

$$\begin{cases} a < b, a \leq c, a < d, c < d \\ \displaystyle\int_a^b f(x)\left[\theta(x-c) - \theta(x-d)\right] \mathrm{d}x \\ \displaystyle= \theta(b-c)\left[\int_c^b f(x)\mathrm{d}x + \theta(a-c)\int_a^c f(x)\mathrm{d}x\right] - \theta(b-d)\int_d^b f(x)\mathrm{d}x. \end{cases} \tag{B.2}$$

The simple integral writes

$$\begin{aligned} &\bullet \int_{\frac{2}{h_{l'}}(x_{\min}-x_{l'})}^{\frac{2}{h_{l'}}(x-x_{l'})} f_1(\xi_{l'})\left[\theta\left(\xi_{l'} - \frac{2}{h_{l'}}(x_{l'-1/2}-x_{l'})\right) - \theta\left(\xi_{l'} - \frac{2}{h_{l'}}(x_{l'+1/2}-x_{l'})\right)\right]\mathrm{d}\xi_{l'} \\ &= \theta(x - x_{l'-1/2})\left[\int_{\frac{2}{h_{l'}}(x_{l'-1/2}-x_{l'})}^{\frac{2}{h_{l'}}(x-x_{l'})} f_1(\xi_{l'})\mathrm{d}\xi_{l'} + \underbrace{\theta(x_{\min} - x_{l'-1/2})\int_{\frac{2}{h_{l'}}(x_{\min}-x_{l'})}^{\frac{2}{h_{l'}}(x_{l'-1/2}-x_{l'})} f_1(\xi_{l'})\mathrm{d}\xi_{l'}}_{0 \text{ since } x_{l-1/2} \geq x_{\min}}\right] \\ &\quad - \theta(x - x_{l'+1/2})\int_{\frac{2}{h_{l'}}(x_{l'+1/2}-x_{l'})}^{\frac{2}{h_{l'}}(x-x_{l'})} f_1(\xi_{l'})\mathrm{d}\xi_{l'} \\ &= \theta(x - x_{l'-1/2})\int_{\frac{2}{h_{l'}}(x_{l'-1/2}-x_{l'})}^{\frac{2}{h_{l'}}(x-x_{l'})} f_1(\xi_{l'})\mathrm{d}\xi_{l'} - \theta(x - x_{l'+1/2})\int_{\frac{2}{h_{l'}}(x_{l'+1/2}-x_{l'})}^{\frac{2}{h_{l'}}(x-x_{l'})} f_1(\xi_{l'})\mathrm{d}\xi_{l'}. \end{aligned} \tag{B.3}$$

B.1.2 *First double integral*

The rule for the first double integral with the Heaviside function is

$$
\begin{cases}
a < b, a \leq c, a < d, c < d, e \leq b \\
\int_a^b f(x)\left[\theta(x-c) - \theta(x-d)\right]\theta(e-x)\mathrm{d}x \\
= \theta(b-c)\left[-\theta(a-c)\theta(e-a)\left\{\int_e^a f(x)\mathrm{d}x + \theta(e-b)\int_b^e f(x)\mathrm{d}x\right\}\right. \\
\qquad + (1-\theta(a-c))\left[\theta(b-c)\theta(e-c)\left\{\int_c^e f(x)\mathrm{d}x + \theta(e-b)\int_e^b f(x)\mathrm{d}x\right\}\right. \\
\qquad\qquad \left.\left. +\theta(c-b)\theta(e-b)\left\{\int_e^b f(x)\mathrm{d}x + \theta(e-c)\int_c^e f(x)\mathrm{d}x\right\}\right]\right] \\
\quad - \theta(b-d)\left[\theta(b-d)\theta(e-d)\left\{\int_d^e f(x)\mathrm{d}x + \theta(e-b)\int_e^b f(x)\mathrm{d}x\right\}\right. \\
\qquad\qquad \left. +\theta(d-b)\theta(e-b)\left\{\int_e^b f(x)\mathrm{d}x + \theta(e-d)\int_d^e f(x)\mathrm{d}x\right\}\right].
\end{cases}
\tag{B.4}
$$

The double integral writes

$$
\begin{aligned}
(1) & \int_{\frac{2}{h_{l'}}(x_{\min}-x_{l'})}^{\frac{2}{h_{l'}}(x-x_{l'})} f_1(\xi_{l'})F_{2,1}(\xi_{l'})\left[\theta\left(\xi_{l'}-\frac{2}{h_{l'}}(x_{l'-1/2}-x_{l'})\right)-\theta\left(\xi_{l'}-\frac{2}{h_{l'}}(x_{l'+1/2}-x_{l'})\right)\right] \\
& \qquad \theta\left(\frac{2}{h_{l'}}(x-x_{l-1/2}+x_{\min}-x_{l'})-\xi_{l'}\right)\mathrm{d}\xi_l\mathrm{d}\xi_{l'} \\
& = \theta(x-x_{l'-1/2}) \\
& \Bigg[-\theta(x_{\min}-x_{l'-1/2}) \\
& \quad \Bigg\{ \int_{\frac{2}{h_{l'}}(x-x_{l-1/2}+x_{\min}-x_{l'})}^{\frac{2}{h_{l'}}(x_{\min}-x_{l'})} f_1(\xi_{l'})F_{2,1}(\xi_{l'})\mathrm{d}\xi_{l'} + \underbrace{\theta(x_{\min}-x_{l-1/2}) \int_{\frac{2}{h_{l'}}(x-x_{l'})}^{\frac{2}{h_{l'}}(x-x_{l-1/2}+x_{\min}-x_{l'})} f_1(\xi_{l'})F_{2,1}(\xi_{l'})\mathrm{d}\xi_{l'}}_{0 \text{ since } x_{l-1/2}\geq x_{\min}} \Bigg\} \\
& \quad + (1-\theta(x_{\min}-x_{l'-1/2})) \\
& \qquad \Bigg[\theta(x-x_{l'-1/2})\theta(x-x_{l-1/2}+x_{min}-x_{l'-1/2}) \\
& \qquad \Bigg\{ \int_{\frac{2}{h_{l'}}(x_{l'-1/2}-x_{l'})}^{\frac{2}{h_{l'}}(x-x_{l-1/2}+x_{\min}-x_{l'})} f_1(\xi_{l'})F_{2,1}(\xi_{l'})\mathrm{d}\xi_{l'} + \underbrace{\theta(x_{\min}-x_{l-1/2}) \int_{\frac{2}{h_{l'}}(x-x_{l-1/2}+x_{\min}-x_{l'})}^{\frac{2}{h_{l'}}(x-x_{l'})} f_1(\xi_{l'})F_{2,1}(\xi_{l'})\mathrm{d}\xi_{l'}}_{0 \text{ since } x_{l-1/2}\geq x_{\min}} \Bigg\} \\
& \qquad + \theta(x_{l'-1/2}-x)\theta(x_{\min}-x_{l-1/2}) \\
& \qquad \Bigg\{ \underbrace{\int_{\frac{2}{h_{l'}}(x-x_{l-1/2}+x_{\min}-x_{l'})}^{\frac{2}{h_{l'}}(x-x_{l'})} f_1(\xi_{l'})F_{2,1}(\xi_{l'})\mathrm{d}\xi_{l'}}_{0 \text{ since } x_{l-1/2}\geq x_{\min}} \\
& \qquad\qquad + \theta(x-x_{l-1/2}+x_{\min}-x_{l'-1/2}) \int_{\frac{2}{h_{l'}}(x_{l'-1/2}-x_{l'})}^{\frac{2}{h_{l'}}(x-x_{l-1/2}+x_{\min}-x_{l'})} f_1(\xi_{l'})F_{2,1}(\xi_{l'})\mathrm{d}\xi_{l'} \Bigg\} \Bigg] \Bigg]
\end{aligned}
\tag{b.5}
$$

$$
\begin{aligned}
&- \theta(x - x_{l'+1/2}) \\
&\quad \Bigg[\theta(x - x_{l'+1/2})\theta(x - x_{l-1/2} + x_{\min} - x_{l'+1/2}) \\
&\qquad \Bigg\{ \int_{\frac{2}{h_{l'}}(x_{l'+1/2} - x_{l'})}^{\frac{2}{h_{l'}}(x - x_{l-1/2} + x_{\min} - x_{l'})} f_1(\xi_{l'}) F_{2,1}(\xi_{l'}) \mathrm{d}\xi_{l'} \\
&\qquad\quad \underbrace{+ \theta(x_{\min} - x_{l-1/2}) \int_{\frac{2}{h_{l'}}(x - x_{l-1/2} + x_{\min} - x_{l'})}^{\frac{2}{h_{l'}}(x - x_{l'})} f_1(\xi_{l'}) F_{2,1}(\xi_{l'}) \mathrm{d}\xi_{l'}}_{0 \text{ since } x_{l-1/2} \geq x_{\min}} \Bigg\} \\
&\quad + \theta(x_{l'+1/2})\theta(x_{\min} - x_{l-1/2}) \\
&\qquad \Bigg\{ \int_{\frac{2}{h_{l'}}(x - x_{l-1/2} + x_{\min} - x_{l'})}^{\frac{2}{h_{l'}}(x - x_{l'})} f_1(\xi_{l'}) F_{2,1}(\xi_{l'}) \mathrm{d}\xi_{l'} \\
&\qquad\quad + \theta(x - x_{l-1/2} + x_{\min} - x_{l'+1/2}) \int_{\frac{2}{h_{l'}}(x_{l'+1/2} - x_{l'})}^{\frac{2}{h_{l'}}(x - x_{l-1/2} + x_{\min} - x_{l'})} f_1(\xi_{l'}) F_{2,1}(\xi_{l'}) \mathrm{d}\xi_{l'} \Bigg\} \Bigg] .
\end{aligned}
\tag{b.6}
$$

$$
\begin{aligned}
(1) = {} & \theta(x - x_{l'-1/2}) \\
& \Bigg[-\theta(x_{\min} - x_{l'-1/2})\theta(x - x_{l-1/2}) \int_{\frac{2}{h_{l'}}(x - x_{l-1/2} + x_{\min} - x_{l'})}^{\frac{2}{h_{l'}}(x_{\min} - x_{l'})} f_1(\xi_{l'}) F_{2,1}(\xi_{l'}) \mathrm{d}\xi_{l'} \\
& \quad + (1 - \theta(x_{min} - x_{l'-1/2})) \\
& \quad \Bigg[\theta(x - x_{l'-1/2})\theta(x - x_{l-1/2} + x_{min} - x_{l'-1/2}) \int_{\frac{2}{h_{l'}}(x_{l'-1/2} - x_{l'})}^{\frac{2}{h_{l'}}(x - x_{l-1/2} + x_{\min} - x_{l'})} f_1(\xi_{l'}) F_{2,1}(\xi_{l'}) \mathrm{d}\xi_{l'} \\
& \quad\quad + \theta(x_{l'-1/2} - x)\theta(x_{\min} - x_{l-1/2}) \times \\
& \quad\quad \underbrace{\theta(x - x_{l-1/2} + x_{\min} - x_{l'-1/2}) \int_{\frac{2}{h_{l'}}(x_{l'-1/2} - x_{l'})}^{\frac{2}{h_{l'}}(x - x_{l-1/2} + x_{\min} - x_{l'})} f_1(\xi_{l'}) F_{2,1}(\xi_{l'}) \mathrm{d}\xi_{l'}}_{0 \text{ since } x_{l-1/2} \geq x_{\min}} \Bigg] \Bigg] \\
& \quad - \theta(x - x_{l'+1/2}) \\
& \quad \Bigg[\theta(x - x_{l'+1/2})\theta(x - x_{l-1/2} + x_{\min} - x_{l'+1/2}) \int_{\frac{2}{h_{l'}}(x_{l'+1/2} - x_{l'})}^{\frac{2}{h_{l'}}(x - x_{l-1/2} + x_{\min} - x_{l'})} f_1(\xi_{l'}) F_{2,1}(\xi_{l'}) \mathrm{d}\xi_{l'} \\
& \quad\quad + \theta(x_{l'+1/2} - x)\theta(x_{\min} - x_{l-1/2}) \\
& \quad\quad \underbrace{\theta(x - x_{l-1/2} + x_{\min} - x_{l'+1/2}) \int_{\frac{2}{h_{l'}}(x_{l'+1/2} - x_{l'})}^{\frac{2}{h_{l'}}(x - x_{l-1/2} + x_{\min} - x_{l'})} f_1(\xi_{l'}) F_{2,1}(\xi_{l'}) \mathrm{d}\xi_{l'}}_{0 \text{ since } x_{l-1/2} \geq x_{\min}} \Bigg]
\end{aligned}
$$

$$
\begin{aligned}
(1) = {} & \theta(x - x_{l'-1/2})\theta(x - x_{l-1/2} + x_{min} - x_{l'-1/2}) \int_{\frac{2}{h_{l'}}(x_{l'-1/2} - x_{l'})}^{\frac{2}{h_{l'}}(x - x_{l-1/2} + x_{\min} - x_{l'})} f_1(\xi_{l'}) F_{2,1}(\xi_{l'}) \mathrm{d}\xi_{l'} \\
& + \theta(x - x_{l'+1/2})\theta(x - x_{l-1/2} + x_{\min} - x_{l'+1/2}) \int_{\frac{2}{h_{l'}}(x - x_{l-1/2} + x_{\min} - x_{l'})}^{\frac{2}{h_{l'}}(x_{l'+1/2} - x_{l'})} f_1(\xi_{l'}) F_{2,1}(\xi_{l'}) \mathrm{d}\xi_{l'}.
\end{aligned}
\tag{b.7}
$$

B.1.3 *Second double integral*

The rule for the second double integral with the Heaviside function is

$$\begin{cases} a < b, a \leq c, a < d, c < d, e < b \\ \int_a^b f(x)\left[\theta(x-c) - \theta(x-d)\right]\theta(e-x)\mathrm{d}x \\ = \theta(b-d)\theta(e-d)\int_e^d f(x)\mathrm{d}x \\ \quad + \theta(b-c)\left[(\theta(a-c)-1)\theta(b-c)\theta(e-c)\int_e^c f(x)\mathrm{d}x + \theta(a-c)\theta(e-a)\int_a^e f(x)\mathrm{d}x\right], \end{cases} \tag{b.8}$$

The double integral writes

$$\begin{aligned} (1) \quad & \int_{\frac{2}{h_{l'}}(x_{\min}-x_{l'})}^{\frac{2}{h_{l'}}(x-x_{l'})} f_1(\xi_{l'})F_{2,2}(\xi_{l'})\left[\theta\left(\xi_{l'} - \frac{2}{h_{l'}}(x_{l'-1/2}-x_{l'})\right) - \theta\left(\xi_{l'} - \frac{2}{h_{l'}}(x_{l'+1/2}-x_{l'})\right)\right] \\ & \qquad \theta\left(\frac{2}{h_{l'}}(x - x_{l+1/2} + x_{\min} - x_{l'}) - \xi_{l'}\right)\mathrm{d}\xi_l \mathrm{d}\xi_{l'} \\ (1) = {} & \theta(x - x_{l'+1/2})\theta(x - x_{l+1/2} - x_{l'+1/2} + x_{\min}) \int_{\frac{2}{h_{l'}}(x-x_{l+1/2}+x_{\min}-x_{l'})}^{\frac{2}{h_{l'}}(x_{l'+1/2}-x_{l'})} f_1(\xi_{l'})F_{2,2}(\xi_{l'})\mathrm{d}\xi_{l'} \\ & + \theta(x - x_{l'-1/2}) \\ & \Bigg[(\theta(x_{\min} - x_{l'-1/2}) - 1) \times \\ & \quad \theta(x - x_{l'-1/2})\theta(x - x_{l+1/2} - x_{l'-1/2} + x_{\min}) \int_{\frac{2}{h_{l'}}(x-x_{l+1/2}+x_{\min}-x_{l'})}^{\frac{2}{h_{l'}}(x_{l'-1/2}-x_{l'})} f_1(\xi_{l'})F_{2,2}(\xi_{l'})\mathrm{d}\xi_{l'} \\ & \quad + \theta(x_{\min} - x_{l'-1/2})\theta(x - x_{l+1/2} + x_{\min} - x_{\min}) \int_{\frac{2}{h_{l'}}(x_{\min}-x_{l'})}^{\frac{2}{h_{l'}}(x-x_{l+1/2}+x_{\min}-x_{l'})} f_1(\xi_{l'})F_{2,2}(\xi_{l'})\mathrm{d}\xi_{l'}\Bigg], \end{aligned} \tag{b.9}$$

$$
\begin{aligned}
(1) = {} & \theta(x - x_{l'-1/2})\theta(x_{\min} - x_{l'-1/2}) \times \\
& \theta(x - x_{l+1/2} - x_{l'-1/2} + x_{\min}) \int_{\frac{2}{h_{l'}}(x - x_{l+1/2} + x_{\min} - x_{l'})}^{\frac{2}{h_{l'}}(x_{l'-1/2} - x_{l'})} f_1(\xi_{l'}) F_{2,2}(\xi_{l'}) \mathrm{d}\xi_{l'} \\
& \underbrace{+\theta(x - x_{l'-1/2})\theta(x_{\min} - x_{l'-1/2})\theta(x - x_{l+1/2}) \int_{\frac{2}{h_{l'}}(x_{\min} - x_{l'})}^{\frac{2}{h_{l'}}(x - x_{l+1/2} + x_{\min} - x_{l'})} f_1(\xi_{l'}) F_{2,2}(\xi_{l'}) \mathrm{d}\xi_{l'}}_{0 \text{ since } x_{l'-1/2} \geq x_{\min}} \\
& + \theta(x - x_{l'+1/2})\theta(x - x_{l+1/2} - x_{l'+1/2} + x_{\min}) \int_{\frac{2}{h_{l'}}(x - x_{l+1/2} + x_{\min} - x_{l'})}^{\frac{2}{h_{l'}}(x_{l'+1/2} - x_{l'})} f_1(\xi_{l'}) F_{2,2}(\xi_{l'}) \mathrm{d}\xi_{l'} \\
& - \theta(x - x_{l'-1/2})\theta(x - x_{l+1/2} - x_{l'-1/2} + x_{\min}) \int_{\frac{2}{h_{l'}}(x - x_{l+1/2} + x_{\min} - x_{l'})}^{\frac{2}{h_{l'}}(x_{l'-1/2} - x_{l'})} f_1(\xi_{l'}) F_{2,2}(\xi_{l'}) \mathrm{d}\xi_{l'}.
\end{aligned}
\tag{b.10}
$$

$$
\begin{aligned}
(1) = {} & \theta(x - x_{l'+1/2})\theta(x - x_{l+1/2} - x_{l'+1/2} + x_{\min}) \int_{\frac{2}{h_{l'}}(x - x_{l+1/2} + x_{\min} - x_{l'})}^{\frac{2}{h_{l'}}(x_{l'+1/2} - x_{l'})} f_1(\xi_{l'}) F_{2,2}(\xi_{l'}) \mathrm{d}\xi_{l'} \\
& + \theta(x - x_{l'-1/2})\theta(x - x_{l+1/2} - x_{l'-1/2} + x_{\min}) \int_{\frac{2}{h_{l'}}(x_{l'-1/2} - x_{l'})}^{\frac{2}{h_{l'}}(x - x_{l+1/2} + x_{\min} - x_{l'})} f_1(\xi_{l'}) F_{2,2}(\xi_{l'}) \mathrm{d}\xi_{l'}.
\end{aligned}
\tag{b.11}
$$

Then, T writes

$$
\begin{aligned}
T(x, x_{\min}, x_{\max}, i', i, l', l) = \frac{h_l}{2}\frac{h_{l'}}{2} \\
\Bigg[\int_{\frac{2}{h_l}(x_{l-1/2}-x_l)}^{\frac{2}{h_l}(x_{l+1/2}-x_l)} f_2(\xi_l)\mathrm{d}\xi_l \\
\left(\theta(x - x_{l'-1/2}) \int_{\frac{2}{h_{l'}}(x_{l'-1/2}-x_{l'})}^{\frac{2}{h_{l'}}(x-x_{l'})} f_1(\xi_{l'})\mathrm{d}\xi_{l'} - \theta(x - x_{l'+1/2}) \int_{\frac{2}{h_{l'}}(x_{l'+1/2}-x_{l'})}^{\frac{2}{h_{l'}}(x-x_{l'})} f_1(\xi_{l'})\mathrm{d}\xi_{l'} \right) \\
+ \theta(x - x_{l'-1/2}) \\
\Bigg[\theta(x - x_{l-1/2} + x_{\min} - x_{l'-1/2}) \\
\int_{\frac{2}{h_{l'}}(x_{l'-1/2}-x_{l'})}^{\frac{2}{h_{l'}}(x-x_{l-1/2}+x_{\min}-x_{l'})} \int_{\frac{2}{h_l}(x-\frac{h_{l'}}{2}\xi_{l'}-x_{l'}+x_{\min}-x_l)}^{\frac{2}{h_l}(x_{l-1/2}-x_l)} f_1(\xi_{l'})f_2(\xi_l)\mathrm{d}\xi_l\mathrm{d}\xi_{l'} \\
- \theta(x_{\max} - x_{l+1/2})\theta(x - x_{l+1/2} + x_{\min} - x_{l'-1/2}) \\
\int_{\frac{2}{h_{l'}}(x_{l'-1/2}-x_{l'})}^{\frac{2}{h_{l'}}(x-x_{l+1/2}+x_{\min}-x_{l'})} \int_{\frac{2}{h_l}(x-\frac{h_{l'}}{2}\xi_{l'}-x_{l'}+x_{\min}-x_l)}^{\frac{2}{h_l}(x_{l+1/2}-x_l)} f_1(\xi_{l'})f_2(\xi_l)\mathrm{d}\xi_l\mathrm{d}\xi_{l'} \Bigg] \\
+ \theta(x - x_{l'+1/2}) \\
\Bigg[\theta(x - x_{l-1/2} + x_{\min} - x_{l'+1/2}) \\
\int_{\frac{2}{h_{l'}}(x-x_{l-1/2}+x_{\min}-x_{l'})}^{\frac{2}{h_{l'}}(x_{l'+1/2}-x_{l'})} \int_{\frac{2}{h_l}(x-\frac{h_{l'}}{2}\xi_{l'}-x_{l'}+x_{\min}-x_l)}^{\frac{2}{h_l}(x_{l-1/2}-x_l)} f_1(\xi_{l'})f_2(\xi_l)\mathrm{d}\xi_l\mathrm{d}\xi_{l'} \\
- \theta(x_{\max} - x_{l+1/2})\theta(x - x_{l+1/2} + x_{\min} - x_{l'+1/2}) \\
\int_{\frac{2}{h_{l'}}(x-x_{l+1/2}+x_{\min}-x_{l'})}^{\frac{2}{h_{l'}}(x_{l'+1/2}-x_{l'})} \int_{\frac{2}{h_l}(x-\frac{h_{l'}}{2}\xi_{l'}-x_{l'}+x_{\min}-x_l)}^{\frac{2}{h_l}(x_{l+1/2}-x_l)} f_1(\xi_{l'})f_2(\xi_l)\mathrm{d}\xi_l\mathrm{d}\xi_{l'} \Bigg] \Bigg] .
\end{aligned}
\tag{B.12}
$$

B.1.4 *Fortran scheme for flux term*

The `Fortran` scheme to evaluate $T(x, x_{\min}, x_{\max}, i', i, l', l)$ writes with terms in equation 3.32

```
res1=0
res2=0
if (x > x_{l'+1/2}) then
   res1 = T_{φ_i} × T_{φ_{i'},mix}
   if (x > x_{l+1/2} + x_{l'+1/2} − x_min) then
      res2 = T_{φ_{i'},φ_i,allmix}
   else if (x ≤ x_{l+1/2} + x_{l'+1/2} − x_min and x > x_{l+1/2} + x_{l'−1/2} − x_min and
       x > x_{l−1/2} + x_{l'+1/2} − x_min) then
      res2 = T_{φ_{i'},φ_i,mix_P1term1_P2term1} − T_{φ_{i'},φ_i,P1term2}
   else if (x ≤ x_{l+1/2} + x_{l'+1/2} − x_min and x ≤ x_{l+1/2} + x_{l'−1/2} − x_min and
       x > x_{l−1/2} + x_{l'+1/2} − x_min) then
      res2 = T_{φ_{i'},φ_i,mix_P1term1_P2term1}
   else if (x ≤ x_{l+1/2} + x_{l'+1/2} − x_min and x > x_{l+1/2} + x_{l'−1/2} − x_min and
       x ≤ x_{l−1/2} + x_{l'+1/2} − x_min) then
      res2 = T_{φ_{i'},φ_i,P1term1} − T_{φ_{i'},φ_i,P1term2}
   else if (x ≤ x_{l+1/2} + x_{l'+1/2} − x_min and x ≤ x_{l+1/2} + x_{l'−1/2} − x_min
            and x ≤ x_{l−1/2} + x_{l'+1/2} − x_min and x > x_{l−1/2} + x_{l'−1/2} − x_min) then
      res2 = T_{φ_{i'},φ_i,P1term1}
   else
      res2 = 0
   endif
else if (x ≤ x_{l'+1/2} and x > x_{l'−1/2}) then
   res1 = T_{φ_i} × T_{φ_{i'},term1}
   if (x > x_{l+1/2} + x_{l'−1/2} − x_min) then
      res2 = T_{φ_{i'},φ_i,P1term1} − T_{φ_{i'},φ_i,P1term2}
   else if (x ≤ x_{l+1/2} + x_{l'−1/2} − x_min and x > x_{l−1/2} + x_{l'−1/2} − x_min) then
      res2 = T_{φ_{i'},φ_i,P1term1}
   else
      res2 = 0
else
   res1=0
   res2=0
endif

T = (res1+res2)*hl*hl'/4
```

B.2 DERIVATION OF INTEGRAL OF THE FLUX

The term with the integral of the numerical flux, that we note $\mathcal{F}^{\text{nc}}_{\text{coag}}$, writes

$$\begin{cases} \mathcal{F}^{\text{nc}}_{\text{coag}}[\tilde{g}, j, k](t) = \sum_{l'=1}^{N} \sum_{i'=0}^{k} \sum_{l=1}^{N} \sum_{i=0}^{k} g^{i'}_{l'}(t)\, g^{i}_{l}(t) \mathcal{T}\left(x_{\min}, x_{\max}, j, k, i', i, l', l\right) \\ \mathcal{T}\left(x_{\min}, x_{\max}, j, k, i', i, l', l\right) \equiv \\ \int_{I_j} \int_{x_{\min}}^{x} \int_{x-u+x_{\min}}^{x_{\max}} \frac{\mathcal{K}(u,v)}{v} \partial_x \phi_k(\xi_j(x)) \\ \qquad\qquad \phi_{i'}(\xi_{l'}(u))[\theta(u - x_{l'-1/2}) - \theta(u - x_{l'+1/2})] \\ \qquad\qquad \phi_{i}(\xi_{l}(v))[\theta(v - x_{l-1/2}) - \theta(v - x_{l+1/2})] \mathrm{d}v\, \mathrm{d}u\, \mathrm{d}x, \\ \mathcal{T}\left(x_{\min}, x_{\max}, j, k, i', i, l', l\right) \equiv \int_{I_j} T(x, x_{\min}, x_{\max}, i', i, l', l) \partial_x \phi_k(\xi_j(x)) \mathrm{d}x \end{cases} \tag{b.13}$$

Multiplying $T(x, x_{\min}, x_{\max}, i', i, l', l)$ in equation b.12 by $\partial_x \phi_k\left(\xi_j(x)\right)$, $\mathcal{T}$ writes, with $\xi_j = \frac{2}{h_j}\left(x - x_j\right)$,

$$
\begin{aligned}
&\mathcal{T}\left(x_{\min}, x_{\max}, j, k, i', i, l', l\right) = \frac{h_l}{2}\frac{h_{l'}}{2} \\
&\Bigg[\int_{\frac{2}{h_l}(x_{l-1/2}-x_l)}^{\frac{2}{h_l}(x_{l+1/2}-x_l)} f_2(\xi_l)\mathrm{d}\xi_l \times \\
&\Bigg(\int_{\frac{2}{h_j}\left(x_{j-1/2}-x_j\right)}^{\frac{2}{h_j}\left(x_{j+1/2}-x_j\right)} \int_{\frac{2}{h_{l'}}\left(x_{l'-1/2}-x_{l'}\right)}^{\frac{2}{h_{l'}}\left(\frac{h_j}{2}\xi_j+x_j-x_{l'}\right)} f_1(\xi_{l'})\partial_{\xi_j}\phi_k(\xi_j)\theta\left(\xi_j - \frac{2}{h_j}(x_{l'-1/2}-x_j)\right)\mathrm{d}\xi_j \\
&- \int_{\frac{2}{h_j}\left(x_{j-1/2}-x_j\right)}^{\frac{2}{h_j}\left(x_{j+1/2}-x_j\right)} \int_{\frac{2}{h_{l'}}\left(x_{l'+1/2}-x_{l'}\right)}^{\frac{2}{h_{l'}}\left(\frac{h_j}{2}\xi_j+x_j-x_{l'}\right)} f_1(\xi_{l'})\partial_{\xi_j}\phi_k(\xi_j)\theta\left(\xi_j - \frac{2}{h_j}(x_{l'+1/2}-x_j)\right)\mathrm{d}\xi_{l'}\mathrm{d}\xi_j\Bigg) \\
&+ \int_{\frac{2}{h_j}\left(x_{j-1/2}-x_j\right)}^{\frac{2}{h_j}\left(x_{j+1/2}-x_j\right)} \int_{\frac{2}{h_{l'}}\left(x_{l'-1/2}-x_{l'}\right)}^{\frac{2}{h_{l'}}\left(\frac{h_j}{2}\xi_j+x_j-x_{l-1/2}+x_{\min}-x_{l'}\right)} \int_{\frac{2}{h_l}\left(\frac{h_j}{2}\xi_j+x_j-\frac{h_{l'}}{2}\xi_{l'}-x_{l'}+x_{\min}-x_l\right)}^{\frac{2}{h_l}(x_{l-1/2}-x_l)} f_1(\xi_{l'})f_2(\xi_l)\partial_{\xi_j}\phi_k(\xi_j) \\
&\quad\times\theta\left(\xi_j - \frac{2}{h_j}(x_{l'-1/2}-x_j)\right)\theta\left(\xi_j - \frac{2}{h_j}(x_{l-1/2}+x_{l'-1/2}-x_{\min}-x_j)\right)\mathrm{d}\xi_l\mathrm{d}\xi_{l'}\mathrm{d}\xi_j \\
&- \int_{\frac{2}{h_j}\left(x_{j-1/2}-x_j\right)}^{\frac{2}{h_j}\left(x_{j+1/2}-x_j\right)} \int_{\frac{2}{h_{l'}}\left(x_{l'-1/2}-x_{l'}\right)}^{\frac{2}{h_{l'}}\left(\frac{h_j}{2}\xi_j+x_j-x_{l+1/2}+x_{\min}-x_{l'}\right)} \int_{\frac{2}{h_l}\left(\frac{h_j}{2}\xi_j+x_j-\frac{h_{l'}}{2}\xi_{l'}-x_{l'}+x_{\min}-x_l\right)}^{\frac{2}{h_l}(x_{l+1/2}-x_l)} f_1(\xi_{l'})f_2(\xi_l)\partial_{\xi_j}\phi_k(\xi_j) \\
&\quad\times\theta\left(\xi_j - \frac{2}{h_j}(x_{l'-1/2}-x_j)\right)\theta\left(\xi_j - \frac{2}{h_j}(x_{l+1/2}+x_{l'-1/2}-x_{\min}-x_j)\right)\mathrm{d}\xi_l\mathrm{d}\xi_{l'}\mathrm{d}\xi_j \\
&+ \int_{\frac{2}{h_j}\left(x_{j-1/2}-x_j\right)}^{\frac{2}{h_j}\left(x_{j+1/2}-x_j\right)} \int_{\frac{2}{h_{l'}}\left(\frac{h_j}{2}\xi_j+x_j-x_{l-1/2}+x_{\min}-x_{l'}\right)}^{\frac{2}{h_{l'}}\left(x_{l'+1/2}-x_{l'}\right)} \int_{\frac{2}{h_l}\left(\frac{h_j}{2}\xi_j+x_j-\frac{h_{l'}}{2}\xi_{l'}-x_{l'}+x_{\min}-x_l\right)}^{\frac{2}{h_l}(x_{l-1/2}-x_l)} f_1(\xi_{l'})f_2(\xi_l)\partial_{\xi_j}\phi_k(\xi_j) \\
&\quad\times\theta\left(\xi_j - \frac{2}{h_j}(x_{l'+1/2}-x_j)\right)\theta\left(\xi_j - \frac{2}{h_j}(x_{l-1/2}+x_{l'+1/2}-x_{\min}-x_j)\right)\mathrm{d}\xi_l\mathrm{d}\xi_{l'}\mathrm{d}\xi_j \\
&- \int_{\frac{2}{h_j}\left(x_{j-1/2}-x_j\right)}^{\frac{2}{h_j}\left(x_{j+1/2}-x_j\right)} \int_{\frac{2}{h_{l'}}\left(\frac{h_j}{2}\xi_j+x_j-x_{l+1/2}+x_{\min}-x_{l'}\right)}^{\frac{2}{h_{l'}}\left(x_{l'+1/2}-x_{l'}\right)} \int_{\frac{2}{h_l}\left(\frac{h_j}{2}\xi_j+x_j-\frac{h_{l'}}{2}\xi_{l'}-x_{l'}+x_{\min}-x_l\right)}^{\frac{2}{h_l}(x_{l+1/2}-x_l)} f_1(\xi_{l'})f_2(\xi_l)\partial_{\xi_j}\phi_k(\xi_j) \\
&\quad\times\theta\left(\xi_j - \frac{2}{h_j}(x_{l'+1/2}-x_j)\right)\theta\left(\xi_j - \frac{2}{h_j}\left(x_{l+1/2}+x_{l'+1/2}-x_{\min}-x_j\right)\right)\mathrm{d}\xi_l\mathrm{d}\xi_{l'}\mathrm{d}\xi_j\Bigg].
\end{aligned}
\tag{b.14}
$$

B.2.1 *Derivation of double integrals*

The rule for the double integrals is

$$\begin{cases} a < b \\ \int_a^b f(x)\theta(x-c)\mathrm{d}x = \theta(b-c)\left(\int_c^b f(x)\mathrm{d}x + \theta(a-c)\int_a^c f(x)\mathrm{d}x\right). \end{cases} \tag{b.15}$$

Then we obtain

$$\begin{aligned}
&\bullet \int_{\frac{2}{h_j}(x_{j-1/2}-x_j)}^{\frac{2}{h_j}(x_{j+1/2}-x_j)} \int_{\frac{2}{h_{l'}}(x_{l'-1/2}-x_{l'})}^{\frac{2}{h_{l'}}(x-x_{l'})} f_1(\xi_{l'})\partial_{\xi_j}\phi_k(\xi_j)\theta\left(\xi_j - \frac{2}{h_j}(x_{l'-1/2}-x_j)\right)\mathrm{d}\xi_j \\
&\quad = \theta(x_{j+1/2}-x_{l'-1/2})\left(\int_{\frac{2}{h_j}(x_{l'-1/2}-x_j)}^{\frac{2}{h_j}(x_{j+1/2}-x_j)} \int_{\frac{2}{h_{l'}}(x_{l'-1/2}-x_{l'})}^{\frac{2}{h_{l'}}(x-x_{l'})} f_1(\xi_{l'})\partial_{\xi_j}\phi_k(\xi_j)\mathrm{d}\xi_j\right. \\
&\qquad \left. +\theta(x_{j-1/2}-x_{l'-1/2})\int_{\frac{2}{h_j}(x_{j-1/2}-x_j)}^{\frac{2}{h_j}(x_{l'-1/2}-x_j)} \int_{\frac{2}{h_{l'}}(x_{l'-1/2}-x_{l'})}^{\frac{2}{h_{l'}}(x-x_{l'})} f_1(\xi_{l'})\partial_{\xi_j}\phi_k(\xi_j)\mathrm{d}\xi_j\right),
\end{aligned} \tag{b.16}$$

$$\begin{aligned}
&\bullet \int_{\frac{2}{h_j}(x_{j-1/2}-x_j)}^{\frac{2}{h_j}(x_{j+1/2}-x_j)} \int_{\frac{2}{h_{l'}}(x_{l'+1/2}-x_{l'})}^{\frac{2}{h_{l'}}(x-x_{l'})} f_1(\xi_{l'})\partial_{\xi_j}\phi_k(\xi_j)\theta\left(\xi_j - \frac{2}{h_j}(x_{l'+1/2}-x_j)\right)\mathrm{d}\xi_j \\
&\quad = \theta(x_{j+1/2}-x_{l'+1/2})\left(\int_{\frac{2}{h_j}(x_{l'+1/2}-x_j)}^{\frac{2}{h_j}(x_{j+1/2}-x_j)} \int_{\frac{2}{h_{l'}}(x_{l'+1/2}-x_{l'})}^{\frac{2}{h_{l'}}(x-x_{l'})} f_1(\xi_{l'})\partial_{\xi_j}\phi_k(\xi_j)\mathrm{d}\xi_j\right. \\
&\qquad \left. +\theta(x_{j-1/2}-x_{l'+1/2})\int_{\frac{2}{h_j}(x_{j-1/2}-x_j)}^{\frac{2}{h_j}(x_{l'+1/2}-x_j)} \int_{\frac{2}{h_{l'}}(x_{l'+1/2}-x_{l'})}^{\frac{2}{h_{l'}}(x-x_{l'})} f_1(\xi_{l'})\partial_{\xi_j}\phi_k(\xi_j)\mathrm{d}\xi_j\right).
\end{aligned}$$

B.2.2 *Derivation of the triple integrals*

The rule for the first and third triple integrals is

$$\begin{cases} a < b, c \leq d \\ \int_a^b f(x)\theta(x-c)\theta(x-d)\mathrm{d}x = \\ \theta(b-c)\left[\theta(a-c)\theta(b-d)\left\{\int\limits_d^b f(x)\mathrm{d}x + \theta(a-d)\int\limits_a^d f(x)\mathrm{d}x\right\}\right. \\ +(1-\theta(a-c))\left[\theta(c-b)\theta(c-d)\left\{\int\limits_c^d f(x)\mathrm{d}x + \theta(b-d)\int\limits_d^b f(x)\mathrm{d}x\right\}\right. \\ \left.\left.+\theta(b-c)\theta(b-d)\left\{\int\limits_d^b f(x)\mathrm{d}x + \theta(c-d)\int\limits_c^d f(x)\mathrm{d}x\right\}\right]\right] \end{cases} \tag{b.17}$$

Let denote

$$F_1(\xi_j) \equiv \int\limits_{\frac{2}{h_{l'}}\left(x_{l'-1/2}-x_{l'}\right)}^{\frac{2}{h_{l'}}\left(\frac{h_j}{2}\xi_j+x_j-x_{l-1/2}+x_{\min}-x_{l'}\right)} \int\limits_{\frac{2}{h_l}\left(\frac{h_j}{2}\xi_j+x_j-\frac{h_{l'}}{2}\xi_{l'}-x_{l'}+x_{\min}-x_l\right)}^{\frac{2}{h_l}(x_{l-1/2}-x_l)} f_1(\xi_{l'})f_2(\xi_l)\partial_{\xi_j}\phi_k(\xi_j)\mathrm{d}\xi_l\mathrm{d}\xi_{l'},$$

$$F_3(\xi_j) \equiv \int\limits_{\frac{2}{h_{l'}}\left(\frac{h_j}{2}\xi_j+x_j-x_{l-1/2}+x_{\min}-x_{l'}\right)}^{\frac{2}{h_{l'}}\left(x_{l'+1/2}-x_{l'}\right)} \int\limits_{\frac{2}{h_l}\left(\frac{h_j}{2}\xi_j+x_j-\frac{h_{l'}}{2}\xi_{l'}-x_{l'}+x_{\min}-x_l\right)}^{\frac{2}{h_l}(x_{l-1/2}-x_l)} f_1(\xi_{l'})f_2(\xi_l)\partial_{\xi_j}\phi_k(\xi_j)\mathrm{d}\xi_l\mathrm{d}\xi_{l'}. \tag{b.18}$$

The first triple integral writes

$$
\begin{aligned}
&(1) \int_{\frac{2}{h_j}(x_{j-1/2}-x_j)}^{\frac{2}{h_j}(x_{j+1/2}-x_j)} F_1(\xi_j)\theta\left(\xi_j - \frac{2}{h_j}(x_{l'-1/2}-x_j)\right)\theta\left(\xi_j - \frac{2}{h_j}(x_{l-1/2}+x_{l'-1/2}-x_{\min}-x_j)\right)\mathrm{d}\xi_j \\
&= \theta(x_{j+1/2}-x_{l'-1/2}) \\
&\Bigg[\theta(x_{j-1/2}-x_{l'-1/2})\theta(x_{j+1/2}+x_{\min}-x_{l-1/2}-x_{l'-1/2})\Bigg\{\int_{\frac{2}{h_j}(x_{l-1/2}+x_{l'-1/2}-x_{\min}-x_j)}^{\frac{2}{h_j}(x_{j+1/2}-x_j)} F_1(\xi_j)\mathrm{d}\xi_j \\
&\qquad +\theta(x_{j-1/2}+x_{\min}-x_{l-1/2}-x_{l'-1/2})\int_{\frac{2}{h_j}(x_{j-1/2}-x_j)}^{\frac{2}{h_j}(x_{l-1/2}+x_{l'-1/2}-x_{\min}-x_j)} F_1(\xi_j)\mathrm{d}\xi_j\Bigg\} \\
&+(1-\theta(x_{j-1/2}-x_{l'-1/2})) \\
&\Bigg[\theta(x_{l'-1/2}-x_{j+1/2})\theta(x_{l'-1/2}+x_{\min}-x_{l-1/2}-x_{l'-1/2})\Bigg\{\int_{\frac{2}{h_j}(x_{l'-1/2}-x_j)}^{\frac{2}{h_j}(x_{l-1/2}+x_{l'-1/2}-x_{\min}-x_j)} F_1(\xi_j)\mathrm{d}\xi_j \\
&\qquad +\theta(x_{j+1/2}+x_{\min}-x_{l-1/2}-x_{l'-1/2})\int_{\frac{2}{h_j}(x_{l-1/2}+x_{l'-1/2}-x_{\min}-x_j)}^{\frac{2}{h_j}(x_{j+1/2}-x_j)} F_1(\xi_j)\mathrm{d}\xi_j\Bigg\} \\
&\quad +\theta(x_{j+1/2}-x_{l'-1/2})\theta(x_{j+1/2}+x_{\min}-x_{l-1/2}-x_{l'-1/2})\Bigg\{\int_{\frac{2}{h_j}(x_{l-1/2}+x_{l'-1/2}-x_{\min}-x_j)}^{\frac{2}{h_j}(x_{j+1/2}-x_j)} F_1(\xi_j)\mathrm{d}\xi_j \\
&\qquad \underbrace{+\theta(x_{l'-1/2}+x_{\min}-x_{l-1/2}-x_{l'-1/2})\int_{\frac{2}{h_j}(x_{l'-1/2}-x_j)}^{\frac{2}{h_j}(x_{l-1/2}+x_{l'-1/2}-x_{\min}-x_j)} F_1(\xi_j)\mathrm{d}\xi_j}_{0 \text{ since } x_{l-1/2}\geq x_{\min}}\Bigg\}\Bigg]\Bigg]
\end{aligned}
\tag{b.19}
$$

$$
\begin{aligned}
(1) &= \theta(x_{j+1/2} - x_{l'-1/2}) \\
&\Bigg[\theta(x_{j-1/2} - x_{l'-1/2})\theta(x_{j+1/2} + x_{\min} - x_{l-1/2} - x_{l'-1/2}) \Bigg\{ \int_{\frac{2}{h_j}(x_{l-1/2}+x_{l'-1/2}-x_{\min}-x_j)}^{\frac{2}{h_j}(x_{j+1/2}-x_j)} F_1(\xi_j)\mathrm{d}\xi_j \\
&\qquad + \theta(x_{j-1/2} + x_{\min} - x_{l-1/2} - x_{l'-1/2}) \int_{\frac{2}{h_j}(x_{j-1/2}-x_j)}^{\frac{2}{h_j}(x_{l-1/2}+x_{l'-1/2}-x_{\min}-x_j)} F_1(\xi_j)\mathrm{d}\xi_j \Bigg\} \\
&+ (1 - \theta(x_{j-1/2} - x_{l'-1/2})) \\
&\Bigg[\theta(x_{l'-1/2} - x_{j+1/2})\theta(x_{\min} - x_{l-1/2}) \int_{\frac{2}{h_j}(x_{l'-1/2}-x_j)}^{\frac{2}{h_j}(x_{l-1/2}+x_{l'-1/2}-x_{\min}-x_j)} F_1(\xi_j)\mathrm{d}\xi_j \\
&\quad + \theta(x_{l'-1/2} - x_{j+1/2})\theta(x_{\min} - x_{l-1/2}) \times \\
&\quad \underbrace{\theta(x_{j+1/2} + x_{\min} - x_{l-1/2} - x_{l'-1/2}) \int_{\frac{2}{h_j}(x_{l-1/2}+x_{l'-1/2}-x_{\min}-x_j)}^{\frac{2}{h_j}(x_{j+1/2}-x_j)} F_1(\xi_j)\mathrm{d}\xi_j}_{0 \text{ since } x_{l-1/2} \geq x_{\min}} \\
&\quad + \theta(x_{j+1/2} - x_{l'-1/2})\theta(x_{j+1/2} + x_{\min} - x_{l-1/2} - x_{l'-1/2}) \int_{\frac{2}{h_j}(x_{l-1/2}+x_{l'-1/2}-x_{\min}-x_j)}^{\frac{2}{h_j}(x_{j+1/2}-x_j)} F_1(\xi_j)\mathrm{d}\xi_j \Bigg]\Bigg] \\
&= \theta(x_{j+1/2} - x_{l'-1/2})\theta(x_{j-1/2} - x_{l'-1/2}) \times \\
&\quad \cancel{\theta(x_{j+1/2} + x_{\min} - x_{l-1/2} - x_{l'-1/2}) \int_{\frac{2}{h_j}(x_{l-1/2}+x_{l'-1/2}-x_{\min}-x_j)}^{\frac{2}{h_j}(x_{j+1/2}-x_j)} F_1(\xi_j)\mathrm{d}\xi_j} \\
&\quad + \theta(x_{j+1/2} - x_{l'-1/2})\theta(x_{j-1/2} - x_{l'-1/2})\theta(x_{j+1/2} + x_{\min} - x_{l-1/2} - x_{l'-1/2}) \\
&\quad \theta(x_{j-1/2} + x_{\min} - x_{l-1/2} - x_{l'-1/2}) \int_{\frac{2}{h_j}(x_{j-1/2}-x_j)}^{\frac{2}{h_j}(x_{l-1/2}+x_{l'-1/2}-x_{\min}-x_j)} F_1(\xi_j)\mathrm{d}\xi_j \\
&\quad - \theta(x_{j-1/2} - x_{l'-1/2})\theta(x_{j+1/2} - x_{l'-1/2})^2 \times \\
&\quad \cancel{\theta(x_{j+1/2} + x_{\min} - x_{l-1/2} - x_{l'-1/2}) \int_{\frac{2}{h_j}(x_{l-1/2}+x_{l'-1/2}-x_{\min}-x_j)}^{\frac{2}{h_j}(x_{j+1/2}-x_j)} F_1(\xi_j)\mathrm{d}\xi_j} \\
&\quad + \theta(x_{j+1/2} - x_{l'-1/2})^2\theta(x_{j+1/2} + x_{\min} - x_{l-1/2} - x_{l'-1/2}) \int_{\frac{2}{h_j}(x_{l-1/2}+x_{l'-1/2}-x_{\min}-x_j)}^{\frac{2}{h_j}(x_{j+1/2}-x_j)} F_1(\xi_j)\mathrm{d}\xi_j
\end{aligned}
\tag{b.20}
$$

$$
\begin{aligned}
(1) &= \theta(x_{j+1/2} - x_{l'-1/2})\theta(x_{j+1/2} + x_{\min} - x_{l-1/2} - x_{l'-1/2}) \\
&\left[\int_{\frac{2}{h_j}(x_{l-1/2}+x_{l'-1/2}-x_{\min}-x_j)}^{\frac{2}{h_j}(x_{j+1/2}-x_j)} F_1(\xi_j)\mathrm{d}\xi_j \right. \\
&\left. +\theta(x_{j-1/2} - x_{l'-1/2})\theta(x_{j-1/2} + x_{\min} - x_{l-1/2} - x_{l'-1/2}) \int_{\frac{2}{h_j}(x_{j-1/2}-x_j)}^{\frac{2}{h_j}(x_{l-1/2}+x_{l'-1/2}-x_{\min}-x_j)} F_1(\xi_j)\mathrm{d}\xi_j \right].
\end{aligned}
\tag{b.21}
$$

The third triple integral writes, with the similar simplifications,

$$
\begin{aligned}
(3) &\int_{\frac{2}{h_j}(x_{j-1/2}-x_j)}^{\frac{2}{h_j}(x_{j+1/2}-x_j)} F_3(\xi_j)\theta\left(\xi_j - \frac{2}{h_j}(x_{l'+1/2} - x_j)\right)\theta\left(\xi_j - \frac{2}{h_j}(x_{l-1/2} + x_{l'+1/2} - x_{\min} - x_j)\right)\mathrm{d}\xi_j \\
&= \theta(x_{j+1/2} - x_{l'+1/2})\theta(x_{j+1/2} + x_{\min} - x_{l-1/2} - x_{l'+1/2}) \\
&\left[\int_{\frac{2}{h_j}(x_{l-1/2}+x_{l'+1/2}-x_{\min}-x_j)}^{\frac{2}{h_j}(x_{j+1/2}-x_j)} F_3(\xi_j)\mathrm{d}\xi_j \right. \\
&\left. +\theta(x_{j-1/2} - x_{l'+1/2})\theta(x_{j-1/2} + x_{\min} - x_{l-1/2} - x_{l'+1/2}) \int_{\frac{2}{h_j}(x_{j-1/2}-x_j)}^{\frac{2}{h_j}(x_{l-1/2}+x_{l'+1/2}-x_{\min}-x_j)} F_3(\xi_j)\mathrm{d}\xi_j \right].
\end{aligned}
\tag{b.22}
$$

The rule for the second and fourth triple integrals is

$$\begin{cases} a < b, c < d \\ \int_a^b f(x)\theta(x-c)\theta(x-d)\mathrm{d}x = \\ \theta(b-c)\theta(b-d)\left[(1-\theta(a-c))\theta(b-c)\int_d^b f(x)\mathrm{d}x \right. \\ \qquad \left. +\theta(a-c)\left(\int_d^b f(x)\mathrm{d}x + \theta(a-d)\int_a^d f(x)\mathrm{d}x\right)\right] \\ = \theta(b-d)\left[\int_d^b f(x)\mathrm{d}x \cancel{-\theta(a-c)\theta^2(b-c)\int_d^b f(x)\mathrm{d}x} \right. \\ \qquad \left. \cancel{+\theta(b-c)\theta(a-c)\int_d^b f(x)\mathrm{d}x} + \theta(b-c)\theta(a-c)\theta(a-d)\int_a^d f(x)\mathrm{d}x\right] \\ = \theta(b-c)\theta(b-d)\left[\int_d^b f(x)\mathrm{d}x + \theta(a-c)\theta(a-d)\int_a^d f(x)\mathrm{d}x\right]. \end{cases} \tag{b.23}$$

Let denote

$$\begin{aligned} F_2(\xi_j) &\equiv \int_{\frac{2}{h_{l'}}\left(x_{l'-1/2}-x_{l'}\right)}^{\frac{2}{h_{l'}}\left(\frac{h_j}{2}\xi_j+x_j-x_{l+1/2}+x_{\min}-x_{l'}\right)} \int_{\frac{2}{h_l}\left(\frac{h_j}{2}\xi_j+x_j-\frac{h_{l'}}{2}\xi_{l'}-x_{l'}+x_{\min}-x_l\right)}^{\frac{2}{h_l}(x_{l+1/2}-x_l)} f_1(\xi_{l'})f_2(\xi_l)\partial_{\xi_j}\phi_k(\xi_j)\mathrm{d}\xi_l\mathrm{d}\xi_{l'}, \\ F_4(\xi_j) &\equiv \int_{\frac{2}{h_{l'}}\left(\frac{h_j}{2}\xi_j+x_j-x_{l+1/2}+x_{\min}-x_{l'}\right)}^{\frac{2}{h_{l'}}\left(x_{l'+1/2}-x_{l'}\right)} \int_{\frac{2}{h_l}\left(\frac{h_j}{2}\xi_j+x_j-\frac{h_{l'}}{2}\xi_{l'}-x_{l'}+x_{\min}-x_l\right)}^{\frac{2}{h_l}(x_{l+1/2}-x_l)} f_1(\xi_{l'})f_2(\xi_l)\partial_{\xi_j}\phi_k(\xi_j)\mathrm{d}\xi_l\mathrm{d}\xi_{l'}. \end{aligned} \tag{b.24}$$

The second triple integral writes

$$\begin{aligned} (2) &\int_{\frac{2}{h_j}(x_{j-1/2}-x_j)}^{\frac{2}{h_j}(x_{j+1/2}-x_j)} F_2(\xi_j)\,\theta\left(\xi_j - \frac{2}{h_j}(x_{l'-1/2}-x_j)\right) \\ &\qquad \theta\left(\xi_j - \frac{2}{h_j}(x_{l+1/2}+x_{l'-1/2}-x_{\min}-x_j)\right)\mathrm{d}\xi_l\mathrm{d}\xi_{l'}\mathrm{d}\xi_j \\ &= \theta(x_{j+1/2}-x_{l'-1/2})\theta(x_{j+1/2}-x_{l+1/2}-x_{l'-1/2}+x_{\min}) \\ &\left[\int_{\frac{2}{h_j}(x_{l+1/2}+x_{l'-1/2}-x_{\min}-x_j)}^{\frac{2}{h_j}(x_{j+1/2}-x_j)} F_2(\xi_j)\,\mathrm{d}\xi_j \right. \\ &\qquad \left. +\theta(x_{j-1/2}-x_{l'-1/2})\theta(x_{j-1/2}-x_{l+1/2}-x_{l'-1/2}+x_{\min})\int_{\frac{2}{h_j}(x_{j-1/2}-x_j)}^{\frac{2}{h_j}(x_{l+1/2}+x_{l'-1/2}-x_{\min}-x_j)} F_2(\xi_j)\,\mathrm{d}\xi_j\right]. \end{aligned}$$

(b.25)

The fourth triple integral writes

$$
\begin{aligned}
(4) & \int_{\frac{2}{h_j}(x_{j-1/2}-x_j)}^{\frac{2}{h_j}(x_{j+1/2}-x_j)} F_4\left(\xi_j\right)\theta\left(\xi_j-\frac{2}{h_j}(x_{l'+1/2}-x_j)\right) \\
& \qquad \theta\left(\xi_j-\frac{2}{h_j}(x_{l+1/2}+x_{l'+1/2}-x_{\min}-x_j)\right)\mathrm{d}\xi_l\mathrm{d}\xi_{l'}\mathrm{d}\xi_j \\
&= \theta(x_{j+1/2}-x_{l'+1/2})\theta(x_{j+1/2}-x_{l+1/2}-x_{l'+1/2}+x_{\min}) \\
& \left[\int_{\frac{2}{h_j}(x_{l+1/2}+x_{l'+1/2}-x_{\min}-x_j)}^{\frac{2}{h_j}(x_{j+1/2}-x_j)} F_4\left(\xi_j\right)\mathrm{d}\xi_j\right. \\
& \qquad \left.+\theta(x_{j-1/2}-x_{l'+1/2})\theta(x_{j-1/2}-x_{l+1/2}-x_{l'+1/2}+x_{\min})\int_{\frac{2}{h_j}(x_{j-1/2}-x_j)}^{\frac{2}{h_j}(x_{l+1/2}+x_{l'+1/2}-x_{\min}-x_j)} F_4\left(\xi_j\right)\mathrm{d}\xi_j\right].
\end{aligned}
$$

(b.26)

Then $\mathcal{T}$ writes

$$
\begin{aligned}
&\mathcal{T}\left(x_{\min}, x_{\max}, j, k, i', i, l', l\right) = \frac{h_l}{2}\frac{h_{l'}}{2}\times \\
&\left[\int_{\frac{2}{h_l}(x_{l-1/2}-x_l)}^{\frac{2}{h_l}(x_{l+1/2}-x_l)} f_2(\xi_l)\mathrm{d}\xi_l \times\right. \\
&\left\{\theta(x_{j+1/2}-x_{l'-1/2})\left(\int_{\frac{2}{h_j}(x_{l'-1/2}-x_j)}^{\frac{2}{h_j}(x_{j+1/2}-x_j)}\int_{\frac{2}{h_{l'}}(x_{l'-1/2}-x_{l'})}^{\frac{2}{h_{l'}}(\frac{h_j}{2}\xi_j+x_j-x_{l'})} f_1(\xi_{l'})\partial_{\xi_j}\phi_k(\xi_j)\mathrm{d}\xi_j\right.\right. \\
&\qquad\left.+\theta(x_{j-1/2}-x_{l'-1/2})\int_{\frac{2}{h_j}(x_{j-1/2}-x_j)}^{\frac{2}{h_j}(x_{l'-1/2}-x_j)}\int_{\frac{2}{h_{l'}}(x_{l'-1/2}-x_{l'})}^{\frac{2}{h_{l'}}(\frac{h_j}{2}\xi_j+x_j-x_{l'})} f_1(\xi_{l'})\partial_{\xi_j}\phi_k(\xi_j)\mathrm{d}\xi_j\right) \\
&\quad-\theta(x_{j+1/2}-x_{l'+1/2})\left(\int_{\frac{2}{h_j}(x_{l'+1/2}-x_j)}^{\frac{2}{h_j}(x_{j+1/2}-x_j)}\int_{\frac{2}{h_{l'}}(x_{l'+1/2}-x_{l'})}^{\frac{2}{h_{l'}}(\frac{h_j}{2}\xi_j+x_j-x_{l'})} f_1(\xi_{l'})\partial_{\xi_j}\phi_k(\xi_j)\mathrm{d}\xi_j\right. \\
&\qquad\left.\left.+\theta(x_{j-1/2}-x_{l'+1/2})\int_{\frac{2}{h_j}(x_{j-1/2}-x_j)}^{\frac{2}{h_j}(x_{l'+1/2}-x_j)}\int_{\frac{2}{h_{l'}}(x_{l'+1/2}-x_{l'})}^{\frac{2}{h_{l'}}(\frac{h_j}{2}\xi_j+x_j-x_{l'})} f_1(\xi_{l'})\partial_{\xi_j}\phi_k(\xi_j)\mathrm{d}\xi_j\right)\right\} \\
&+\theta(x_{j+1/2}-x_{l'-1/2})\theta(x_{j+1/2}+x_{\min}-x_{l-1/2}-x_{l'-1/2}) \\
&\quad\left[\int_{\frac{2}{h_j}(x_{l-1/2}+x_{l'-1/2}-x_{\min}-x_j)}^{\frac{2}{h_j}(x_{j+1/2}-x_j)} F_1(\xi_j)\mathrm{d}\xi_j\right. \\
&\quad\left.+\theta(x_{j-1/2}-x_{l'-1/2})\theta(x_{j-1/2}+x_{\min}-x_{l-1/2}-x_{l'-1/2})\int_{\frac{2}{h_j}(x_{j-1/2}-x_j)}^{\frac{2}{h_j}(x_{l-1/2}+x_{l'-1/2}-x_{\min}-x_j)} F_1(\xi_j)\mathrm{d}\xi_j\right] \\
&+\theta(x_{j+1/2}-x_{l'+1/2})\theta(x_{j+1/2}+x_{\min}-x_{l-1/2}-x_{l'+1/2}) \\
&\quad\left[\int_{\frac{2}{h_j}(x_{l-1/2}+x_{l'+1/2}-x_{\min}-x_j)}^{\frac{2}{h_j}(x_{j+1/2}-x_j)} F_3(\xi_j)\mathrm{d}\xi_j\right. \\
&\quad\left.+\theta(x_{j-1/2}-x_{l'+1/2})\theta(x_{j-1/2}+x_{\min}-x_{l-1/2}-x_{l'+1/2})\int_{\frac{2}{h_j}(x_{j-1/2}-x_j)}^{\frac{2}{h_j}(x_{l-1/2}+x_{l'+1/2}-x_{\min}-x_j)} F_3(\xi_j)\mathrm{d}\xi_j\right]
\end{aligned}
\tag{b.27}
$$

$$
\begin{aligned}
&- \theta(x_{j+1/2} - x_{l'-1/2})\theta(x_{j+1/2} - x_{l+1/2} - x_{l'-1/2} + x_{\min}) \\
&\quad \left[\int_{\frac{2}{h_j}(x_{l+1/2}+x_{l'-1/2}-x_{\min}-x_j)}^{\frac{2}{h_j}(x_{j+1/2}-x_j)} F_2\left(\xi_j\right) \mathrm{d}\xi_j \right. \\
&\quad \left. + \theta(x_{j-1/2} - x_{l'-1/2})\theta(x_{j-1/2} - x_{l+1/2} - x_{l'-1/2} + x_{\min}) \int_{\frac{2}{h_j}(x_{j-1/2}-x_j)}^{\frac{2}{h_j}(x_{l+1/2}+x_{l'-1/2}-x_{\min}-x_j)} F_2\left(\xi_j\right) \mathrm{d}\xi_j \right] \\
&- \theta(x_{j+1/2} - x_{l'+1/2})\theta(x_{j+1/2} - x_{l+1/2} - x_{l'+1/2} + x_{\min}) \\
&\quad \left[\int_{\frac{2}{h_j}(x_{l+1/2}+x_{l'+1/2}-x_{\min}-x_j)}^{\frac{2}{h_j}(x_{j+1/2}-x_j)} F_4\left(\xi_j\right) \mathrm{d}\xi_j \right. \\
&\quad \left. + \theta(x_{j-1/2} - x_{l'+1/2})\theta(x_{j-1/2} - x_{l+1/2} - x_{l'+1/2} + x_{\min}) \int_{\frac{2}{h_j}(x_{j-1/2}-x_j)}^{\frac{2}{h_j}(x_{l+1/2}+x_{l'+1/2}-x_{\min}-x_j)} F_4\left(\xi_j\right) \mathrm{d}\xi_j \right] \Bigg] .
\end{aligned}
$$

To reduce as much as possible the number of integrals to evaluate, we define the following term for the scheme

$$
\begin{aligned}
\mathcal{T}_{\phi_i} &\equiv \int_{\frac{2}{h_l}(x_{l-1/2}-x_l)}^{\frac{2}{h_l}(x_{l+1/2}-x_l)} f_2(\xi_l)\mathrm{d}\xi_l \\
\mathcal{T}_{\phi_{i'},\text{allmix}} &\equiv \int_{\frac{2}{h_j}(x_{j-1/2}-x_j)}^{\frac{2}{h_j}(x_{j+1/2}-x_j)} \int_{\frac{2}{h_{l'}}(x_{l'-1/2}-x_{l'})}^{\frac{2}{h_{l'}}(x_{l'+1/2}-x_{l'})} f_1(\xi_{l'})\partial_{\xi_j}\phi_k(\xi_j)\mathrm{d}\xi_{l'}\mathrm{d}\xi_j \\
\mathcal{T}_{\phi_{i'},\text{mixP1}} &\equiv \int_{\frac{2}{h_j}(x_{j-1/2}-x_j)}^{\frac{2}{h_j}(x_{j+1/2}-x_j)} \int_{\frac{2}{h_{l'}}(x_{l'-1/2}-x_{l'})}^{\frac{2}{h_{l'}}(\frac{h_j}{2}\xi_j+x_j-x_{l'})} f_1(\xi_{l'})\partial_{\xi_j}\phi_k(\xi_j)\mathrm{d}\xi_{l'}\mathrm{d}\xi_j \\
\mathcal{T}_{\phi_{i'},\text{P1term1}} &\equiv \int_{\frac{2}{h_j}(x_{l'-1/2}-x_j)}^{\frac{2}{h_j}(x_{j+1/2}-x_j)} \int_{\frac{2}{h_{l'}}(x_{l'-1/2}-x_{l'})}^{\frac{2}{h_{l'}}(\frac{h_j}{2}\xi_j+x_j-x_{l'})} f_1(\xi_{l'})\partial_{\xi_j}\phi_k(\xi_j)\mathrm{d}\xi_{l'}\mathrm{d}\xi_j \\
\mathcal{T}_{\phi_{i'},\text{P2term1}} &\equiv \int_{\frac{2}{h_j}(x_{l'+1/2}-x_j)}^{\frac{2}{h_j}(x_{j+1/2}-x_j)} \int_{\frac{2}{h_{l'}}(x_{l'+1/2}-x_{l'})}^{\frac{2}{h_{l'}}(\frac{h_j}{2}\xi_j+x_j-x_{l'})} f_1(\xi_{l'})\partial_{\xi_j}\phi_k(\xi_j)\mathrm{d}\xi_{l'}\mathrm{d}\xi_j \\
\mathcal{T}_{\phi_{i'},\phi_i,\text{allmix}} &\equiv \int_{\frac{2}{h_j}(x_{j-1/2}-x_j)}^{\frac{2}{h_j}(x_{j+1/2}-x_j)} \int_{\frac{2}{h_{l'}}(x_{l'-1/2}-x_{l'})}^{\frac{2}{h_{l'}}(x_{l'+1/2}-x_{l'})} \int_{\frac{2}{h_l}(x_{l+1/2}-x_l)}^{\frac{2}{h_l}(x_{l-1/2}-x_l)} f_1(\xi_{l'})f_2(\xi_l)\partial_{\xi_j}\phi_k(\xi_j)\mathrm{d}\xi_l\mathrm{d}\xi_{l'}\mathrm{d}\xi_j \\
\mathcal{T}_{\phi_{i'},\phi_i,\text{mixterm1term3}} &\equiv \int_{\frac{2}{h_j}(x_{j-1/2}-x_j)}^{\frac{2}{h_j}(x_{j+1/2}-x_j)} \int_{\frac{2}{h_{l'}}(x_{l'-1/2}-x_{l'})}^{\frac{2}{h_{l'}}(x_{l'+1/2}-x_{l'})} \\
&\qquad \int_{\frac{2}{h_l}(\frac{h_j}{2}\xi_j+x_j-\frac{h_{l'}}{2}\xi_{l'}-x_{l'}+x_{\min}-x_l)}^{\frac{2}{h_l}(x_{l-1/2}-x_l)} f_1(\xi_{l'})f_2(\xi_l)\partial_{\xi_j}\phi_k(\xi_j)\mathrm{d}\xi_l\mathrm{d}\xi_{l'}\mathrm{d}\xi_j \\
\mathcal{T}_{\phi_{i'},\phi_i,\text{mixterm1}} &\equiv \int_{\frac{2}{h_j}(x_{j-1/2}-x_j)}^{\frac{2}{h_j}(x_{j+1/2}-x_j)} \int_{\frac{2}{h_{l'}}(x_{l'-1/2}-x_{l'})}^{\frac{2}{h_{l'}}(\frac{h_j}{2}\xi_j+x_j-x_{l-1/2}+x_{\min}-x_{l'})} \\
&\qquad \int_{\frac{2}{h_l}(\frac{h_j}{2}\xi_j+x_j-\frac{h_{l'}}{2}\xi_{l'}-x_{l'}+x_{\min}-x_l)}^{\frac{2}{h_l}(x_{l-1/2}-x_l)} f_1(\xi_{l'})f_2(\xi_l)\partial_{\xi_j}\phi_k(\xi_j)\mathrm{d}\xi_l\mathrm{d}\xi_{l'}\mathrm{d}\xi_j
\end{aligned}
\tag{b.28}
$$

$$\mathcal{T}_{\phi_{i'},\phi_i,\text{mixterm2}} \equiv \int_{\frac{2}{h_j}(x_{j-1/2}-x_j)}^{\frac{2}{h_j}(x_{j+1/2}-x_j)} \int_{\frac{2}{h_{l'}}(x_{l'-1/2}-x_{l'})}^{\frac{2}{h_{l'}}(\frac{h_j}{2}\xi_j+x_j-x_{l+1/2}+x_{\min}-x_{l'})} \int_{\frac{2}{h_l}(\frac{h_j}{2}\xi_j+x_j-\frac{h_{l'}}{2}\xi_{l'}-x_{l'}+x_{\min}-x_l)}^{\frac{2}{h_l}(x_{l+1/2}-x_l)} f_1(\xi_{l'})f_2(\xi_l)\partial_{\xi_j}\phi_k(\xi_j)\mathrm{d}\xi_l\mathrm{d}\xi_{l'}\mathrm{d}\xi_j$$

$$\mathcal{T}_{\phi_{i'},\phi_i,\text{term1}} \equiv \int_{\frac{2}{h_j}(x_{l-1/2}+x_{l'-1/2}-x_{\min}-x_j)}^{\frac{2}{h_j}(x_{j+1/2}-x_j)} \int_{\frac{2}{h_{l'}}(x_{l'-1/2}-x_{l'})}^{\frac{2}{h_{l'}}(\frac{h_j}{2}\xi_j+x_j-x_{l-1/2}+x_{\min}-x_{l'})} \int_{\frac{2}{h_l}(\frac{h_j}{2}\xi_j+x_j-\frac{h_{l'}}{2}\xi_{l'}-x_{l'}+x_{\min}-x_l)}^{\frac{2}{h_l}(x_{l-1/2}-x_l)} f_1(\xi_{l'})f_2(\xi_l)\partial_{\xi_j}\phi_k(\xi_j)\mathrm{d}\xi_l\mathrm{d}\xi_{l'}\mathrm{d}\xi_j$$

$$\mathcal{T}_{\phi_{i'},\phi_i,\text{term2}} \equiv \int_{\frac{2}{h_j}(x_{l+1/2}+x_{l'-1/2}-x_{\min}-x_j)}^{\frac{2}{h_j}(x_{j+1/2}-x_j)} \int_{\frac{2}{h_{l'}}(x_{l'-1/2}-x_{l'})}^{\frac{2}{h_{l'}}(\frac{h_j}{2}\xi_j+x_j-x_{l+1/2}+x_{\min}-x_{l'})} \int_{\frac{2}{h_l}(\frac{h_j}{2}\xi_j+x_j-\frac{h_{l'}}{2}\xi_{l'}-x_{l'}+x_{\min}-x_l)}^{\frac{2}{h_l}(x_{l+1/2}-x_l)} f_1(\xi_{l'})f_2(\xi_l)\partial_{\xi_j}\phi_k(\xi_j)\mathrm{d}\xi_l\mathrm{d}\xi_{l'}\mathrm{d}\xi_j$$

$$\mathcal{T}_{\phi_{i'},\phi_i,\text{term3}} \equiv \int_{\frac{2}{h_j}(x_{l-1/2}+x_{l'+1/2}-x_{\min}-x_j)}^{\frac{2}{h_j}(x_{j+1/2}-x_j)} \int_{\frac{2}{h_{l'}}(\frac{h_j}{2}\xi_j+x_j-x_{l-1/2}+x_{\min}-x_{l'})}^{\frac{2}{h_{l'}}(x_{l'+1/2}-x_{l'})} \int_{\frac{2}{h_l}(\frac{h_j}{2}\xi_j+x_j-\frac{h_{l'}}{2}\xi_{l'}-x_{l'}+x_{\min}-x_l)}^{\frac{2}{h_l}(x_{l-1/2}-x_l)} f_1(\xi_{l'})f_2(\xi_l)\partial_{\xi_j}\phi_k(\xi_j)\mathrm{d}\xi_l\mathrm{d}\xi_{l'}\mathrm{d}\xi_j$$

$$\mathcal{T}_{\phi_{i'},\phi_i,\text{term4}} \equiv \int_{\frac{2}{h_j}(x_{l+1/2}+x_{l'+1/2}-x_{\min}-x_j)}^{\frac{2}{h_j}(x_{j+1/2}-x_j)} \int_{\frac{2}{h_{l'}}(\frac{h_j}{2}\xi_j+x_j-x_{l+1/2}+x_{\min}-x_{l'})}^{\frac{2}{h_{l'}}(x_{l'+1/2}-x_{l'})} \int_{\frac{2}{h_l}(\frac{h_j}{2}\xi_j+x_j-\frac{h_{l'}}{2}\xi_{l'}-x_{l'}+x_{\min}-x_l)}^{\frac{2}{h_l}(x_{l+1/2}-x_l)} f_1(\xi_{l'})f_2(\xi_l)\partial_{\xi_j}\phi_k(\xi_j)\mathrm{d}\xi_l\mathrm{d}\xi_{l'}\mathrm{d}\xi_j.$$

B.2.3 *Fortran scheme for integral of the flux term*

Finally, the `Fortran` scheme to evaluate $\mathcal{T}(x, x_{\min}, x_{\max}, j, k, i', i, l', l)$ writes

```
1  res1 = 0
2  if (x_{j+1/2} > x_{l'+1/2}) then
3     if (x_{j-1/2} > x_{l'+1/2}) then
4        res1 = T_{φ_i} × T_{φ_{i'},allmix}
5     else if (x_{j-1/2} ≤ x_{l'+1/2} and x_{j-1/2} > x_{l'-1/2}) then
6        res1 = T_{φ_i} × (T_{φ_{i'},mixP1} − T_{φ_{i'},P2term1})
7     else
8        res1 = T_{φ_i} × (T_{φ_{i'},P1term1} − T_{φ_{i'},P2term1})
9     endif
10
11 else if (x_{j+1/2} ≤ x_{l'+1/2} and x_{j+1/2} > x_{l'-1/2}) then
12    if (x_{j-1/2} > x_{l'-1/2}) then
13       res1 = T_{φ_i} × T_{φ_{i'},mixP1}
14    else
15       res1 = T_{φ_i} × T_{φ_{i'},P1term1}
16    endif
17 else
18    res1 = 0
19 endif
20
21
22 res2 = 0
23 if (x_{j+1/2} > x_{l'+1/2}) then
24    if (x_{j+1/2} > x_{l+1/2} + x_{l'+1/2} − x_min) then
25       if (x_{j-1/2} > x_{l'+1/2}) then
26          if (x_{j-1/2} > x_{l+1/2} + x_{l'+1/2} − x_min) then
27             res2 = T_{φ_{i'},φ_i,allmix}
28          else if (x_{j-1/2} ≤ x_{l+1/2} + x_{l'+1/2} − x_min
29                   and x_{j-1/2} > x_{l-1/2} + x_{l'+1/2} − x_min
30                   and x_{j-1/2} > x_{l+1/2} + x_{l'-1/2} − x_min) then
31             res2 = T_{φ_{i'},φ_i,mixterm1term3} − T_{φ_{i'},φ_i,mixterm2} − T_{φ_{i'},φ_i,term4}
32          else if (x_{j-1/2} ≤ x_{l+1/2} + x_{l'+1/2} − x_min
33                   and x_{j-1/2} > x_{l-1/2} + x_{l'+1/2} − x_min
34                   and x_{j-1/2} ≤ x_{l+1/2} + x_{l'-1/2} − x_min) then
35             res2 = T_{φ_{i'},φ_i,mixterm1term3} − T_{φ_{i'},φ_i,term2} − T_{φ_{i'},φ_i,term4}
36          else if (x_{j-1/2} ≤ x_{l+1/2} + x_{l'+1/2} − x_min
37                   and x_{j-1/2} ≤ x_{l-1/2} + x_{l'+1/2} − x_min
38                   and x_{j-1/2} > x_{l+1/2} + x_{l'-1/2} − x_min) then
39             res2 = T_{φ_{i'},φ_i,mixterm1} − T_{φ_{i'},φ_i,mixterm2} + T_{φ_{i'},φ_i,term3} − T_{term4}
40          else if (x_{j-1/2} ≤ x_{l+1/2} + x_{l'+1/2} − x_min
41                   and x_{j-1/2} ≤ x_{l-1/2} + x_{l'+1/2} − x_min
42                   and x_{j-1/2} ≤ x_{l+1/2} + x_{l'-1/2} − x_min
43                   and x_{j-1/2} > x_{l-1/2} + x_{l'-1/2} − x_min) then
44             res2 = T_{φ_{i'},φ_i,mixterm1} − T_{φ_{i'},φ_i,term2} + T_{φ_{i'},φ_i,term3} − T_{φ_{i'},φ_i,term4}
45          else
46             res2 = T_{φ_{i'},φ_i,term1} − T_{φ_{i'},φ_i,term2} + T_{φ_{i'},φ_i,term3} − T_{φ_{i'},φ_i,term4}
```

```
47          endif
48       else if (x_{j-1/2} ≤ x_{l'+1/2} and x_{j-1/2} > x_{l'-1/2}) then
49          if (x_{j-1/2} > x_{l+1/2} + x_{l'-1/2} - x_min) then
50             res2 = T_{φ_i',φ_i,mixterm1} - T_{φ_i',φ_i,mixterm2} + T_{φ_i',φ_i,term3} - T_{φ_i',φ_i,term4}
51          else if (x_{j-1/2} ≤ x_{l+1/2} + x_{l'-1/2} - x_min
52                   and x_{j-1/2} > x_{l-1/2} + x_{l'-1/2} - x_min) then
53             res2 = T_{φ_i',φ_i,mixterm1} - T_{φ_i',φ_i,term2} + T_{φ_i',φ_i,term3} - T_{φ_i',φ_i,term4}
54          else
55             res2 = T_{φ_i',φ_i,term1} - T_{φ_i',φ_i,term2} + T_{φ_i',φ_i,term3} - T_{φ_i',φ_i,term4}
56          endif
57       else
58          res2 = T_{φ_i',φ_i,term1} - T_{φ_i',φ_i,term2} + T_{φ_i',φ_i,term3} - T_{φ_i',φ_i,term4}
59       endif
60    else if (x_{j+1/2} ≤ x_{l+1/2} + x_{l'+1/2} - x_min
61             and x_{j+1/2} > x_{l-1/2} + x_{l'+1/2} - x_min
62             and x_{j+1/2} > x_{l+1/2} + x_{l'-1/2} - x_min) then
63       if (x_{j-1/2} > x_{l'+1/2}) then
64          if (x_{j-1/2} > x_{l-1/2} + x_{l'+1/2} - x_min
65              and x_{j-1/2} > x_{l+1/2} + x_{l'-1/2} - x_min) then
66             res2 = T_{φ_i',φ_i,mixterm1term3} - T_{φ_i',φ_i,mixterm2}
67          else if (x_{j-1/2} > x_{l-1/2} + x_{l'+1/2} - x_min
68                   and x_{j-1/2} ≤ x_{l+1/2} + x_{l'-1/2} - x_min) then
69             res2 = T_{φ_i',φ_i,mixterm1term3} - T_{φ_i',φ_i,term2}
70          else if (x_{j-1/2} ≤ x_{l-1/2} + x_{l'+1/2} - x_min
71                   and x_{j-1/2} > x_{l+1/2} + x_{l'-1/2} - x_min) then
72             res2 = T_{φ_i',φ_i,mixterm1} - T_{φ_i',φ_i,mixterm2} + T_{φ_i',φ_i,term3}
73          else if (x_{j-1/2} ≤ x_{l-1/2} + x_{l'+1/2} - x_min
74                   and x_{j-1/2} ≤ x_{l+1/2} + x_{l'-1/2} - x_min
75                   and x_{j-1/2} > x_{l-1/2} + x_{l'-1/2} - x_min) then
76             res2 = T_{φ_i',φ_i,mixterm1} - T_{φ_i',φ_i,term2} + T_{φ_i',φ_i,term3}
77          else
78             res2 = T_{φ_i',φ_i,term1} - T_{φ_i',φ_i,term2} + T_{φ_i',φ_i,term3}
79          endif
80       else if (x_{j-1/2} ≤ x_{l'+1/2} and x_{j-1/2} > x_{l'-1/2}) then
81          if (x_{j-1/2} > x_{l+1/2} + x_{l'-1/2} - x_min) then
82             res2 = T_{φ_i',φ_i,mixterm1} - T_{φ_i',φ_i,mixterm2} + T_{φ_i',φ_i,term3}
83          else if (x_{j-1/2} ≤ x_{l+1/2} + x_{l'-1/2} - x_min
84                   and x_{j-1/2} > x_{l-1/2} + x_{l'-1/2} - x_min) then
85             res2 = T_{φ_i',φ_i,mixterm1} - T_{φ_i',φ_i,term2} + T_{φ_i',φ_i,term3}
86          else
87             res2 = T_{φ_i',φ_i,term1} - T_{φ_i',φ_i,term2} + T_{φ_i',φ_i,term3}
88          endif
89       else
90          res2 = T_{φ_i',φ_i,term1} - T_{φ_i',φ_i,term2} + T_{φ_i',φ_i,term3}
91       endif
92    else if (x_{j+1/2} ≤ x_{l+1/2} + x_{l'+1/2} - x_min
93             and x_{j+1/2} > x_{l-1/2} + x_{l'+1/2} - x_min
94             and x_{j+1/2} ≤ x_{l+1/2} + x_{l'-1/2} - x_min) then
95       if (x_{j-1/2} > x_{l'+1/2}) then
```

```
96          if (x_{j-1/2} > x_{l-1/2} + x_{l'+1/2} - x_min) then
97             res2 = T_{φ_i',φ_i,mixterm1term3}
98          else if (x_{j-1/2} ≤ x_{l-1/2} + x_{l'+1/2} - x_min
99                   and x_{j-1/2} > x_{l-1/2} + x_{l'-1/2} - x_min) then
100            res2 = T_{φ_i',φ_i,mixterm1} + T_{φ_i',φ_i,term3}
101         else
102            res2 = T_{φ_i',φ_i,term1} + T_{φ_i',φ_i,term3}
103         endif
104      else if (x_{j-1/2} ≤ x_{l'+1/2} and x_{j-1/2} > x_{l'-1/2}) then
105         if (x_{j-1/2} > x_{l-1/2} + x_{l'-1/2} - x_min) then
106            res2 = T_{φ_i',φ_i,mixterm1} + T_{φ_i',φ_i,term3}
107         else
108            res2 = T_{φ_i',φ_i,term1} + T_{φ_i',φ_i,term3}
109         endif
110      else
111         res2 = T_{φ_i',φ_i,term1} + T_{φ_i',φ_i,term3}
112      endif
113   else if (x_{j+1/2} ≤ x_{l+1/2} + x_{l'+1/2} - x_min
114            and x_{j+1/2} ≤ x_{l-1/2} + x_{l'+1/2} - x_min
115            and x_{j+1/2} > x_{l+1/2} + x_{l'-1/2} - x_min) then
116      if (x_{j-1/2} > x_{l'-1/2}) then
117         if (x_{j-1/2} > x_{l+1/2} + x_{l'-1/2} - x_min) then
118            res2 = T_{φ_i',φ_i,mixterm1} - T_{φ_i',φ_i,mixterm2}
119         else if (x_{j-1/2} ≤ x_{l+1/2} + x_{l'-1/2} - x_min
120                  and x_{j-1/2} > x_{l-1/2} + x_{l'-1/2} - x_min) then
121            res2 = T_{φ_i',φ_i,mixterm1} - T_{φ_i',φ_i,term2}
122         else
123            res2 = T_{φ_i',φ_i,term1} - T_{φ_i',φ_i,term2}
124         endif
125      else
126         res2 = T_{φ_i',φ_i,term1} - T_{φ_i',φ_i,term2}
127      endif
128   else if (x_{j+1/2} ≤ x_{l+1/2} + x_{l'+1/2} - x_min
129            and x_{j+1/2} ≤ x_{l-1/2} + x_{l'+1/2} - x_min
130            and x_{j+1/2} ≤ x_{l+1/2} + x_{l'-1/2} - x_min
131            and x_{j+1/2} > x_{l-1/2} + x_{l'-1/2} - x_min) then
132      if (x_{j-1/2} > x_{l'-1/2}) then
133         if (x_{j-1/2} > x_{l-1/2} + x_{l'-1/2} - x_min) then
134            res2 = T_{φ_i',φ_i,mixterm1}
135         else
136            res2 = T_{φ_i',φ_i,term1}
137         endif
138      else
139         res2 = T_{φ_i',φ_i,term1}
140      endif
141   else
142      res2 = 0
143   endif
144 else if (x_{j+1/2} ≤ x_{l'+1/2} and x_{j+1/2} > x_{l'-1/2}) then
```

```
145     if (x_{j+1/2} > x_{l+1/2} + x_{l'-1/2} - x_min) then
146        if (x_{j-1/2} > x_{l'-1/2}) then
147           if (x_{j-1/2} > x_{l+1/2} + x_{l'-1/2} - x_min) then
148              res2 = T_{φ_{i'},φ_i,mixterm1} - T_{φ_{i'},φ_i,mixterm2}
149           else if (x_{j-1/2} ≤ x_{l+1/2} + x_{l'-1/2} - x_min
150                    and x_{j-1/2} > x_{l-1/2} + x_{l'-1/2} - x_min) then
151              res2 = T_{φ_{i'},φ_i,mixterm1} - T_{φ_{i'},φ_i,term2}
152           else
153              res2 = T_{φ_{i'},φ_i,term1} - T_{φ_{i'},φ_i,term2}
154           endif
155        else
156           res2 = T_{φ_{i'},φ_i,term1} - T_{φ_{i'},φ_i,term2}
157        endif
158     else if (x_{j+1/2} ≤ x_{l+1/2} + x_{l'-1/2} - x_min
159        and x_{j+1/2} > x_{l-1/2} + x_{l'-1/2} - x_min) then
160        if (x_{j-1/2} > x_{l'-1/2}) then
161           if (x_{j-1/2} > x_{l-1/2} + x_{l'-1/2} - x_min) then
162              res2 = T_{φ_{i'},φ_i,mixterm1}
163           else
164              res2 = T_{φ_{i'},φ_i,term1}
165           endif
166        else
167           res2 = T_{φ_{i'},φ_i,term1}
168        endif
169     else
170        res2 = 0
171     endif
172  else
173     res2 = 0
174  endif
```

C

CHAPTER 4

C.1 DERIVATION OF THE FLUX FOR BALLISTIC KERNEL

The double integral with terms $\sigma_1^1\sigma_2^1$ from equation 4.17 writes

$$\int_{I_{l'}} \int_{x_{j+1/2}-u+x_{\min}}^{x_{\max}-u+x_{\min}} \sigma_1^1(u)\sigma_2^1(v)\phi_{i'}\left(\xi_{l'}(u)\right) \frac{\phi_i\left(\xi_l(v)\right)}{v} \left[\theta(v - x_{l-1/2}) - \theta(v - x_{l+1/2})\right] \mathrm{d}v\mathrm{d}u. \quad \text{(c.1)}$$

Calculations for $\sigma_1^2\sigma_2^2$ and $\sigma_1^3\sigma_2^3$ are similar.

C.1.1 *Inner integral*

The rule for the inner integral is

$$\begin{cases} a < b, c < d \\ \displaystyle\int_a^b f(x)[\theta(x-c) - \theta(x-d)]\mathrm{d}x = \\ \theta(b-c)\left\{\displaystyle\int_c^b f(x)\mathrm{d}x + \theta(a-c)\int_a^c f(x)\mathrm{d}x\right\} \\ \qquad - \theta(b-d)\left\{\displaystyle\int_d^b f(x)\mathrm{d}x + \theta(a-d)\int_a^d f(x)\mathrm{d}x\right\} \end{cases} \quad \text{(c.2)}$$

With the change of variable $\xi_l(x) = \frac{2}{h_l}(x - x_l)$, the inner integral on ξ_l writes

$$
\begin{aligned}
\tilde{F}(\xi_{l'}) \equiv & \int_{\frac{2}{h_l}(x_{j+1/2}-\frac{h_{l'}}{2}\xi_{l'}-x_{l'}+x_{\min}-x_l)}^{\frac{2}{h_l}(x_{\max}-\frac{h_{l'}}{2}\xi_{l'}-x_{l'}+x_{\min}-x_l)} f(\xi_l)\left[\theta(\xi_l - \frac{2}{h_l}(x_{l-1/2}-x_l)) - \theta(\xi_l - \frac{2}{h_l}(x_{l+1/2}-x_l))\right] \mathrm{d}\xi_l \\
= & \, \theta(x_{\max} - \frac{h_{l'}}{2}\xi_{l'} - x_{l'} + x_{\min} - x_{l-1/2}) \\
& \Bigg\{ \underbrace{\int_{\frac{2}{h_l}(x_{l-1/2}-x_l)}^{\frac{2}{h_l}(x_{\max}-\frac{h_{l'}}{2}\xi_{l'}-x_{l'}+x_{\min}-x_l)} f(\xi_l)\mathrm{d}\xi_l}_{F_1} \\
& \quad + \theta(x_{j+1/2} - \frac{h_{l'}}{2}\xi_{l'} - x_{l'} + x_{\min} - x_{l-1/2}) \underbrace{\int_{\frac{2}{h_l}(x_{j+1/2}-\frac{h_{l'}}{2}\xi_{l'}-x_{l'}+x_{\min}-x_l)}^{\frac{2}{h_l}(x_{l-1/2}-x_l)} f(\xi_l)\mathrm{d}\xi_l}_{F_2} \Bigg\} \\
& - \theta(x_{\max} - \frac{h_{l'}}{2}\xi_{l'} - x_{l'} + x_{\min} - x_{l+1/2}) \\
& \Bigg\{ \underbrace{\int_{\frac{2}{h_l}(x_{l+1/2}-x_l)}^{\frac{2}{h_l}(x_{\max}-\frac{h_{l'}}{2}\xi_{l'}+x_{\min}-x_l)} f(\xi_l)\mathrm{d}\xi_l}_{F_3} \\
& \quad + \theta(x_{j+1/2} - \frac{h_{l'}}{2}\xi_{l'} - x_{l'} + x_{\min} - x_{l+1/2}) \underbrace{\int_{\frac{2}{h_l}(x_{j+1/2}-\frac{h_{l'}}{2}\xi_{l'}-x_{l'}+x_{\min}-x_l)}^{\frac{2}{h_l}(x_{l+1/2}-x_l)} f\xi_l\mathrm{d}\xi_l}_{F_4} \Bigg\},
\end{aligned}
\tag{c.3}
$$

where $f(\xi_l) \equiv \sigma_2^1\left(\frac{h_l}{2}\xi_l + x_l\right)\frac{\phi_i}{\frac{h_l}{2}\xi_l + x_l}$. The double integral writes

$$\int_{\frac{2}{h_l'}(x_{l'-1/2}-x_{l'})}^{\frac{2}{h_l'}(x_{l'+1/2}-x_{l'})} \phi_{i'}(\xi_{l'})\sigma_1^1(\xi_{l'})\tilde{F}(\xi_{l'})\mathrm{d}\xi_{l'} = \theta\left(x_{\max} + x_{\min} - x_{j+1/2}\right)$$
$$\Bigg[\int_{I_{l'}} \phi_{i'}\sigma_1 F_1\theta\left(\frac{2}{h_{l'}}(x_{\max} + x_{\min} - x_{l-1/2} - x_{l'}) - \xi_{l'}\right)\mathrm{d}\xi_{l'}$$
$$+ \int_{I_{l'}} \phi_{i'}\sigma_1 F_2\theta\left(\frac{2}{h_{l'}}(x_{\max} + x_{\min} - x_{l-1/2} - x_{l'}) - \xi_{l'}\right)\theta\left(\frac{2}{h_{l'}}(x_{j+1/2} + x_{\min} - x_{l-1/2} - x_{l'}) - \xi_{l'}\right)\mathrm{d}\xi_{l'}$$
$$- \int_{I_{l'}} \phi_{i'}\sigma_1 F_3\theta\left(\frac{2}{h_{l'}}(x_{\max} + x_{\min} - x_{l+1/2} - x_{l'}) - \xi_{l'}\right)\mathrm{d}\xi_{l'}$$
$$- \int_{I_{l'}} \phi_{i'}\sigma_1 F_4\theta\left(\frac{2}{h_{l'}}(x_{\max} + x_{\min} - x_{l+1/2} - x_{l'}) - \xi_{l'}\right)\theta\left(\frac{2}{h_{l'}}(x_{j+1/2} + x_{\min} - x_{l+1/2} - x_{l'}) - \xi_{l'}\right)\mathrm{d}\xi_{l'}\Bigg]. \tag{c.4}$$

C.1.2 *Outer integral*

The rules for the outer integral are

$$\begin{cases} a < b \\ \displaystyle\int_a^b f(x)\theta(e-x)\mathrm{d}x = \theta(e-a)\left\{\int_a^e f(x)\mathrm{d}x + \theta(e-b)\int_e^b f(x)\mathrm{d}x\right\}, \end{cases} \tag{c.5}$$

$$\begin{cases} a < b, i < e \\ \displaystyle\int_a^b f(x)\theta(e-x)\theta(i-x)\mathrm{d}x \\ \displaystyle= \theta(e-a)\theta(i-a)\Bigg[\theta(e-a)(\theta(e-b)-1)\int_i^a f(x)\mathrm{d}x \\ \displaystyle\qquad +\theta(e-b)\left\{\int_a^i f(x)\mathrm{d}x + \theta(i-b)\int_i^b f(x)\mathrm{d}x\right\}\Bigg]. \end{cases} \tag{c.6}$$

Then the four integrals on $\xi_{l'}$ writes

$$\begin{aligned} &\int_{I_{l'}} \phi_{i'}\sigma_1^1 F_1\theta\left(\frac{2}{h_{l'}}(x_{\max} + x_{\min} - x_{l-1/2} - x_{l'}) - \xi_{l'}\right)\mathrm{d}\xi_{l'} \\ &= \theta(x_{\max} + x_{\min} - x_{l-1/2} - x_{l'-1/2}) \\ &\quad\Bigg\{\int_{\frac{2}{h_{l'}}(x_{l'-1/2}-x_{l'})}^{\frac{2}{h_{l'}}(x_{\max}+x_{\min}-x_{l-1/2}-x_{l'})} \phi_{i'}\sigma_1^1 F_1\mathrm{d}\xi_{l'} \\ &\qquad +\theta(x_{\max} + x_{\min} - x_{l-1/2} - x_{l'+1/2})\int_{\frac{2}{h_{l'}}(x_{\max}+x_{\min}-x_{l-1/2}-x_{l'})}^{\frac{2}{h_{l'}}(x_{l'+1/2}-x_{l'})} \phi_{i'}\sigma_1^1 F_1\mathrm{d}\xi_{l'}\Bigg\}, \end{aligned} \tag{c.7}$$

$$
\begin{aligned}
&\int_{I_{l'}} \phi_{i'}\sigma_1^1 F_3 \theta\left(\frac{2}{h_{l'}}(x_{\max}+x_{\min}-x_{l+1/2}-x_{l'})-\xi_{l'}\right)\mathrm{d}\xi_{l'} \\
&= \theta(x_{\max}+x_{\min}-x_{l+1/2}-x_{l'-1/2}) \\
&\quad \left\{ \int_{\frac{2}{h_{l'}}(x_{l'-1/2}-x_{l'})}^{\frac{2}{h_{l'}}(x_{\max}+x_{\min}-x_{l+1/2}-x_{l'})} \phi_{i'}\sigma_1^1 F_3 \mathrm{d}\xi_{l'} \right. \\
&\qquad \left. +\theta(x_{\max}+x_{\min}-x_{l+1/2}-x_{l'+1/2}) \int_{\frac{2}{h_{l'}}(x_{\max}+x_{\min}-x_{l+1/2}-x_{l'})}^{\frac{2}{h_{l'}}(x_{l'+1/2}-x_{l'})} \phi_{i'}\sigma_1^1 F_3 \mathrm{d}\xi_{l'} \right\},
\end{aligned}
\tag{c.8}
$$

$$
\begin{aligned}
&\int_{I_{l'}} \phi_{i'}\sigma_1^1 F_2 \theta\left(\frac{2}{h_{l'}}(x_{\max}-x_{l-1/2}-x_{l'})-\xi_{l'}\right)\theta\left(\frac{2}{h_{l'}}(x_{j+1/2}-x_{l-1/2}-x_{l'})-\xi_{l'}\right)\mathrm{d}\xi_{l'} \\
&= \theta(x_{\max}-x_{l-1/2}-x_{l'-1/2})\theta(x_{j+1/2}-x_{l-1/2}-x_{l'-1/2}) \\
&\quad \Bigg[\theta(x_{\max}-x_{l-1/2}-x_{l'-1/2})(\theta(x_{\max}-x_{l-1/2}-x_{l'-1/2})-1) \\
&\qquad \times \int_{\frac{2}{h_{l'}}(x_{j+1/2}-x_{l-1/2}-x_{l'})}^{\frac{2}{h_{l'}}(x_{l'-1/2}-x_{l'})} \phi_{i'}\sigma_1^1 F_2 \mathrm{d}\xi_{l'} \\
&\qquad + \theta(x_{\max}-x_{l-1/2}-x_{l'+1/2}) \\
&\qquad \left\{ \int_{\frac{2}{h_{l'}}(x_{l'-1/2}-x_{l'})}^{\frac{2}{h_{l'}}(x_{j+1/2}-x_{l-1/2}-x_{l'})} \phi_{i'}\sigma_1^1 F_2 \mathrm{d}\xi_{l'} \right. \\
&\qquad\quad \left. +\theta(x_{j+1/2}-x_{l-1/2}-x_{l'+1/2}) \int_{\frac{2}{h_{l'}}(x_{j+1/2}-x_{l-1/2}-x_{l'+1/2})}^{\frac{2}{h_{l'}}(x_{l'+1/2}-x_{l'})} \phi_{i'}\sigma_1^1 F_2 \mathrm{d}\xi_{l'} \right\} \Bigg],
\end{aligned}
\tag{c.9}
$$

$$
\begin{aligned}
&\int_{I_{l'}} \phi_{i'}\sigma_1^1 F_4 \theta\left(\frac{2}{h_{l'}}(x_{\max}+x_{\min}-x_{l+1/2}-x_{l'})-\xi_{l'}\right)\theta\left(\frac{2}{h_{l'}}(x_{j+1/2}+x_{\min}-x_{l+1/2}-x_{l'})-\xi_{l'}\right)\mathrm{d}\xi_{l'}\\
&=\theta(x_{\max}-x_{l+1/2}-x_{l'-1/2})\theta(x_{j+1/2}-x_{l+1/2}-x_{l'-1/2})\\
&\quad\Bigg[\theta(x_{\max}+x_{\min}-x_{l+1/2}-x_{l'-1/2})(\theta(x_{\max}+x_{\min}-x_{l+1/2}-x_{l'-1/2})-1)\\
&\qquad\times\int_{\frac{2}{h_{l'}}(x_{j+1/2}+x_{\min}-x_{l+1/2}-x_{l'})}^{\frac{2}{h_{l'}}(x_{l'-1/2}-x_{l'})}\phi_{i'}\sigma_1^1 F_4\mathrm{d}\xi_{l'}\\
&\qquad+\theta(x_{\max}+x_{\min}-x_{l+1/2}-x_{l'+1/2})\\
&\qquad\Bigg\{\int_{\frac{2}{h_{l'}}(x_{l'-1/2}-x_{l'})}^{\frac{2}{h_{l'}}(x_{j+1/2}+x_{\min}-x_{l+1/2}-x_{l'})}\phi_{i'}\sigma_1^1 F_4\mathrm{d}\xi_{l'}\\
&\qquad\quad+\theta(x_{j+1/2}+x_{\min}-x_{l+1/2}-x_{l'+1/2})\int_{\frac{2}{h_{l'}}(x_{j+1/2}+x_{\min}-x_{l+1/2}-x_{l'+1/2})}^{\frac{2}{h_{l'}}(x_{l'+1/2}-x_{l'})}\phi_{i'}\sigma_1^1 F_4\mathrm{d}\xi_{l'}\Bigg\}\Bigg].
\end{aligned}
\tag{C.10}
$$

The integrals are similar for $\sigma_1^2\sigma_2^2$ and $\sigma_1^3\sigma_2^3$.

C.1.3 *Fortran scheme*

For the scheme we define the following terms

$$
\begin{aligned}
f_{1,i'}(\xi_{l'}) &\equiv \sigma_1\left(\frac{h_{l'}}{2}\xi_{l'}+x_{l'}\right)\phi_{i'}\left(\xi_{l'}\right),\\
f_{2,i}(\xi_l) &\equiv \sigma_2\left(\frac{h_l}{2}\xi_l+x_l\right)\frac{\phi_i(\xi_l)}{\frac{h_l}{2}\xi_l+x_l},\\
T_{\phi_{i'},\phi_i,\text{mixterm1term3}} &\equiv \int_{I_{l'}}\int_{I_l} f_{1,i'}(\xi_{l'})f_{2,i}(\xi_l)\mathrm{d}\xi_l\mathrm{d}\xi_{l'},\\
T_{\phi_{i'},\phi_i,\text{mixterm1}} &\equiv \int_{I_{l'}}\int_{\frac{2}{h_l}(x_{l-1/2}-x_l)}^{\frac{2}{h_l}(x_{\max}-\frac{h_{l'}}{2}\xi_{l'}-x_{l'}+x_{\min}-x_l)} f_{1,i'}(\xi_{l'})f_{2,i}(\xi_l)\mathrm{d}\xi_l\mathrm{d}\xi_{l'},\\
T_{\phi_{i'},\phi_i,\text{mixterm2}} &\equiv \int_{I_{l'}}\int_{\frac{2}{h_l}(x_{j+1/2}-\frac{h_{l'}}{2}\xi_{l'}-x_{l'}+x_{\min}-x_l)}^{\frac{2}{h_l}(x_{l-1/2}-x_l)} f_{1,i'}(\xi_{l'})f_{2,i}(\xi_l)\mathrm{d}\xi_l\mathrm{d}\xi_{l'},\\
T_{\phi_{i'},\phi_i,\text{mixterm1term2}} &\equiv \int_{I_{l'}}\int_{\frac{2}{h_l}(x_{j+1/2}-\frac{h_{l'}}{2}\xi_{l'}-x_{l'}+x_{\min}-x_l)}^{\frac{2}{h_l}(x_{\max}-\frac{h_{l'}}{2}\xi_{l'}-x_{l'}+x_{\min}-x_l)} f_{1,i'}(\xi_{l'})f_{2,i}(\xi_l)\mathrm{d}\xi_l\mathrm{d}\xi_{l'},\\
T_{\phi_{i'},\phi_i,\text{term1}} &\equiv \int_{\frac{2}{h_{l'}}(x_{l'-1/2}-x_{l'})}^{\frac{2}{h_{l'}}(x_{\max}-x_{l-1/2}+x_{\min}-x_{l'})}\int_{\frac{2}{h_l}(x_{l-1/2}-x_l)}^{\frac{2}{h_l}(x_{\max}-\frac{h_{l'}}{2}\xi_{l'}-x_{l'}+x_{\min}-x_l)} f_{1,i'}(\xi_{l'})f_{2,i}(\xi_l)\mathrm{d}\xi_l\mathrm{d}\xi_{l'},\\
T_{\phi_{i'},\phi_i,\text{term2}} &\equiv \int_{\frac{2}{h_{l'}}(x_{l'-1/2}-x_{l'})}^{\frac{2}{h_{l'}}(x_{j+1/2}-x_{l-1/2}+x_{\min}-x_{l'})}\int_{\frac{2}{h_l}(x_{j+1/2}-\frac{h_{l'}}{2}\xi_{l'}-x_{l'}+x_{\min}-x_l)}^{\frac{2}{h_l}(x_{l-1/2}-x_l)} f_{1,i'}(\xi_{l'})f_{2,i}(\xi_l)\mathrm{d}\xi_l\mathrm{d}\xi_{l'},\\
T_{\phi_{i'},\phi_i,\text{term3}} &\equiv \int_{\frac{2}{h_{l'}}(x_{l'-1/2}-x_{l'})}^{\frac{2}{h_{l'}}(x_{\max}-x_{l+1/2}+x_{\min}-x_{l'})}\int_{\frac{2}{h_l}(x_{l+1/2}-x_l)}^{\frac{2}{h_l}(x_{\max}-\frac{h_{l'}}{2}\xi_{l'}-x_{l'}+x_{\min}-x_l)} f_{1,i'}(\xi_{l'})f_{2,i}(\xi_l)\mathrm{d}\xi_l\mathrm{d}\xi_{l'},\\
T_{\phi_{i'},\phi_i,\text{term4}} &\equiv \int_{\frac{2}{h_{l'}}(x_{l'-1/2}-x_{l'})}^{\frac{2}{h_{l'}}(x_{j+1/2}-x_{l+1/2}+x_{\min}-x_{l'})}\int_{\frac{2}{h_l}(x_{j+1/2}-\frac{h_{l'}}{2}\xi_{l'}-x_{l'}+x_{\min}-x_l)}^{\frac{2}{h_l}(x_{l+1/2}-x_l)} f_{1,i'}(\xi_{l'})f_{2,i}(\xi_l)\mathrm{d}\xi_l\mathrm{d}\xi_{l'}.
\end{aligned}
\tag{C.11}
$$

The scheme to calculate the first part of the flux, i.e. with $\sigma_1^1\sigma_2^1$, for $k=0$ writes

```
res = 0
if (x_max > x_{j+1/2}) then
   if (x_max > x_{l+1/2} + x_{l'+1/2} - x_min) then
      if (x_{j+1/2} > x_{l+1/2} + x_{l'+1/2} - x_min) then
         res = 0
      else if (x_{j+1/2} ≤ x_{l+1/2} + x_{l'+1/2} - x_min and x_{j+1/2} > x_{l+1/2} + x_{l'-1/2} - x_min
               and x_{j+1/2} > x_{l-1/2} + x_{l'+1/2} - x_min) then
         res = T_{φ_{i'},φ_i,mixterm1term3} + T_{φ_{i'},φ_i,mixterm2} - T_{φ_{i'},φ_i,term4}
      else if (x_{j+1/2} ≤ x_{l+1/2} + x_{l'+1/2} - x_min and x_{j+1/2} ≤ x_{l+1/2} + x_{l'-1/2} - x_min
               and x_{j+1/2} > x_{l-1/2} + x_{l'+1/2} - x_min) then
         res = T_{φ_{i'},φ_i,mixterm1term3} + T_{φ_{i'},φ_i,mixterm2}
      else if (x_{j+1/2} ≤ x_{l+1/2} + x_{l'+1/2} - x_min and x_{j+1/2} > x_{l+1/2} + x_{l'-1/2} - x_min
               and x_{j+1/2} ≤ x_{l-1/2} + x_{l'+1/2} - x_min) then
         res = T_{φ_{i'},φ_i,mixterm1term3} + T_{φ_{i'},φ_i,term2} - T_{φ_{i'},φ_i,term4}
      else if (x_{j+1/2} ≤ x_{l+1/2} + x_{l'+1/2} - x_min and x_{j+1/2} ≤ x_{l+1/2} + x_{l'-1/2} - x_min
               and x_{j+1/2} ≤ x_{l-1/2} + x_{l'+1/2} - x_min and
                   x_{j+1/2} > x_{l-1/2} + x_{l'-1/2} - x_min) then
         res = T_{φ_{i'},φ_i,mixterm1term3} + T_{φ_{i'},φ_i,term2}
```

```
18        else
19            res = T_{φ_{i'},φ_i,mixterm1term3}
20        endif
21    else if (x_max ≤ x_{l+1/2} + x_{l'+1/2} − x_min and x_max > x_{l+1/2} + x_{l'−1/2} − x_min
22            and x_max > x_{l−1/2} + x_{l'+1/2} − x_min) then
23        if (x_{j+1/2} > x_{l+1/2} + x_{l'−1/2} − x_min and x_{j+1/2} > x_{l−1/2} + x_{l'+1/2} − x_min) then
24            res = T_{φ_{i'},φ_i,mixterm1term2} - T_{φ_{i'},φ_i,term3} - T_{φ_{i'},φ_i,term4}
25        else if (x_{j+1/2} ≤ x_{l+1/2} + x_{l'−1/2} − x_min and x_{j+1/2} > x_{l−1/2} + x_{l'+1/2} − x_min)
              then
26            res = T_{φ_{i'},φ_i,mixterm1term2} - T_{φ_{i'},φ_i,term3}
27        else if (x_{j+1/2} > x_{l+1/2} + x_{l'−1/2} − x_min and x_{j+1/2} ≤ x_{l−1/2} + x_{l'+1/2} − x_min)
              then
28            res = T_{φ_{i'},φ_i,mixterm1} + T_{φ_{i'},φ_i,term2} - T_{φ_{i'},φ_i,term3} - T_{φ_{i'},φ_i,term4}
29        else if (x_{j+1/2} ≤ x_{l+1/2} + x_{l'−1/2} − x_min and x_{j+1/2} ≤ x_{l−1/2} + x_{l'+1/2} − x_min
30                and x_{j+1/2} > x_{l−1/2} + x_{l'−1/2} − x_min) then
31            res = T_{φ_{i'},φ_i,mixterm1} + T_{φ_{i'},φ_i,term2} - T_{φ_{i'},φ_i,term3}
32        else
33            res = T_{φ_{i'},φ_i,mixterm1} - T_{φ_{i'},φ_i,term3}
34        endif
35    else if (x_max ≤ x_{l+1/2} + x_{l'+1/2} − x_min and x_max ≤ x_{l+1/2} + x_{l'−1/2} − x_min
36            and x_max > x_{l−1/2} + x_{l'+1/2} − x_min) then
37        if (x_{j+1/2} > x_{l−1/2} + x_{l'+1/2} − x_min) then
38            res = T_{φ_{i'},φ_i,mixterm1term2}
39        else if (x_{j+1/2} ≤ x_{l−1/2} + x_{l'+1/2} − x_min and x_{j+1/2} > x_{l−1/2} + x_{l'−1/2} − x_min)
              then
40            res = T_{φ_{i'},φ_i,mixterm1} + T_{φ_{i'},φ_i,term2}
41        else
42            res = T_{φ_{i'},φ_i,mixterm1}
43        endif
44    else if (x_max ≤ x_{l+1/2} + x_{l'+1/2} − x_min and x_max > x_{l+1/2} + x_{l'−1/2} − x_min
45            and x_max ≤ x_{l−1/2} + x_{l'+1/2} − x_min) then
46        if (x_{j+1/2} > x_{l+1/2} + x_{l'−1/2} − x_min) then
47            res = T_{φ_{i'},φ_i,term1} + T_{φ_{i'},φ_i,term2} - T_{φ_{i'},φ_i,term3} - T_{φ_{i'},φ_i,term4}
48        else if (x_{j+1/2} ≤ x_{l+1/2} + x_{l'−1/2} − x_min and x_{j+1/2} > x_{l−1/2} + x_{l'−1/2} − x_min)
              then
49            res = T_{φ_{i'},φ_i,term1} + T_{φ_{i'},φ_i,term2} - T_{φ_{i'},φ_i,term3}
50        else
51            res = T_{φ_{i'},φ_i,term1} - T_{φ_{i'},φ_i,term3}
52        endif
53    else if (x_max ≤ x_{l+1/2} + x_{l'+1/2} − x_min and x_max ≤ x_{l+1/2} + x_{l'−1/2} − x_min
54            and x_max ≤ x_{l−1/2} + x_{l'+1/2} − x_min and x_max > x_{l−1/2} + x_{l'−1/2} − x_min)
                then
55        if (x_{j+1/2} > x_{l−1/2} + x_{l'−1/2} − x_min) then
56            res = T_{φ_{i'},φ_i,term1} + T_{φ_{i'},φ_i,term2}
57        else
58            res = T_{φ_{i'},φ_i,term1}
59        endif
60    else
61        res = 0
```

```
   endif
else
   res = 0
endif
```

The two other parts are similar with $\sigma_1^2\sigma_2^2$ and $\sigma_1^3\sigma_2^3$. The total flux F^c_{coag} is the sum of the three parts.

CHAPTER 5

D.1 DERIVATION OF THE LIMITING EQUATIONS

D.1.1 *Analysis in Regime 1*

The derivation of the limiting SDE in Regime 1 follows from standard arguments and does not contain any difficulty or unexpected additional term. We thus only provide the heuristic arguments. A rigorous analysis may be performed using the tools developed below to deal with the other regimes.

For the first step, the parameter $\delta > 0$ is held fixed, and one needs to pass to the limit $\epsilon \to 0$. Observe that

$$\begin{aligned} \mathrm{d}Z^{\epsilon,\delta} &= \frac{V^{\epsilon,\delta}}{\epsilon}\mathrm{d}t \\ &= -\frac{g(Z^{\epsilon,\delta})}{f(Z^{\epsilon,\delta})}\mathrm{d}t + \frac{\sigma\sqrt{2}}{\delta}h(Z^{\epsilon,\delta})\zeta^{\delta}\mathrm{d}t - \epsilon\mathrm{d}V^{\epsilon,\delta}, \end{aligned} \tag{d.1}$$

and as a consequence the limiting SDE when $\epsilon \to 0$ is given by

$$\begin{cases} \mathrm{d}Z^{0,\delta} = -\frac{g(Z^{0,\delta})}{f(Z^{0,\delta})}\mathrm{d}t + \frac{\sigma\sqrt{2}}{\delta}h(Z^{0,\delta})\zeta^{\delta}\mathrm{d}t, \\ \mathrm{d}\zeta^{\delta} = -\frac{\zeta^{\delta}}{\delta^2}\mathrm{d}t + \frac{1}{\delta}\mathrm{d}\beta(t). \end{cases} \tag{d.2}$$

With the notation $\eta^{\delta}(t) = \delta^{-1}\int_0^t \zeta^{\delta}(s)\mathrm{d}s$, one has

$$\frac{1}{\delta}\zeta^{\delta}\mathrm{d}t = \mathrm{d}\eta^{\delta} = \mathrm{d}\beta(t) - \delta\mathrm{d}\zeta^{\delta}, \tag{d.3}$$

which heuristically justifies convergence of η^{δ} to Brownian Motion. At the limit, noise needs to be interpreted with the Stratonovich convention, which is a classical result when Brownian Motion is approximated by a smooth process. Thus, passing to the limit $\delta \to 0$, one obtains the limit SDE

$$\mathrm{d}Z = -\frac{g(Z)}{f(Z)}\mathrm{d}t + \sigma\sqrt{2}h(Z) \circ \mathrm{d}W(t), \tag{d.4}$$

where $\big(W(t)\big)_{t\geq 0}$ is a real-valued standard Wiener process.

The equivalent Itô formulation of the SDE is

$$\mathrm{d}Z = -\frac{g(Z)}{f(Z)}\mathrm{d}t + \sigma^2 h(Z)h'(Z)\mathrm{d}t + \sigma\sqrt{2}h(Z)\mathrm{d}W(t). \tag{d.5}$$

D.1.2 *Analysis in Regime 2*

In this regime, one needs to be careful in order to exhibit the noise-induced drift term when f is not constant. We thus provide all the details of the derivation.

Note that the first step below still follows from a standard argument (which is made rigorous below): for fixed $\epsilon > 0$, when $\delta \to 0$, one obtains the limiting SDE

$$\begin{cases} \mathrm{d}Z^\epsilon = \frac{V^\epsilon}{\epsilon}\mathrm{d}t \\ \mathrm{d}V^\epsilon + \frac{f(Z^\epsilon)V^\epsilon}{\epsilon^2}\mathrm{d}t + \frac{g(Z^\epsilon)}{\epsilon}\mathrm{d}t = \frac{\sigma\sqrt{2}}{\epsilon}f(Z^\epsilon)h(Z^\epsilon)\mathrm{d}\tilde{W}(t), \end{cases} \tag{d.6}$$

where $\big(\tilde{W}(t)\big)_{t\geq 0}$ is a real-valued standard Wiener process. Observe that Itô and Stratonovich interpretations of the noise coincide for this SDE (the diffusion coefficient depends only on the position component, whereas the noise acts only on the velocity component). However, an heuristic argument to pass to the limit $\epsilon \to 0$ would not explain the presence of the noise-induced drift term (when f is not constant), and thus would not provide the correct limiting SDE.

Let us now present a rigorous derivation of the limiting SDE in Regime 2. For the first step, the parameter $\epsilon > 0$ is held fixed. One needs to construct an asymptotic expansion in terms of the small parameter δ, of the form

$$u^{\epsilon,\delta}(t,z,v,\zeta) = u^{\epsilon,0}(t,z,v) + \delta r^{\epsilon,1}(t,z,v,\zeta) + \delta^2 r^{\epsilon,2}(t,z,v,\zeta) + \mathrm{O}(\delta^3), \tag{d.7}$$

where the zero-order term $u^{\epsilon,0}$ does not depend on ζ and describes the limiting process. Then one needs to identify the limiting generator $\overline{\mathcal{L}}^{\epsilon,0}$ such that one has $\partial_t u^{\epsilon,0} = \overline{\mathcal{L}}^{\epsilon,0}u^{\epsilon,0}$.

Inserting the asymptotic expansion in the backward Kolmogorov equation (5.64) and using the expression (5.62) of the infinitesimal generator $\mathcal{L}^{\epsilon,\delta}$, one obtains the following hierarchy of equations when matching terms of size δ^{-2}, δ^{-1} and 1 respectively:

$$\begin{aligned} \mathcal{A}_4 u^{\epsilon,0} &= 0, \\ \mathcal{A}_4 r^{\epsilon,1} + \frac{1}{\epsilon}\mathcal{A}_2 u^{\epsilon,0} &= 0, \\ \mathcal{A}_4 r^{\epsilon,2} + \frac{1}{\epsilon}\mathcal{A}_2 r^{\epsilon,1} + \big(\frac{1}{\epsilon}\mathcal{A}_1 + \frac{1}{\epsilon^2}\mathcal{A}_3\big)u^{\epsilon,0} &= \partial_t u^{\epsilon,0}. \end{aligned} \tag{d.8}$$

The first equation is consistent with the assumption that $u^{\epsilon,0}$ does not depend on ζ. A solution of the second equation is given by

$$r^{\epsilon,1}(t,z,v,\zeta) = \frac{\sigma\sqrt{2}f(z)h(z)}{\epsilon}\zeta\partial_v u^{\epsilon,0}(t,z,v). \tag{d.9}$$

Let $\nu = \mathcal{N}(0,\frac{1}{2})$ denote the invariant distribution of the Ornstein-Uhlenbeck process $\mathrm{d}\zeta = -\zeta\mathrm{d}t + \mathrm{d}\beta(t)$. The partial differential equation satisfied by $u^{\epsilon,0}$ is obtained by taking the average of the last equation of the hierarchy, with respect to $\mathrm{d}\nu(\zeta)$, and using the property $\int \mathcal{A}_4\psi(\zeta)\mathrm{d}\nu(\zeta) = 0$, for any smooth function ψ. Using that $\int \zeta^2\mathrm{d}\nu(\zeta) = \frac{1}{2}$, one obtains

$$\begin{aligned} \partial_t u^{\epsilon,0} &= \frac{\sigma^2 f(z)^2 h(z)^2}{\epsilon^2}\partial^2_{vv}u^{\epsilon,0} + \big(\frac{1}{\epsilon}\mathcal{A}_1 + \frac{1}{\epsilon^2}\mathcal{A}_3\big)u^{\epsilon,0} \\ &= \overline{\mathcal{L}}^{\epsilon,0}u^{\epsilon,0}. \end{aligned} \tag{d.10}$$

For completeness, $r^{\epsilon,2}$ is constructed as solution of the Poisson equation

$$-\mathcal{A}_4 r^{\epsilon,2}(t,z,v,\zeta) = \frac{1}{\epsilon}\big(\mathcal{A}_2 r^{\epsilon,1}(t,z,v,\zeta) - \int \mathcal{A}_2 r^{\epsilon,1}(t,z,v,\cdot)\mathrm{d}\nu\big), \tag{d.11}$$

which is solvable since the right-hand side is centered with respect to ν.

The limiting generator $\overline{\mathcal{L}}^{\epsilon,0}$ is associated with the SDE (d.6). It remains now to pass to the limit $\epsilon \to 0$. This is performed by constructing an asymptotic expansion in terms of the small parameter ϵ of the form

$$u^{\epsilon,0}(t,z,v) = u^{0,0}(t,z) + \epsilon r^{0,1}(t,z,v) + \epsilon^2 r^{0,2}(t,z,v) + \mathrm{O}(\epsilon^3), \tag{d.12}$$

where the zero-order term $u^{0,0}$ does not depend on v, and by identifying the limiting generator $\overline{\mathcal{L}}^{0,0}$ such that one has $\partial_t u^{0,0} = \overline{\mathcal{L}}^{0,0} u^{0,0}$. Observe that one can write

$$\overline{\mathcal{L}}^{\epsilon,0} = \frac{1}{\epsilon}\mathcal{A}_1 + \frac{1}{\epsilon^2}\overline{\mathcal{A}}_3, \tag{d.13}$$

where $\overline{\mathcal{A}}_3$ is defined by

$$\overline{\mathcal{A}}_3\varphi(z,v) = \sigma^2 f(z)^2 h(z)^2 \partial^2_{vv}\varphi(z,v) - f(z)v\partial_v\varphi(z,v). \tag{d.14}$$

Inserting the asymptotic expansion in the backward Kolmogorov equation yields the following hierarchy of equations, when matching terms of size ϵ^{-2}, ϵ^{-1} and 1 respectively:

$$\begin{aligned} \overline{\mathcal{A}}_3 u^{0,0} &= 0, \\ \overline{\mathcal{A}}_3 r^{0,1} + \mathcal{A}_1 u^{0,0} &= 0, \\ \overline{\mathcal{A}}_3 r^{0,2} + \mathcal{A}_1 r^{0,1} &= \partial_t u^{0,0}. \end{aligned} \tag{d.15}$$

The first equation is consistent with the assumption that $u^{0,0}$ does not depend on v. It is then straightforward to check that a solution of the second equation is given by

$$r^{0,1}(t,z,v) = \frac{v\partial_z u^{0,0}(t,z)}{f(z)}. \tag{d.16}$$

Finally, for any fixed z, let $\mu_z = \mathcal{N}(0, \sigma^2 h(z)^2 f(z))$ denote the invariant distribution of the Ornstein-Uhlenbeck process solving the SDE $\mathrm{d}V_z = -f(z)V_z\mathrm{d}t + \sigma\sqrt{2}f(z)h(z)\mathrm{d}W(t)$. The PDE satisfied by $u^{0,0}$ is obtained by taking the average of the last equation of the hierarchy, with respect to $\mathrm{d}\mu_z(v)$, and using the property $\int \overline{\mathcal{A}}_3\psi(v)\mathrm{d}\mu_z(v) = 0$ for any smooth function ψ. Using that $\int v^2\mathrm{d}\mu_z(v) = \sigma^2 h(z)^2 f(z)$, one obtains

$$\begin{aligned} \partial_t u^{0,0}(t,z) &= \int \partial_t u^{0,0}(t,z)d\mu_z(v) \\ &= \int \mathcal{A}_1 r^{0,1}(t,z,v)d\mu_z(v) \\ &= \sigma^2 h(z)^2 f(z)\partial_z\Big(\frac{\partial_z u^{0,0}}{f(z)}\Big) - \frac{g(z)}{f(z)}\partial_z u^{0,0} \\ &= -\Big(\frac{\sigma^2 h(z)^2 f'(z)}{f(z)} + \frac{g(z)}{f(z)}\Big)\partial_z u^{0,0} + \sigma^2 h(z)^2 \partial^2_{zz} u^{0,0} \\ &= \overline{\mathcal{L}}^{0,0} u^{0,0}. \end{aligned} \tag{d.17}$$

The origin of the noise-induced drift term when f is not constant appears clearly in the computation above. For completeness, for fixed t and z, the function $r^{0,2}(t,z,\cdot)$ is constructed as solution of the Poisson equation

$$-\overline{\mathcal{A}}_3 r^{0,2}(t,z,v) = \mathcal{A}_1 r^{0,1}(t,z,v) - \int \mathcal{A}_1 r^{0,1}(t,z,\cdot)\mathrm{d}\mu_z, \tag{d.18}$$

which is solvable since the right-hand side is centered with respect to μ_z.

The limiting generator $\overline{\mathcal{L}}^{0,0}$ is associated with the SDE written in Itô form

$$\mathrm{d}Z = -\frac{g(Z)}{f(Z)}\mathrm{d}t - \frac{\sigma^2 h(Z)^2 f'(Z)}{f(Z)}\mathrm{d}t + \sigma\sqrt{2}h(Z)\mathrm{d}W(t) \tag{d.19}$$

where $\big(W(t)\big)_{t\geq 0}$ is a standard real-valued Wiener process.

The Stratonovich form of the SDE is written as

$$\mathrm{d}Z = -\frac{g(Z)}{f(Z)}\mathrm{d}t - \frac{\sigma^2 h(Z)(fh)'(Z)}{f(Z)}\mathrm{d}t + \sigma\sqrt{2}h(Z)\circ\mathrm{d}W(t). \tag{d.20}$$

D.1.3 *Analysis in Regime 3*

In Regime 3, the parameters δ and ϵ go to 0, with the constraint $\delta = \lambda\epsilon$, where $\lambda \in (0,\infty)$ is held fixed. In the sequel, we consider ϵ as the unique small parameter. Let $u_\lambda^\epsilon = u^{\epsilon,\lambda\epsilon}$.

Using the relation $\delta = \lambda\epsilon$, the infinitesimal generator $\mathcal{L}^{\epsilon,\delta}$ given by (5.62) is written as

$$\mathcal{L}_\lambda^\epsilon = \frac{1}{\epsilon}\mathcal{B}_1 + \frac{1}{\epsilon^2}\mathcal{B}_{2,\lambda}, \tag{d.21}$$

where $\mathcal{B}_1 = \mathcal{A}_1$ and $\mathcal{B}_{2,\lambda} = \frac{1}{\lambda}\mathcal{A}_2 + \mathcal{A}_3 + \frac{1}{\lambda^2}\mathcal{A}_4$.

One needs to construct an asymptotic expansion in terms of the small parameter ϵ, of the form

$$u_\lambda^\epsilon(t,z,v,\zeta) = u_\lambda(t,z) + \epsilon r_\lambda^1(t,z,v,\zeta) + \epsilon^2 r_\lambda^2(t,z,v,\zeta) + \mathrm{O}\left(\epsilon^3\right), \tag{d.22}$$

where the zero-order term u_λ does not depend on v and ζ and describes the limiting process. Then, one needs to identify the limiting generator $\overline{\mathcal{L}}_\lambda$ such that one has $\partial_t u_\lambda = \overline{\mathcal{L}}_\lambda u_\lambda$. Inserting the asymptotic expansion in the backward Kolmogorov equation (5.64) and using the expression (d.21) of the infinitesimal generator $\mathcal{L}_\lambda^\epsilon$, one obtains the following hierarchy of equations when matching terms of size ϵ^{-2}, ϵ^{-1} and 1 respectively:

$$\begin{aligned} \mathcal{B}_{2,\lambda}u_\lambda &= 0, \\ \mathcal{B}_{2,\lambda}r_\lambda^1 + \mathcal{B}_1 u_\lambda &= 0, \\ \mathcal{B}_{2,\lambda}r_\lambda^2 + \mathcal{B}_1 r_\lambda^1 &= \partial_t u_\lambda. \end{aligned} \tag{d.23}$$

The first equation is consistent with the assumption that u_λ does not depend on v and ζ.

The infinitesimal generator $\mathcal{B}_{2,\lambda}$ is associated with the two-dimensional SDE system for the components v and ζ, with frozen position component z:

$$\begin{cases} \mathrm{d}V_{\lambda,z} = -f(z)V_{\lambda,z}\mathrm{d}t + \frac{\sigma\sqrt{2}f(z)h(z)}{\lambda}\zeta_\lambda\mathrm{d}t \\ \mathrm{d}\zeta_\lambda = -\frac{\zeta_\lambda}{\lambda^2}\mathrm{d}t + \frac{1}{\lambda}\mathrm{d}\beta(t). \end{cases} \tag{d.24}$$

The process $(V_{\lambda,z},\zeta_\lambda)$ is a two-dimensional Ornstein-Uhlenbeck process, which converges when $t\to\infty$ to a centered Gaussian distribution $\mu_{\lambda,z}$ with covariance matrix characterized by

$$\begin{aligned} \int \zeta^2 \mathrm{d}\mu_{\lambda,z}(v,\zeta) &= \frac{1}{2}, \\ \int v\zeta \mathrm{d}\mu_{\lambda,z}(v,\zeta) &= \frac{\lambda\sigma f(z)h(z)}{\sqrt{2}(1+\lambda^2 f(z))}, \\ \int v^2 \mathrm{d}\mu_{\lambda,z}(v,\zeta) &= \frac{\sigma^2 h(z)^2 f(z)}{1+\lambda^2 f(z)}. \end{aligned} \tag{d.25}$$

In fact, $\langle \zeta^2 \rangle_{\lambda,z} = \int \zeta^2 \mathrm{d}\mu_z(v,\zeta)$, $\langle v\zeta \rangle_{\lambda,z} = \int v\zeta \mathrm{d}\mu_z(v,\zeta)$ and $\langle v^2 \rangle_z = \int v^2 \mathrm{d}\mu_{\lambda,z}(v,\zeta)$ are obtained in the large time limit, and solve the system (derived for instance by Shapiro-Loginov procedure)

$$\begin{cases} 0 = -\frac{\langle \zeta^2 \rangle_{\lambda,z}}{\lambda^2} + \frac{1}{2\lambda^2}, \\ 0 = -\big(\frac{1}{\lambda^2} + f(z)\big)\langle v\zeta \rangle_{\lambda,z} + \frac{\sigma\sqrt{2}f(z)h(z)}{\lambda}\langle \zeta^2 \rangle_{\lambda,z}, \\ 0 = -f(z)\langle v^2 \rangle_{\lambda,z} + \frac{\sigma\sqrt{2}f(z)h(z)}{\lambda}\langle v\zeta \rangle_{\lambda,z}. \end{cases} \tag{d.26}$$

Define

$$r^1_\lambda(z,v,\zeta) = \frac{\partial_z u_\lambda}{f(z)} v + \lambda\sigma\sqrt{2}h(z)\partial_z u_\lambda \zeta, \tag{d.27}$$

then one has $\mathcal{B}_{2,\lambda} r^1_\lambda + \mathcal{B}_1 u_\lambda = 0$. To identify the generator of the limiting SDE, it suffices to exploit the identity $\int \mathcal{B}_{2,\lambda}\psi(v,\zeta)\mathrm{d}\mu_{\lambda,z}(v,\zeta) = 0$ for all smooth functions ψ, and to compute from the last equation of the hierarchy

$$\begin{aligned} \partial_t u_\lambda(t,z) &= \int \partial_t u_\lambda(t,z)\mathrm{d}\mu_{\lambda,z}(v,\zeta) \\ &= \int \mathcal{B}_1 r^1_\lambda(t,z,v,\zeta)\mathrm{d}\mu_{\lambda,z}(v,\zeta) \\ &= -\frac{g(z)}{f(z)}\partial_z u_\lambda + \langle v^2 \rangle_{\lambda,z}\partial_z\big(\frac{\partial_z u_\lambda}{f(z)}\big) + \lambda\sigma\sqrt{2}\langle v\zeta \rangle_{\lambda,z}\partial_z\big(h(z)\partial_z u_\lambda\big) \\ &= -\frac{g(z)}{f(z)}\partial_z u_\lambda \\ &\quad + \frac{\sigma^2 h(z)^2 f(z)}{1+\lambda^2 f(z)}\partial_z\big(\frac{\partial_z u_\lambda}{f(z)}\big) + \frac{\lambda^2\sigma^2 h(z) f(z)}{1+\lambda^2 f(z)}\partial_z\big(h(z)\partial_z u_\lambda\big) \\ &= -\frac{g(z)}{f(z)}\partial_z u_\lambda + \sigma^2 h(z)^2\partial^2_{zz}u_\lambda + \sigma^2 h(z)h'(z)\partial_z u_\lambda \\ &\quad - \frac{\sigma^2 (fh)'(z)h(z)}{f(z)(1+\lambda^2 f(z))}\partial_z u_\lambda \\ &= \overline{\mathcal{L}}_\lambda u_\lambda. \end{aligned} \tag{d.28}$$

The limiting generator $\overline{\mathcal{L}}_\lambda$ is associated with the SDE written in Itô form

$$\begin{aligned} \mathrm{d}Z = &-\frac{g(Z)}{f(Z)}\mathrm{d}t + \sigma^2 h(Z)h'(Z)\mathrm{d}t \\ &- \frac{\sigma^2 h(Z)(fh)'(Z)}{(1+\lambda^2 f(Z))f(Z)}\mathrm{d}t + \sigma\sqrt{2}h(Z)\mathrm{d}W(t), \end{aligned} \tag{d.29}$$

where $\big(W(t)\big)_{t\geq 0}$ is a standard real-valued Wiener process. One checks that the Stratonovich form of the SDE is

$$\mathrm{d}Z = -\frac{g(Z)}{f(Z)}\mathrm{d}t - \frac{\sigma^2 h(Z)(fh)'(Z)}{(1+\lambda^2 f(Z))f(Z)}\mathrm{d}t + \sigma\sqrt{2}h(Z)\circ\mathrm{d}W(t). \tag{d.30}$$

CHAPTER 6

E.1 MCMC ORBITAL FIT OF HIP 117452 BABB

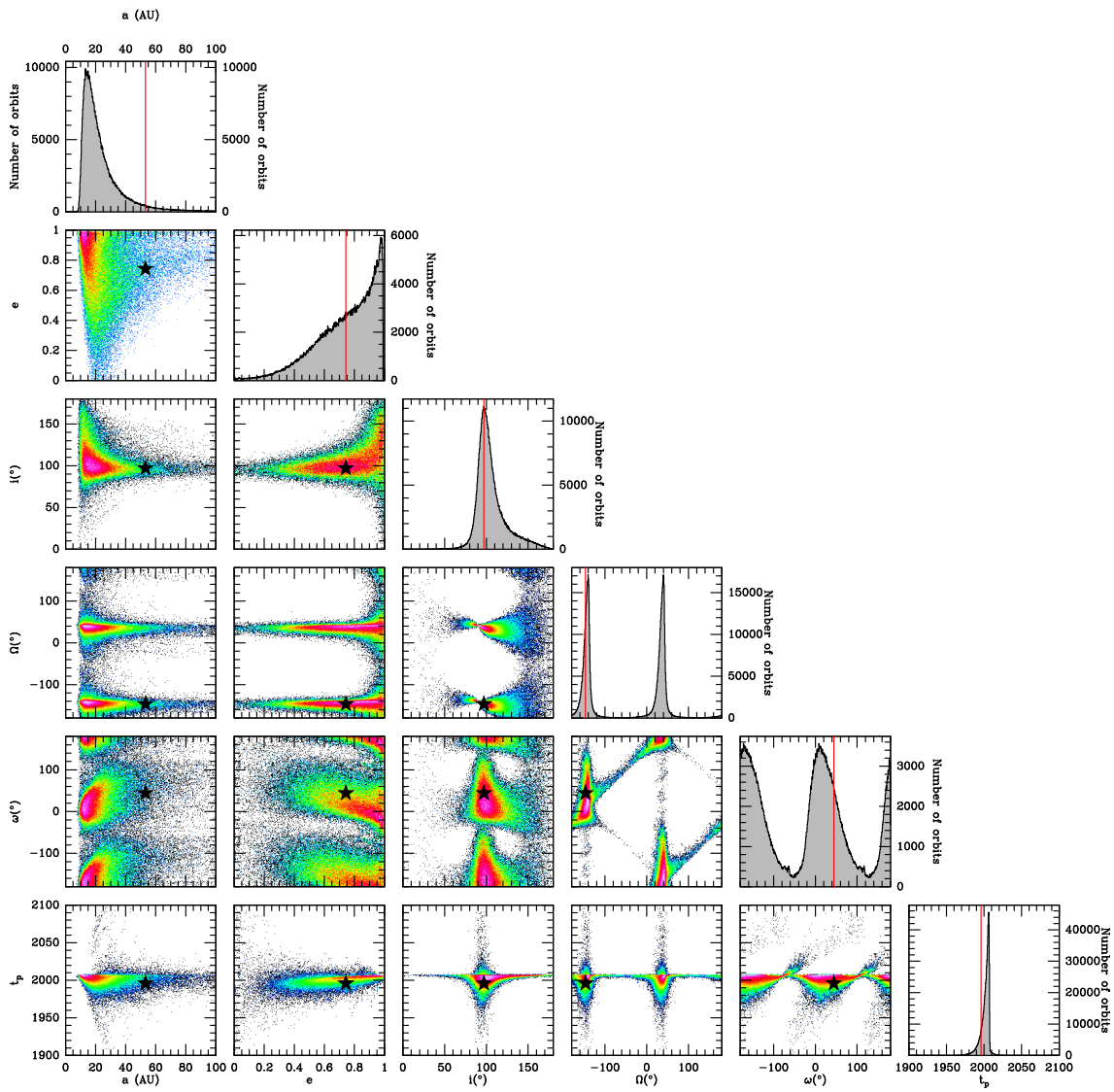

Figure e.1: Results of the MCMC fit of the NaCo and SPHERE combined astrometric data of HIP 117452 Ba and Bb reported in terms of statistical distribution matrix of the orbital elements a, e, i,Ω,ω, and t_p. The red line in the histograms and the black star in the correlation plots indicate the position of the best LSLM-χ^2 model obtained for comparison.

BIBLIOGRAPHY

Links to the journal or editor website are in red, links to the ADS are in blue.

Adachi, I. et al., *Progress of Theoretical Physics* **56**, 1756–1771 (1976), linkADS.
Akimkin, V. V., *Astronomy Reports* **59**, 747–761 (2015), linkADS.
Akimkin, V. V. et al., *ApJ* **889**, 64, 64 (2020), linkADS.
Aldous, D. J., *Bernoulli* **5**, 3–48 (1999).
Alibert, Y. et al., *A&A* **434**, 343–353 (2005), linkADS.
ALMA Partnership et al., *ApJ* **808**, L3, L3 (2015), linkADS.
Andrews, S. M., *ARA&A* **58**, 483–528 (2020), linkADS.
Andrews, S. M. and J. P. Williams, *ApJ* **659**, 705–728 (2007), linkADS.
Andrews, S. M. et al., *ApJ* **820**, L40, L40 (2016), linkADS.
Andrews, S. M. et al., *ApJ* **869**, L41, L41 (2018), linkADS.
Apai, D. et al., *A&A* **426**, L53–L57 (2004), linkADS.
Arena, S. E. and J.-F. Gonzalez, *MNRAS* **433**, 98–116 (2013), linkADS.
Armitage, P. J., *Saas-Fee Advanced Course* **45**, 1 (2019), linkADS.
Avenhaus, H. et al., *ApJ* **790**, 56, 56 (2014), linkADS.
Avenhaus, H. et al., *AJ* **154**, 33, 33 (2017), linkADS.
Avenhaus, H. et al., *ApJ* **863**, 44, 44 (2018), linkADS.
Bai, X.-N. and J. Goodman, *ApJ* **701**, 737–755 (2009), linkADS.
Baines, M. J. et al., *MNRAS* **130**, 63 (1965), linkADS.
Balbus, S. A. and J. F. Hawley, *ApJ* **376**, 214–233 (1991), linkADS.
Balbus, S. A., 'Magnetohydrodynamics of Protostellar Disks,' in *Physical processes in circumstellar disks around young stars*, edited by P. J. V. Garcia (), pp. 237–282, linkADS.
Balbus, S. A. and J. C. B. Papaloizou, *ApJ* **521**, 650–658 (1999), linkADS.
Baraffe, I. et al., *A&A* **402**, 701–712 (2003), linkADS.
Barrière-Fouchet, L. et al., *A&A* **443**, 185–194 (2005), linkADS.
Baruteau, C. et al., in Protostars and planets vi, edited by H. Beuther et al. (), p. 667, linkADS.
Batchelor, G. K., *QJRAS* **76**, 133–146 (1950), linkADS.
Beckwith, K. et al., *MNRAS* **416**, 361–382 (2011), linkADS.
Bell, C. P. M. et al., *MNRAS* **454**, 593–614 (2015), linkADS.
Benisty, M. et al., *A&A* **578**, L6, L6 (2015), linkADS.
Benisty, M. et al., *A&A* **597**, A42, A42 (2017), linkADS.
Benítez-Llambay, P. and F. S. Masset, *ApJS* **223**, 11, 11 (2016), linkADS.
Benítez-Llambay, P. et al., *ApJS* **241**, 25, 25 (2019), linkADS.
Berry, E. X., *JAS* **24**, 688–701 (1967), linkADS.
Berry, E. X. and R. L. Reinhardt, *JAS* **31**, 1814–1824 (1974), linkADS.
Beuzit, J. .-.-L. et al., *A&A* **631**, A155, A155 (2019), linkADS.
Birnstiel, T. et al., *A&A* **513**, A79, A79 (2010), linkADS.
Birnstiel, T. et al., *A&A* **539**, A148, A148 (2012), linkADS.
Birnstiel, T. et al., *Space Sci. Rev.* **205**, 41–75 (2016), linkADS.
Bleck, R., *J. Geophys. Res.* **75**, 5165–5171 (1970), linkADS.
Blum, J. and G. Wurm, *ARA&A* **46**, 21–56 (2008), linkADS.
Blum, J., *Research in Astronomy and Astrophysics* **10**, 1199–1214 (2010), linkADS.
Blum, J., *Space Sci. Rev.* **214**, 52, 52 (2018), linkADS.
Blum, J. and M. Münch, *icarus* **106**, 151–167 (1993), linkADS.

Blum, J. and G. Wurm, *icarus* **143**, 138–146 (2000), linkADS.
Blum, J. et al., *MNRAS* **469**, S755–S773 (2017), linkADS.
Boccaletti, A. et al., in Adaptive optics systems, Vol. 7015, *Proc. SPIE* (), 70151B, linkADS.
Boccaletti, A. et al., *A&A* **637**, L5, L5 (2020), linkADS.
Boccaletti, A. et al., *arXiv e-prints* (2020), linkADS.
Bodenheimer, P. et al., *icarus* **143**, 2–14 (2000), linkADS.
Bodrova, A. S. et al., *Journal of Physics A Mathematical General* **52**, 205001, 205001 (2019), linkADS.
Boley, A. C., *ApJ* **695**, L53–L57 (2009), linkADS.
Bonavita, M. et al., *A&A* **537**, A67, A67 (2012), linkADS.
Bonnefoy, M. et al., *A&A* **618**, A63, A63 (2018), linkADS.
Bott, A., *JAS* **55**, 2284–2293 (1998), linkADS.
Bourgade, J.-P. and F. Filbet, *Mathematics of Computation* **77**, 851–882 (2008), linkADS.
Bowler, B. P., *PASP* **128**, 102001 (2016), linkADS.
Brandl, B. R. et al., in Ground-based and airborne instrumentation for astronomy vi, Vol. 9908, edited by C. J. Evans et al., Society of Photo-Optical Instrumentation Engineers (SPIE) Conference Series (), p. 990820, linkADS.
Brandt, T. D. et al., *ApJ* **794**, 159, 159 (2014), linkADS.
Brauer, F. et al., *A&A* **480**, 859–877 (2008), linkADS.
Brazier-Smith, P. R. et al., *Proceedings of the Royal Society of London Series A* **326**, 393–408 (1972), linkADS.
Brilliantov, N. et al., *Proceedings of the National Academy of Science* **112**, 9536–9541 (2015), linkADS.
Bromley, B. C. and S. J. Kenyon, *ApJ* **796**, 141, 141 (2014), linkADS.
Burbine, T. H. et al., 'Meteoritic Parent Bodies: Their Number and Identification,' in *Asteroids iii* (), pp. 653–667, linkADS.
Cameron, A. G. W., *icarus* **18**, 407–450 (1973), linkADS.
Cameron, A. G. W., 'The primitive solar accretion disk and the formation of the planets.,' in *Origin of the solar system*, edited by S. F. Dermott (), pp. 49–74, linkADS.
Cameron, A. G. W. and M. R. Pine, *icarus* **18**, 377–406 (1973), linkADS.
Cantalloube, F. et al., *A&A* **582**, A89, A89 (2015), linkADS.
Carballido, A. et al., *MNRAS* **373**, 1633–1640 (2006), linkADS.
Carballido, A. et al., *MNRAS* **415**, 93–102 (2011), linkADS.
Carrillo, J. A. and T. Goudon, *J. Sci. Comput.* **20**, 69–113 (2004).
Cassan, A. et al., *Nature* **481**, 167–169 (2012), linkADS.
Charnoz, S. and E. Taillifet, *ApJ* **753**, 119, 119 (2012), linkADS.
Charnoz, S. et al., *ApJ* **737**, 33, 33 (2011), linkADS.
Chauvin, G. et al., *A&A* **509**, A52, A52 (2010), linkADS.
Chauvin, G. et al., *A&A* **542**, A41, A41 (2012), linkADS.
Chauvin, G. et al., *A&A* **573**, A127, A127 (2015), linkADS.
Chauvin, G. et al., *A&A* **617**, A76, A76 (2018), linkADS.
Chen, C. H. et al., *ApJS* **211**, 25, 25 (2014), linkADS.
Chen, J.-P. and D. Lamb, *JAS* **51**, 2613–2630 (1994), linkADS.
Cheng, Z. and S. Redner, *Phys. Rev. Lett.* **60**, 2450–2453 (1988), linkADS.
Cheng, Z. and S. Redner, *Journal of Physics A Mathematical General* **23**, 1233–1258 (1990), linkADS.
Chiang, E., *ApJ* **675**, 1549–1558 (2008), linkADS.
Chiang, E. I. and P. Goldreich, *ApJ* **490**, 368–376 (1997), linkADS.
Chiang, E. and A. N. Youdin, *Annual Review of Earth and Planetary Sciences* **38**, 493–522 (2010), linkADS.

Chokshi, A. et al., *ApJ* **407**, 806 (1993), linkADS.
Christiaens, V. et al., *ApJ* **877**, L33, L33 (2019), linkADS.
Ciesla, F. J., *ApJ* **654**, L159–L162 (2007), linkADS.
Ciesla, F. J., *ApJ* **723**, 514–529 (2010), linkADS.
Claudi, R. U. et al., in Ground-based and airborne instrumentation for astronomy ii, Vol. 7014, *Proc. SPIE* (), 70143E, linkADS.
Cockburn, B. and C.-W. Shu, *Mathematics of Computation* **52**, 411–435 (1989).
Connelly, J. N. et al., *Science* **338**, 651 (2012), linkADS.
Coradini, A. et al., *Moon and Planets* **22**, 47–61 (1980), linkADS.
Crida, A. et al., *ApJ* **705**, L148–L152 (2009), linkADS.
Cuzzi, J. N. et al., *icarus* **106**, 102–134 (1993), linkADS.
Da Costa, F., 'Mathematical aspects of coagulation-fragmentation equations,' in *Mathematics of energy and climate change* (Springer), pp. 83–162.
D'Alessio, P. et al., *ApJ* **500**, 411–427 (1998), linkADS.
David, T. J. and L. A. Hillenbrand, *ApJ* **804**, 146, 146 (2015), linkADS.
Davies, C. N., *Journal of Aerosol Science* **10**, 233 (1979), linkADS.
de Boer, J. et al., *MNRAS* **466**, L7–L12 (2017), linkADS.
De Rosa, R. J. et al., *MNRAS* **415**, 854–866 (2011), linkADS.
De Rosa, R. J. et al., *MNRAS* **445**, 3694–3705 (2014), linkADS.
Debry, E. et al., *Journal of Computational Physics* **184**, 649–669 (2003), linkADS.
Delichatsios, M. A. and R. F. Probstein, *Journal of Colloid and Interface Science* **51**, 394–405 (1975), linkADS.
Delorme, P. et al., in Sf2a-2017: proceedings of the annual meeting of the french society of astronomy and astrophysics, edited by C. Reylé et al. (), p. Di, linkADS.
Dent, W. R. F. et al., *PASP* **125**, 477–505 (2013), linkADS.
Derjaguin, B. V. et al., *Journal of Colloid and Interface Science* **53**, 314–326 (1975), linkADS.
Devir (Weinstock), S. E., *Journal of Colloid Science* **18**, 744–756 (1963).
Devir (Weinstock), S. E., *Journal of Colloid and Interface Science* **21**, 9–23 (1966).
di Stasio, S. et al., *Journal of Colloid and Interface Science* **247**, 33–46 (2002), linkADS.
Dipierro, G. and G. Laibe, *MNRAS* **469**, 1932–1948 (2017), linkADS.
Dipierro, G. et al., *MNRAS* **451**, 974–986 (2015), linkADS.
Dohlen, K. et al., in Ground-based and airborne instrumentation for astronomy ii, Vol. 7014, *Proc. SPIE* (), p. 70143L, linkADS.
Dohnanyi, J. S., *J. Geophys. Res.* **74**, 2531–2554 (1969), linkADS.
Dohnanyi, J. S., 'Fragmentation and Distribution of Asteroids,' in *Nasa special publication*, Vol. 267, edited by T. Gehrels (), p. 263, linkADS.
Dominik, C. and A. G. G. M. Tielens, *ApJ* **480**, 647–673 (1997), linkADS.
Dominik, C. et al., *arXiv e-prints* (2016), linkADS.
Drake, R. L., *JAS* **29**, 537–547 (1972), linkADS.
Drążkowska, J. et al., *ApJ* **885**, 91, 91 (2019), linkADS.
Dubovskiui, P. B., *Mathematical theory of coagulation* (National Univ.).
Dubrulle, B. et al., *icarus* **114**, 237–246 (1995), linkADS.
Dullemond, C. P. and C. Dominik, *A&A* **417**, 159–168 (2004), linkADS.
Dullemond, C. P. and C. Dominik, *A&A* **421**, 1075–1086 (2004), linkADS.
Dullemond, C. P. and C. Dominik, *A&A* **434**, 971–986 (2005), linkADS.
Dullemond, C. P. and C. Dominik, *A&A* **434**, 971–986 (2005), linkADS.
Dullemond, C. P. et al., *ApJ* **869**, L46, L46 (2018), linkADS.
Dzyurkevich, N. et al., *A&A* **515**, A70, A70 (2010), linkADS.
Enukashvily, I. M., *JAS* **37**, 2521–2534 (1980), linkADS.
Epstein, P. S., *Physical Review* **23**, 710–733 (1924), linkADS.

Erasmus, L. et al., *Computers Chemical Engineering* **18**, An International Journal of Computer Applications in Chemical Engineering, 775–783 (1994).
Ernst, M. H. et al., *Journal of Colloid and Interface Science* **97**, 266–277 (1984), linkADS.
Ernst, M. H. and I. Pagonabarraga, *Journal of Physics A Mathematical General* **40**, F331–F337 (2007), linkADS.
Escobedo, M. and S. Mischler, *Annales de l'Institut Henri Poincare (C) Non Linear Analysis* **23**, 331–362 (2006).
Escobedo, M. et al., *Annales de l'Institut Henri Poincare (C) Non Linear Analysis* **22**, 99–125 (2005).
Espaillat, C. et al., in Protostars and planets vi, edited by H. Beuther et al. (), p. 497, linkADS.
Estrada, P. R. and J. N. Cuzzi, *ApJ* **682**, 515–526 (2008), linkADS.
Eyre, D. et al., *Journal of Computational Physics* **78**, 288–304 (1988), linkADS.
Fang, J. and J.-L. Margot, *ApJ* **767**, 115 (2013).
Fernández-Díaz, J. M. and G. J. Gómez-García, *EPL (Europhysics Letters)* **78**, 56002 (2007), linkADS.
Filbet, F., *AIP Conference Proceedings* **1048**, 921–921 (2008).
Filbet, F. and P. Laurencot, *SIAM Journal on Scientific Computing* **25**, 2004–2028 (2004).
Finlayson, B., *The method of weighted residuals and variational principles, mathematics in science and engineering* (Academic Press New York).
Ford, E. B. and P. C. Gregory, in Statistical challenges in modern astronomy iv, Vol. 371, edited by G. J. Babu and E. D. Feigelson, Astronomical Society of the Pacific Conference Series (), p. 189, linkADS.
Forestier-Coste, L. and S. Mancini, *SIAM Journal on Scientific Computing* **34**, B840–B860 (2012).
Freidlin, M. and W. Hu, *J. Math. Sci. (N.Y.)* **179**, Problems in mathematical analysis. No. 61, 184–207 (2011).
Friedlander, S. K., *JAS* **17**, 373–374 (1960), linkADS.
Friedlander, S. K., *JAS* **17**, 479–483 (1960), linkADS.
Friedlander, S. K. and C. S. Wang, *Journal of Colloid and Interface Science* **22**, 126–132 (1966), linkADS.
Friedlander, S. K. et al., *Smoke, dust, and haze*, Vol. 198 (Oxford university press New York).
Fromang, S., *A&A* **514**, L5, L5 (2010), linkADS.
Fromang, S. and R. P. Nelson, *A&A* **496**, 597–608 (2009), linkADS.
Fromang, S. and J. Papaloizou, *A&A* **452**, 751–762 (2006), linkADS.
Fuerstenau, D. et al., *International Journal of Mineral Processing* **74**, Special Issue Supplement Comminution 2002, S317–S327 (2004).
Furlan, E. et al., *ApJS* **165**, 568–605 (2006), linkADS.
Fusco, T. et al., *Optics Express* **14**, 7515 (2006), linkADS.
Gabriel, P. and L. M. Tine, *ESAIM: Proc.* **30**, 53–69 (2010).
Gaia Collaboration et al., *A&A* **616**, A1, A1 (2018), linkADS.
Galicher, R. et al., *ApJ* **739**, L41, L41 (2011), linkADS.
Galicher, R. et al., *A&A* **594**, A63, A63 (2016), linkADS.
Galicher, R. et al., *A&A* **615**, A92, A92 (2018), linkADS.
Garaud, P. and D. N. C. Lin, *ApJ* **608**, 1050–1075 (2004), linkADS.
Garaud, P. et al., *ApJ* **764**, 146, 146 (2013), linkADS.
Garcia, A. J. L. and J.-F. Gonzalez, *MNRAS* **493**, 1788–1800 (2020), linkADS.
Gardner, J. P. et al., *Space Science Reviews* **123**, 485–606 (2006).
Gáspár, A. et al., *ApJ* **749**, 14, 14 (2012), linkADS.

Gauza, B. et al., *ApJ* **804**, 96, 96 (2015), linkADS.
Gelbard, F. and J. H. Seinfeld, *Journal of Computational Physics* **28**, 357–375 (1978), linkADS.
Gelbard, F. and J. H. Seinfeld, *Journal of Colloid and Interface Science* **78**, 485–501 (1980), linkADS.
Gelbard, F. et al., *Journal of Colloid and Interface Science* **76**, 541–556 (1980), linkADS.
Geretshauser, R. J. et al., *A&A* **513**, A58, A58 (2010), linkADS.
Gillespie, D. T., *JAS* **32**, 600–607 (1975), linkADS.
Gillespie, J. R. and R. List, *Pure and Applied Geophysics* **117**, 599–626 (1978), linkADS.
Goldreich, P. and S. Tremaine, *ApJ* **241**, 425–441 (1980), linkADS.
Golovin, A., *Izv. Geophys. Ser* **5**, 482–487 (1963).
Gonzalez, J. .-.-F. et al., *MNRAS* **467**, 1984–1996 (2017), linkADS.
Gottlieb, S. et al., *SIAM Review* **43**, 89–112 (2001), linkADS.
Gottlieb, S. et al., *J. Sci. Comput.* **38**, 251–289 (2009).
Goudon, T. et al., *Mathematical Models and Methods in Applied Sciences* **23**, 10.1142/S0218202513500061 (2013).
Greco, J. P. and T. D. Brandt, *ApJ* **833**, 134, 134 (2016), linkADS.
Greenwood, A. J. et al., *A&A* **626**, A6, A6 (2019), linkADS.
Gundlach, B. et al., *MNRAS* **479**, 1273–1277 (2018), linkADS.
Güttler, C. et al., *A&A* **513**, A56, A56 (2010), linkADS.
Güttler, C. et al., *A&A* **630**, A24, A24 (2019), linkADS.
Handbury, M. J. and I. P. Williams, *Ap&SS* **50**, 55–62 (1977), linkADS.
Haworth, T. J. et al., **33**, e053, e053 (2016), linkADS.
Hayashi, C., *Progress of Theoretical Physics Supplement* **70**, 35–53 (1981), linkADS.
Hayashi, C. and Y. Nakagawa, *Progress of Theoretical Physics* **54**, 93–103 (1975), linkADS.
Hellyer, B., *MNRAS* **148**, 383 (1970), linkADS.
Hennebelle, P. et al., *A&A* **635**, A67, A67 (2020), linkADS.
Hernandez-Machado, A. et al., English, *Zeitschrift für Physik B Condensed Matter* **52**, 335–343 (1983).
Hertz, H. et al., *Miscellaneous papers* (Macmillan and Company).
Herzog, D. P. et al., *J. Stat. Phys.* **163**, 659–673 (2016).
Hidy, G., *Aerosols: an industrial and environmental science* (Elsevier).
Hidy, G. and J. Brock, *Topics in current aerosol research. part 2* (Pergamon Press).
Higuchi, W. et al., *Journal of Pharmaceutical Sciences* **52**, 49–54 (1963).
Hill, P. J. and K. M. Ng, *AIChE Journal* **42**, 1600–1611 (1996).
Hirashita, H. and H. Yan, *MNRAS* **394**, 1061–1074 (2009), linkADS.
Ho, P. T. P. et al., *ApJ* **616**, L1–L6 (2004), linkADS.
Hottovy, S. et al., *J. Stat. Phys.* **146**, 762–773 (2012).
Hottovy, S. et al., *Comm. Math. Phys.* **336**, 1259–1283 (2015).
Hounslow, M. J. et al., *AIChE Journal* **34**, 1821–1832 (1988).
Hoyle, F., *QJRAS* **1**, 28 (1960), linkADS.
Hu, Z. and R. C. Srivastava, *JAS* **52**, 1761–1783 (1995), linkADS.
Hugot, E. et al., *A&A* **538**, A139, A139 (2012), linkADS.
Hulburt, H. and S. Katz, *Chemical Engineering Science* **19**, 555–574 (1964).
Hung, L.-W. et al., *ApJ* **815**, L14, L14 (2015), linkADS.
Hutchison, M. et al., *MNRAS* **476**, 2186–2198 (2018), linkADS.
Isella, A. et al., *ApJ* **869**, L49, L49 (2018), linkADS.
Jacobson, M. Z., *Fundamentals of Atmospheric Modeling* (), linkADS.
Jacobson, M. Z. et al., *Atmospheric Environment* **28**, 1327–1338 (1994), linkADS.
Jacquet, E., *A&A* **551**, A75, A75 (2013), linkADS.
Jacquet, E. et al., *MNRAS* **415**, 3591–3598 (2011), linkADS.

Jaupart, E. and G. Laibe, *MNRAS* **492**, 4591–4598 (2020), linkADS.
Jiang, G.-S. and D. Peng, *SIAM Journal on Scientific Computing* **21**, 2126–2143 (2000).
Johansen, A. and H. Klahr, *ApJ* **634**, 1353–1371 (2005), linkADS.
Johansen, A. et al., *A&A* **417**, 361–374 (2004), linkADS.
Johansen, A. et al., *ApJ* **643**, 1219–1232 (2006), linkADS.
Johansen, A. et al., *A&A* **529**, A62, A62 (2011), linkADS.
Johnson, K. L. et al., *Proceedings of the Royal Society of London. A. Mathematical and Physical Sciences* **324**, 301–313 (1971).
Jones, A. P. et al., *ApJ* **433**, 797 (1994), linkADS.
Jones, A. P. et al., *ApJ* **469**, 740 (1996), linkADS.
Jones, A. P. et al., *A&A* **602**, A46, A46 (2017), linkADS.
Jullien, R. and P. Meakin, *Journal of Colloid and Interface Science* **127**, 265–272 (1989), linkADS.
Junge, C. E., *Advances in Geophysics* **4**, 1 (1958), linkADS.
Kalas, P. et al., *Science* **322**, 1345 (2008), linkADS.
Kataoka, A. et al., *A&A* **557**, L4, L4 (2013), linkADS.
Kennedy, G. M. and M. C. Wyatt, *MNRAS* **444**, 3164–3182 (2014), linkADS.
Kennedy, G. M. and S. J. Kenyon, *ApJ* **682**, 1264–1276 (2008), linkADS.
Kenyon, S. J. and L. Hartmann, *ApJ* **323**, 714–733 (1987), linkADS.
Keppler, M. et al., *A&A* **617**, A44, A44 (2018), linkADS.
Keppler, M. et al., *A&A* **625**, A118, A118 (2019), linkADS.
Khain, A. P. and M. Pinsky, *Physical processes in clouds and cloud modeling* (Cambridge University Press).
Kobayashi, H. and H. Tanaka, *icarus* **206**, 735–746 (2010), linkADS.
Kobayashi, H. et al., *icarus* **209**, 836–847 (2010), linkADS.
Köhler, M. et al., *A&A* **579**, A15, A15 (2015), linkADS.
Kostoglou, M. and A. J. Karabelas, *Journal of Colloid and Interface Science* **163**, 420–431 (1994), linkADS.
Kostoglou, M. and A. J. Karabelas, *Journal of Physics A Mathematical General* **33**, 1221–1232 (2000), linkADS.
Kostoglou, M. and A. J. Karabelas, *Journal of Colloid and Interface Science* **303**, 419–429 (2006), linkADS.
Kovetz, A. and B. Olund, *JAS* **26**, 1060–1065 (1969), linkADS.
Krapivsky, P. L., *Journal of Statistical Physics* **69**, 135–150 (1992), linkADS.
Kraus, S. et al., *Science* **369**, 1233–1238 (2020), linkADS.
Kruyt, H. and A. Van Arkel, *Recueil des Travaux Chimiques des Pays-Bas* **39**, 656–671 (1920).
Kumar, S. and D. Ramkrishna, *Chemical Engineering Science* **51**, 1311–1332 (1996).
Kusaka, T. et al., *Progress of Theoretical Physics* **44**, 1580–1595 (1970), linkADS.
Kwok, S., *ApJ* **198**, 583–591 (1975), linkADS.
Lafrenière, D. et al., *ApJ* **660**, 770–780 (2007), linkADS.
Lagrange, A. .-.-M. et al., *A&A* **542**, A40, A40 (2012), linkADS.
Lagrange, A.-M. et al., *A&A* **493**, L21–L25 (2009), linkADS.
Lagrange, A.-M. et al., *Science* **329**, 57 (2010), linkADS.
Lai, F. S. et al., *Journal of Colloid and Interface Science* **39**, 395–405 (1972), linkADS.
Laibe, G. and D. J. Price, *MNRAS* **420**, 2345–2364 (2012), linkADS.
Laibe, G., *MNRAS* **437**, 3037–3054 (2014), linkADS.
Laibe, G. and D. J. Price, *MNRAS* **420**, 2345–2364 (2012), linkADS.
Laibe, G. and D. J. Price, *MNRAS* **444**, 1940–1956 (2014), linkADS.
Laibe, G. and D. J. Price, *MNRAS* **440**, 2136–2146 (2014), linkADS.
Laibe, G. et al., *MNRAS* **437**, 3055–3062 (2014), linkADS.

Laibe, G. et al., *MNRAS* **494**, 5134–5147 (2020), linkADS.
Laibe, G. et al., *A&A* **487**, 265–270 (2008), linkADS.
Laibe, G. et al., *MNRAS* **437**, 3025–3036 (2014), linkADS.
Lambrechts, M. and A. Johansen, *A&A* **544**, A32, A32 (2012), linkADS.
Landgrebe, J. D. and S. E. Pratsinis, *Journal of Colloid and Interface Science* **139**, 63–86 (1990), linkADS.
Lannier, J. et al., *A&A* **596**, A83, A83 (2016), linkADS.
Laurençot, P., *Journal of Statistical Physics*, 10.1007/s10955-018-2018-9 (2018), linkADS.
Laurençot, P. and D. Wrzosek, *Journal of Statistical Physics* **104**, 193–220 (2001).
Laws, A. S. E. et al., *ApJ* **888**, 7, 7 (2020), linkADS.
Lebreuilly, U. et al., *A&A* **626**, A96, A96 (2019), linkADS.
Lebreuilly, U. et al., *A&A* **641**, A112, A112 (2020), linkADS.
Lee, K. W. and H. Chen, *Aerosol Science Technology* **3**, 327–334 (1984), linkADS.
Lee, K. and T. Matsoukas, *Powder Technology* **110**, 82–89 (2000).
Lee, M. H., *Journal of Physics A Mathematical General* **34**, 10219–10241 (2001), linkADS.
Leyvraz, F., *Phys. Rep.* **383**, 95–212 (2003), linkADS.
Leyvraz, F. and H. R. Tschudi, *Journal of Physics A Mathematical General* **14**, 3389–3405 (1981), linkADS.
Liffman, K., *Journal of Computational Physics* **100**, 116–127 (1992), linkADS.
Lin, D. N. C. and J. Papaloizou, *ApJ* **307**, 395 (1986), linkADS.
Lin, D. N. C. et al., *Nature* **380**, 606–607 (1996), linkADS.
Lin, M.-K., *MNRAS* **485**, 5221–5234 (2019), linkADS.
List, R. and J. R. Gillespie, *JAS* **33**, 2007–2013 (1976), linkADS.
Lister, J. D. et al., *AIChE Journal* **41**, 591–603 (1995).
Liu, X.-D. and S. Osher, *SIAM Journal on Numerical Analysis* **33**, 760–779 (1996).
Liu, H. et al., *SIAM Journal on Scientific Computing* **41**, B448–B465 (2019).
Lodato, G., **52**, 21–41 (2008), linkADS.
Lombart, M. et al., *A&A* **639**, A54 (2020).
Love, S. G. et al., *icarus* **111**, 227–236 (1994), linkADS.
Lynden-Bell, D. and J. E. Pringle, *MNRAS* **168**, 603–637 (1974), linkADS.
Maaskant, K. M. et al., *A&A* **574**, A140, A140 (2015), linkADS.
Macintosh, B. et al., *Science* **350**, 64–67 (2015), linkADS.
Mahoney, A. W. and D. Ramkrishna, *Chemical Engineering Science* **57**, 1107–1119 (2002).
Maire, A.-L. et al., in Society of photo-optical instrumentation engineers (spie) conference series, Vol. 9908, *Proc. SPIE* (), p. 990834, linkADS.
Makino, J. et al., **3**, 411–417 (1998), linkADS.
Marchisio, D. L. et al., *Journal of Colloid and Interface Science* **258**, 322–334 (2003), linkADS.
Marleau, G.-D. and A. Cumming, *MNRAS* **437**, 1378–1399 (2014), linkADS.
Marleau, G.-D. et al., *A&A* **624**, A20, A20 (2019), linkADS.
Marois, C. et al., in Adaptive optics systems iv, Vol. 9148, edited by E. Marchetti et al., Society of Photo-Optical Instrumentation Engineers (SPIE) Conference Series (), 91480U, linkADS.
Marois, C. et al., *ApJ* **641**, 556–564 (2006), linkADS.
Marois, C. et al., *Nature* **468**, 1080–1083 (2010), linkADS.
Masoliver, J. and J. M. Porrà, *Phys. Rev. E* **48**, 4309–4319 (1993), linkADS.
Masset, F. S. and J. C. B. Papaloizou, *ApJ* **588**, 494–508 (2003), linkADS.
Matsoukas, T. et al., English (US), *AICHE Journal* **52**, 3088–3099 (2006).
Matthews, B. C. et al., in Protostars and planets vi, edited by H. Beuther et al. (), p. 521, linkADS.
Matthews, E. et al., *MNRAS* **480**, 2757–2783 (2018), linkADS.

Mawet, D. et al., *ApJ* **792**, 97, 97 (2014), linkADS.
Mayor, M. and D. Queloz, *Nature* **378**, 355–359 (1995), linkADS.
McGrady, E. D. and R. M. Ziff, *Phys. Rev. Lett.* **58**, 892–895 (1987), linkADS.
McLeod, J. B., *Proc. of the London Mathematical Society* **s3-14**, 445–458 (1962).
Melzak, Z. A., *Transactions of the American Mathematical Society* **85**, 547–560 (1957).
Mendoza V., E. E., *ApJ* **143**, 1010 (1966), linkADS.
Menon, G. and R. L. Pego, *Communications on Pure and Applied Mathematics* **57**, 1197–1232 (2004).
Menon, G. and R. L. Pego, *SIAM Review* **48**, 745–768 (2006).
Mesa, D. et al., *A&A* **576**, A121, A121 (2015), linkADS.
Mesa, D. et al., *A&A* **593**, A119, A119 (2016), linkADS.
Meshkat, T. et al., *AJ* **154**, 245, 245 (2017), linkADS.
Middleton, P. and J. Brock, *Journal of Colloid and Interface Science* **54**, 249–264 (1976), linkADS.
Mignone, A. et al., *ApJS* **198**, 7, 7 (2012), linkADS.
Mignone, A. et al., *ApJS* **244**, 38, 38 (2019), linkADS.
Miller, K. A. and J. M. Stone, *ApJ* **534**, 398–419 (2000), linkADS.
Moór, A. et al., *ApJ* **826**, 123 (2016).
Morbidelli, A. et al., *AJ* **140**, 1391–1401 (2010), linkADS.
Morfill, G. E. and H. J. Voelk, *ApJ* **287**, 371–395 (1984), linkADS.
Mouillet, D. et al., *MNRAS* **292**, 896 (1997), linkADS.
Müller, A. et al., *A&A* **617**, L2, L2 (2018), linkADS.
Müller, H., *Fortschrittsberichte über Kolloide und Polymere* **27**, 223–250 (1928).
Musiolik, G. and G. Wurm, *ApJ* **873**, 58, 58 (2019), linkADS.
Musiolik, G. et al., *ApJ* **827**, 63, 63 (2016), linkADS.
Muto, T. et al., *ApJ* **748**, L22, L22 (2012), linkADS.
Nakagawa, Y. et al., *icarus* **45**, 517–528 (1981), linkADS.
Nakagawa, Y. et al., *icarus* **67**, 375–390 (1986), linkADS.
Nesvold, E. R. and M. J. Kuchner, *ApJ* **798**, 83, 83 (2015), linkADS.
Niethammer, B. and J. J. L. Velázquez, *Communications in Mathematical Physics* **318**, 505–532 (2013), linkADS.
Niethammer, B. et al., *Journal of Statistical Physics* **164**, 399–409 (2016), linkADS.
Niethammer, B. et al., *Annales de L'Institut Henri Poincare Section (C) Non Linear Analysis* **33**, 1223–1257 (2016), linkADS.
Nittler, L. R. and F. Ciesla, *ARA&A* **54**, 53–93 (2016), linkADS.
O'dell, C. R. and Z. Wen, *ApJ* **436**, 194 (1994), linkADS.
Ogilvie, G. I., *MNRAS* **325**, 231–248 (2001), linkADS.
Ohtsuki, K. et al., *icarus* **83**, 205–215 (1990), linkADS.
Okuzumi, S. et al., *ApJ* **707**, 1247–1263 (2009), linkADS.
Okuzumi, S. et al., *ApJ* **731**, 95, 95 (2011), linkADS.
Okuzumi, S. et al., *ApJ* **752**, 106, 106 (2012), linkADS.
Ormel, C. W. and B. Liu, *A&A* **615**, A178, A178 (2018), linkADS.
Ormel, C. W. et al., *A&A* **461**, 215–232 (2007), linkADS.
Paszun, D. and C. Dominik, *A&A* **507**, 1023–1040 (2009), linkADS.
Paul, J. and J. Kumar, *Mathematical Methods in the Applied Sciences* **41**, 2715–2732 (2018), linkADS.
Pavliotis, G. A. and A. M. Stuart, *Multiscale methods*, Vol. 53, Texts in Applied Mathematics, Averaging and homogenization (Springer, New York), pp. xviii+307.
Pavlov, A. et al., in Advanced software and control for astronomy ii, Vol. 7019, *Proc. SPIE* (), p. 701939, linkADS.

Pawellek, N. and A. V. Krivov, *MNRAS* **454**, 3207–3221 (2015), linkADS.
Petit, C. et al., in Adaptive optics systems iv, Vol. 9148, *Proc. SPIE* (), 91480O, linkADS.
Petit, J.-M. and P. Farinella, *Celestial Mechanics and Dynamical Astronomy* **57**, 1–28 (1993), linkADS.
Pilinis, C., *Atmospheric Environment* **24**, 1923–1928 (1990), linkADS.
Pilinis, C. et al., *Atmospheric Environment* **21**, 943–955 (1987), linkADS.
Pinte, C. and G. Laibe, *A&A* **565**, A129, A129 (2014), linkADS.
Pinte, C. et al., *A&A* **459**, 797–804 (2006), linkADS.
Pinte, C. et al., *A&A* **469**, 963–971 (2007), linkADS.
Pinte, C. et al., *A&A* **609**, A47, A47 (2018), linkADS.
Pinte, C. et al., *ApJ* **890**, L9, L9 (2020), linkADS.
Piotrowski, S. I., *Acta Astronomica* **6**, 115–138 (1953), linkADS.
Piskunov, V. N. and A. I. Golubev, *Journal of Aerosol Science* **33**, 51–63 (2002), linkADS.
Pollack, J. B. et al., *icarus* **124**, 62–85 (1996), linkADS.
Pope, S. B., *Physics of Fluids* **14**, 2360–2375 (2002), linkADS.
Pratsinis, S. E., *Journal of Colloid and Interface Science* **124**, 416–427 (1988), linkADS.
Press, W. H. et al., *Numerical recipes in FORTRAN. The art of scientific computing* (Cambridge Univ. Press), linkADS.
Price, D. J. et al., **35**, e031, e031 (2018), linkADS.
Pringle, J. E., *ARA&A* **19**, 137–162 (1981), linkADS.
Pruppacher, H. R. and J. D. Klett, *Nature* **284**, 88 (1980), linkADS.
Pruppacher, H. and J. Klett, 'Microstructure of atmospheric clouds and precipitation,' in *Microphysics of clouds and precipitation* (Springer Netherlands, Dordrecht), pp. 10–73.
Racine, R. et al., *PASP* **111**, 587–594 (1999), linkADS.
Rajagopal, E., *Kolloid-Zeitschrift* **167**, 17–23 (1959).
Rajesh Kumar Jitendra Kumar, G. W., *Kinetic Related Models* **7**, 713 (2014).
Rameau, J. et al., *A&A* **553**, A60, A60 (2013), linkADS.
Ramkrishna, D., *Population balances: theory and applications to particulate systems in engineering* (Elsevier).
Rhee, J. H. et al., *ApJ* **660**, 1556–1571 (2007), linkADS.
Rigopoulos, S. and A. G. Jones, *AIChE Journal* **49**, 1127–1139 (2003).
Riols, A. and G. Lesur, *A&A* **617**, A117, A117 (2018), linkADS.
Risken, H. and H. Haken, *The Fokker-Planck Equation: Methods of Solution and Applications Second Edition* (Springer).
Risken, H., 'Fokker-planck equation,' in *The fokker-planck equation* (Springer), pp. 63–95.
Ros, K. and A. Johansen, *A&A* **552**, A137, A137 (2013), linkADS.
Ros, K. et al., *A&A* **629**, A65, A65 (2019), linkADS.
Safronov, V. S., *Evolution of the protoplanetary cloud and formation of the earth and planets.* (), linkADS.
Saito, O., *Journal of the Physical Society of Japan* **13**, 198–206 (1958), linkADS.
Samland, M. et al., *A&A* **603**, A57, A57 (2017), linkADS.
Sandu, A., *Aerosol Science Technology* **40**, 261–273 (2006), linkADS.
Sauvage, J.-F. et al., in Adaptive optics systems ii, Vol. 7736, *Proc. SPIE* (), 77360F, linkADS.
Sawford, B., *Atmospheric Environment (1967)* **18**, 2405–2411 (1984).
Schneider, G. et al., *AJ* **148**, 59, 59 (2014), linkADS.
Schräpler, R. and T. Henning, *The Astrophysical Journal* **614**, 960 (2004).
Schumann, T. E. W., *QJRAS* **66**, 195–208 (1940), linkADS.
Scott, E. R. D., *Annual Review of Earth and Planetary Sciences* **35**, 577–620 (2007), linkADS.
Scott, W. T., *JAS* **25**, 54–65 (1968), linkADS.
Sengupta, D. et al., *ApJ* **874**, 26, 26 (2019), linkADS.

Shakura, N. I. and R. A. Sunyaev, *A&A* **500**, 33–51 (1973), linkADS.
Shannon, A. et al., *MNRAS* **462**, L116–L120 (2016), linkADS.
Shao, Y., *Physica D Nonlinear Phenomena* **83**, 461–477 (1995), linkADS.
Sheng, C. and X. Shen, *Journal of Aerosol Science* **37**, 16–36 (2006), linkADS.
Shu, C.-W. and S. Osher, *Journal of Computational Physics* **77**, 439–471 (1988), linkADS.
Siess, L. et al., *A&A* **358**, 593–599 (2000), linkADS.
Silk, J. and T. Takahashi, *ApJ* **229**, 242–256 (1979), linkADS.
Simha, R., *Journal of Applied Physics* **12**, 569–578 (1941), linkADS.
Simmel, M. et al., *Atmospheric Research* **61**, 135–148 (2002), linkADS.
Simpson, J. C. et al., *Ap&SS* **61**, 65–80 (1979), linkADS.
Smith, M. and T. Matsoukas, *Chemical Engineering Science* **53**, 1777–1786 (1998).
Smoluchowski, M. V., *Zeitschrift fur Physik* **17**, 557–585 (1916), linkADS.
Soong, S.-T., *JAS* **31**, 1262–1285 (1974), linkADS.
Soummer, R., *ApJ* **618**, L161–L164 (2005), linkADS.
Soummer, R. et al., *ApJ* **755**, L28, L28 (2012), linkADS.
Spitzer Lyman, J., *ApJ* **93**, 369 (1941), linkADS.
Srivastava, R. C., *JAS* **35**, 108–117 (1978), linkADS.
Steinpilz, T. et al., *ApJ* **874**, 60, 60 (2019), linkADS.
Stepinski, T. F. and P. Valageas, *A&A* **319**, 1007–1019 (1997), linkADS.
Stoll, M. H. R. and W. Kley, *A&A* **594**, A57, A57 (2016), linkADS.
Stone, J. M. et al., *ApJS* **178**, 137–177 (2008), linkADS.
Stone, J. M. et al., *ApJS* **249**, 4, 4 (2020), linkADS.
Stone, J. M. et al., *ApJ* **818**, L12, L12 (2016), linkADS.
Strom, K. M. et al., *AJ* **97**, 1451 (1989), linkADS.
Su, K. Y. L. et al., *ApJ* **799**, 146, 146 (2015), linkADS.
Suck, S. H. and J. R. Brock, *Journal of Aerosol Science* **10**, 581–590 (1979), linkADS.
Swift, D. L. and S. Friedlander, *Journal of Colloid Science* **19**, 621–647 (1964).
Takeuchi, T. and D. N. C. Lin, *ApJ* **581**, 1344–1355 (2002), linkADS.
Tamura, M., in Exoplanets and disks: their formation and diversity, Vol. 1158, edited by T. Usuda et al., American Institute of Physics Conference Series (), pp. 11–16, linkADS.
Tanaka, H. et al., *icarus* **123**, 450–455 (1996), linkADS.
Tanaka, H. et al., *ApJ* **625**, 414–426 (2005), linkADS.
Taylor, G. I., *Proceedings of The London Mathematical Society* **s2-20**, 196–212 (1922).
Teague, R. et al., *ApJ* **860**, L12, L12 (2018), linkADS.
Testi, L. et al., in Protostars and planets vi, edited by H. Beuther et al. (), p. 339, linkADS.
Teyssier, R., *A&A* **385**, 337–364 (2002), linkADS.
Thalmann, C. et al., in Ground-based and airborne instrumentation for astronomy ii, Vol. 7014, *Proc. SPIE* (), 70143F, linkADS.
Thomson, D. J., *Journal of Fluid Mechanics* **180**, 529–556 (1987), linkADS.
Trautmann, T. and C. Wanner, *Atmospheric Environment* **33**, 1631–1640 (1999), linkADS.
Tsiganis, K. et al., *Nature* **435**, 459–461 (2005), linkADS.
Turkevich, J., *American Scientist* **47**, 97–119 (1959).
Turner, N. J. et al., *ApJ* **708**, 188–201 (2010), linkADS.
Tzivion (Tzitzvashvili), S. et al., *Journal of the Atmospheric Sciences* **46**, 3312–3328 (1989).
Tzivion, S. et al., *Journal of Computational Physics* **148**, 527–544 (1999), linkADS.
Uyama, T. et al., *AJ* **156**, 63, 63 (2018), linkADS.
van der Marel, N. et al., *Science* **340**, 1199–1202 (2013), linkADS.
van Dongen, P. G. J. and M. H. Ernst, *Phys. Rev. Lett.* **54**, 1396–1399 (1985), linkADS.
van Dongen, P. G. J. and M. H. Ernst, *Journal of Statistical Physics* **50**, 295–329 (1988), linkADS.

Vericel, A. and J.-F. Gonzalez, *MNRAS* **492**, 210–222 (2020), linkADS.
Vigan, A. et al., *MNRAS* **407**, 71–82 (2010), linkADS.
Vigan, A. et al., *A&A* **544**, A9, A9 (2012), linkADS.
Vigan, A. et al., *A&A* **603**, A3, A3 (2017), linkADS.
Villermaux, E., *Annual Review of Fluid Mechanics* **39**, 419–446 (2007), linkADS.
Voelk, H. J. et al., *A&A* **85**, 316–325 (1980), linkADS.
Wada, K. et al., *ApJ* **661**, 320–333 (2007), linkADS.
Wada, K. et al., *ApJ* **677**, 1296–1308 (2008), linkADS.
Wahhaj, Z. et al., *ApJ* **773**, 179, 179 (2013), linkADS.
Wallis, G., *ZAMM - Journal of Applied Mathematics and Mechanics / Zeitschrift für Angewandte Mathematik und Mechanik* **70**, 508–508 (1990).
Walsh, K. J. et al., *Meteoritics and Planetary Science* **47**, 1941–1947 (2012), linkADS.
Wang, C.-S., 'a Mathematical Study of the Particle Size Distribution of Coagulating Disperse Systems.,' PhD thesis (California Institute of Technology.), linkADS.
Wang, K.-G. and J. Masoliver, *Physica A Statistical Mechanics and its Applications* **231**, 615–630 (1996), linkADS.
Wang, L.-P. et al., *Journal of Computational Physics* **226**, 59–88 (2007), linkADS.
Weidenschilling, S. J., *MNRAS* **180**, 57–70 (1977), linkADS.
Weidenschilling, S. J., *Ap&SS* **51**, 153–158 (1977), linkADS.
Weidenschilling, S. J., *Icarus* **44**, 172–189 (1980), linkADS.
Weintraub, D. A. et al., *ApJ* **340**, L69 (1989), linkADS.
Werner, M. W., *Advances in Space Research* **36**, 1048–1049 (2005), linkADS.
Wetherill, G. W., *icarus* **88**, 336–354 (1990), linkADS.
Whipple, F. L., in From plasma to planet, edited by A. Elvius (), p. 211, linkADS.
Wilkins, D., *Journal of Physics A Mathematical General* **15**, 1175–1178 (1982), linkADS.
Williams, M. M. R. and S. K. Loyalka, (1991).
Windmark, F. et al., *A&A* **540**, A73, A73 (2012), linkADS.
Woitke, P., in European physical journal web of conferences, Vol. 102, European Physical Journal Web of Conferences (), p. 7, linkADS.
Yamamoto, T. et al., *ApJ* **783**, L36, L36 (2014), linkADS.
Yang, M.-l. et al., *Applied Mathematics and Mechanics* **35**, 1353–1360 (2014).
Youdin, A. N. and J. Goodman, *ApJ* **620**, 459–469 (2005), linkADS.
Youdin, A. N. and Y. Lithwick, *icarus* **192**, 588–604 (2007), linkADS.
Young, K. C., *JAS* **32**, 965–973 (1975), linkADS.
Ysard, N. et al., *A&A* **631**, A88, A88 (2019), linkADS.
Zhang, X. and C.-W. Shu, *Journal of Computational Physics* **229**, 3091–3120 (2010), linkADS.
Zhu, Z. et al., *ApJ* **801**, 81, 81 (2015), linkADS.
Ziff, R. M. and E. D. McGrady, *Journal of Physics A Mathematical General* **18**, 3027–3037 (1985), linkADS.
Ziff, R. M. and E. D. McGrady, *Macromolecules* **19**, 2513–2519 (1986), linkADS.
Zsom, A. and C. P. Dullemond, *A&A* **489**, 931–941 (2008), linkADS.
Zsom, A. et al., *A&A* **534**, A73, A73 (2011), linkADS.
Zuckerman, B., *ARA&A* **39**, 549–580 (2001), linkADS.
Zuckerman, B. and I. Song, *ARA&A* **42**, 685–721 (2004), linkADS.
Zuckerman, B. and I. Song, *ApJ* **603**, 738–743 (2004), linkADS.
Zuckerman, B. and I. Song, *ApJ* **758**, 77, 77 (2012), linkADS.
Zuckerman, B. et al., *Nature* **373**, 494–496 (1995), linkADS.
Zuckerman, B. et al., *ApJ* **732**, 61, 61 (2011), linkADS.
Zuckerman, B. et al., *ApJ* **778**, 5, 5 (2013), linkADS.